INVESTIGATION ON THE SYNTHESIS AND APPLICATION ASPECTS OF ORGANIC-INORGANIC METAL HALIDE PEROVSKITES

Submitted by

Nripen Besra

To

Jadavpur University

For the degree of

DOCTOR OF PHILOSOPHY (SCIENCE)

Department of Physics

Jadavpur University
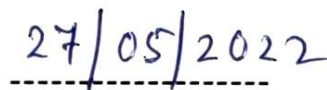
Kolkata-700032

India

April 2022

1

DECLARATION

I hereby declare that this thesis entitled *"Investigation on the synthesis and application aspects of organic-inorganic metal halide perovskites"* contains literature survey and my original research work as a part for the degree of **Doctor of Philosophy (Science)** during academic session 2016-2021. It has not been submitted for any degree or examination in any other university. I further declare that all the resources I have used or quoted have been indicated and acknowledged by complete references.

27/05/2022

(Nripen Besra)   Date

CERTIFICATE FROM THE SUPERVISOR

This is to certify that the thesis entitled "*Investigation on the synthesis and application aspects of organic-inorganic metal halide perovskites*" is submitted by **Mr. Nripen Besra**, who got his name registered on 17th August 2016 for the award of **Ph.D. (Science)** degree in the **Dept. of Physics, Jadavpur University, Kolkata 700032, India.** This thesis is absolutely based upon his own work under the supervision of **Prof. Kalyan Kumar Chattopadhyay.** Neither his thesis nor any part of it has been submitted for any degree/diploma or any other academic award anywhere before.

26.5.22

[Dr. Kalyan Kumar Chattopadhyay]

Professor

Dept. of Physics

Jadavpur University

Kolkata-700032, India

Dr. K. K. Chattopadhyay
Professor
Department of Physics
Jadavpur University, Kolkata-700 032

5

Dedicated to

All the enthusiastic minds who are working towards a vision of serving human kind through continuous striving for knowledge and wisdom with an indomitable willpower against the various adversities and obstacles in life

ACKNOWLEDGEMENTS

Mr. Suvankar Mandal, Mr. Souvik Bhattacharjee and Mrs. Shrabani Ghosh for their cooperation and help at various occasions. I was really lucky to have a group of friends like them who were always available at any circumstance. This 5-6 years span was one of the most precious and golden times of my life, the memory of which will be cherished in my mind for ever.

At this precious moment, let me convey my gratitude to my parents, my granny and my younger brother, Mr. Bidyut Besra. Their exceptional support, love and sacrifices gave me the courage and strength to struggle in life and achieve the goals which was once beyond imagination. In addition to them, I am also blessed with a special person in my life, Smt. Shilpam Goswami, who supported me with her unconditional love, patience and adjustability during various ups and downs.

I am grateful to all my teachers who shaped and moulded my inner being, my reviewers who helped improve the quality of my research works and all my well wishers. I am also grateful to the lessons which I learnt from the failures and tough situations in life.

In the last but not the least, I must acknowledge my special gratitude to the Director, NPOL (Naval Physical & Oceanographic Laboratory), Kochi-21 for allowing me to write and submit this thesis.

April 2022   (Nripen Besra)

Thin Film and Nanoscience Laboratory

Department of Physics, Jadavpur University

Kolkata 700032, INDIA

LIST OF FIGURES

(b) after FE measurements

Figure 6.1: X-ray diffraction (XRD) pattern of the as prepared pristine $CH_3NH_3PbI_3$ powder

Figure 6.2: (a) Low magnification FESEM image of the upper surface, (b) high magnification FESEM image of the upper surface, (c) low magnification cross FESEM image, (d) high magnification cross image of the sample grown in AAO template respectively

Figure 6.3: UV-Vis. reflectance spectrum of the as synthesized sample

Figure 6.4: (a) Schematic of the FE set up, (b & c) J-E characteristic curves and the corresponding FN plots at different illumination conditions

Figure 6.5: Plots of turn on field and enhancement factor at various light intensities

Figure 6.6: Schematic of (a) photo induced field emission, emission mechanism under (b) dark, (c) 0.2 mW/cm^2 and (d) 0.5 mW/cm^2 light intensities

Figure 6.7: 2D electric field simulation for (a) array and (b) single NR under dark; Simulation for single NR under plane polarized light with electric field components (c-f) 60, 80, 100 and 120 V/m respectively under no bias

Figure 7.1: (a) XRD patterns of MALI, V_2O_5, S1, S2 and S3; FESEM images of (b) MALI, (c) V_2O_5 and (d) S2; Insets showing their high magnification images respectively

Figure 7.2: (a&b) Low magnification FESEM images of S1 and S3; (c&d) their respective high magnification images

Figure 7.3: (a&b) High resolution TEM images of S2; (c&d) Crystal planes captured in HRTEM images

Figure 7.4: Full XPS survey scan of S2 (charge corrected)

LIST OF TABLES

LIST OF PUBLICATIONS

(A) Journal papers

[1] **Perovskites beyond photovoltaics: Field emissions from morphology-tailored nanostructured methylammonium lead triiodide**
Nripen Besra, Shreyasi Pal, Bikram Kr. Das and Kalyan Kr. Chattopadhyay
Physical Chemistry Chemical Physics, 2017, **19**, 26708-26717.

[2] **Incorporation of V_2O_5 Nanorods as an Alternative Approach to Enhance the Device Performance of Perovskite Photodetector: A Step towards Stability against Ambient Water Species**
Nripen Besra, Kausik Sardar, Soumen Maiti, Pranab Kumar Sarkar, Tufan Paul, Subhasish Thakur, Gautam Majumdar, and Kalyan Kumar Chattopadhyay
Dalton Transactions, 2020, **49**, 15788-15799.

[3] **$CH_3NH_3PbI_3$ as a radio-frequency decoupling capacitor: Interplay between Maxwell-Wagner polarization and pseudo inductive response**
Nripen Besra, Kausik Sardar, Nilesh Majumder, Souvik Bhattacharjee, Anjan Das, Bikram Das, Saikat Sarkar and Kalyan Kr. Chattopadhyay
Journal of Physics D: Applied Physics, 2021, **54**, 175105.

[4] **Photo Enhanced Electron Field Emission from Vertically Aligned $CH_3NH_3PbI_3$ Nanorods Grown in AAO Template**
Nripen Besra, Supratim Maity, Tufan Paul and Kalyan Kr. Chattopadhyay
Journal of Physics and Chemistry of Solids, 2022, **161**, 110457.

[5] **Enhanced electron emission from ternary solid solution-MWCNT hybrid with theoretical validation**
Shrabani Ghosh, Supratim Maity, Ankita Chandra, Bikram Kumar Das, **Nripen Besra**, Samrat Sarkar, Sourav Sarkar and Kalyan Kumar Chattopadhyay
Materials Science in Semiconductor Processing, 2021, **127**, 105674.

[6] **New Class of Trimetallic Oxide Hierarchical Mesoporous Array on Woven Fabric: Electrode for high-Performance and Stable battery type Ultracapacitor**
Subhasish Thakur, Soumen Maiti, Kausik Sardar, Kausik Chanda, **Nripen Besra**, Partha Bairi, Karamjyoti Panigrahi, Tufan Paul and Kalyan Kr. Chattopadhyay

Journal of Energy Storage, 2021, **35**, 102249.

[7] **Hybrid piezoelectric nanogenerator based on PVDF film and vertically aligned ZnO nanorods for energy harvesting applications**

Suvankar Mondal, Sayantani Das, Soumen Maiti, **Nripen Besra**, Tufan Paul and Kalyan Kr. Chattopadhyay

International Journal of Nanotechnology, 2021, **18**, 669-678.

[8] **Graphene anchored P-type CuBO$_2$ nanocrystals for a transparent cold cathode**

Saswati Santra, Nirmalya Sankar Das, **Nripen Besra**, Diptonil Banerjee and Kalyan Kr. Chattopadhyay

Langmuir, 2017, **33**, 9961-9971.

[9] **Tunable cathodoluminescence over the entire visible window from all-inorganic perovskite CsPbX$_3$ 1D architecture**

Tufan Paul, Biplab Kr. Chatterjee, Soumen Maiti, Saikat Sarkar, **Nripen Besra**, Bikram Kr. Das, Karamjyoti Panigrahi, Subhasish Thakur, Uttam Kr. Ghorai and Kalyan Kr. Chattopadhyay

Journal of Materials Chemistry C, 2018, **6**, 3322-3333.

[10] **Geometrically intricate sheet-on-rod/flake hierarchy embracing cobaltosic and manganese oxides over flexible carbon scaffold for binder free high energy density supercapacitor**

Subhasish Thakur, Soumen Maiti, Tufan Paul, **Nripen Besra**, Saikat Sarkar, Kalyan Kr. Chattopadhyay

CrystEngComm, 2018, **20**, 6183-6196.

[11] **Tailored CsPbX$_3$ Nanorods for Electron-Emission Nanodevices**

Tufan Paul, Soumen Maiti, **Nripen Besra**, Biplab Kr. Chatterjee, Bikram Kumar Das, Subhasish Thakur, Saikat Sarkar, Nirmalya Sankar Das and Kalyan Kumar Chattopadhyay

ACS Applied Nano Materials, 2019, 2 (9), 5942–5951.

[12] **Hierarchical Assembly of MnO$_2$ Nanosheet on CuCo$_2$O$_4$ Nanoflake over fabric scaffold for Symmetric Supercapacitor**

Kausik Chanda, Soumen Maiti, Samrat Sarkar, Partha Bairi, Subhasish Thakur, Kausik Sardar, **Nripen Besra**, Nirmalya Das and Kalyan Chattopadhyay

ACS Applied Nano Materials, 2021, **4**, 1420−1433.

[13]   Amalgamation of MnWO4 nanorods with amorphous carbon nanotubes for highly stabilized energy efficient supercapacitor electrodes

Kausik Sardar, Subhasish Thakur, Soumen Maiti, **Nripen Besra**, Partha Bairi, Kausik Chanda, Gautam Majumdar and Kalyan Kr. Chattopadhyay

Dalton Transactions, 2021, **50**, 5327-5341.

(B) Conference proceedings

[1] Low dimensional CH₃NH₃PbBr₃ cubes for persistent luminescence: Energy variation of electron excitation

Nripen Besra, Tufan Paul, Subhasish Thakur, Saikat Sarkar, Kausik Sardar, Kausik Chanda, Anjan Das and Kalyan Kr. Chattopadhyay

AIP Conference Proceedings 1942, 120027 (2018)

[2] Room Temperature Solution Processed Low Dimensional CH₃NH₃PbI₃ NIR Detector

Nripen Besra, Tufan Paul, Pranab Kr. Sarkar, Subhasish Thakur, Saikat Sarkar, Anjan Das, Kausik Chanda, Kausik Sardar and Kalyan Kr. Chattopadhyay

AIP Conference Proceedings 1953, 030210 (2018)

[3] Efficient blue emission from ambient processed all-inorganic CsPbBr₂Cl perovskite cubes

Tufan Paul, Biplab Kr. Chatterjee, Soumen Maiti, **Nripen Besra**, Subhasish Thakur, Saikat Sarkar, Kausik Chanda, Anjan Das, Kausik Sardar and Kalyan Kr. Chattopadhyay

AIP Conference Proceedings 1942, 120026 (2018)

[4] Fabrication of all-inorganic CsPbBr₃ perovskite nanocubes for enhanced green photoluminescence

Tufan Paul, Biplab Kr. Chatterjee, **Nripen Besra**, Subhasish Thakur, Saikat Sarkar and Kalyan Kr. Chattopadhyay

Materials Today: Proceedings 5 (2018) 2234–2240

[5] Luminescence Behaviour of Room Temperature Chemical Processed All-Inorganic CsPbCl₃ Perovskite Cubes

Tufan Paul, Biplab Kr. Chatterjee, Soumen Maiti, **Nripen Besra**, Subhasish Thakur, Saikat Sarkar, Kausik Chanda, Anjan Das, Pranab Kr. Sarkar, Kausik Sardar and Kalyan Kr. Chattopadhyay

AIP Conference Proceedings 1953, 030085 (2018)

[6] 3D hierarchical architecture based on 1D TiO$_2$ nanorod and 2D MnO$_2$ nanoflake for high performance supercapacitor electrode

Subhasish Thakur, Soumen Maiti, Anubhab Acharya, Tufan Paul, **Nripen Besra**, Saikat Sarkar and Kalyan Kr. Chattopadhyay

AIP Conference Proceedings 1942, 140071 (2018)

[7] Hierarchical heterostructure of MoS$_2$ flake anchored on TiO$_2$ sphere for supercapacitor application

Kausik Chanda, Subhasish Thakur, Soumen Maiti, Anubhab Acharya, Tufan Paul, **Nripen Besra**, Saikat Sarkar, Anjan Das, Kausik Sardar and Kalyan Kr. Chattopadhyay

AIP Conference Proceedings 1953, 030138 (2018)

TABLE OF CONTENTS

ABSTRACT

Metal oxides having the chemical formula of ABO_3 are in general known as perovskite materials. They exhibit many interesting and intriguing properties from both the theoretical and the application point of view. Many interesting properties such as colossal magnetoresistance, ferroelectricity, superconductivity, charge ordering, spin dependent transport, high thermo power etc. and the interplay of structural, magnetic and transport properties are commonly observed features in this family. Recently there is tremendous interest on organic-inorganic metal halide perovskites (for example, Methylammonium lead halide), the most popular being Methylammonium lead iodide i.e., $CH_3NH_3PbI_3$. Such hybrid metal halides have shown very good performance in photovoltaics with more than 22% efficiency. Large carrier diffusion length, high mobility, low excitonic binding energy, tunability of the energy band gap over a wide range, etc. are the reasons for its excellent optoelectronic properties. Besides these intriguing features, facile and budgetary preparation methods also add up an additional advantage to their widespread usage.

This dissertation describes facile synthesis procedures to prepare such beautiful and functional materials i.e. Methylammonium lead halide and some devices based upon them. After characterizing the synthesized materials having various morphological features, their non-trivial device applications, such as electron field emission, have been explored in detail. Starting from a formal and preliminary idea of perovskites and their classes, Chapter 1 elaborates the emergence and significance of Methylammonium lead halides from application point of view. In addition to the various advantages such as wide band tunability and easy synthesis routes, the intriguing properties and the current challenges have also been discussed in this chapter.

With a literature review of past work in Chapter 2, Chapter 3 demonstrates the characterization techniques and tools used in this study. Chapter 4 describes the materials synthesis and device fabrication protocols adopted in this work. Identifying the necessity to explore nontrivial application possibilities of hybrid metal halide perovskites other than photovoltaics, Chapter 5 presents a detail investigation of electron field emission from Methylammonium lead triiodide ($CH_3NH_3PbI_3$) nanostructures which were prepared by a facile room-temperature wet chemical method via simple variation of the synthesis parameters. Prominent electron emission was obtained from nanorods emitters which was also corroborated with theoretical simulations.

Chapter 6 describes further enhancement in the emission performance by vertical orientations of the nanorods emitters under light illumination. The vertically aligned nanostructures showed superior emission behavior compared to what obtained in the earlier studies with scattered nanostructures. Excitation with near infrared light boosted the emission parameters furthermore. Susceptibility of $CH_3NH_3PbI_3$ towards atmospheric water is an alarming issue, which hinders its long-term commercial application. Chapter 7 addresses this issue and demonstrates a strategy to improve photodetection performance with robust moisture resistance by low dimensional V_2O_5 incorporation into $CH_3NH_3PbI_3$. The modified sample showed manifold improvement in the device performance in terms of better on/off ratio, responsivity, detectivity, external quantum efficiency and response times.

Chapter 8 describes bias dependent impedance spectroscopy of $CH_3NH_3PbI_3$ and unlocks the possible relaxation mechanisms in radio frequency regime. Two relaxation entities were identified to manifest into capacitive/inductive switching in form of pseudo-negative capacitance. The findings indicate application possibility of $CH_3NH_3PbI_3$ as decoupling capacitor in electrical circuits.

The thesis finally ends with Chapter 9 where it concludes with a summary of the research works and findings during the execution of this Ph.D. work. The chapter also projects a future outlook to take up further research in this direction.

(Nripen Besra)

April 2022
Thin Film and Nanoscience Laboratory
Department of Physics, Jadavpur University
Kolkata 700032, INDIA

Introduction

For thousands of years, ages have been named after the materials prevailed at those eras e.g. Stone Age, Bronze Age, Iron Age and so on.[1] Materials have always defined and shaped human civilization by their technological uses. We, the present generation, are not any exception. When the entire globe is at the bottleneck of the conventional energy, scientists are desperately looking for something (a material) that can harness energy for meeting our gigantic energy demand. When talking about the alternative unconventional energy solutions, solar cells come into our mind first. Solar cells based on Silicon (Si) or other materials like Cadmium Telluride (CdTe), etc. have captured the markets as alternative energy technologies. But researchers are trying theirbest to make these cells cheaper, more durable, more efficient and obviously more environment friendly. Perovskites in this context can help us a great deal. With easy and cost-effective synthesis techniques, the materials come with large band gap tunability, high carrier mobility and most importantly, large light absorption coefficient. Apart from solar cells, other important technologies like LED (**L**ight **e**mitting **d**iode), photodetector, etc. have also been devised with it.

1.1. A brief idea on perovskites and their classifications

The origin of the nomenclature 'Perovskite' dates back to the discovery of a calcium titanate based mineral in the Ural Mountains by a German scientist Gustav Rose in the year 1839. In the honor of a Russian Mineralogist Lev Von Perovski, the mineral was later named as 'Perovskite'.[2] However after a certain time, the terminology became more generic to cover a large class of materials. Materials with the crystal structure of ABO_3 i.e. similar to that of $CaTiO_3$ are now generally identified as perovskites. The simplest crystal structure of a perovskite unit cell is a cubic one which is shown in Figure 1.1. The cell parameters are defined as: a = b = c and $\alpha = \beta = \gamma = 90^0$. Allowing different elements or groups in place of A, B or O sites can lead to large spectra of materials under this common name called 'Perovskite'. The stability of these crystal structures, however, depends on Goldschmidt tolerance factor (t) defined as follows.[3]

$$t = \frac{(R_A + R_O)}{\sqrt{2}(R_B + R_O)} \tag{1.1}$$

Here R_A, R_B and R_O are ionic radii of A and B site elements and oxygen, with $R_A > R_B$. Hence, tolerance factor t is simply a ratio of distance between A and O site elements to the distance between B and O site elements considered in an ideal solid sphere model. The ratio R_B/R_O is sometimes referred to as octahedral factor μ. A stable structure should have t value in the range of $0.75 - 1$.
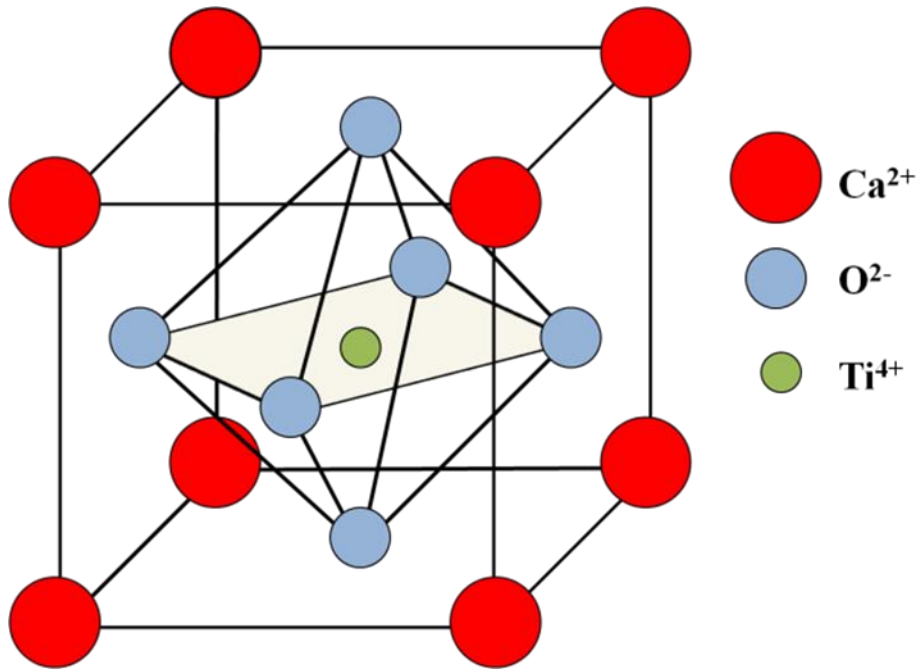
Figure 1.1: Crystal structure of $CaTiO_3$ (showing the general perovskite structure of ABO_3)

Perovskites can be mainly classified as oxide (ABO_3) and halide (ABX_3) types, where X stands for halogens i.e. Cl, Br, I, etc. A picture showing the classifications of this class of materials is provided in Figure 1.2. Further classification of oxide perovskites apart from ABO_3 (for example, $CaTiO_3$, $BaSnO_3$, etc.) e.g. layered types, double perovskites and triple perovskites are also found in literature. Chemical formulae for these types of oxide perovskites are given as: A_2BO_4 (for example, Sr_2RuO_4), $A_2BB'O_6$ (for example, Ba_2TiRuO_6) and $A_2A'B_2B'O_9$ (for example, $La_2SrCo_2FeO_9$) respectively. [4-6] Sometimes mention of other oxide type perovskites are also reported by research groups, called as homologous series comprising of $A_{n+1}B_nO_{3n+1}$, $A_nB_nO_{3n+1}$ and $Bi_2A_{n-1}B_nO_{3n+3}$. These are named as Ruddlesden-Popper, Dion-Jacobson and Aurivillius

series respectively. [7-9] The halide type, on the other side, can be classified as inorganic (e.g. $CsPbX_3$) and organic metal halide (e.g. $CH_3NH_3PbX_3$-methylammonium lead halide) types mainly. However, mixing of different types of cations ('A' part in ABX_3) can also lead to another

category of halide perovskites, which may be called organic-inorganic or hybrid types. It is to be mentioned that researchers possess a holistic view while referring $CH_3NH_3PbX_3$ as both organometal halide perovskite as well as hybrid organic-inorganic metal halide perovskite is to occasionally. [10-13]
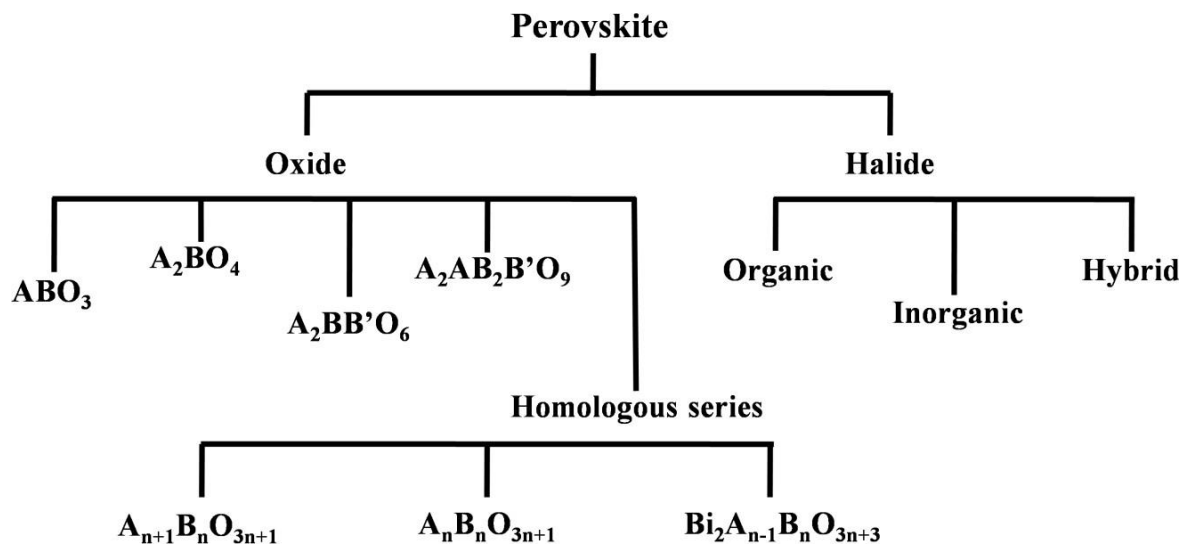
Figure 1.2: Classifications of perovskite
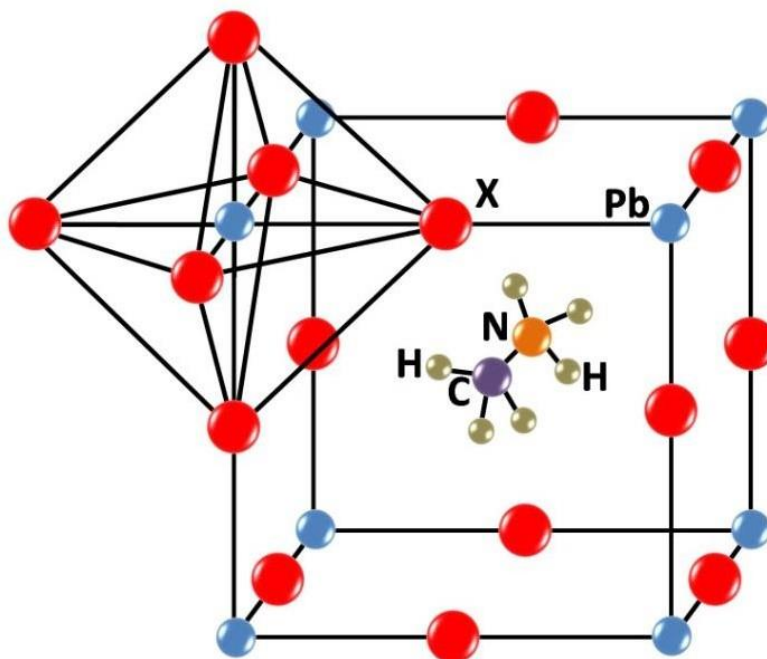
Figure 1.3: Crystal structure schematic of $CH_3NH_3PbX_3$

Exploration with Chalcogenide perovskites is also under progress.[14] Mainly found as materials for capacitor, memory devices and superconductors, low energy band gap and high crystalline distortions make them unsuitable for photovoltaics and related sectors. Coming to this thesis, it will be focused with research activities related to the organic-inorganic metal halide perovskite $CH_3NH_3PbX_3$ (mainly $CH_3NH_3PbI_3$-methylammonium lead iodide), a schematic picture of the crystal structure of which is given below (Figure 1.3). Ionic radii i.e. RA for methylamine and RB for lead cation are 0.18 and 0.119 nm respectively; whereas Rx for the halogen anions i.e. chlorine, bromine and iodine are 0.181, 0.196 and 0.220 nm respectively. The tolerance and octahedral factors for these halide materials come in the range 0.81-1.11 and 0.44-0.9 respectively.[15] The lower t values correspond to tetragonal/orthorhombic crystal structure, whereas comparatively higher t values (t > 0.89) do the cubic one. Transitions between these phases are highly dependent on temperature for all these halide perovskites. Heating the material generally leads to phase transition from low temperature tetragonal phase to high temperature cubic one. The less symmetric tetragonal phase of $CH_3NH_3PbI_3$ is reportedly the most important one, available at room temperature.

1.2. Emergence and various advantages

1.2.1. Emergence of hybrid metal halide perovskites

Although the first report on hybrid halide perovskites was documented long back in nineteenth century,[16] effective research output has come only recently during studies with thin films.[17,18] Despite anticipating photovoltaic outcomes from these studies, it wasn't taken up further due to lead toxicity and instability with tin. In 2006, it once again came back on track when solar cell based on Methylammonium lead bromide was reported to have an efficiency of 2.2%,[19] driven by the motivation grained from a work on dye sensitized solar cells showing self-organizing capability of perovskites among TiO_2 layer. An efficiency of 3.8% was achieved the next year with Methylammonium lead iodide,[20] which was further increased to 6.5% in 2011[21] by surface treatment with titanium oxide. Problems with liquid electrolytes were solved by the introduction of spiroMeOTAD (2,2',7,7'-tetrakis(N,N-di-p-methoxyphenylamine)-9,9'- spirobifluorene), a solid state hole transporting material (HTM), which stopped perovskites to dissolve into the so far used liquid dye sensitizers and thus stabilized the device with an improved efficiency of 9.7%.[22] A parallel research activity was also going on by Snaith and his team to enhance the device stability

and carrier transport by partial chlorine substitution into iodine sites.[23,24] In addition to this, introduction of thin layer of perovskite as well as replacement of TiO_2 by Al_2O_3 pushed the efficiency to 10.9%, thereby establishing electron and hole transporting character of perovskites. The cell efficiency continued to improve by partial substitution of iodine with bromine, which has smaller ionic radius.[25] The device gained more immunity in humid ambience. Efficiency of 14.1% was achieved by Gratzel et al. with morphological engineering via two step deposition technique.[26]
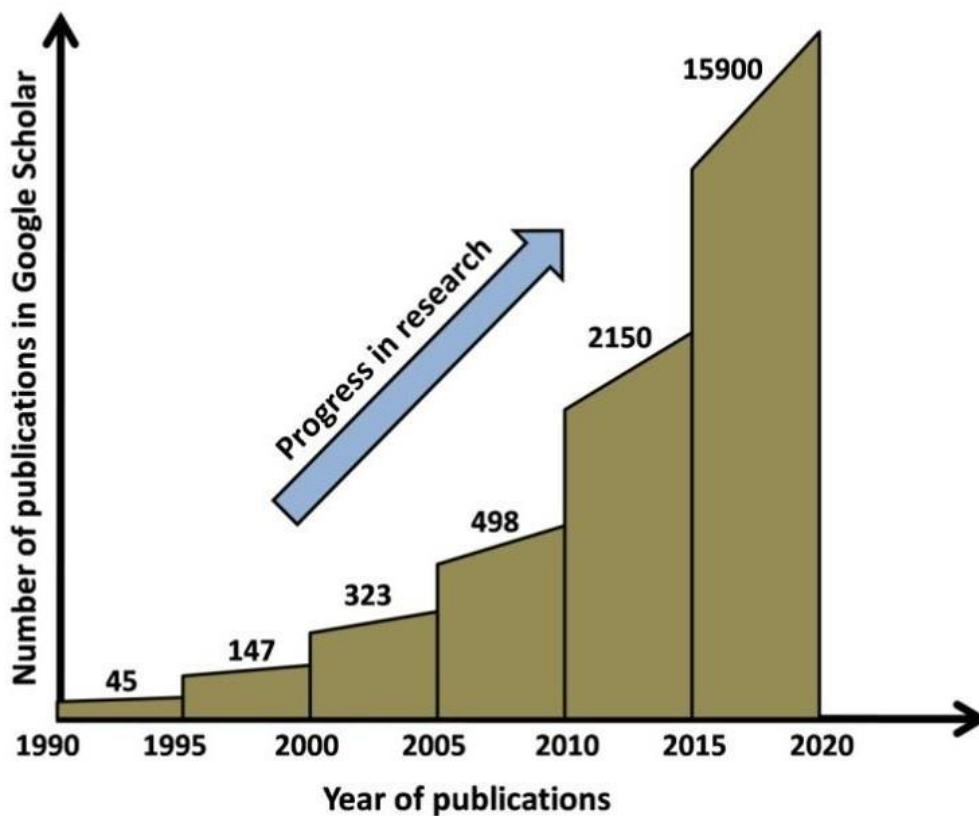
Figure 1.4: Schematic representing yearly research progress

Further morphological tuning, halide mixing and optimization of HTM layer boosted the device efficiency to 19.3% by 2014.[27,28] In 2015, efficiency of perovskite based solar cells reached a certified value of 22.1%.[39] Currently recorded efficiency of 25.2% was achieved via further device optimizations,[29] involving in situ formation of perovskite from separate PbI_2 deposition and CH_3NH_3I vapor,[30] compositional tuning of both the cations and halogen sites, specially halide mixing,[31-34] optimization of hole transport and electron transport layers,[35-38] etc. With the

experience gained so far in dye sensitized and organic device technologies, rapid progress in the research activities on halide perovskites took place owing mainly to their easy preparation methods and remarkable optoelectronic properties. A survey on the number of publications on organic-inorganic metal halide perovskites at every 5 years duration is made based on the results from Google Scholar search (Figure 1.4). Till 1990, the total number of publications is found to be 77. As revealed from this survey, the number of publications in the periods 1991-1995 and 1996-2000 were 45 and 147 respectively, increasing further to 323 in the next 5 years span i.e. from 2001 to 2005. In the period 2006-2010, total 498 documents were published on such perovskites; whereas this number reached 2150 in 2011-2016. A huge number of publications were registered in the tenure 2017-2020, with a surge of 15900. Even within this worldwide pandemic situation, a huge volume of publications (as large as 2480) has been documented till date (March 2022).

1.2.2. Technological importance of hybrid metal halide perovskites

Apart from solar cells, various other device applications have been found for organic-inorganic metal halide perovskites, some of which include lasers, LEDs, photodetectors, transistors, memory devices, charge storage devices, and so on. Advantage of using organic-inorganic hybrid halide perovskites is very prominent from these device realizations, some of which being discussed as follows.

(i) Laser: Documentation on organic-inorganic metal halide perovskite lasing was made in 2015 by Zhu et al. using solution phase recrystallized $CH_3NH_3PbI_3$ single crystal nanowires of dimensions comparable with the emitted light wavelength to play the role of Fabry Perot nanocavities.[40] With threshold value and quality factor of ~220 nJ/cm^2 and 3600 at room temperature, wideband tuning over wavelength was demonstrated using variation in stoichiometry. Stoichiometric variation in the A (cation) and X (halide) sites of ABX_3 can lead to broad wavelength tunability over the range 420-820 nm. This performance superiority in comparison to the values obtained from lasers based on its polycrystalline films, other nanostructures [41,42] and some other III-V semiconductor materials as well [43,44] mainly owe to its extraordinarily less number of non-radiative carrier recombination and high quantum yield of ~87% without any passivation treatment on its surface. Lasing from polycrystalline $CH_3NH_3PbX_3$ nanowires was also reported by Xing and his group,[45] but with inferior device performance because of poor crystalline nature of the material. This morphology dependence on lasing has been discussed in detail by Zhang et al. in a review in 2017.[46] Despite remarkable lasing outputs, the devices suffer from instability issues under long light exposure.[47-49]

Large cross-sectional absorption of multi-photons and population inversion with low threshold values were utilized by Gu et al. and Zhang et al. for devising multi-photonic pumped perovskite lasers.[50,51] In a communication published in 2019 by Kim et al., the research group reported lasing from metal halide perovskite, driven via optical pumping.[52] With two separate emitting diodes (top and bottom), nanoimprinting technology was used to design 2nd order feedback distribution into $CH_3NH_3PbI_3$. With a low threshold value of ~ 6 µJcm^{-2} with ~ 0.1 % quantum efficiency at room temperature, maximum value of the device current density was registered as ~ 2 Acm^{-2}. Maximum possible current density was projected to be ~ 2 kAcm^{-2}, which can be realized by upgraded film qualities, reduced area, low temperature and improved design in electronics. Random lasing action in $CH_3NH_3PbI_3$ 2D structure is observed with low threshold value < 0.5 nm, revealing its gain property[53] with vertical cavity surface emitting laser (VCSEL) design.[54,55] Zhang et al. in 2014 demonstrated hybrid mixed halide nanoplatelets showing solid state lasing in near infra-red regime.[41] The good lasing qualities achieved with this whispering gallery mode (WGM) design were attributed to large value of excitonic binding energy, long carrier diffusion and very good quantum yield. Similar findings are also reported with self-assembled bromine based perovskite.[56] Pioneered in 1971,[57] distributed feedback (DFB) type perovskite lasers come with cost effective mirror less architecture and broadband tunability in single mode operation having high scalability.[58] Furthermore, lasing based on halide perovskites with various morphological features e.g. micro crystals,[59] micro rods,[60] and quantum dots,[61] etc. has also been explored for achieving better quality factor.

(ii) LED: Hybrid metal halide perovskites, owing to high quantum yield with long carrier diffusion length and low non-radiative carrier recombination, have established their credentials as light emitting devices (LED).[62-64] The usual sandwich architecture allows multilayer design and a better play over device optimization with wavelength tunability. Halide varied red to green emission was demonstrated in 2014 from sandwiched halide perovskites with very good efficiency due to carrier confinement within perovskite.[65] Band gap optimized bright LEDs of 1.7 eV was also devised by energy band gap tuning via halide mixing technique.[66] Utilizing excitonic quenching and enhanced hole injection, bright light emission with increased efficiency from bromine based perovskite was reported at room temperature.[67] Solution processed $CH_3NH_3PbI_{3-x}Cl_x$ based LED emitted bright NIR photons, with very low nonradiative carrier recombination as supported by the strong photoluminescence signal.[68] The efficient light emission, gained in this work, was attributed

to very good carrier injection as a result of optimum band alignment. Among the various small-scale morphologies of halide perovskite used in LEDs, nanorods of Methylammonium lead halide are to be mentioned.[69] When compared to its thin film counterpart, the nanostructures provide larger surface area with better carrier injection and thus improve the overall device qualities.

(iii) Photodetector: Typically fabricated via room temperature solution processed cost-effective techniques,[70-76] hybrid halide perovskite showed its potential application as photodetectors covering a wide spectrum of detection range, i.e. from UV (ultra violet) to near infrared (NIR). The debut work on visible-blind UV detection from single crystalline Methylammonium lead chloride was reported in 2016.[77] Because of the large carrier mobility with long lifetime as well as the presence of heavy elements e.g. lead, iodine, bromine, etc., the detection range occasionally extends even to X-ray and gamma rays as well. Detection of energy varied X-ray (≤50 keV) with 16.4% efficiency was reportedly achieved by single crystalline halide perovskite,[78] followed by another report on X-ray detection in 2017.[79] However, the work came up with improved sensitivity of 2.1×10^4 $\mu C.Gy_{air}^{-1}.cm^{-2}$ at 8 keV radiations, achieved through dark current suppression. Bulk halide perovskite crystals suffer from various kinds of defects, which can be reduced dramatically in lower dimensions. 2D planar structures of perovskites in form of nanoflakes showed enhanced device performance due to improvements in crystal quality.[56, 80-82] Photodetector based on extremely thin Methylammonium lead halide registered photo-responsivity as high as 22 AW^{-1} at an operating bias of 1 V.[83] Photodetector made of Methylammonium lead chloride demonstrated robust detection with high detectivity and good response time (~millisecond).[84] Similar work with Methylammonium lead iodide single crystals also proved better device performance compared to its other polycrystalline counterparts.[85] Engineering of high quality single crystal helps achieve very low dark current with high gain due to less number of defects. Owing to this property, photodetectors based on single crystalline Methylammonium lead iodide nanowires were fabricated, delivering extraordinary outputs so far.[86,87] Having a dynamic range > 150 dB and 0.8 MHz frequency bandwidth (max), the device showed photoresponsivity and detectivity reaching to 10^4 A/W and 10^{12} Jones respectively. Moreover, photodetectors which can run on their own i.e. self-powered type have also been devised from hybrid halide perovskites.[88] Heterojunction architecture with metal oxides (for example, ZnO)[89] and chalcogenides (for example, MoS_2)[90] can also be found to produce very high responsivity of 1.94×10^6 A/W.

(iv) Field-effect transistor: The first documentation reporting successful fabrication of field effect

36

transistor (FET) based on hybrid halide perovskite demonstrated room temperature electrical studies with carrier mobility ~ 1 cm^2/Vs.[91] Although creating room for flexible polymer technologies, the device however suffered from instability due to material degradation. In an attempt to investigate carrier transport in $CH_3NH_3PbI_3$ thin films, use of FET demonstrated device architecture and its optimization could lead to improved device stability and reduced hysteresis loss.[92] With room temperature electron mobility of 0.5 cm^2/Vs, the work explored temperature dependence on charge transport which includes ion migration induced by point defects, disordered MA^+ orientations and temperature induced vibrations of PbX_6 octahedrons. Application possibility of halide perovskites in FETs with generic configurations was investigated by designing bottom gate devices on semitransparent and flexible substrates.[93] Ambipolar transistors based on micrometer thick high quality Methylammonium lead halide single crystals were fabricated using inverse temperature crystallization, generating less contaminated highly smooth perovskite surface.[94] With low turn on bias voltage and carrier mobility of 1.5 cm^2/Vs, the devices gave very high on/off ratio of the order of 10^5. Gate modulated room temperature FET was achieved by incorporation of dielectrics with high k value.[95] Highly reduced hysteresis was observed with balanced carrier transport throughout 100 operational cycles under dynamic bias conditions, correlating structural configuration with illumination and external electric field. To have overall performance enhancement, defect density and ion migration were reduced through cation (i.e. Cs and Rb) mixing in the 'A' sites of ABX_3.[96] The method resulted into constant retention of threshold voltage over duration as long as 10 hrs.

(v) Resistive memory devices: Potential application of hybrid metal halide perovskites as nonvolatile type memory devices were demonstrated on transparent and flexible substrate.[97] Originating from defect migration, the perovskite layer formed internal conducting channels through it and thus changed its resistance property upon external field. $CH_3NH_3PbI_{3-x}Br_x$ based low power resistive random access memory (ReRAM) was fabricated with the lowest set value for $CH_3NH_3PbBr_3$ owing to easy migration of bromine vacancies in comparison to iodine ones.[98] The lowest electric field set value was achieved to be 3.44×10^4 V/cm along with a very good retention over 10^4 s. Using ZnO and AlO_x as passivation layers, lifetime of such devices was further extended to as long as over a month in the ambient condition.[99] Core shell architecture, formed by decorating Methylammonium lead bromide nanocrystals upon Cadmium sulfide nanoribbon, was used in high performance memory device.[100] This low dimensional perovskite based device came up with a large potential window of 77.4 V and on/off ratio of 7×10^7. Paving ways toward a generic fabrication protocol applicable for other perovskite nanostructures as well, the device achieved stability for as long as 50 days with retention of 12000 s. In the context of using low-dimensional

perovskites, nanoparticles based ReRAM also gave excellent and substantial memory characteristics.[101] Passivation with ZnO layer on Methylammonium lead iodide film extended the device stability further to 3 months.[102] Resistive switching (RS) based on 2D/3D heterojunction structure gave an on/off ratio of 10^6, enduring for 2700 cycles with operating speed 0.64 ms. The highly conducting (thermal) 2D layer was speculated to obstruct silver ions to migrate into the 3D film and protect the filament from rupture.[103] Recent work on bipolar RS used bias dependent Schottky barrier formation upon accumulation of iodine interstitials and oxygen vacancies near $CH_3NH_3PbI_3/TiO_2$ interface, being asymmetrically polarized by a surrounding space charge as a consequence. Biased at -0.85 V, the device showed very good retention for > 10000 s.[104]

(vi) Energy storage devices: Methylammonium lead halide perovskite found its application as the electrode in Li ion batteries. Almost undistorted by the topotactic intercalation of Li^+ ions into perovskite structure, the device gave stable performance with ~ 200 mAhg^{-1} specific capacity.[105] When operated at 100 Hz, device based on $CH_3NH_3PbI_3$ pellets recorded energy density 34.2 Wh/kg, allowing an operating potential window as broad as 10 V. Limited by the Pb-I stretching mode, room temperature average areal capacitance of 432 mF/cm^2 was registered up to 100 kHz, followed by a significant dip afterwards.[106] Size varied microcrystals of $CH_3NH_3PbBr_3$ were prepared and their impact upon electrochemical properties in Li^+ battery was investigated. Owing to the presence of less defects and good interfacial charge transfer, stable device performance over 1000 cycles of operation was achieved.[107] Superficial faradaic process with improved rate capability was obtained in $CH_3NH_3PbI_3$ based supercapacitors.[108] Determined by pseudo-capacitance and diffusion induced intercalation processes, more than 90% capacitance retention was gained in this study, accompanied by a specific capacitance and energy density of 407 Fg^{-1} and 56.5 Whkg^{-1} respectively. Fabricating all-solid-state architecture with symmetric electrodes configuration with halide perovskites, Popoola et al. exhibited supercapacitors with the areal capacitance of 21.5 μF/cm^2, which is reportedly the highest value so far.[109] Along with power density of 5.05 W/cm^2 and performance retention > 98 % even after 1000 operational cycles, the supercapacitor showed relaxation time of 251.19 μs interpreting excellent discharging properties.

1.2.3. Advantages of hybrid metal halide perovskites

Among several advantages of organic-inorganic metal halide perovskites, ease of preparation and broadband tunability have boosted research communities to take up further investigations with this class of material from the very beginning. These two aspects, as briefed below, highly determine the materials characteristics and device performance in the ultimate.

(i) Easy synthesis routes: With inherent low formation enthalpy, crystallizing metal halide perovskites is just a matter of seconds. They are mostly deposited in form of uniform thin films by solution process and vapor phase deposition techniques at room temperature. The solution process uses a polar solvent for the precursors and films are deposited using some coating or printing technique. Rapid crystallization of perovskites with high quality is achieved by this facile technique at ambient condition. The film qualities are controlled by solution concentration and the coating related operational parameters. Uniform and pin-hole free films with high surface coverage can be deposited by vapor deposition method, driven by the high rate of ion migration in perovskites. A combination of these two methods i.e. solution processing as well as evaporation technique avoids requirement of vacuum during film formation and hence reduces cost. Chemical vapor deposition (CVD) method leads to cost-effective, large scale fabrication of perovskite thin films. With a very good control over size and ability of compositional variations, wide spectrum of morphological features in nano domain can be unlocked by colloidal and ligand assisted reprecipitation (LARP) techniques. Nanoparticles (NP) of Methylammonium lead halide are also synthesized from hot injection and template assisted methods. In addition to inexpensiveness, the later possesses a very good control over uniformity and scalability. High quality single crystalline $CH_3NH_3PbX_3$ can be formed by anti-solvent crystallization technique, yielding excellent carrier transport properties. Nanowires (NW) formed via ion exchange show large compositional variations.

(ii) Wide range tunability: The optoelectronic features of halide perovskites can be very easily enhanced by tuning the energy band gap of these materials via compositional modification over a wide range of solar spectrum.[110,111] Entire visible part i.e. 1.5-2.3 eV can be accessed by bromine mixing with iodine in Methylammonium lead iodide, giving well control over the cell efficiency with more ambient stability.[25,33] Halide varied strong luminescence was achieved with wavelength tunability giving bright green to red emission. Very good broadband photodetection with regulated spectral response was realized from bromine doped single crystalline Methylammonium lead chloride.[65,66,77] In addition to anion/halide mixing, complete or partial cation modification, for example incorporation of Formamidinium (FA) in place of Methylammonium (MA) ion, also results into tuned band gap with enlarged carrier extraction and improved thermal stability.[32,33,112] Replacing toxic lead (Pb) with tin (Sn) not only shrinks the band gap to 1 eV, but also make the device eco-friendlier with better carrier transports

properties.[113-116] Doping with other impurities also has similar functional impacts on the material properties.[117-121] In situ morphological variations from bulk to numerous low- dimensional features were obtained to unlock the quantum effects.[122] Methylammonium lead halide nanocrystals (NC) with varying size were prepared by bifurcated capping agents.[123] Size variation (3-8 nm) of Methylammonium lead bromide nanoplatelets can also be seen to be influenced by precursor treatment.[124]

1.3. The intriguing properties

With a high photo absorption coefficient ($\sim 10^5$ cm^{-1}) of solar light around 1.5-1.6 eV, Methylammonium lead iodide comes with a direct energy band gap in the IR/NIR region. Whereas the energy band gaps of its other counterparts i.e. $CH_3NH_3PbBr_3$ and $CH_3NH_3PbCl_3$ lie around 2 and 2.5 eV respectively. The observed absorption features, in very good alignment with theoretical findings,[125,126] make them compatible for photovoltaic applications. The monovalent cations situated in the innermost center of the unit cell of metal halide perovskites govern the lattice parameters, which in turn decide the absorption onset of the material. Although possessing all direct gap material features, presence of mixed optical transition i.e. direct and indirect both has been found in literature.[127] Like other III-IV direct gap semiconductors, two absorption signatures are seen to arise from excitonic response and spin orbit interaction,[128] the unbroadened part being addressed by Elliott et al.[129] The band gap for $CH_3NH_3PbI_3$ is defined by the energy levels corresponding to the two electronic orbitals i.e. iodine 5p and lead 6p. The first one generates its valence band whereas the latter does the conduction band.[130,131] The conduction band splits due to temperature dependent[132,133] reversely ordered band edge.[134]

Binding energy of excitons in metal halide perovskites decides the dominant transport mechanism under excitation.[135] Identified as Wannier-Mott type, these excitons reportedly come up with binding energy of 2-60 meV at room temperature, with discrepancy and lack of proper modelling.[136-138] Temperature dependent photoluminescence study reveals 50 and 75 meV for $CH_3NH_3PbI_3$ and $CH_3NH_3PbBr_3$ respectively. Described by Elliott's theory, prominent quantum confinement effect on the binding energy can be seen in low dimensional 2D perovskites.[139] The derived binding energy (hundreds of eV) for these low size features are much higher than that of bulk counterparts[140-142] due to less screened electron-hole Coulomb interaction.[143] Room temperature Bose-Einstein condensate was achieved from exciton- polariton, a bosonic quasi-

particle produced from strongly interacting excitons with cavity photons in perovskite nanowires systems.[144,145] Lasing with low value of threshold can be based upon such condensate states, even without any population inversion scheme. Stronger interaction between exciton and cavity photon in Methylammonium lead bromide nanowires is accredited to enhanced surface Plasmon effect with localized excitation.[146]

The nonradiative type low charge recombination in metal halide perovskites results into high efficiency value of external radiative emission[147] or small difference (450 meV, for example) between the open circuit voltage (V_{OC}) of the device and potential corresponding to energy band gap i.e. E_g/q.[148] Such low nonradiative recombination results from large crystalline grains with low grain boundary defects. First principle study on intergranular defects in Methylammonium lead iodide categories these defects into Schottky type and Frenkel type,[149] neither leading to nonradiative recombination. Similar studies attribute Pb vacancies and MA interstitials to the main defect mechanisms in these perovskites.[150]

Radiative transitions obtained in PL studies revealed that carrier lifetime as long as 1 μs manifests in low dimensional halide perovskites at very low temperature due to Rashba effect.[130,151] Such long lifetime is attributed to high tolerance of the material to defects. Along with the experimentally found high carrier mobility of 100 cm^2/Vs, a value up to 1000 cm^2/Vs is also predicted theoretically.[152] Time resolved luminescence studies demonstrate nano- picoseconds lifetime as a result of large polaron formation and screened Coulomb potential in consequence.[153,154] In attempt to the carrier diffusion mechanism in hybrid metal halide nanowires and nanoplates[155] mobilities of 34 and 80 cm^2/Vs were found for the bromide and iodide sample; whereas their corresponding diffusion lengths came to be 6 and 14 μm respectively. Xiao and his team mapped the photocurrent in single crystalline nanowires of $CH_3NH_3PbI_3$, which showed long carrier diffusion of 21 μm with mobility of 170 cm^2/Vs.[156] Absence of grain boundaries in large single crystals can extend the carrier diffusion length even up to 175 μm.[157,158] Study with single crystalline systems also demonstrates cation independent low trapping and recombination rates of 10^7 and 10^{-10} cm^3 per second respectively.[159]

1.4. Critical areas and challenges

Instability of hybrid halide perovskite and the devices based on them are a common concern among researchers. Degradation due to moisture, oxygen, temperature and electric field limit the operational life cycle of the material. Radiation exposure in the form of UV light, in presence of ambient water and oxygen, also poses great threat to the material stability.[160] Such degradation is mainly attributed to ion migration,[161] covering defect generation, charge accumulation across interface, interlayer degradation and electrode corrosion. Point defects in form of halide vacancy channelizes the ions to migrate through.[162] With formation energy of 0.1-0.6 eV, the halide vacancies, as per the experimental findings, are the quickest migrants. Moreover, electrodes and electron/hole transport layers also impact device life. Electrode metal ions drifting and diffusing through perovskite leads to redox reactive degradation of the device, which gets more effective under external electric field. Methylammonium lead iodide rapidly degrades to lead iodide in humid environment through complex intermediate hydrates.[163] Non-radiative recombination in Perovskite quantum wells produces large Joule heating due to localized carrier density.[164,165] Effect of annealing temperature during synthesis also creates dimensional distribution in its structure. Strategies to immune the system from atmospheric hydro species include substituting some of the halide ions by pseudo halides and incorporating large organic cations into the system, etc.[160] The migrating ions can be mitigated via defect reduction with passivation measures and control of crystallization processes.[166,167] Water resistant encapsulation film reportedly blocks ambient water and moisture to penetrate into the system and hence enhance device stability.[168,169] Aristidou et al. attributed O^{2-} superoxide reacting with the crystal Methylammonium ions (MA^+) to trigger degradation process in perovskite.[182] These superoxides are produced from the reaction of ambient O_2 with the photogenerated electrons. The group suggested use of aprotic acid in place of MA component for obtaining improved immunity against oxygen and thus greater stability.

Solar cells based on hybrid halide perovskites show anomalous hysteresis in current voltage characteristics.[170] Depending on scanning rate and direction of the applied bias, the phenomenon produces inaccuracies in the measurement of device efficiencies. Although not fully understood yet, ferroelectricity,[171,172] ion migration associated defects,[173,174] and unbalanced collection of charges[175] are identified as reason behind this hysteretic effect. Tresset al. speculated hysteresis to be produced from electric field screening by migrated ions at the interfaces.[173] Observation of

hysteresis in resistivity experiments and presence of residual polarization indicate room temperature paraelectric/ferroelectric signatures in Methylammonium lead iodide. Crystallographic symmetry of 4mm point group also supports the existence of such ferroelectric nature at and above room temperature. However, controversies regarding its occurrence still exists. Reports suggest reduction in hysteresis through efficient charge transfer by using mesoporous TiO_2,[176,170,149] surface defect passivation,[177] low temperature,[178] PbI_2 assisted reduced recombination,[179,180] and also with aged devices.[173]

Although water solubility of halide perovskites makes them comparatively more bio-available than other popular solar cell materials e.g. cadmium telluride, however the presence of lead in these halide perovskites still is a great concern to the environmental scientists. Compositional modifications can lead to some way outs in this regard.[110] Replacing lead with tin can help get rid of the toxicity, but with a compromise with the device performance at the same time.[181]

1.5. Objective and structure of the thesis

1.5.1. Objective of the thesis

This doctoral thesis undertakes research works with objective to investigate cost-effective synthesis procedures to prepare Methylammonium lead halide particularly Methylammonium lead iodide and also to explore mainly its other non-trivial application aspects apart from solar cells. The objective additionally covers finding new ways towards enhancement of device stability with better performance. Efforts have also been given to understand the underlying charge relaxation mechanisms, particularly in the radio frequency regime. Hence the work comes with the following objectives.

- Tailoring the morphology with facile synthesis techniques

- Detailed material characterizations e.g. structural, morphological, electrical, etc.

- Exploring electron field emission behavior with synthesized nanostructures

- Hybridizing with other materials such as V_2O_5 for improved device stability

- Introducing hydrophobicity with V_2O_5 incorporation

- Probing bi-relaxation process due to pseudo-inductive switching

1.5.2. Structure of the thesis

Starting from a formal and preliminary idea of perovskites and their classes, Chapter 1 elaborates the emergence and significance of Methylammonium lead halides from application point of view. In addition to the various advantages such as wide band tunability and easy synthesis routes, the intriguing properties and the current challenges have also been discussed. With a literature review of past work on the adopted synthesis protocols and some of the important application aspects in Chapter 2, Chapter 3 demonstrates a number of characterization techniques and tools used in this study, such as XRD, FESEM, TEM, EDS, XPS, UV-Vis. spectroscopy, FTIR spectroscopy, impedance spectroscopy, cathodoluminescence, photoluminescence, current-voltage characteristics and so on. The synthesis and device fabrication procedures followed in this study is described in Chapter 4.

Major applications based upon this material have been utilizing its photovoltaic character mainly. To the best of our knowledge, very few studies has so far been reported regarding the field emission behavior of $CH_3NH_3PbI_3$ nanostructures. Additionally, theoretical and experimental studies on the electronic band related properties of this novel halide are also contradictory to each other and are of wide range. Even if the photovoltaic applications are considered to be the sole purpose of this material, work function related studies are utmost important to achieve better control over excitation parameters and explanation of experimental outputs. In addition to the mentioned issues, production cost often emerges as a decisive factor for commercial application of any novel and multifunctional material. Chapter 5 hence focuses on a thorough investigation of field emission (FE) properties of low dimensional $CH_3NH_3PbI_3$ synthesized via cost effective chemical route. Prior knowledge of work function being essential to figure out the enhancement factor, considering the ambiguities in its reported values in literature, first principle DFT approach was employed to evaluate it. The outcome of this study was further used in calculation of various field emission parameters. The dependence of the field emission parameters upon the shape of $CH_3NH_3PbI_3$ emitters has also been studied through ANSYS MAXWEL simulation and the results were correlated with experimental findings. Finally, emission stability which is an important criterion for practical device implications was checked for as long as 2 hrs.

Although given promising results, the work presented in Chapter 5 had further scope for emission enhancement by orientational modification of the nanorods emitters. Literatures suggest that materials having vertically aligned nanostructures prove to be superior electron field emitters in

comparison with ones having no directionalities. Moreover, performance of electron field emission tuned by incident photons has its own importance not only from its application point of view but also for the fundamental understanding of the emitter material under investigation. Metal halide perovskite, $CH_3NH_3PbI_3$ is already renowned for its high absorption coefficient. Hence, study was taken up to investigate the impact of NIR photons on the electron field emission behavior from vertically aligned $CH_3NH_3PbI_3$ nanorods, as illustrated in Chapter 6. Vertically aligned nanorods were first grown with the help of AAO (Anodic aluminum oxide) template to investigate their electron emission performance. The impact of different illumination conditions on the emission performance was finally probed by shining appropriate photons with varying intensities. The experimental observations were also corroborated with simulation of the local electric field distribution near the NRs under plane polarized light of different field strengths.

Inspired by relatively superior carrier transport through one dimensional nanostructure, Chapter 7 presents an attempt to upgrade the qualities of perovskite-based photodetector by incorporating V_2O_5 nanorods into $CH_3NH_3PbI_3$. Optimized hybrid sample exhibited 3-fold improved performance than the pristine perovskite sample. The improved photodetection performance of the modified sample was scrutinized thoroughly by current-voltage characteristics under dark and illumination conditions. Additionally, impedance spectroscopy was employed to probe the charge transport. To check the real time applicability of the devices, their detectivity was monitored under ambient condition at some intervals with no encapsulation. The stability of the devices was also checked in direct contact with water droplets by contact angle measurements. Although in ferroelectric and non-ferroelectric materials appearance of negative capacitance corresponds to completely different origins, pseudo inductance which generally arises in the high frequency regimes can also make the capacitance value negative sometimes. Internal defects, vacancies, delocalized charge-carriers, etc. can also have their additional contributions.

However, most of the impedance studies on these aspects in literature are focused mainly in the low and moderate frequency regimes up to the order of a few tens of MHz. It would be interesting to explore the underlying carrier dynamics and other aspects of $CH_3NH_3PbI_3$ halide perovskite by pushing this frequency limit further particularly in the radio-frequency (RF) regime. Hence, Chapter 8 deals with bias-dependent impedance analysis of $CH_3NH_3PbI_3$ near the radio-frequency (RF) region, keeping also in mind the influence of external electric field on carrier movement and ultimately on the device performance. The switching of capacitance from positive to negative values

was observed and the spectra across that neighborhood of the transient frequency were modeled with an equivalent LCR circuit. The frequency-dispersion of capacitance with negative values was fitted as a function of frequency, thereby revealing two interplaying relaxation mechanisms. The Breit-Wigner-Fano (BWF) type asymmetric line-shapes were corroborated with density functional theory (DFT)-based calculations. In conclusion, Chapter 9 discusses summary of the thesis and provides a future research prospect.

References

[1] https://eandt.theiet.org/content/articles/2019/09/the-seven-ages-of-materials/

[2] https://en.wikipedia.org/wiki/Perovskite#:~:text=The%20mineral%20was%20discovered%20in%20the%20Ural%20Mountains,in%201926%20in%20his%20work%20on%20tolerance%20factors.

[3] M. A. Peña and J. L. Fierro, Chemical structures and performance of perovskite oxides, Chemical Reviews. 7 (2001) 1981–2017.

[4] W. J. Merz, Switching time in ferroelectric $BaTiO_3$ and its dependence on crystal thickness, Journal of Applied Physics, 27 (1956) 938-943

[5] A. Mackenzie, S. Julian, A. Diver, G. McMullan, M. Ray, G. Lonzarich, Y. Maeno, S. Nishizaki and T. Fujita, Quantum Oscillations in the Layered Perovskite Superconductor Sr_2RuO_4, Physical review letters, 76 (1996) 3786

[6] H. Asano, J. Hayakawa and M. Matsui, Preparation and properties of triple perovskite $La_{\{3-3x\}}Ca_{\{1+3x\}}Mn_3O_{10}$ ferromagnetic thin films, Applied physics letters, 71 (1997) 844-846

[7] R. E. Schaak, T. E. Mallouk, Prying apart Ruddlesden-Popper phases: Exfoliation into sheets and nanotubes for assembly of perovskite thin films, Chem. Mater., 12 (2000) 3427-3434

[8] S. Uma, A. R. Raju, J. Gopalakrishnan, Bridging the Ruddlesden–Popper and the Dion–Jacobson series of layered perovskites: synthesis of layered oxides, $A_{2-x}La_2Ti_{3-x}Nb_xO_{10}$ (A = K, Rb), exhibiting ion exchange, Journal of Materials Chemistry, 3 (1993) 709-713

[9] Y. Tsunoda, W. Sugimoto, Y. Sugahara, Intercalation behavior of n-alkylamines into a protonated form of a layered perovskite derived from aurivillius phase $Bi_2SrTa_2O_9$, Chemistry of materials, 15 (2003) 632-635.

[10]   Q. Liu, Y. C. Hsiao, M. Ahmadi, T. Wu, L. Liu, S. Haacke, H. Wang and B. Hu, N and p-type properties in organo-metal halide perovskites studied by Seebeck effects, Organic

Electronics, 35 (2016) 216-220.

[11]   J. Peng, Y. Chen, K. Zheng, T. Pullerits and Z. Liang, Insights into charge carrier dynamics in organo-metal halide perovskites: from neat films to solar cells, Chem. Soc. Rev., 46 (2017) 5714-5729.

[12]   K. P. Bhandari and R. J. Ellingson, An Overview of Hybrid Organic–Inorganic Metal Halide Perovskite Solar Cells, A Comprehensive Guide to Solar Energy Systems, (2018) 233-254. DOI: 10.1016/B978-0-12-811479-7.00011-7

[13]   A. Maiti, S. Chatterjee, L. Peedikakkandy and A. J. Pal, Defects and Their Passivation in Hybrid Halide Perovskites toward Solar Cell Applications, RRL Solar, 4 (2020) 2000505.

[14]   W. Meng, B. Saparov, F. Hong, J. Wang, D. B. Mitzi and Y. Yan, Alloying and Defect Control within Chalcogenide Perovskites for Optimized Photovoltaic Application, Chem. Mater. (2016) acs.chemmater.5b04213. doi:10.1021/acs.chemmater.5b04213

[15]   Li, C. et al. Formability of ABX_3 (X = F, Cl, Br, I) halide perovskites. Acta Crystallogr. B 64, 702–707 (2008).

[16]   H. Topsöe, Krystallographisch-chemische untersuchungen homologer verbindungen. Zeitschrift für Kristallographie, 1884, 8, 246–296.

[17]   D. B. Mitzi, S. Wang, C. A. Feild, C. A. Chess and A. M. Guloy, Conducting layered organic–inorganic halides containing -oriented perovskite sheets. Science, 1995, 267, 1473–1476.

[18]   D. B. Mitzi, K. Chondroudis and C. R. Kagan, Organic-inorganic electronics. IBM J. Res. Dev. 45, 29–45 (2001)

[19]   Kojima, A., Teshima, K., Miyasaka, T. & Shirai, Y. Novel photoelectrochemical cell with mesoscopic electrodes sensitized by lead-halide compounds (2). in Proc. 210th ECS Meeting (ECS, 2006)

[20]   Kojima, A., Teshima, K., Shirai, Y. & Miyasaka, T. Organometal halide perovskites as visible-light sensitizers for photovoltaic cells. J. Am. Chem. Soc. 131, 6050–6051 (2009).

[21]   Im, J.-H., Lee, C.-R., Lee, J.-W., Park, S.-W. & Park, N.-G. 6.5% efficient perovskite quantum-dot-sensitized solar cell. Nanoscale 3, 4088–4093 (2011).

[22]   Kim, H.-S. et al. Lead iodide perovskite sensitized all-solid-state submicron thin film mesoscopic solar cell with efficiency exceeding 9%. Sci. Rep. 2, 591 (2012).

[23]   Lee, M. M., Teuscher, J., Miyasaka, T., Murakami, T. N. & Snaith, H. J. Efficient hybrid solar cells based on meso-superstructured organometal halide perovskites. Science 338, 643–

647 (2012).

[24]   Stranks, S. D. et al. Electron–hole diffusion lengths exceeding 1 micrometer in an organometal trihalide perovskite absorber. Science 342, 341–344 (2013).

[25]   Noh, J. H, Im, S. H., Heo, J. H., Mandal, T. N. & Seok, S. I. Chemical management for colorful, efficient, and stable inorganic-organic hybrid nanostructured solar cells. Nano Lett. 13, 1764–1769 (2013).

[26]   Burschka, J. et al. Sequential deposition as a route to high-performance perovskite-sensitized solar cells. Nature 499, 316–319 (2013).

[27]   Liu, M., Johnston, M. B. & Snaith, H. J. Efficient planar heterojunction perovskite solar cells by vapour deposition. Nature 501, 395–398 (2013).

[28]   Burschka, J. High performance solid-state mesoscopic solar cells. PhD thesis, École Polytechnique Fédérale de Lausanne 107 (2013).

[29]   NREL   Efficiency   Chart,   https://www.nrel.gov/pv/assets/pdfs/   best-research-cell-efficiencies.20190802.pdf (accessed: December 2019).

[30]   Chen, Q. et al. Planar heterojunction perovskite solar cells via vapor-assisted solution process. J. Am. Chem. Soc. 136, 622–625 (2014).

[31]   Im, J.-H., Chung, J., Kim, S.-J. & Park, N.-G. Synthesis, structure, and photovoltaic property of a nanocrystalline 2H perovskite-type novel sensitizer ($CH_3CH_2NH_3$)PbI_3, Nanoscale Res. Lett. 7, 353 (2012)

[32]   Koh TM, Fu K, Fang Y, Chen S, Sum TC, Mathews N, et al.: Formamidinium-containing metal-halide: an alternative material for near-IR absorption perovskite solar cells, J Phys Chem C 118:16458–16462, 2014.

[33]   Eperon, G. E. et al. Formamidinium lead trihalide: a broadly tunable perovskite for efficient planar heterojunction solar cells. Energy Environ. Sci. 7, 982–988 (2014).

[34]   Pang, S. et al. $NH_2CH=NH_2PbI_3$: An alternative organolead iodide perovskite sensitizer for mesoscopic solar cells. Chem. Mater. 26, 1485–1491 (2014).

[35]   Liu, D. & Kelly, T. L. Perovskite solar cells with a planar heterojunction structure prepared using room-temperature solution processing techniques. Nature Photon. 8, 133–138 (2014).

[36]   Docampo, P., Ball, J. M., Darwich, M., Eperon, G. E. & Snaith, H. J. Efficient organometal trihalide perovskite planar-heterojunction solar cells on flexible polymer substrates, Nature Commun. 4, 2761 (2013)

[37]   Malinkiewicz, O. et al. Perovskite solar cells employing organic charge transport layers. Nature Photon. 8, 128–132 (2014).

[38]   Sun, S. et al. The origin of high efficiency in low-temperature solution processable bilayer organometal halide hybrid solar cells. Energy Environ. Sci. 7, 399–407 (2014).

[39]   Yang W S, Noh J H, Jeon N J, Kim Y C, Ryu S, Seo J, et al.: High-performance photovoltaic perovskite layers fabricated through intramolecular exchange, Science 348:1234–1237, 2015.

[40]   Zhu, H. et al. Lead halide perovskite nanowire lasers with low lasing thresholds and high quality factors. Nat. Mater. 14, 636–642 (2015).

[41]   Zhang, Q., Ha, S. T., Liu, X., Sum, T. C. & Xiong, Q. Room-temperature near-infrared high-Q perovskite whispering-gallery planar nanolasers. Nano Lett. 14, 5995–6001 (2014).

[42]   Sutherland, B. R., Hoogland, S., Adachi, M. M., Wong, C. T. O. & Sargent, E. H. Conformal organohalide perovskites enable lasing on spherical resonators. ACS Nano 8, 10947–10952 (2014).

[43]   Mayer, B. et al. Lasing from individual GaAs-AlGaAs core-shell nanowires up to room temperature. Nat. Commun. 4, 2931 (2013).

[44]   Saxena, D. et al. Optically pumped room-temperature GaAs nanowire lasers. Nat. Photonics 7, 963–968 (2013).

[45]   Xing, J. et al. Vapor phase synthesis of organometal halide perovskite nanowires for tunable room temperature nanolasers. Nano Lett. 15, 4571–4577 (2015).

[46]   Zhang, Q. et al. Advances in small perovskite-based lasers. Small Methods 1, 1700163 (2017).

[47]   Fu, Y. et al. Nanowire lasers of formamidinium lead halide perovskites and their stabilized alloys with improved stability. Nano Lett. 16, 1000–1008 (2016).

[48]   Fu, Y. et al. Broad wavelength tunable robust lasing from single-crystal nanowires of Cesium lead halide perovskites ($CsPbX_3$, X = Cl, Br, I). ACS Nano 10, 7963–7972 (2016).

[49]   Eaton, S. W. et al. Lasing in robust cesium lead halide perovskite nanowires. Proc. Natl Acad. Sci. USA 113, 1993–1998 (2016).

[50]   Gu, Z. et al. Two-photon pumped $CH_3NH_3PbBr_3$ perovskite microwire lasers. Adv. Opt. Mater. 4, 472–479 (2016).

[51]   Zhang, W. et al. Controlling the cavity structures of two-photon pumped perovskite microlasers. Adv. Mater. 28, 4040–4046 (2016).

[52]   H. Kim, K. Roh, J. P. Murphy, L. Zhao, W. B. Gunnarsson, E. Longhi, S. Barlow, S. R. Marder, B. P. Rand, and N. C. Giebink. Optically Pumped Lasing from Hybrid Perovskite Light Emitting Diodes. Adv. Optical Mater. 2019, 1901297.

[53]   R. Dhanker, A. N. Brigeman, A. V. Larsen, R. J. Stewart, J. B. Asbury, N. C. Giebink, Appl. Phys. Lett. 2014, 105, 151112.

[54]   K. Vahala, Nature 2003, 424, 839.

[55]   L. Mahler, A. Tredicucci, F. Beltram, C. Walther, J. Faist, B. Witzigmann, H. E. Beere, D. A. Ritchie, Nat. Photonics 2009, 3, 46.

[56]   Q. Liao, K. Hu, H. Zhang, X. Wang, J. Yao, H. Fu, Adv. Mater. 2015, 27, 3405.

[57]   H. Kogelnik, C. V. Shank, Appl. Phys. Lett. 1971, 18, 152.

[58]   M. Saliba et al., Adv. Mater. 2016, 28, 923.

[59]   Zhang et al., Phys. Chem. Chem. Phys. 2017, 19, 2217.

[60]   Zhang et al., Adv. Opt. Mater. 2016, 4, 2057.

[61]   W. Deng, X. Xu, X. Zhang, Y. Zhang, X. Jin, L. Wang, S.-T. Lee, J. Jie, Adv. Funct. Mater. 2016, 26, 4797.

[62]   K. Chondroudis, D. Mitzi, Chem. Mater. 1999, 11, 3028.

[63]   T. Matsushima, K. Fujita, T. Tsutsui, Jpn. J. Appl. Phys., Part 1 2005, 44, 1457.

[64]   I. Koutselas, P. Bampoulis, E. Maratou, T. Evagelinou, G. Pagona, G. C. Papavassiliou, J. Phys. Chem. C 2011, 115, 8475.

[65]   Tan et al., Nat. Nanotechnol. 2014, 9, 687.

[66]   L. Gil-Escrig, A. Miquel-Sempere, M. Sessolo, H. J. Bolink, J. Phys. Chem. Lett. 2015, 6, 3743.

[67]   Y.-H. Kim, H. Cho, J. H. Heo, T.-S. Kim, N. Myoung, C.-L. Lee, S. H. Im, T.-W. Lee, Adv. Mater. 2015, 27, 1248.

[68]   O. A. Jaramillo-Quintero, R. S. Sanchez, M. Rincon, I. Mora-Sero, J. Phys. Chem. Lett. 2015, 6, 1883.

[69]   A. B. Wong, M. Lai, S. W. Eaton, Y. Yu, E. Lin, L. Dou, A. Fu, P. Yang, Nano Lett. 2015, 15, 5519.

[70]   L. Dou, Y. (Micheal) Yang, J. You, Z. Hong, W.-H. Chang, G. Li, Y. Yang, Nat. Commun. 2014, 5, 5404.

[71]   X. Hu, X. Zhang, L. Liang, J. Bao, S. Li, W. Yang, Y. Xie, Adv. Funct. Mater. 2014, 24, 7373.

[72]   Y. Guo, C. Liu, H. Tanaka, E. Nakamura, J. Phys. Chem. Lett. 2015, 6, 535.

[73]   H.-R. Xia, J. Li, W.-T. Sun, L.-M. Peng, Chem. Commun. 2014, 50, 13695.

[74]   C. Liu, K. Wang, C. Yi, X. Shi, P. Du, A. W. Smith, A. Karim, X. Gong, J. Mater. Chem. C 2015, 3, 6600.

[75]   V. Bhatt, K. Pandey, S. K. Gupta, Y. Sonvane, P. Yadav, M. Kumar, RSC Adv. 2016, 6, 111942.

[76]   Y. Wang, Z. Xia, S. Du, F. Yuan, Z. Li, Z. Li, Q. Dai, H. Wang, S. Luo, S. Zhang, H. Zhou, Nanotechnology 2016, 27, 175201.

[77]   V. Adinolfi, O. Ouellette, M. I. Saidaminov, G. Walters, A. L. Abdelhady, O. M. Bakr, E. H. Sargent, Adv. Mater. 2016, 28, 7264.

[78]   H. Wei, Y. Fang, P. Mulligan, W. Chuirazzi, H.-H. Fang, C. Wang, B. R. Ecker, Y. Gao, M. A. Loi, L. Cao, J. Huang, Nat. Photonics 2016, 10, 333.

[79]   W. Wei, Y. Zhang, Q. Xu, H. Wei, Y. Fang, Q. Wang, Y. Deng, T. Li, A. Gruverman, L. Cao, J. Huang, Nat. Photonics 2017, 11, 315.

[80]   W. Niu, A. Eiden, G. V. Prakash, J. J. Baumberg, Appl. Phys. Lett. 2014, 17, 171111.

[81]   S. T. Ha, X. Liu, Q. Zhang, D. Giovanni, T. C. Sum, Q. Xiong, Adv. Opt. Mater. 2014, 2, 838.

[82]   L. Dou et al. Science 2015, 349, 1518.

[83]   J. Liu, Y. Xue, Z. Wang, Z.-Q. Xu, C. Zheng, B. Weber, J. Song, Y. Wang, Y. Lu, Y. Zhang, Q. Bao, ACS Nano 2016, 10, 3536.

[84]   G. Maculan, A. D. Sheikh, A. L. Abdelhady, M. I. Saidaminov, M. A. Hague, B. Murali, E. Alarousu, O. F. Mohammed, T. Wu, O. M. Bakr, J. Phys. Chem. Lett. 2015, 6, 3781.

[85]   J. Ding, H. Fang, Z. Lian, J. Li, Q. Lv, L. Wang, J.-L. Sun, Q. Yan, CrystEngComm 2016, 18, 4405.

[86]   Deng, W. et al. Aligned single-crystalline perovskite microwire arrays for high-performance flexible image sensors with long-term stability. Adv. Mater. 28, 2201–2208 (2016).

[87]   Deng, W. et al. Ultrahigh-responsivity photodetectors from perovskite nanowire arrays for sequentially tunable spectral measurement. Nano Lett. 17, 2482–2489 (2017).

[88]   L. Su, Z. X. Zhao, H. Y. Li, J. Yuan, Z. L. Wang, G. Z. Cao, G. Zhu, ACS Nano 2015, 9, 11310.

[89]   J. Yu, X. Chen, Y. Wang, H. Zhou, M. Xue, Y. Xu, Z. Li, C. Ye, J. Zhang, P. A. van

Aken, P. D. Lund, H. Wang, J. Mater. Chem. C 2016, 4, 7302.

[90]   D.-H. Kang, S. R. Pae, J. Shim, G. Yoo, J. Jeon, J. W. Leem, J. S. Yu, S. Lee, B. Shin, J.-H. Park, Adv. Mater. 2016, 28, 7799.

[91]   Y. Mei, C. Zhang, Z. V. Vardeny and O. D. Jurchescu, Electrostatic gating of hybrid halide perovskite field-effect transistors: balanced ambipolar transport at room-temperature, MRS Communications , Vol. 5, 2015, 297–301.

[92]   Senanayak et al., Understanding charge transport in lead iodide perovskite thin-film field-effect transistors, *Science Advances* Vol. 3, 2017, e1601935.

[93]   JW Ward et al., Solution-Processed Organic and Halide Perovskite Transistors on Hydrophobic Surfaces, *ACS Appl. Mater. Interfaces* 2017, 9, 21, 18120–18126.

[94]   Yu et al., Single crystal hybrid perovskite field-effect transistors, *Nature Communications* volume 9, Article number: 5354 (2018).

[95]   N. D. Canicoba et al., Halide Perovskite High-*k* Field Effect Transistors with Dynamically Reconfigurable Ambipolarity, *ACS Materials Lett.* 2019, 1, 6, 633–640.

[96]   S. P. Senanayak et al., A general approach for hysteresis-free, operationally stable metal halide perovskite field-effect transistors, Science Advances Vol. 6 (2020). DOI: 10.1126/sciadv.aaz4948

[97]   C. Gu and J. S. Lee, Flexible Hybrid Organic–Inorganic Perovskite Memory, *ACS Nano* 2016, 10, 5, 5413–5418.

[98]   B. Hwang, C. Gu, D. Lee and J. S. Lee, Effect of halide-mixing on the switching behaviours of organic-inorganic hybrid perovskite memory, *Scientific Reports*, Vol. 7, Article number: 43794 (2017).

[99]   B. Hwang and J. S. Lee, Hybrid Organic-Inorganic Perovskite Memory with Long-Term Stability in Air, *Scientific Reports,* Vol. 7, Article number: 673 (2017).

[100] T. Jiang, Z. Shao, H. Fang, W. Wang, Q. Zhang, D. Wu, X. Zhang and J. Jie, High-Performance Nanofloating Gate Memory Based on Lead Halide Perovskite Nanocrystals *ACS Appl. Mater. Interfaces* 2019, 11, 27, 24367–24376.

[101] Muthu et al., Hybrid perovskite nanoparticles for high-performance resistive random access memory devices: control of operational parameters through chloride doping, Adv. Mater. Inter., 2016, 1600092. DOI:10.1002/admi.201600092

[102] Eunji Yoo, S. V. N. Pammi, Kyu Young Kim, Tran-Van Dang, Ji-Ho Eom, Young Jin Choi, Soon-Gil Yoon, Strategic extended air stability of organolead halide perovskite

nonvolatile memory devices, Journal of Alloys and Compounds, Vol. 811, 2019, 151999.

[103]   S. M. Lee et al., Tailored 2D/3D Halide Perovskite Heterointerface for Substantially Enhanced Endurance in Conducting Bridge Resistive Switching Memory, *ACS Appl. Mater. Interfaces* 2020, 12, 14, 17039–17045.

[104]   S. Lee, S. Wolfe, J. Torres, M. Yun and J. K. Lee, Asymmetric Bipolar Resistive Switching of Halide Perovskite Film in Contact with TiO_2 Layer, *ACS Appl. Mater. Interfaces* 2021, DOI: 10.1021/acsami.1c06278.

[105]   N. Vicente and G. G. Belmonte, Methylammonium Lead Bromide Perovskite Battery Anodes Reversibly Host High Li-Ion Concentrations, *J. Phys. Chem. Lett.* 2017, 8, 7, 1371–1374.

[106]   A. Slonopas, H. Ryan and P. Norris, Ultrahigh energy density $CH_3NH_3PbI_3$ perovskite based supercapacitor with fast discharge, Electrochimica Acta, Vol. 307, 2019, 334-340.

[107]   Q. Wang, T. Yang, H. Wang, J. Zhang, X. Guo, Z. Yang, S. Lu and W. Qin, Morphological and chemical tuning of lead halide perovskite mesocrystals as long-life anode materials in lithium-ion batteries, *CrystEngComm*, 2019, 21, 1048-1059.

[108]   L. E. Oloore, M. A. Gondal, A. Popoola and I. K. Popoola, Pseudocapacitive contributions to enhanced electrochemical energy storage in hybrid perovskite-nickel oxide nanoparticles composites electrodes, Electrochimica Acta, Vol. 361, 2020, 137082.

[109]   I. Popoola, M. Gondal, L. Oloore, A. Popoola and J. AlGhamdi, Fabrication of organometallic halide perovskite electrochemical supercapacitors utilizing quasi-solid-state electrolytes for energy storage devices, Electrochimica Acta, Vol. 332, 2020, 135536.

[110]   G. E. Eperon et al., Perovskite-perovskite tandem photovoltaics with optimized band gaps, Science (80-.). 354 (2016) 861–865. doi:10.1126/science.aaf9717.

[111]   M. Saliba et al., Incorporation of rubidium cations into perovskite solar cells improves photovoltaic performance, Science (80-.). 354 (2016).

[112]   Stoumpos CC, Malliakas CD, Kanatzidis MG: Semiconducting tin and lead iodide perovskites with organic cations: phase transitions, high mobilities, and near-infrared photoluminescent properties, Inorg Chem 52: 9019–9038, 2013.

[113]   Hao F, Stoumpos CC, Guo P, Zhou N, Marks TJ, Chang RPH, et al.: Solvent-mediated crystallization of $CH_3NH_3SnI_3$ films for heterojunction depleted perovskite solar cells, J Am Chem Soc 137:11445–11452, 2015.

[114]   Umari P, Mosconi E, De Angelis F: Relativistic GW calculations on $CH_3NH_3PbI_3$ and

$CH_3NH_3SnI_3$ perovskites for solar cell applications, Sci Rep: 4, 2014.

[115]   Hao F, Stoumpos CC, Cao DH, Chang RPH, Kanatzidis MG: Lead-free solid-state organic-inorganic halide perovskite solar cells, Nat Photonics 8:489–494, 2014.

[116]   Noel NK, Stranks SD, Abate A, Wehrenfennig C, Guarnera S, Haghighirad A-A, et al.: Lead-free organic-inorganic tin halide perovskites for photovoltaic applications, Energy Environ Sci 7:3061–3068, 2014.

[117]   Goede O, Heimbrodt W. Optical properties of (Zn, Mn) and (Cd, Mn) chalcogenide mixed crystals and superlattices. Phys Status Solidi B. 1988; 146:11–62.

[118]   Pradhan N, Goorskey D, Thessing J, et al. An alternative of CdSe nanocrystal emitters: pure and tunable impurity emissions in ZnSe nanocrystals. J Am Chem Soc. 2005; 127: 17586–17587.

[119]   Bhargava RN, Gallagher D, Hong X, et al. Optical properties of manganese-doped nanocrystals of ZnS. Phys Rev Lett. 1994; 72: 416–419.

[120]   Norris D J, Yao N, Charnock F T, et al. High-quality manganese-doped ZnSe nanocrystals. Nano Lett. 2001; 1:3–7.

[121]   Bol AA, Meijerink A. Long-lived Mn^{2+} emission in nanocrystalline ZnS: Mn^{2+}. Phys Rev B. 1998; 58: R15997– R16000.

[122]   Sichert, J. A.; Tong, Y.; Mutz, N.; Vollmer, M.; Fischer, S.; Milowska, K. Z.; García Cortadella, R.; Nickel, B.; Cardenas-Daw, C.; Stolarczyk, J. K.; et al. Quantum Size Effect in Organometal Halide Perovskite Nanoplatelets. Nano Lett. 2015, 15, 6521−6527.

[123]   Luo, B.; Pu, Y.-C.; Lindley, S. A.; Yang, Y.; Lu, L.; Li, Y.; Li, X.; Zhang, J. Z. Organolead Halide Perovskite Nanocrystals: Branched Capping Ligands Control Crystal Size and Stability. Angew. Chem., Int. Ed. 2016, 55, 8864−8868.

[124]   Cho, J.; Choi, Y. H.; O'Loughlin, T. E.; De Jesus, L.; Banerjee, S. Ligand-Mediated Modulation of Layer Thicknesses of Perovskite Methylammonium Lead Bromide Nanoplatelets. Chem. Mater. 2016, 28, 6909−6916.

[125]   Umari, P., Mosconi, E. & De Angelis, F. Relativistic GW calculations on $CH_3NH_3PbI_3$ and $CH_3NH_3SnI_3$ perovskites for solar cell applications. Sci. Rep. 4, 4467 (2014).

[126]   Even, J., Pedesseau, L., Jancu, J.-M. & Katan, C. Importance of spin-orbit coupling in hybrid organic/inorganic perovskites for photovoltaic applications. J. Phys. Chem. Lett. 4, 2999–3005 (2013).

[127]   F. Zheng, L. Z. Tan, S. Liu, A. M. Rappe, Rashba Spin-Orbit Coupling Enhanced Carrier

Lifetime in $CH_3NH_3PbI_3$, Nano Lett. (2015). DOI: 10.1021/acs.nanolett.5b01854.

[128] Sell, D. D. & Lawaetz, P. New analysis of direct exciton transitions: application to GaP. Phys. Rev. Lett. 26, 311–314 (1971).

[129] Elliott, R. J. Intensity of optical absorption by excitons. Phys. Rev. 108, 1384–1389 (1957).

[130] M. a. Green, Y. Jiang, A. M. Soufiani, A. Ho-Baillie, Optical Properties of Photovoltaic Organic-Inorganic Lead Halide Perovskites, J. Phys. Chem. Lett. 6 (2015) 4774–4785.

[131] W. J. Yin, T. Shi, Y. Yan, Superior photovoltaic properties of lead halide perovskites: Insights from first-principles theory, J. Phys. Chem. C. 119 (2015) 5253–5264.

[132] Ishihara, T. Optical properties of PbI-based perovskite structures. J. Luminescence 60, 269–274 (1994).

[133] D'Innocenzo, V. et al. Excitons versus free charges in organo-lead tri-halide perovskites. Nature Commun. 5, 3586 (2014).

[134] Even, J., Pedesseau, L., Dupertuis, M.-A., Jancu, J.-M. & Katan, C. Electronic model for self-assembled hybrid organic/perovskite semiconductors: reverse band edge electronic states ordering and spin-orbit coupling. Phys. Rev. B 86, 205301 (2012).

[135] Correa-Baena, J. P.; Saliba, M.; Buonassisi, T.; Gratzel, M.; Abate, A.; Tress, W.; Hagfeldt, A. Promises and challenges of perovskite solar cells. Science 2017, 358, 739−744.

[136] Herz, L. M. Charge-Carrier Dynamics in Organic-Inorganic Metal Halide Perovskites. Annu. Rev. Phys. Chem. 2016, 67, 65−89.

[137] Amgar, D.; Wierzbowska, M.; Uvarov, V.; Gutkin, V.; Etgar, L. Novel rubidium lead chloride nanocrystals: synthesis and characterization. Nano Futures 2017, 1, No. 021002.

[138] Yang, Y.; Ostrowski, D. P.; France, R. M.; Zhu, K.; van de Lagemaat, J.; Luther, J. M.; Beard, M. C. Observation of a hot-phonon bottleneck in lead-iodide perovskites. Nat. Photonics 2016, 10, 53−59.

[139] Stoumpos, C. C.; Cao, D. H.; Clark, D. J.; Young, J.; Rondinelli, J. M.; Jang, J. I.; Hupp, J. T.; Kanatzidis, M. G. Ruddlesden−Popper Hybrid Lead Iodide Perovskite 2D Homologous Semiconductors. Chem. Mater. 2016, 28, 2852−2867.

[140] Hintermayr et al., Tuning the Optical Properties of Perovskite Nanoplatelets through Composition and Thickness by Ligand Assisted Exfoliation. Adv. Mater. 2016, 28, 9478−9485.

[141] Tanaka, K.; Kondo, T. Bandgap and exciton binding energies in lead-iodide-based

natural quantum-well crystals. Sci. Technol. Adv. Mater. 2003, 4, 599−604.

[142]   Wang, Q.; Liu, X.-D.; Qiu, Y.-H.; Chen, K.; Zhou, L.; Wang, Q.-Q. Quantum Confinement Effect and Exciton Binding Energy of Layered Perovskite Nanoplatelets. AIP Adv. 2018, 8, No. 025108.

[143]   Chernikov, A.; Berkelbach, T. C.; Hill, H. M.; Rigosi, A.; Li, Y.; Aslan, O. B.; Reichman, D. R.; Hybertsen, M. S.; Heinz, T. F. Exciton binding energy and nonhydrogenic Rydberg series in monolayer WS_2. Phys. Rev. Lett. 2014, 113, No. 076802.

[144]   Sanvitto, D. & Kéna-Cohen, S. The road towards polaritonic devices. Nat. Mater. 15, 1061–1073 (2016).

[145]   Fraser, M. D., Höfling, S. & Yamamoto, Y. Physics and applications of exciton–polariton lasers. Nat. Mater. 15, 1049–1052 (2016).

[146]   Shang, Q. et al. Surface plasmon enhanced strong exciton–photon coupling in hybrid inorganic–organic perovskite nanowires. Nano Lett. 18, 3335–3343 (2018).

[147]   Ungár, T. The meaning of size obtained from broadened X-ray diffraction peaks. Adv. Eng. Mater. 5, 323–329 (2003).

[148]   Snaith, H. J. Perovskites: the emergence of a new era for low-cost, high efficiency solar cells. J. Phys. Chem. Lett. 4, 3623–3630 (2013).

[149]   Kim, J., Lee, S.-H., Lee, J. H. & Hong, K.-H. The role of intrinsic defects in methylammonium lead iodide perovskite. J. Phys. Chem. Lett. 5, 1312–1317 (2014).

[150]   Yin, W.-J., Shi, T. & Yan, Y. Unusual defect physics in CH3NH3PbI3 perovskite solar cell absorber. Appl. Phys. Lett. 104, 063903 (2014).

[151]   M. Saba, F. Quochi, A. Mura and G. Bongiovanni, Excited State Properties of Hybrid Perovskites, Acc. Chem. Res. (2015) DOI: 10.1021/acs.accounts.5b00445

[152]   T. M. Brenner, D. a Egger, A. M. Rappe, L. Kronik, G. Hodes, D. Cahen, Are Mobilities in Hybrid Organic Inorganic Halide Perovskites Actually "High"?, Http://Dx.Doi.Org/10.1021/Acs.Jpclett.5B02390. (2015) 3–6.

[153]   Zhu, H. et al. Screening in crystalline liquids protects energetic carriers in hybrid perovskites. Science 353, 1409–1413 (2016).

[154]   Miyata, K. & Zhu, X. Y. Ferroelectric large polarons. Nat. Mater. 17, 379–381 (2018).

[155]   Tian, W., Zhao, C., Leng, J., Cui, R. & Jin, S. Visualizing carrier diffusion in individual single-crystal organolead halide perovskite nanowires and nanoplates. J. Am. Chem. Soc. 137, 12458–12461 (2015).

[156]   Xiao, R. et al. Photocurrent mapping in single crystal methylammonium lead iodide perovskite nanostructures. Nano Lett. 16, 7710–7717 (2016).

[157]   Shi, D. et al. Low trap-state density and long carrier diffusion in organolead trihalide perovskite single crystals. Science 347, 519–522 (2015).

[158]   Dong, Q. et al. Electron-hole diffusion lengths >175μm in solution-grown CH3NH3PbI3 single crystals. Science 347, 967–970 (2015).

[159]   Zhu, H. et al. Organic cations might not be essential to the remarkable properties of band edge carriers in lead halide perovskites. Adv. Mater. 29, 1603072 (2017).

[160]   S. N. Habisreutinger, D. P. McMeekin, H. J. Snaith, R. J. Nicholas, Research Update: Strategies for improving the stability of perovskite solar cells, APL Mater. 4 (2016).

[161]   Yuan, Y. & Huang, J. Ion migration in organometal trihalide perovskite and its impact on photovoltaic efficiency and stability. Acc. Chem. Res. 49, 286–293 (2016).

[162]   Senocrate, A. et al. Te nature of ion conduction in methylammonium lead iodide: a multimethod approach. Angew. Chem. Int. Ed. 56, 7755–7759 (2017).

[163]   J. S. Manser, M. I. Saidaminov, O. M. Bakr, P. V Kamat, Making and Breaking of Lead Halide Perovskites, (2015). DOI: 10.1021/acs.accounts.5b00455.

[164]   W. Zou, R. Li, S. Zhang, Y. Liu, N. Wang, Y. Cao, Y. Miao, M. Xu, Q. Guo, D. Di, L. Zhang, C. Yi, F. Gao, R. H. Friend, J. Wang, W. Huang, Nat. Commun. 2018, 9, 1.

[165]   C. Zuo, Y. Liu, D. S. Ginger, L. Y. Lin, ACS Nano 2020, 5, 6076.

[166]   Xu, W. et al. Rational molecular passivation for high-performance perovskite light-emitting diodes. Nat. Photon. 13, 418–424 (2019).

[167]   Wang, H. et al. Perovskite-molecule composite thin films for efficient and stable light-emitting diodes. Nat. Commun. 11, 891 (2020).

[168]   H. Zhang, Q. Liao, X. Wang, J. Yao, H. Fu, Adv. Opt. Mater. 2016, 4, 1718.

[169]   Y. Guo, C. Liu, H. Tanaka, E. Nakamura, J. Phys. Chem. Lett. 2015, 6, 535.

[170]   Snaith HJ, Abate A, Ball JM, Eperon GE, Leijtens T, Noel NK, et al.: Anomalous hysteresis in perovskite solar cells, J Phys Chem Lett 5:1511–1515, 2014.

[171]   Wei J, Zhao Y, Li H, Li G, Pan J, Xu D, et al.: Hysteresis analysis based on the ferroelectric effect in hybrid perovskite solar cells, J Phys Chem Lett 5:3937–3945, 2014.

[172]   Frost JM, Butler KT, Walsh A: Molecular ferroelectric contributions to anomalous hysteresis in hybrid perovskite solar cells, APL Mater 2:081506, 2014.

[173]   Tress et al., Understanding the rate dependent J–V hysteresis, slow time component, and

aging in $CH_3NH_3PbI_3$ perovskite solar cells: the role of a compensated electric field, Energy Environ Sci 8:995–1004, 2015.

[174]   Eames C, Frost JM, Barnes PR, O'regan BC, Walsh A, Islam MS: Ionic transport in hybrid lead iodide perovskite solar cells, Nat Commun:6, 2015.

[175]   Bergmann VW, Weber SA, Ramos FJ, Nazeeruddin MK, Grätzel M, Li D, et al.: Real-space observation of unbalanced charge distribution inside a perovskite-sensitized solar cell, Nat Commun:5, 2014.

[176]   Jeon NJ, Noh JH, Kim YC, Yang WS, Ryu S, Seok SI: Solvent engineering for high-performance inorganic–organic hybrid perovskite solar cells, Nat Mater 13:897–903, 2014.

[177]   Chiang C-H, Tseng Z-L, Wu C-G: Planar heterojunction perovskite/PC71BM solar cells with enhanced open-circuit voltage via a (2/1)-step spin-coating process, J Mater Chem A 2:15897–15903, 2014.

[178]   Bryant D, Wheeler S, O'Regan BC, Watson T, Barnes PR, Worsley D, et al.: Observable hysteresis at low temperature in "hysteresis free" organic–inorganic lead halide perovskite solar cells, J Phys Chem Lett 6:3190–3194, 2015.

[179]   Y. C. Kim, N. J. Jeon, J. H. Noh, W. S. Yang, J. Seo, J. S. Yun, A. Ho-Baillie, S. Huang, M. A. Green, J. Seidel, T. K. Ahn, S. I. Seok, Adv. Energy Mater. 2016, 6, 1502104.

[180]   Q. Chen, H. Zhou, T.-B. Song, S. Luo, Z. Hong, H.-S. Duan, L. Dou, Y. Liu, Y. Yang, Nano Lett. 2014, 14, 4158.

[181]   A. Babayigit, A. Ethirajan, M. Muller, B. Conings, Toxicity of organometal halide perovskite solar cells, Nat. Mater. 15 (2016) 247–251.

[182]   N. Aristidou, I. Sanchez-Molina, T. Chotchuangchutchaval, M. Brown, L. Martinez, T. Rath, S. A. Haque, The Role of Oxygen in the Degradation of Methylammonium Lead Trihalide Perovskite Photoactive Layers, Angew. Chem., Int. Ed. 2015, 54, 8208-8212.

Literature Survey

2.1. Synthesis protocols

Scientists and researchers have so far come up with a broad spectrum of synthesis techniques to prepare metal halide perovskites, so as to achieve better device performances in a cost-effective way. Literatures document numerous protocols for synthesizing single and polycrystalline thin films till date.[1, 2] Performance of perovskite based photovoltaics highly depends on these film qualities which in turn depend on their preparation methods,[1, 3] with a comprehensive idea given on the involved kinetics of film formation affecting device performances by Kamat et al.[2] Solution processability of halide perovskites opened up a variety of deposition techniques e.g. printing, coating, etc. with the provision of scalability and wearable flexible technologies as well.[4] Some of these commonly adopted synthesis techniques are presented in the following.

2.1.1. Solution deposition

Perovskite deposition by solution process techniques such as spin coating, spray coating or printing methods are very easy and advantageous as well. In these methods, the precursors of AX and BX_2 taken in proper stoichiometric ratio are mixed in polar solvents e.g. N, N-dimethyl formamide (DMF), dimethyl sulfoxide (DMSO), etc. at normal ambient conditions and then spin coated on substrates. Crystallization through rapid evaporation of the solvent finally leads to desired perovskite phase. Although the earlier thin films were mostly deposited by such spin coating via a single step (popular as one step) route producing perovskite crystals very fast,[5-8] they suffered several drawbacks. Quick evaporation of the solvents led to poor coverage with highly rough surface and numerous crystalline grains of small size, which resulted into inferior device performance owing to increased leakage current and carrier recombination.[9] Dissolved in a common solvent, the two components i.e. AX and BX_2 generally produce numerous pin holes because of their mutual reaction tendency. These pin holes leave ample scope for short circuiting the device and lack of reproducibility. To make up the lack of control over crystallization via this

one step method, Seok et al. introduced an intermediate phase by using methylbenzene as an antisolvent.[10] Film coverage was further improved when the one step method was extended to two steps by Burschka et al.[11] They dissolved CH_3NH_3I and PbI_2 in two separate solvents and spin coated PbI_2 into TiO_2 nanopores. High quality $CH_3NH_3PbI_3$ was formed by dipping TiO_2/PbI_2 film into CH_3NH_3I precursor solution of IPA (2-propanol). It is understood that perovskite films can be deposited very easily in cost-effective ways through solution process techniques at room temperature.

2.1.2. Vapor deposition

Introduced by Liu et al., this method produces highly uniform smooth surface with reduced pin holes.[12] Deposition takes place from evaporation of CH_3NH_3I and $PbCl_2$ sources (powder form) equipped with sensors for monitoring and controlling the deposition rates by temperature. The device was fabricated on fluorine doped tin oxide (FTO) coated glass substrate in nitrogen glove box. At first, TiO_2 layer was spin coated on FTO and then the organic and inorganic precursor salts were deposited at 4:1 molar ratio at 10^{-5} mbar pressure. Immediate perovskite formation started with the evaporation of the precursor sources, which resulted into complete crystallization after annealing. Electrode deposition at 10^{-6} mbar vacuum through thermal evaporation technique was performed after deposition of hole transport layer (HTL) by spin coating. Although yielding very uniform and high-quality perovskite thin film, the requirement of high vacuum system during the entire film formation process makes this method highly expensive.

2.1.3. Vapor-assisted solution

A middle way is found by combining both spin coating and evaporation techniques together in 2014 by Chen et al.[13] In a typical vapor assisted solution method, first PbI_2 film is deposited on FTO glass substrate with TiO_2 layer. The film is then exposed to CH_3NH_3I vapor and annealed for 2 hours at 150 ^0C in nitrogen environment. Thus, the method produces high quality $CH_3NH_3PbI_3$ films at ambient without using vacuum system, thereby reducing the synthesis costs to a great extent.

2.1.4. Chemical vapor deposition (CVD)

The first report of perovskite film formation by chemical vapor deposition (CVD) in is documented by Leyden et al.[14] They first deposited PbI$_2$ film (180 nm thick) on substrates by evaporating PbI$_2$ powder thermally at a rate of 0.5 Å/s at a pressure of ~ 1 mPa. The substrate was then transferred to CVD furnace which was also loaded with CH$_3$NH$_3$I powder. Under nitrogen flow and 100 Pa pressure, the substrate with PbI$_2$ film was heated at 160 ^{0}C, whereas the CH$_3$NH$_3$I powder was heated at 210 ^{0}C. Once source and substrate were cooled, the substrate was taken out after venting the furnace. Similar methodology was adopted for depositing formamidinium based perovskite film as well. The group demonstrated large area solar cell fabrication based on organic/inorganic metal halide perovskite film in ambient.

2.1.5. Colloidal synthesis

In 2012, a novel strategy was proposed by Vybornyi et al. for nanocrystals synthesis of hybrid metal halide perovskites without using any polar solvent.[15] In their colloidal synthesis, the Methylamine and lead halide precursors were allowed to react in the presence of non-polar solvents which acted as capping ligands. The method offered wide shape tunability with high luminescence from these highly crystalline colloidal perovskites. CH$_3$NH$_3$PbBr$_3$ nanoparticles (size: 6 nm) were synthesized by Schmidt et al.[16] The method involves use of long chain capping ligands for achieving stable dispersion of the nanoparticles in organic solvents for > 3 months. Similar method was also adopted by Teunis et al. for preparing Methylammonium lead bromide nanocrystals by dissolving long chain ligands into a mixture of two cosolvents i.e. trichlorobenzene (TCB) and 1-octadecene (ODE).[17] In their colloidal synthesis route, they first dissolved oleic acid, octylammonium bromide and hexadecylamine in the cosolvents mixture at a temperature of 60 ^{0}C and then injected separately prepared Methylammonium bromide and lead bromide precursors into the TCB+ODE mixture. Quantum platelets of CH$_3$NH$_3$PbBr$_3$ were formed immediately when the organic cation and lead precursors were added to the cosolvents, being indicated by the rapid yellowish change of the solution. Highly luminescent quantum dots (diameter ~ 3.3 nm) of Methylammonium lead halide were synthesized by ligand assisted reprecipitation (LARP) technique.[18] Color tuned bright emission at room temperature was obtained from these colloidal nanocrystals with quantum yield of 70%, which was attributed to their enhanced exciton binding energy due to size reduction. A wide spectrum of low

dimensional morphologies of Methylammonium lead iodide and Methylammonium lead bromide were also prepared by Zhu et al. by similar method.[19]

2.1.6. Miscellaneous techniques

(A) Hydrothermal synthesis: A simple hydrothermal approach was reported by Xia and his team in 2015.[20] The group synthesized both $CH_3NH_3PbI_3$ and $CH_3NH_3PbBr_3$ for using them as the anode material in Li ion batteries. $Pb(CH_3COO)_2 \cdot 3H_2O$ and CH_3NH_2 solution (27-32%) were mixed with 40% HBr solution and put into 100 mL autoclave to be heated in an oven for 1-12 h at 150 ^{0}C. The product was then allowed to cool to room temperature by itself and finally filtered and washed with isopropanol solution. Sharp crystalline $CH_3NH_3PbBr_3$ with the room temperature cubic phase was obtained. The method was further extended for preparing $CH_3NH_3PbI_3$ in a similar way by replacing HBr solution with HI during synthesis. Highly crystalline $CH_3NH_3PbI_3$ microwires with room temperature tetragonal phase were derived finally.

(B) Geometry confinement: Anodized alumina membrane (thickness: 2 μm) with hexagonal stand-alone nanochannels has been used for growing Methylammonium lead iodide perovskite nanowires in it.[21] In addition to flexibility of uniform array structures with individually addressable each nanowire, this template assisted growth allows chemical and mechanical robustness to perovskite for protecting them from ambient water and oxygen which lead to degradation in the material. The nanowires length can be varied by tuning the lead content and reaction time. Similar templated synthesis of perovskite nanotubes was also reported by Xu et al.[22] Using μ-Alkylammonium emulsion, 100 μm long Methylammonium (MA) and Formamidinium (FA) lead bromide nanotubes of diameter 300 nm were prepared from $[PbBr_6]^{4-}$, MA^+ and FA^+ cations. In 2017, Lee et al. prepared single crystalline $CH_3NH_3PbI_3$ film by confining its geometry during growth.[23] They first filled the perovskite precursor solution into an ink supplier fitted on on a metal cylinder. An array structured polymer mould was wrapped over this cylindrical roller. The mould array contained numerous nanochannels (Width: 10 mm, Depth: 200 nm, Spacing: 400 nm). The roller was then placed on a hot silica substrate (preheated at 180 ^{0}C which resulted into immediate lateral crystallization along the vertical mould channel direction. Independent of surface epitaxy, this scalable crystallization allowed complete dimensional control over patterning through distance and speed of rolling. Synthesis of high-quality large scale microwire arrays of Methylammonium lead iodide via one-step blade coating process

was reported by Deng et al. in 2016.[24]

In addition to its cost-effectiveness, the method allowed provision for use of flexible substrates as well. In a typical process, a blade is used to drag perovskite precursor solution over the hot (100 ^{0}C) surface of a substrate. The solution after evaporation produced centimeter long and 2-3 μm wide highly uniform perovskite wires orientedalong the dragging direction of the blade.

(C) Direct patterning, lithography and capillary growth: In 2015, two-step processed Methylammonium lead bromide perovskite was patterned by focused ion beam (FIB) technology.[25] The research group fabricated highly uniform nanograting of subwavelength dimension for studying photonic behavior of the perovskite crystal. The patterning was optimized by controlling dwell time, ion dosage, beam current, angle of incidence, etc. In 2018, Gharajeh et al. devised distributed feedback type perovskite laser with low pumping of 0.1 W/cm^2 at ambient by pattering perovskite nanostructures via thermal nanoimprint lithography (NIL) technology.[26] For making the cavity, a silica mold was first fabricated by electron beam lithography, followed by plasma etching of SiO2 which was masked with chromium. After applying a non-adhesive coating over the mold, perovskite precursor solution was deposited on silicon substrate by spin coating and finally thermal NIL was performed for obtaining the feedback structure.

2.2. Electron field emission as a non-trivial application

Exploiting its excellent photo-absorption properties, solar cell related applications have always been in lime light for hybrid metal halide perovskites. Indeed, the material drew worldwide attention with its performance as a solar material in the first decade of 21st century. Electron field emission (also known as cold cathode emission) is one of its unexplored application possibilities, which is of tremendous importance owing to low power consumption with high quality display.

The phrase 'electron field emission' is inspired by the fact that electrons are emitted or generated by the application of very high electrostatic field, sometimes even beyond GV/m. Also known as cold cathode emission, the phenomenon describes emission of electrons from bulk metals to vacuum through quantum mechanical tunneling. As shown in the schematic (Figure 2.1), electrons percolate through the triangular potential distribution function (x: inter-electrode separation). The giant electric field helps electrons overcome the surface potential barrier, which

is called the work function (Φ). With certain modifications, the theory which is given by Ralph H. Fowler and Lothar W. Nordheim can also be applied to crystalline solids. Under the application of an external
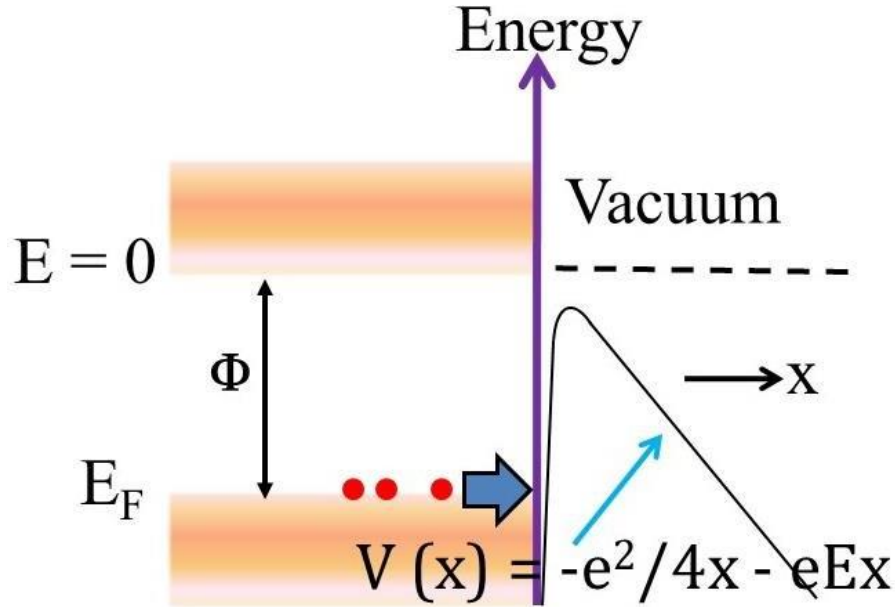
Figure 2.1: Schematic of electron field emission mechanism

field (E), the emitted electrons constitute a current, the density of which (J) is approximated by the following equation. [27]

$$J = \frac{a\beta^2 E^2}{\emptyset} e^{-b\emptyset^{3/2}/\beta E} \tag{2.1a}$$

Here β is the field enhancement factor (a measure defining the quality of field emission), A is the emission area, a and b are called Fowler–Nordheim (F-N) constants with values: 1.54 μA eV/V^2 and 6830 eV$^{-3/2}$ V/μm respectively. When represented in logarithmic expressions, equation (2.1a) takes the following form (known as FN equation).

$$ln\left(\frac{J}{E^2}\right) = ln\left(\frac{a\beta^2}{\emptyset}\right) - \frac{b\emptyset^{3/2}}{\beta E} \tag{2.1b}$$

Plotting ln (J/E^2) vs. 1/E to generate a straight line with slope - bφ$^{3/2}$/β and intercept ln (aβ^2/φ) defines the emission to be FN type field emission. Under the application of E, the field gets manifold near the nanostructure emitters locally by the factor β. Thus, the effective field at these places enhances to βE. Electrons emitted via this approach consume very low power and don't

64

heat up the material due to any Joule loss (hence the name: cold cathode). Materials such as tungsten (W), lanthanum hexaboride (LaB$_6$) etc. are already used as electron gun in Field emission microscopy due to their excellent emission behavior.

Although there are plenty of reports on the electron field emission properties on oxide based perovskites in literature, very limited resources can however be found with the hybrid metal halide counterparts. In 2017, Arquer and his team utilized field emission to achieve NIR photodetection by solution processed CH$_3$NH$_3$PbI$_{2.5}$Br$_{0.5}$ quantum dots.[28] Photogenerated carrier extraction was realized by field emission and excellent detection with detectivity $> 10^{12}$ Jones was accessed efficiently. In the same year, a detail investigation on the electron field emission properties from room temperature solution processed Methylammonium lead iodide nanostructures was published by Besra et al.[29] With a turn-on field of 4.2 V/μm, the study demonstrated considerable and sustainable electron emission for as long as 2 hrs. Inspired by this study, Tufan et al. carried out a similar investigation with inorganic halides and reported electron field emission behaviour from room temperature processed Cesium lead halide nanorods in 2019. Owing to low work function and highest aspect ratio among all the halide variations, the iodide nanowires showed best emission performance with current density 133 μA/cm^2 at an external electric field of 8 V/μm. They enhanced its performance further by reduced graphene oxide (rGO) wrapping over the perovskite nanostructures, which they attributed to the better electron transport through highly conductive rGO layers.[30] Next year in 2020, Du and his group prepared [100] oriented single crystalline nanobelts of Cesium lead iodide via solvothermal route and studied the field emission aspect. With a calculated work function of 3.56 eV, remarkable emission was achieved with a turn-on field value as low as 2.62 V/μm and field enhancement factor ~ 3550.[31]

2.3. Improvement of photodetection performance

A photodetector is nothing but a device to sense light, whether it be visible or any other part of the electromagnetic spectrum. In a typical semiconductor, light when falling to the p-n junction, creates electron-hole pairs. The internal electric field existing across the junction sweeps away these carriers to the suitable electrode peripherals connected with external battery. A fraction of the incident light energy is converted into electric energy in this process. Unlike a photodiode, it is reverse biased to allow only a small reverse saturation current through it during dark

conditions. A photodetector is generally characterized by its responsivity (R), spectral response (R_λ), quantum efficiency (η), detectivity (D_λ), response (rise/decay) times (t_{rise}/t_{decay}), dark current (I_d), noise spectral density, etc.[32] some of which are defined below.

$$R = \frac{I_{out}}{P_{in}}, \ R_\lambda = \frac{I_{ph}}{P_{in}}, \ \eta = \frac{I_{ph}/e}{P_{in}/h\nu}, \ D_\lambda = \frac{R_\lambda}{\sqrt{(2eJ_d)}} \tag{2.2}$$

(I_{out}: Current generated at the device output, I_{ph}: Current produced due to a certain light of wavelength λ, P_{in}: Input power supplied to the device, e: electronic charge, hν: energy of the incident photon, J_d: dark current density) It is seen that quantum efficiency is nothing but the number of photogenerated carriers corresponding to each absorbed photon. Since different wavelengths have different responsivities, detectivity is also a function of the wavelength of the incident photons. Response speed of detection is typically defined in terms of rise time and decay time-the time taken to rise the photocurrent from 10% to 90% and to fall from 90% to a to 10% of the maximum possible photocurrent respectively. The responsivity and response times are generally influenced by the energy band structure, crystalline characteristics and electrode configuration of the device. The response times also depend on carrier transport and parasitic effects. Device noise during photodetection leads to degraded signal to noise ratio (SNR). Mostly characterized by noise spectral density, it measures the intrinsic noise voltage/current in the device corresponding to unit differential wavelength shift.

Among the various methodologies, which have so far been adopted to upgrade the photodetector performances based upon hybrid metal halide perovskites, some recent ones are discussed below. Integration of metal nanoparticles into graphene/$CH_3NH_3PbI_3$ structure led to higher responsivity and faster response due to resonating surface plasmons of gold.[33] The metallic surface plasmons improves light absorption by enhancing the near field very close to the graphene/perovskite interface. Swati et al. achieved improved photodetection from two step spin coated uniform thin film with reduced pin holes.[34] The improved surface and crystal qualities obtained through the two-step spin coating process delivered a photoresponsivity of ~ 1 A/W and detectivity of > 10^{11} Jones at a bias of -1 V, which are ~ 55 and 10^2 times larger than the obtained values with one step spin coating. Relatively less charge recombination with longer carrier life time were revealed by impedance spectroscopy. Pressure induced reversible enhancement in $CH_3NH_3PbBr_3$ based photodetector was investigated by Boopathi and his team.[35] Stronger emission from the edges of the synthesized single crystal was utilized to device photodetector with detectivity > 10^{13} Jones, attributed to lesser trap densities in the crystal. A recent study reported excellent

photodetection with responsivity and efficiency of 3×10^4 A/W and 10^5 % from spontaneously grown N-rGO/perovskite hybrid with optimized interfacial carrier transport properties.[36] Improved and stable detection was achieved by using MgO/ZnO bilayer.[37] Efficient light harvesting due to ZnO arrays and promoted charge transport due to MgO led to stable on/off ratio of ~ 10^4 even after 15 days in air. The incorporation of MgO resulted into a dynamic range of ~ 88 dB, with almost unattenuated photocurrent for 30 min under 314 mW/cm^2 illumination. Exploiting efficient photon conversion, thermal stability and relatively easy exciton dissociation, triple cation and halide mixing in combination with plasmonic functionalization modulated perovskite photodetector showed detectivity and quantum efficiency of 1.5×10^{12} Jones and 188.8% respectively, with improvement of approximately 3000% over the convenient photodetectors.[38] Similar halide mixing along with surface passivation technique is also reported by other research groups.[39] Core shell structure of CdSe/ZnS quantum dots, in their study, reduced the defect states and thus increased carrier transport in the device.

2.4. Impedance studies and charge relaxation

Hybrid metal halide perovskites come with high value of dielectric polarization and ambipolar type charge transport properties. In this context, Bisquert et al. proposed a model which was based on ac dielectric constant of the material.[40] Starting from classical drift-diffusion and Poisson's eqns., transmission line was derived and the corresponding impedance spectra were analyzed. The fitted arcs at low, mid and high frequencies were attributed to dielectric relaxation, charge recombination and geometrical capacitance respectively. The static part of the dielectric constant depending on density led to inductive feature through current generation in the material. Dualeh and his group extended the prevalent models to understand the impedance behavior of solar cells based on Methylammonium lead iodide.[41] Effects of additive amount and hole transporting layer thickness on overall impedance parameters were also incorporated in this study. Ionic as well as electronic charge transports were ascribed to generate low frequency slow response and mid frequency RC (R: resistance, C: capacitance) electrical feature in the impedance spectra. Guerrero et al. attempted to generalize the understanding of impedance behavior of hybrid metal halide perovskites.[42] The impedance responses of $(FA_{0.85}MA_{0.15}Pb(I_{0.85}Br_{0.15})_3)$ were classified by tuning the electron transport layers and perovskite film thickness. Interpretation of impedance spectra revealed various capacitive

mechanisms along with charge extraction and a mid-frequency inductive signature. Low frequency interfacial ion accumulation has immense impact on device performance. Hysteresis in such perovskites can be seen to occur from ion transport across interface and the extraction layers. The unbiased high frequency capacitance is ascribed to bulk relaxation process which is otherwise linked with depletion type capacitance under bias voltage. Interfacial accumulation of photogenerated electrons also leads to capacitance at low frequency under light illumination. Both ion accumulation near metal contacts under dark and electron accumulation near interface under light result into hysteretic effect in perovskite.[43] In a study to investigate the effect of hole blocking material on device performance, Wang et al. carried out impedance analysis through cyclic voltammetry near milli to hundreds of Hz.[44] The research group identified prominent presence of inductive loop as a clear indication of inferior device performance due to inefficient blocking of carrier recombination. Significance of this inductive loop in impedance spectra was also pointed out by Ghahremanirad et al. in 2017.[45] Surface polarization arising from interfacial charge accumulation at contact electrodes reflects in voltage lag which finally leads to inductive response as well as negative capacitance features. Among other impedance parameters such as R_{CT} (charge transport resistance), R_{rec} (recombination resistance), carrier lifetime, etc., the value of carrier mobility showed well agreement with the same obtained from current-voltage characteristics studies by Upadhyaya et al.[46] Trap mediated charge recombination in Methylammonium lead halide solar cell is explored from incident light illumination influencing the output current-voltage characteristics.[47] The study confirmed presence of distributed trap states across the surface to bulk of the material. With a large value of light and voltage dependent static dielectric constant, dielectric loss was evident from considerable drop in the high frequency chemical capacitance. In a study with Methylammonium lead bromide in direct contact with gold electrode, double layer capacitance was found by Aranda et al.[48] Slow reactivity (time scale > 100 s) between ionic species in perovskite with the contact electrodes reduces carrier recombination under light illumination and thus improves the device performance. Zheng and his research team prepared cation and halide varied perovskites and performed a thorough impedance spectroscopy in 2020.[49] Fitted with equivalent electrical circuit, capacitance and resistance obtained at high frequency were related to the relative permittivity and recombination resistance of the bulk perovskite respectively; whereas those at high frequency were related to current-voltage hysteresis and interfacial recombination respectively. Phase lag occurring in the recombination processes owes its origin to ionic and

68

defect dynamics. Their work suggested a good cation mixing strategy to stabilize the structure with reduced hysteresis by minimizing carrier recombination and ionic mobility. A recent study by Srivastava and her group demonstrated how ionic conductivity can be tuned by not only changing the cation or halide part of perovskite, but also with light illumination and external bias voltage.[50] Based on jump relaxation and vacancy hopping, effect of charge accumulation and carrier transport was scrutinized. The low and mid frequency conductivity followed Jonscher's power law i.e., $\sigma_{AC} = \sigma_{DC} + A\omega^n$ (σ: conductivity; ω: angular frequency of the ac signal; n: power index defining the conduction mechanism), whereas the high frequency region came up with a constant value.

2.5. Cation and halide mixing and their effects

Improved device performance with better stability can be often achieved by compositional changes via cation and halide mixing in hybrid metal halide perovskites. McMeekin et al. fabricated perovskite solar cell with 14.7% efficiency and 1.2V open circuit voltage. A tandem solar cell was designed by them based on the optimized composition $[HC(NH_2)_2]_{0.83}Cs_{0.17}Pb(I_{0.6}Br_{0.4})_3$ with 1.75 eV band gap.[51] Yi et al. demonstrated how Cesium and Methylammonium addition into Formamidinium lead iodide (FAPbI$_3$) could improve light harvesting and stabilized solar cell performance at ambient.[52] Supported by theoretical calculations, entropy increase was ascribed as the cause of reducing δ-phase formation in FAPbI$_3$. Effect of such formamidinium replacement with methylammonium or cesium was probed with bias and photo dependent impedance analysis.[53] In addition to the associated criticalities, various kinds of cation mixing in 2D and 3D perovskites can be found in the review work of Xu et al.[54] In 2017, Barker et al. addressed the segregation of halide ions in perovskite materials under light illumination.[55] The segregation finds its origin in the non-uniform rate of photogenerated carriers and hampers in bandgap tuning of halide varied perovskite, which is otherwise possible over a wide range. Dependent on the number of defects in the material, they suggested a way to minimize it by its uniform distribution. Halide mixing in perovskite has also profound influence on switching characteristics of resistive memory devices. Hwang and his group fabricated solvent engineered Methylammonium lead iodide-bromide based memory switch and studied its performance in terms of halide variation.[56] The migrating bromide/iodide ions serve as vacancy defects in system which form conducting channels under application of

external bias voltage. The group found that increased bromine percentage reduced the set-in voltage of the device. The finding was corroborated with first principle calculations which revealed easier migration of bromine ions in comparison to iodine ones. Compositional tuning through such halide variation also allowed to customize the operating bias voltage. Realizing the impact of halide optimized compositions on the material properties and device performance finally, exclusive investigation in this direction was attempted by Li et al. in 2017.[57] The group deployed a different approach, referring as 'mixture design', to map the interconnection between perovskite composition and the resulting material properties therefrom by compositional tuning and thus achieved an efficiency of ~ 21% from the optimized cell. Simultaneous cation and halide mixing in single crystalline triple cation perovskite demonstrated improved stability under ambient conditions such as temperature, moisture, light and oxygen molecules.[58] Witnessing clear phase segregation beyond a certain compositional tuning, the optimized alloy i.e. $(FAPbI_3)_{0.9}(MAPbBr_3)_{0.05}(CsPbBr_3)_{0.05}$ gave increased lifetime (16 µs) and stability over thousands of hours under ambient. In 2020, Greenland et al. correlated phase behavior of $(FAPbI_3)_{0.85}(MAPbBr_3)_{0.15}$ with its physical properties under photon excitation. Pseudo-cubic α (room temperature) and pseudo-tetragonal β phase (> 260 K) were witnessed for this material. The study established that such structural modifications occurring had immense impact on the recombination processes of charge carriers.[59] Under light illumination, photogenerated electrons from perovskite get injected into the electron transport layers and captured by oxygen molecules, which leads to accumulation of holes in the perovskite film.[60] Such hole accumulation near halide sites, unless extracted to hole transport layers, moves them from their lattice positions to grain boundaries and thus results into structural instability. Very recently, Escrig et al. prepared $FA_{1-n}Cs_nPb(I_{1-x}Br_x)_3$ perovskite with large tunability over the energy bandgap and morphology.[61] Stable photovoltaic output with 16.8% efficiency was achieved from the optimized sample.

2.6. Struggle against degradation

Material and device degradation of perovskites under light, moisture, heat, electric field, etc. is a serious concern to material scientists. This degradation often reflects its signature in optoelectronic properties, which was correlated with the superficial structural changes by Matsumoto et al. in 2015.[62] As per their studies, a single active layer of $CH_3NH_3PbI_3$ undergoes

slower decomposition compared to a layer interfacing with a metal electrode under light and ambient moisture. Spectroscopic analysis suggested rapid surge in surface roughness with reduced photo-absorption near its energy band edge, possibly due to the formation of PbI_2 in the system. The role of electrode interface was systematically investigated by Guerrero et al. with different metal electrodes.[63] Under a constant illumination condition, considerable drop in efficiency from 12% to 1.8% was observed due to electrode corrosion. Interfacial dipole formation near the electrodes as well as ionic movement through perovskite modulate the interfacial energy landscape and thus hinder charge extraction across it. The group finally suggested a remedy for the issue as using chromium alloy instead, which gave more stability to the device although with less efficiency. Brivio et al. carried out a first principle study to address the photo-induced instability in Methylammonium lead iodide/bromide from a Thermodynamic point of view.[64] Based on phase diagram construction giving a large gap in miscibility (T_c: 343 K), the alloy was observed to be subject to spinodal decomposition and a metastable binodal state in presence of excess amount of iodine and bromine. Another theoretical investigation revealed high water solubility of Methylammonium iodide as the main cause of moisture-induced degradation of $CH_3NH_3PbI_3$.[65] However, irrespective of the presence of oxygen or humidity, intrinsic thermodynamic instability was ascribed to be mainly responsible by Zhang et al.[66] Based on density functional calculations, they showed that the phase segregated methylammonium and lead iodide combination is energetically more stable than methylammonium lead iodide itself. As per their calculations, the scenario improves when MA, Pb and I are substituted by Cs, Sn and Cl respectively, i.e. with $CsSnCl_3$. Study by Park et al. also pointed out similar material degradation owing to the presence of organic component and the low formation enthalpy of $CH_3NH_3PbI_3$ and finally came up with a suggestion of using FA in place of MA for getting better stability.[67] Electric field induced reversible/irreversible degradation without/with ambient moisture is seen in hybrid metal halide perovskites.[68] Leijtens and his team in 2015 mapped this distribution of field mediated degradation changes in such perovskite films. The associated time spans for the reversible and irreversible changes were found to be of the order of ~ minutes and hours respectively. The study identified the irreversible structural changes in the material to be mainly arising because of the ambient moisture or tiny polar molecules with H-bonding properties via an intermediate hydrate phase, which often manifests through MA^+ drift along the electric field and PbI_2 formation at the end. In 2018, Yu et al. came up with a new strategy to improve upon the instability issue and proposed application of

atomic layer deposited oxide films such as Al_2O_3 and ZnO on the electron transport layer (PCBM).[69] From their nucleation studies, it is understood that this oxide films served as a protective coating for the underlying perovskite layers and made significant contribution towards achieving better stability even when put in contact with liquid water. In 2019, Li et al. exploited highly electronegative fluoride for passivating diffusing halide and organic ions.[70] The group fabricated high efficiency solar cell based on triple cation mixed halide $(Cs_{0.05}FA_{0.54}MA_{0.41})Pb(I_{0.98}Br_{0.02})_3$ with sodium fluoride treatment suppressing the halide/cation vacancy formations and thereby maintaining the device efficiency up to 90% over as long as thousand hours. A review work published in 2020 presented the governing factors of perovskite instabilities and also pointed out the remedies accordingly.[71] As per the review, ambient moisture produces intermediate hydrated phase which obstructs extraction of the photogenerated charge carriers. This can be avoided by encapsulating the material with some water-resistant transparent polymer coating. Degradation due to light illumination can be reduced by rationally optimizing the material and the device architecture. Thermal instability is generally associated with the rapid formation of PbI_2 owing to its low formation enthalpy. In 2020, Park et al. reported stable photovoltaic performance (95% retention) based on silvered Sn/Pb alloy perovskite.[72] Based on their theoretical calculations using DFT, the doped silver largens the perovskite grain sizes and builds an energy barrier for the adsorbing oxygen moieties. The silver assisted strain relaxation protects perovskite film to react with oxygen molecules. Molecular dynamics (MD) study identified the rapidly rotating MA groups to destroy the structural framework of $MAPbI_3/MAPbBr_3$ crystals and to produce temperature induced degradation in such perovskites.[73]

References

[1] N.-G. Park, Crystal growth engineering for high efficiency perovskite solar cells, Cryst. Eng. Comm. 18 (2016) 5977. doi:10.1186/s40580-016-0074-x.

[2] J. S. Manser, M. I. Saidaminov, O. M. Bakr, P. V Kamat, Making and Breaking of Lead Halide Perovskites, (2015). Doi: 10.1021/acs.accounts.5b00455.

[3] M. Saba, F. Quochi, A. Mura, G. Bongiovanni, Excited State Properties of Hybrid Perovskites, Acc. Chem. Res. (2015) acs.accounts.5b00445. Doi: 10.1021/acs.accounts.5b00445

[4] S. Razza, S. Castro-Hermosa, A. Di Carlo, T. M. Brown, Research Update: Large-area

deposition, coating, printing, and processing techniques for the upscaling of perovskite solar cell technology, APL Mater. 4 (2016). doi:10.1063/1.4962478.

[5] X. Dai, C. Shi, Y. Zhang, N. Wu, J. Semicond. 2015, 36, 074003.

[6] S. Sun, T. Salim, N. Mathews, M. Duchamp, C. Boothroyd, G. Xing, T. C. Sum, Y. M. Lam, Energy Environ. Sci. 2014, 7, 399.

[7] J.-Y. Jeng, Y.-F. Chiang, M.-H. Lee, S.-R. Peng, T.-F. Guo, P. Chen, T.-C. Wen, Adv. Mater. 2013, 25, 3727.

[8] Q. Wang, Y. Shao, Q. Dong, Z. Xiao, Y. Yuan, J. Huang, Energy Environ. Sci. 2014, 7, 2359.

[9] J.-H. Im, H.-S. Kim, N.-G. Park, APL Mater. 2014, 2, 081510.

[10] N. J. Jeon, J. H. Noh, Y. C. Kim, W. S. Yang, S. Ryu, S. Il Seol, Nat. Mater. 2014, 13, 897.

[11] J. Burschka, N. Pellet, S.-J. Moon, R. Humphry-Baker, P. Gao, M. K. Nazeeruddin, M. Graetzel, Nature 2013, 499, 316.

[12] M. Liu, M. B. Johnston, H. J. Snaith, Efficient planar heterojunction perovskite solar cells by vapour deposition, Nature 2013, 501, 395-398. Doi: 10.1038/nature12509

[13] Q. Chen, H. Zhou, Z. Hong, S. Luo, H.-S. Duan, H.-H. Wang, Y. Liu, G. Li, Y. Yang, Planar Heterojunction Perovskite Solar Cells via Vapor-Assisted Solution Process, J. Am. Chem. Soc. 2014, 136, 622-625. Doi: 10.1021/ja411509g

[14] M. R. Leyden, Y. Jiang, Y. Qi, Chemical vapor deposition grown formamidinium perovskite solar modules with high steady state power and thermal stability, J. Mater. Chem. A 2016, 4, 13125-13132. Doi: 10.1039/C6TA04267H

[15] O. Vybornyi, S. Yakunin, and M. V. Kovalenko, Polar-solvent-free colloidal synthesis of highly luminescent alkylammonium lead halide perovskite nanocrystals. Nanoscale, 2016, 8(12), 6278–6283. Doi: 10.1039/c5nr06890h.

[16] L. C. Schmidt, A. Pertegas, S. G. Carrero, O. Malinkiewicz, S. Agouram, G. M. Espallargas, H. J. Bolink, R. E. Galian, and J. P. Prieto, Nontemplate Synthesis of $CH_3NH_3PbBr_3$ Perovskite Nanoparticles, J. Am. Chem. Soc. 2014, 136, 850−853.

[17] M. B. Teunis, M. A. Johnson, B. B. Muhoberac, S. Seifert and R. Sardar, Programmable Colloidal Approach to Hierarchical Structures of Methylammonium Lead Bromide Perovskite Nanocrystals with Bright Photoluminescent Properties, Chem. Mater. 2017, 29, 3526−3537. DOI: 10.1021/acs.chemmater.6b05393

[18]   F. Zhang, C. Chen, X. Wu, X. Hu, H. Huang, J. Han, B. Zou, Y. Dong and H. Zhong, Brightly-Luminescent and Color-Tunable Colloidal $CH_3NH_3PbX_3$ (X=Br, I, Cl) Quantum Dots: Potential Alternatives for Display Technology, International Photonics and Opto-Electronics. 2015. Doi: 10.1364/pfe.2015.pw2e.3

[19]   F. Zhu, L. Men, Y. Guo, Q. Zhu, U. Bhattacharjee, P. M. Goodwin, J. W. Petrich, E. A. Smith and J. Vela, Shape Evolution and Single Particle Luminescence of Organometal Halide Perovskite Nanocrystals, ACS Nano, 2015, 9(3), 2948–2959.

[20]   Hua-Rong Xia, Wen-Tao Sun and Lian-Mao Peng, Hydrothermal synthesis of organometal halide perovskites for Li-ion batteries, Chem. Commun., (2015). DOI: 10.1039/C5CC05053G

[21]   L. Gu, M. M. Tavakoli, D. Zhang, Q. Zhang, A. Waleed, Y. Xiao, K.-H. Tsui, Y. Lin, L. Liao, J. Wang and Z. Fan, 3D Arrays of 1024-Pixel Image Sensors based on Lead Halide Perovskite Nanowires, Adv Mater, 2016, 28(44):9713-9721. Doi: 10.1002/adma.201601603.

[22]   L. Xu, J. Li, Y. Dong, J. Xue, Y. Gu, H. Zeng and J. Song, Self-template Synthesis of Metal Halide Perovskite Nanotubes as Functional Cavities for Tailored Optoelectronic Devices, ACS Appl. Mater. Interfaces 2019, 11, 23, 21100–21108.

[23]   Lee, L., Baek, J., Park, K. S., Lee, Y.-E., Shrestha, N. K., & Sung, M. M. Wafer-scale single-crystal perovskite patterned thin films based on geometrically-confined lateral crystal growth. Nature Communications, (2017) 8, 15882. doi:10.1038/ncomms15882

[24]   W. Deng, X. Zhang, L. Huang, X. Xu, L. Wang, J. Wang, Q. Shang, S. T. Lee and J. Jie, Aligned Single-Crystalline Perovskite Microwire Arrays for High-Performance Flexible Image Sensors with Long-Term Stability. Advanced Materials, 2016, 28(11), 2201–2208.

[25]   M. S. Alias et al., Focused-ion beam patterning of organolead trihalide perovskite for subwavelength grating nanophotonic applications, Journal of Vacuum Science & Technology B 33, 051207 (2015). Doi: 10.1116/1.4927542.

[26]   A. Gharajeh, R. Haroldson, Z. Li, J. Moon, B. Balachandran, W. Hu, A. Zakhidov, and Q. Gu, Continuous-wave operation in directly patterned perovskite distributed feedback light source at room temperature, Optics Letters, Vol. 43, pp. 611-614, (2018).

[27]   Fowler, R. H. and Dr. L. Nordheim, Electron Emission in Intense Electric Fields, Proceedings of the Royal Society A. 1928, 119, 173–181. DOI: 10.1098/rspa.1928.0091.

[28]   Arquer et al., Field-emission from quantum-dot-in-perovskite solids. Nat. Commun. 2017, 8, 14757. DOI: 10.1038/ncomms14757.

[29]   N. Besra, S. Pal, B. K. Das and K. K. Chattopadhyay, Perovskites beyond photovoltaics: field emission from morphology-tailored nanostructured methylammonium lead triiodide, Phys. Chem. Chem. Phys. 19 (2017) 26708-26717, DOI: 10.1039/C7CP04038E.

[30]   T. Paul, S. Maiti, N. Besra, B. K. Chatterjee, B. K. Das, S. Thakur, S. Sarkar, N. S. Das and K. K. Chattopadhyay, Tailored CsPbX3 Nanorods for Electron-Emission Nanodevices, ACS Appl. Nano Mater. 2 (2019) 5942-5951, DOI: 10.1021/acsanm.9b01379.

[31]   Z. Du, F. Jiang, J. Zheng, S. Chen, F. Gao, J. Teng, D. Fu, H. Zhang and W. Yang, Field Emission Behaviors of $CsPbI_3$ Nanobelts, J. Mater. Chem. C 8 (2020) 5156-5162.

[32]   R. A. Yotter and D. M. Wilson, A review of photodetectors for sensing light-emitting reporters in biological systems, IEEE Sensors Journal. 2003, 3, 288–303.

[33]   Z. Sun, L. Aigouy and Z. Chen, Plasmonic-enhanced perovskite–graphene hybrid photodetectors, *Nanoscale*, 2016, 8, 7377-7383. DOI: 10.1039/C5NR08677A.

[34]   S. Chaudhary, S. K. Gupta and C. M. S. Negi, Enhanced performance of perovskite photodetectors fabricated by two-step spin coating approach, Materials Science in Semiconductor Processing, 109, 2020, 104916. Doi: 10.1016/j.mssp.2020.104916.

[35]   Boopathi et al., Permanent Lattice Compression of Lead-Halide Perovskite for Persistently Enhanced Optoelectronic Properties, ACS Energy Lett., 2020, 5, 2, 642–649.

[36]   Y. Tang, M. Liang, M. W. Zhang, A. Honarfar, X. Zou, M. Abdellah, T. Pullerits, K. Zheng and Q. Chi, Photodetector Based on Spontaneously Grown Strongly Coupled $MAPbBr_3$/N-rGO Hybrids Showing Enhanced Performance, ACS Appl. Mater. Interfaces 2020, 12, 1, 858–867. doi:10.1021/acsami.9b18598.

[37]   X. Yang, Y. Zhu, H. Zhou, Z. Song, R. Liu, L. Shen and H. Wang, MgO/ZnO microsphere bilayer structure towards enhancing the stability of the self-powered $MAPbI_3$ perovskite photodetectors with high detectivity, Applied Surface Science, 504, 2020, 144468. DOI: 10.1016/j.apsusc.2019.144468.

[38]   Wang et al., Boosting Perovskite Photodetector Performance in NIR Using Plasmonic Bowtie Nanoantenna Arrays, Small, 16, 2020, 2001417. DOI: 10.1002/smll.202001417.

[39]   T. K. O. Vu, I. W. Cho, J. Oh, D. U. Lee, M. Y. Ryu and E. K. Kim, Defect suppression and photoresponsivity enhancement in methylammonium lead halide perovskites by CdSe/ZnS quantum dots, Journal of Colloid and Interface Science, 590, 2021, 19-27.

[40]   Juan Bisquert, Luca Bertoluzzi, Ivan Mora-Sero and Germà Garcia-Belmonte, Theory of Impedance and Capacitance Spectroscopy of Solar Cells with Dielectric Relaxation, Drift-

Diffusion Transport, and Recombination, J. Phys. Chem. C 2014, 118, 33, 18983–18991.

[41]   Amalie Dualeh, Thomas Moehl, Nicolas Tétreault, Joël Teuscher, Peng Gao, Mohammad Khaja Nazeeruddin, and Michael Grätzel, Impedance Spectroscopic Analysis of Lead Iodide Perovskite-Sensitized Solid-State Solar Cells, ACS Nano 2014, 8, 1, 362–373.

[42]   Antonio Guerrero, Germà Garcia-Belmonte, Ivan Mora-Sero, Juan Bisquert, Yong Soo Kang, T. Jesper Jacobsson, Juan-Pablo Correa-Baena and Anders Hagfeldt, Properties of Contact and Bulk Impedances in Hybrid Lead Halide Perovskite Solar Cells Including Inductive Loop Elements, J. Phys. Chem. C 2016, 120, 15, 8023–8032.

[43]   Juan Bisquert, Germà Garcia-Belmonte and Antonio Guerrero, Impedance Characteristics of Hybrid Organometal Halide Perovskite Solar Cells, Organic-Inorganic Halide Perovskite Photovoltaics, 2016, pp 163-199. Doi: 10.1007/978-3-319-35114-8_7

[44]   Pengjiu Wang, Zhipeng Shao, Maria Ulfa and Thierry Pauporté, Insights into the Hole Blocking Layer Effect on the Perovskite Solar Cell Performance and Impedance Response, J. Phys. Chem. C 2017, 121, 17, 9131–9141.

[45]   Elnaz Ghahremanirad, Agustín Bou, Saeed Olyaee and Juan Bisquert, Inductive Loop in the Impedance Response of Perovskite Solar Cells Explained by Surface Polarization Model, J. Phys. Chem. Lett. 2017, 8, 7, 1402–1406.

[46]   Aditi Upadhyaya, Chandra Mohan Singh Negi, Anjali Yadav, Saral K. Gupta and Ajay Singh Verma, I-V and impedance characterization of a solution processed perovskite based heterojunction photodetector, Superlattices and Microstructures, 2018, 122, 410-418.

[47]   C. Han, K. Wang, X. Zhu, H. Yu, X. Sun, Q. Yang and B. Hu, Unraveling surface and bulk trap states in lead halide perovskite solar cells using impedance spectroscopy, J. Phys. D: Appl. Phys., 2018, 51, 095501. Doi: 10.1088/1361-6463/aaa7cd/meta

[48]   Clara Aranda, Juan Bisquert and Antonio Guerrero, Impedance spectroscopy of perovskite/contact interface: Beneficial chemical reactivity effect, J. Chem. Phys. 2019, 151, 124201.

[49]   Daming Zheng, Tao Zhu and Thierry Pauporté, Using Monovalent- to Trivalent-Cation Hybrid Perovskites for Producing High-Efficiency Solar Cells: Electrical Response, Impedance, and Stability, ACS Appl. Energy Mater. 2020, 3, 11, 10349-10361.

[50]   Priya Srivastava, Ramesh Kumar, and Monojit Bag, Discerning the Role of an A-Site Cation and X-Site Anion for Ion Conductivity Tuning in Hybrid Perovskites by Photoelectrochemical Impedance Spectroscopy, J. Phys. Chem. C 2021, 125, 1, 211–222.

[51]   D. P. McMeekin, G. Sadoughi, W. Rehman, G. E. Eperon, M. Saliba, M. T. Hörantner, A. Haghighirad, N. Sakai, L. Korte, B. Rech, M. B. Johnston, L. M. Herz and H. J. Snaith, A mixed-cation lead mixed-halide perovskite absorber for tandem solar cells, Science, 2016, 351, 151-155.

[52]   C. Yi, J. Luo, S. Meloni, A. Boziki, N. A. Astani, C. Grätzel, S. M. Zakeeruddin, U. Röthlisberger and M. Grätzel, Entropic stabilization of mixed A-cation ABX_3 metal halide perovskites for high performance perovskite solar cells, Energy Environ. Sci., 2016, 9, 656-662.

[53]   P. Wang, M. Ulfa and T. Pauporté, Effects of Perovskite Monovalent Cation Composition on the High and Low Frequency Impedance Response of Efficient Solar Cells, J. Phys. Chem. C 2018, 122, 4, 1973–1981.

[54]   F. Xu, T. Zhang, G. Li and Y. Zhao, Mixed cation hybrid lead halide perovskites with enhanced performance and stability, J. Mater. Chem. A, 2017, 5, 11450-11461.

[55]   A. J. Barker, A. Sadhanala, F. Deschler, M. Gandini, S. P. Senanayak, P. M. Pearce, E. Mosconi, A. J. Pearson, Y. Wu, A. R. S. Kandada, T. Leijtens, F. De Angelis, S. E. Dutton, A. Petrozza and R. H. Friend, Defect-Assisted Photoinduced Halide Segregation in Mixed-Halide Perovskite Thin Films, ACS Energy Lett. 2017, 2, 6, 1416–1424.

[56]   B. Hwang, C. Gu, D. Lee and J. S. Lee, Effect of halide-mixing on the switching behaviours of organic-inorganic hybrid perovskite memory, Scientific Reports, 2017, 7, Article no: 43794, doi:10.1038/srep43794

[57]   L. Li, N. Liu, Z. Xu, Q. Chen, X. Wang and H. Zhou, Precise Composition Tailoring of Mixed-Cation Hybrid Perovskites for Efficient Solar Cells by Mixture Design Methods, ACS Nano 2017, 11, 9, 8804–8813

[58]   L. Chen, Y. Y. Tan, Z. X. Chen, T. Wang, S. Hu, Z. A. Nan, L. Q. Xie, Y. Hui, J. X. Huang, C. Zhan, S. H. Wang, J. Z. Zhou, J. W. Yan, B. W. Mao and Z. Q. Tian, Toward Long-Term Stability: Single-Crystal Alloys of Cesium-Containing Mixed Cation and Mixed Halide Perovskite, J. Am. Chem. Soc. 2019, 141, 4, 1665–1671.

[59]   C. Greenland, A. Shnier, S. K. Rajendran, J. A. Smith, O. S. Game, D. Wamwangi, G. A. Turnbull, I. D. W. Samuel, D. G. Billing and D. G. Lidzey, Correlating Phase Behaviour with Photophysical Properties in Mixed-Cation Mixed-Halide Perovskite Thin Films, Advanced Energy Materials, 2020, 10, 1901350.

[60]   J. T. DuBose and P. V. Kamat, TiO_2-Assisted Halide Ion Segregation in Mixed Halide

Perovskite Films, J. Am. Chem. Soc. 2020, 142, 11, 5362–5370.

[61]   L. G. Escrig, C. Dreessen, F. Palazon, Z. Hawash, E. Moons, S. Albrecht, M. Sessolo and H. J. Bolink, Efficient Wide-Bandgap Mixed-Cation and Mixed-Halide Perovskite Solar Cells by Vacuum Deposition, ACS Energy Lett. 2021, 6, 2, 827–836.

[62]   Fukashi Matsumoto, Sarah M. Vorpahl, Jannel Q. Banks, Esha Sengupta, and David S. Ginger, Photodecomposition and Morphology Evolution of Organometal Halide Perovskite Solar Cells, J. Phys. Chem. C 2015, 119, 36, 20810–20816.

[63]   Antonio Guerrero, Jingbi You, Clara Aranda, Yong Soo Kang, Germà Garcia-Belmonte, Huanping Zhou, Juan Bisquert, and Yang Yang, Interfacial Degradation of Planar Lead Halide Perovskite Solar Cells, ACS Nano 2016, 10, 1, 218–224.

[64]   Federico Brivio, Clovis Caetano, and Aron Walsh, Thermodynamic Origin of Photoinstability in the $CH_3NH_3Pb(I_{1-x}Br_x)_3$ Hybrid Halide Perovskite Alloy, J. Phys. Chem. Lett. 2016, 7, 6, 1083–1087.

[65]   E. Tenuta, C. Zheng and O. Rubel, Thermodynamic origin of instability in hybrid halide perovskites. Sci Rep 6, 37654 (2016). doi:10.1038/srep37654.

[66]   Yue-Yu Zhang, Shiyou Chen, Peng Xu, Hongjun Xiang, Xin-Gao Gong, Aron Walsh and Su-Huai Wei, Intrinsic Instability of the Hybrid Halide Perovskite Semiconductor $CH_3NH_3PbI_3$, Chinese Phys. Lett., 2018, 35, 036104.

[67]   Byung-wook Park and Sang Il Seok, Intrinsic Instability of Inorganic–Organic Hybrid Halide Perovskite Materials, Advanced Materials, 2019, doi:10.1002/adma.201805337.

[68]   T. Leijtens et al., Mapping Electric Field-Induced Switchable Poling and Structural Degradation in Hybrid Lead Halide Perovskite Thin Films, Advanced Energy Materials, 2015, doi:10.1002/aenm.201500962.

[69]   Xiaozhou Yu, Haoming Yan, and Qing Peng, Improve the Stability of Hybrid Halide Perovskite via Atomic Layer Deposition on Activated Phenyl-C_{61} Butyric Acid Methyl Ester, ACS Appl. Mater. Interfaces, 2018, 10, 34, 28948–28954.

[70]   Li et al., Cation and anion immobilization through chemical bonding enhancement with fluorides for stable halide perovskite solar cells, Nature Energy, 2019, 4, 408–415.

[71]   Cai-Xin Zhang, Tao Shen, Dan Guo, Li-Ming Tang, Kaike Yang and Hui-Xiong Deng, Reviewing and understanding the stability mechanism of halide perovskite solar cells, InfoMat, 2020, 2, 1034-1056.

[72]   Chaneui Park, Jinhyeok Choi, Jiwoo Min, and Kilwon Cho, Suppression of Oxidative

Degradation of Tin–Lead Hybrid Organometal Halide Perovskite Solar Cells by Ag Doping, ACS Energy Lett. 2020, 5, 10, 3285–3294.

[73]   Danil W. Boukhvalov, Ivan S. Zhidkov, Azat F. Akbulatov, Andrey I. Kukharenko, Seif O. Cholakh, Keith J. Stevenson, Pavel A. Troshin and Ernst Z. Kurmaev, Thermal Effects and Halide Mixing of Hybrid Perovskites: MD and XPS Studies, J. Phys. Chem. A 2020, 124, 1, 135–140.

Characterizations and Measurement Tools Used

3.1. Crystallographic study: X-ray diffraction (XRD)

To ascertain if the synthesized material is really of our interest or something else is the first and foremost task for proceeding further. Phase matching with the already existing database or other reported values in literature is generally carried out using X-ray diffraction (XRD) technique. The diffraction pattern of any material is like a foot print of the material, revealing almost everything of its crystal structures. As discovered by Laue in 1912, the crystalline lattice planes effectively serve as diffraction grating in atomic-scale for incoming X-rays. Diffraction peaks are obtained when the incident certain orientations in satisfaction of Bragg's condition: $2d \sin \theta = n\lambda$ (d: inter-planar spacing; θ: angle of incidence of X-ray on the sample surface; n: order of diffraction; λ: incident X-ray wavelength) For orthogonal crystals, the above eqn. can be further used to estimate the lattice parameters by: $d = \dfrac{1}{\sqrt{\left(\frac{h^2}{a^2} + \frac{k^2}{b^2} + \frac{l^2}{c^2}\right)}}$ (h, k, l: Miller indices corresponding to (hkl) planes; a, b, c: dimensions of the unit cell)

Figure 3.1: X-ray diffractometer

In our experiments, XRD patterns of the samples were recorded by an X-ray diffractometer (Bruker D8 Advanced diffractometer) using Cu-K$_\alpha$ radiation having wavelength (λ) equal to 1.5418 Å, a weighted average of K$_{\alpha1}$ and K$_{\alpha2}$. A typical diffractometer (Figure 3.1) includes X-ray tube, sample holder and detector. Inside the tube, thermally generated electrons are accelerated by electric field and bombarded upon a target material (such as, copper), knocking out its inner electrons. The vacant shells are then filled by outer shell electrons and characteristic X-ray is thus emitted. The undesired X-ray wavelengths are filtered out by monochromatic crystals. The X-ray beam is then collimated towards the sample placed on a rotatable sample holder. The sample is generally turned into homogenously ground fine powder, exposing all of its possible crystal planes to X-ray. Signals diffracted at different angles (θ) are collected by a detector. It is a common practice to plot the diffraction signals as a function of 2θ, which is the angle of deviation of the incident X-rays. The signal pattern also helps get a rough estimate of the average crystallite size corresponding to a certain planar orientation by Scherrer's formula: $D = k\lambda/\beta cos\theta$ (D: Average crystallite size; k: shape factor; λ: incident X-ray wavelength; β: angular full width at half maxima.) For Gaussian shapes, k value is taken as 0.9 and λ is equal to 1.5418 Å. Therefore, a sharp peak with smaller FWHM value corresponds to large growth of crystalline planes and thus leads to single crystalline character; whereas a diffuse peak with larger FWHM indicates formation of large number of small grains which means polycrystalline feature.

3.2. Spectroscopic techniques

3.2.1. UV-Vis-NIR spectroscopy

Shown in Figure 3.2, the device utilizes the absorption or reflectance properties of materials in response to incident light in the ultraviolet, visible and near infra-red region. Absorption spectrum is generated due to electronic transitions of atoms/molecules from their low energy ground state to excited state having higher energy. Exclusive use of this technique can be seen in quantitative analysis of analytes e.g. organic compound conjugates, transitional metal ions, etc. Moreover, the technique can also be used for measuring thickness and optical properties of films. In addition to solutions, the technique also be applied with liquids and solids as well. As per Beer-Lambert's law, the degree of absorption is proportional to the concentration of solute present in the solvent. When expressed mathematically, it takes the form: $A = log_{10} (I_0/I) = \varepsilon cl$ (A: absorption; I_0: incident light intensity; I: transmitted light intensity; ε: extinction coefficient; c: sample

Figure 3.2: UV-Vis-NIR spectrophotometer

concentration and l: path length) The ratio I/I_0 is defined as transmittance. The experimental data for unknown sample are always calibrated w.r.t. the response from a standard known material such as BaSO4. The major components of a typical UV-Vis-NIR spectrophotometer include light source (e.g. Tungsten, Deuterium, Xenon, etc.), transparent sample holder (cuvette), prism or diffraction grating and detector (e.g. photodiodes, charge coupled device, etc.).

3.2.2. Fourier transformed infra-red (FTIR) spectroscopy

Figure 3.3: FTIR spectrometer

Most of the molecules changes their vibrational energy levels in the infra-red (IR) part of electromagnetic spectrum, 400- 4000 cm^{-1} being the central part of it. Therefore, when an IR light is

incident on them, a fraction of the light is absorbed in considerable amount. The strength and frequency of the absorbed light radiation varies from sample to sample and hence gives information about its molecular structure. An interferometer is used for signal acquisition from the sample. Figure 3.3 shows the setup of a FTIR spectrometer (Shimadzu-8400S, Prestige).

3.2.3. X-ray photoelectron spectroscopy (XPS)
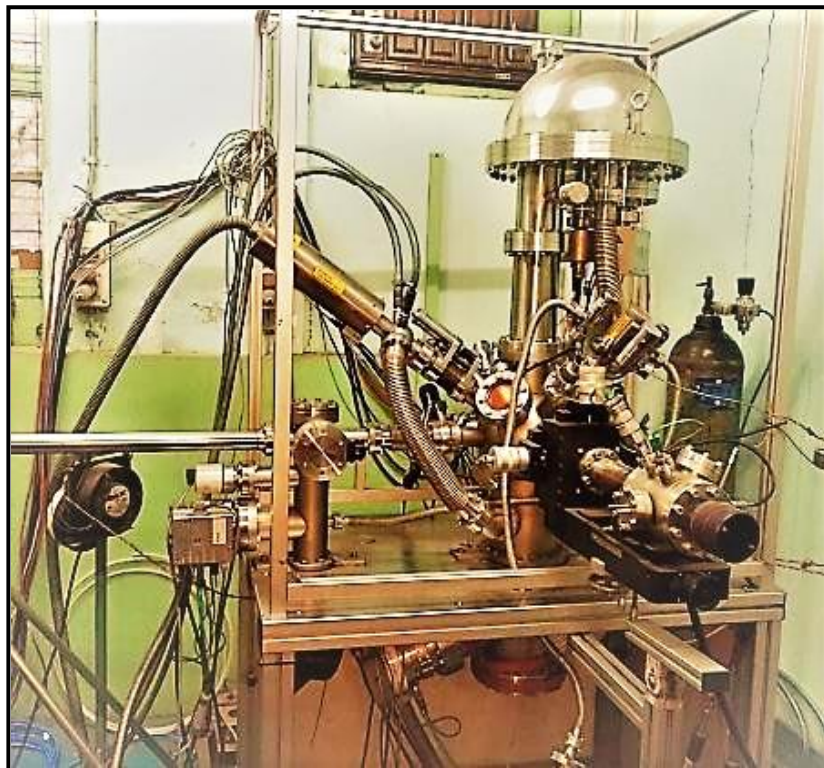
Figure 3.4: X-ray photoelectron spectrometer

X-ray photoelectron spectroscopy (XPS, SPECS, Germany) was employed to know the compositional information, oxidation states and sample purity. A picture of the set up can be seen in Figure 3.4. The sample when irradiated by X-ray emits photoelectrons with kinetic energy: $E_k = h\nu - E_b$ (hv: incident X-ray energy; E_b: electron's binding energy to the sample surface) Generally the photoelectrons are excited by monochromatic K_α X-ray of magnesium/aluminum. Under residual pressure of $< 10^{-9}$ mbar, the instrument is operated at voltage 10 kV and current 17 mA. A hemispherical energy analyzer (HAS 3500) is attached with the system for data analysis. Binding energy is a characteristic of any material. Therefore, with a known X-ray radiation, E_b can be estimated if the kinetic energy of the emitted electrons is measured. Thus, the presence of any particular element can be assured. Moreover, the relative weightage of different elements can be

estimated from area under the binding energy curves, giving a stoichiometric idea of the material. Shift in the recorded binding energy reveals chemical bonding information and charge states.

3.2.4. Energy dispersive X-ray (EDX) spectroscopy

Highly energetic electron beam, when incident on a material, knocks out characteristic X-rays from its bulk. The emitted X-ray carries signature of the material. Thus, an idea of the elemental composition can be obtained using this technique. From the relative intensities of the detected X-ray signals, it can also give an approximate stoichiometric information of the material. In our studies, 15 kV electrons were used (EDX, Hitachi-S4800) to get elemental maps and compositional features of the sample. Generally attached with FESEM set up (Figure 3.7), the unit fails to properly detect light elements with atomic number less than that of carbon.

3.2.5. Impedance analysis

This electrochemical method was employed to study the behavior of materials in the presence of an external perturbation during steady state. Generally, expressed in terms of an equivalent LCR (L: Inductance; C: Capacitance; R: Resistance) circuit, the real and imaginary part of the current in response to an oscillatory voltage is investigated over a wide frequency range. The analysis allows to probe the carrier kinetics across electrode/electrolyte interface. In our studies, following two impedance analyzers were used.

(A) The interface effects in terms of Mott Schottky study were performed using PGSTAT302N AUTOLAB (Figure 3.5). Having a compliance voltage of 30 V and maximum permissible current of 2 A, the device (520x160x420 mm^3) operates in 8 modules with a frequency bandwidth of 1 MHz within the potential range $\pm$ 10 V at step size of 0.3 μV. The device comes with a high input impedanceof 1 TΩ.
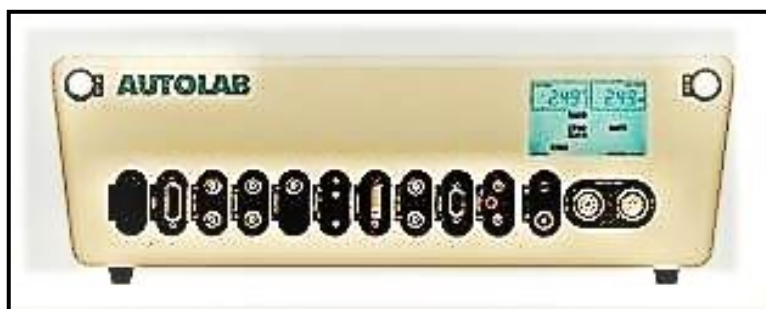
Figure 3.5: AUTOLAB impedance analyser

(B) Frequency dependent dielectric response was obtained by Agilent 4294A precision impedance analyzer (Figure 3.6). Frequency can be swept over a wide range of 40 Hz – 110 MHz, with allowed DC voltage and current in the range ± 40 V and ± 100 mA respectively. The rms voltage and current of theperturbation signal ranges within 0.005-1 V and 0.2-20 mA.
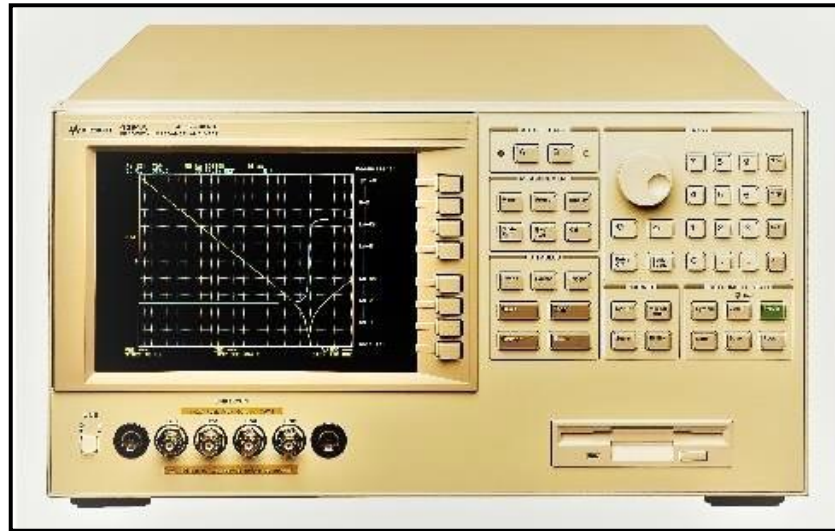
Figure 3.6: AGILENT impedance analyser

3.3. Microscopic techniques

3.3.1. Field emission scanning electron microscopy (FESEM)

The morphological features of samples were probed by using Field emission scanning electron microscope (FESEM, HITACHI S4800), as shown in Figure 3.7. With the minimum feature resolution of 5 nm, maximum magnification of 300,000X was achieved. Having a focal length of 50 mm and a single-lens 35 mm reflex camera (MP35051, CSI3), the microscope comes with two imaging options i.e. secondary   and   backscattered.   Basically, the instrument carriers an electron gun generating highly energetic electrons (≤ 30 keV) by field emission mechanism. LaB_6 or W are used as the electron gun material due to their high electron emission characteristics with low turn-on fields. The field emitted electrons are then accelerated and collimated by electromagnetic arrangements. These electrons, after falling upon sample surface, produces a number of effects such as secondary electrons, backscattered electrons, electromagnetic radiation in form of light emission, characteristics X-rays and so on. In this whole process, a fraction of the incident field emitted electrons also passes through the sample without any interaction. To avoid charge accumulation problems, it is a common

practice to mount the sample on a both side sticky conducting carbon tape and coat the sample surface with metals such as gold particles to passivate the accumulated charges, if any.

Figure 3.7: Field emission scanning electron microscope

3.3.2. Transmission electron microscopy (TEM)

Figure 3.8: Transmission electron microscope

This microscopic technique affords simultaneous operation in diffraction and imaging modes to reveal the crystalline structure and morphology of the sample respectively. When operated in the imaging mode, the higher magnification configuration referred to high resolution transmission electron microscopy (HRTEM) probes atomic scale features. A highly energetic electron beam (up to 250 keV) is allowed to transmit through the sample which is made very thin and then placed in a copper mesh. The highly energetic electrons while passing through the sample interact with the lattice structures and produce electron diffraction patterns. Electrons with and without diffractions are used for dark and bright field imaging respectively. The system also carries a number of lenses to form image on phosphor screen. The microscope used to investigate the crystallinity and microstructures of our prepared samples was JEOL-JEM-2100 (Figure 3.8). With 0.1 nm resolution, the microscope had magnification power up to 1,500,000X.

3.4. Electrical measurements

3.4.1. Field emission set up

This lab-made set up (Figure 3.9) is based on parallel plate configuration including two electrodes consisting of a stainless-steel (SS) platform which acts as the cathode and a stainless-steel conical tip (1.5 mm diameter) which acts as the anode. Mounting the samples on the SS platform was carefully carried out by placing a double-sided conducting carbon tapes (5 mm, Nisshin EM. Co. Ltd.) on this SS platform at first. Then the as prepared powder samples were pasted onto these double-sided conducting carbon tapes by pressing them adequately to form films. The pasting was performed by
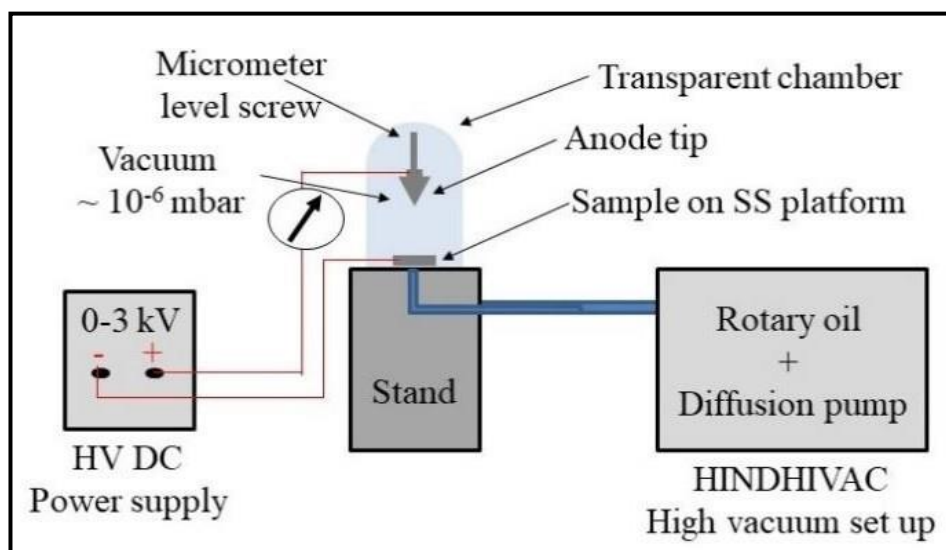
Figure 3.9: Lab made field emission (FE) set up

using a glass slide to ensure maximum smoothness and uniformity of the emitting surface as well as contact of the emitter nanostructures with the tape. Using a screw gauge shifter (10 μm pitch) attached to the conical tip, the sample to anode i.e. the inter-electrode distance was adjusted. Thus, the samples were placed at different inter-electrode distances by a micrometer screw attached to the system. Furthermore, this entire diode system was placed in a transparent chamber which was evacuated upto~10^{-6} mbar base pressure using a combination of rotary and oil diffusion pump via roughing and backing operations. The transparency of the chamber enabled us to ensure that no discharge from the surface of the sample took place while applying high electric field. The emission output was measured by using a multimeter (Agilent, 3440-1A).

3.4.2. High voltage DC power supply

Measurement of electron field emission required application of high electric field across the electrodes. A high voltage DC power supply (Model No: NTPL/91/03-04. Manufacturer: Neo Tele-Tronix Pvt. Ltd.) was used to serve this purpose (Figure 3.10). With voltage regulation facility, the power source was able to supply 3 kV-500 mA with 230 V @ 50 Hz as the input (1 phase AC). Placed inside a steel enclosure, output of this movable power supply can be increased up to 3 kV with 10 V step size.

Figure 3.10: High voltage DC power supply

3.4.3. Electrometer/Current-voltage (I-V) measurements

The current-voltage (I-V) characteristics were studied by using Keithley electrometers (No: 671 and 6517A) (Figure 3.11a) with voltage and current in the range: ± 1000 V and from ± 1 pA to ± 20 mA

respectively. In addition to these, digital multimeters (FLUKE 101 & RISH Multi 18S), depicted in Figures 3.11b & 3.11c, were also in use at several times.

Figure 3.11: (a) Electrometer and (b & c) digital multimeters

3.5. Optical tensiometer or contact angle meter

Surface properties such as surface tension, surface energy, wettability of a solid material is generally measured from the contact angle which is formed at its surface in contact with a liquid droplet. This nondestructive technique allows direct and accurate measurement of surface and interfacial tensions of solids and liquids with repeatability. Depending on various factors like local gravity, surface energy or surface tension of the solid, interfacial density contrast, etc., the droplet takes a particular shape which evolves with time. Figure 3.12 shows a contact angle meter or optical tensiometer or goniometer (OCA 15EC) used for our experiments to measure wettability of perovskite in contact with water. The instrument records the shape evolution of the droplet over time continuously and analyses it by fitting profile method to measure the contact angles as well surface energy.

Figure 3.12: Optical tensiometer or goniometer

Synthesis Protocols and Device Preparation

During the execution of this work, lead halide perovskites with various morphologies and also a number of devices based on them were prepared. All these materials and devices have been used for various studies and applications which are described in Chapters 5-8. The chemicals used to synthesize the materials and devices were of analytical grade and no further purification process was adopted.

4.1. Preparation of $CH_3NH_3PbI_3$ nanocrystals

Path 1 in Figure 4.1 shows schematic of the synthesis procedure adopted to prepare $CH_3NH_3PbI_3$ nanocrystals. 0.5 g lead (II) acetate trihydrate ($Pb(CH_3COO)_2.3H_2O$) was added into 3 mL hydroiodic acid (HI) (55%) solution, followed by ultrasonication for 5 min. 1 mL methylamine solution (CH_3NH_2, 33%) was drop wise added into the aforesaid solution under constant ultrasonication for 10 min. The black precipitate was then collected and washed with IPA (2-propanol, 99.5%) and finally dried at 100 ^{0}C for 30 min.
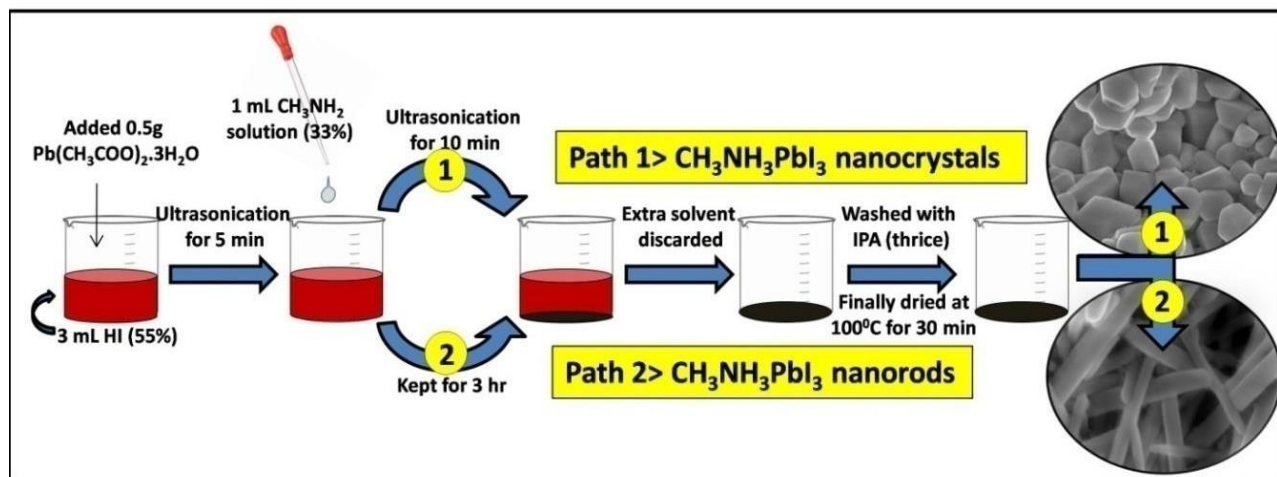
Figure 4.1: Synthesis schematic of $CH_3NH_3PbI_3$ nanocrystals and nanorods

4.2. Preparation of CH₃NH₃PbI₃ nanorods

Path 2 in Figure 4.1 shows schematic of the synthesis procedure adopted to prepare $CH_3NH_3PbI_3$ nanorods. 0.5 g lead (II) acetate trihydrate ($Pb(CH_3COO)_2.3H_2O$) was added into 3 mL hydroiodic acid (HI) (55%) solution, followed by ultrasonication for 5 min. 1 mL methylamine solution (CH_3NH_2, 33%) was drop wise added into the aforesaid solution under constant ultrasonication for 10 min. The solution was allowed to be kept for 3 h and then the extra solvent was discarded, thereby leaving behind numerous reddish yellow needle-like crystals which were formed at the bottom of the beaker and was visible through naked eye. After that, this product was collected by filtering and washing with isopropanol (2- propanol, 99.5%) thrice and finally dried the as filtered product at 100°C for 30 minutes.

4.3. Preparation of vertically aligned CH₃NH₃PbI₃ nanorods

50 mg of as prepared $CH_3NH_3PbI_3$ powder (see section 5.1.) was mixed into 1 mL DMF (Dimethyl formamide) solution and stirred in ultrasonication for 10 minutes. An as purchased AAO (Anodic aluminum oxide, Whatman) template, having pore size of 200 nm diameter, was fixed upon a
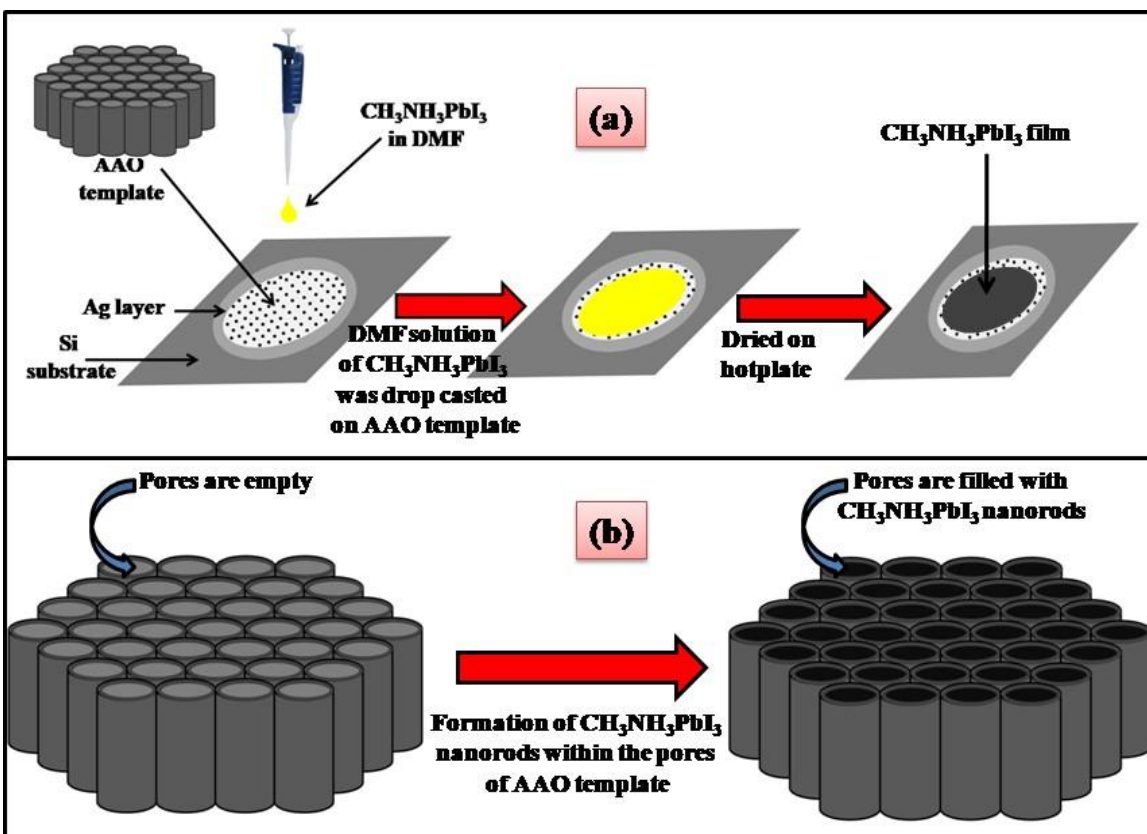
Figure 4.2: Schematic of growth of CH₃NH₃PbI₃ nanorods in AAO template

precleaned silicon substrate by silver paste. A tiny droplet of the precursor solution was carefully dropped right at the center of the template and then dried on a hot plate for half an hour at 100 ^{0}C. The entire preparation process is depicted in a schematic (Figure 4.2) for a clear understanding.

4.4. Preparation of V$_2$O$_5$ nanorods

0.36 g V$_2$O$_5$ powder was dissolved in 30 mL de-ionized (DI) water. Then 5 mL of 30% hydrogen peroxide (H$_2$O$_2$) was drop wise added into the solution under continuous stirring for 30 min. Then this solution was transferred into a 40 mL Teflon autoclave and heated at 190 ^{0}C for 24 h in oven. After cooling, the obtained precipitate was washed with DI and dried at 70 ^{0}C. Finally, the sample was annealed at 450 ^{0}C for 1 h to ascertain the desired oxidation state of V$_2$O$_5$.

4.5. Preparation of FTO/CH$_3$NH$_3$PbI$_3$/FTO

Prior to the deposition, the FTO coated glass substrates were cleaned with soap solution and then ultrasonicated in acetone, ethanol and DI water respectively for 15 minutes each. As prepared 50 mg CH$_3$NH$_3$PbI$_3$ powder was added into 0.5 mL DMF (Dimethyl Formamide) and stirred for 30 min. This precursor solution was then spin coated on the FTO substrate and placed in an oven at 85 ^{0}C for 10 min. Finally, another FTO was used as the top electrode. A schematic diagram showing the stepwise device fabrication process is included in Figure 4.3.

4.6. Preparation of FTO/V$_2$O$_5$/FTO

Prior to the deposition, the FTO coated glass substrates were cleaned with soap solution and then ultrasonicated in acetone, ethanol and DI water respectively for 15 minutes each. Subsequently, 0.5 mg of as synthesized V$_2$O$_5$ NRs powder were immersed into 0.5 mL DMF and stirred ultrasonically for 30 min. The mixture was then spin coated on FTO substrates and dried in an oven at 85 ^{0}C for 10 min. Finally, another FTO was used as the top electrode. A schematic diagram showing the stepwise device fabrication process is included in Figure 4.3.
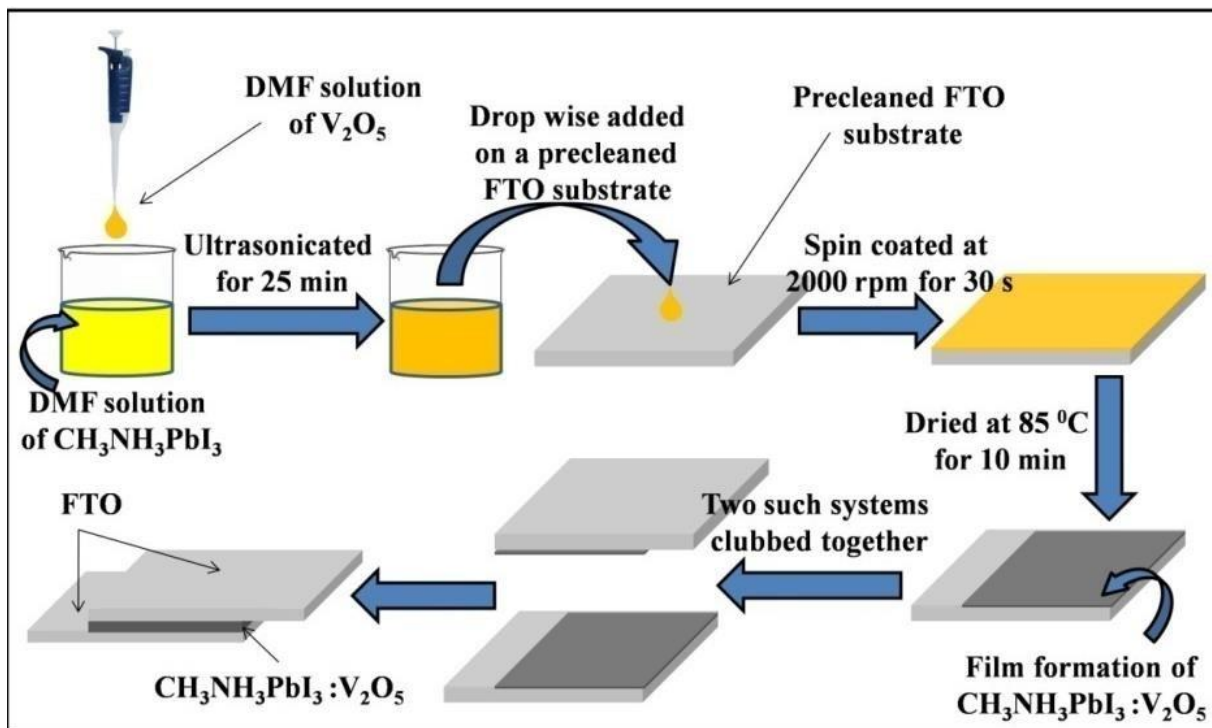
Figure 4.3: Schematic of FTO/CH$_3$NH$_3$PbI$_3$:V$_2$O$_5$/FTO device

4.7. Preparation of FTO/CH$_3$NH$_3$PbI$_3$:V$_2$O$_5$/FTO

Prior to the deposition, the FTO coated glass substrates were cleaned with soap solution and then ultrasonicated in acetone, ethanol and DI water respectively for 15 minutes each. As prepared 50 mg CH$_3$NH$_3$PbI$_3$ powder was added into 0.5 mL DMF (Dimethyl Formamide) and stirred for 30 min. Subsequently, the synthesized V$_2$O$_5$ NRs were immersed into 0.5 mL DMF with concentrations of 0.5, 0.75 and 1.50 mg and stirred ultrasonically for 30 min. The solutions were then drop wise added into CH$_3$NH$_3$PbI$_3$ precursor solution individually and stirred well in ultrasonication for 25 min. To get uniform thin films, these mixtures were then spin coated on FTO substrates and then dried in an oven at 85 ^{0}C for 10 min. Finally, another FTO was used as the top electrode. Here, the samples FTO/CH$_3$NH$_3$PbI$_3$:V$_2$O$_5$/FTO with V$_2$O$_5$ NRs concentrations 0.5, 0.75 and 1.50 mg are referred by S1 (for 1 wt. %), S2 (for 1.5 wt. %) and S3 (for 3 wt. %). The entire process flow is shown in the schematic of Figure 4.3.

Exploring Electron Field Emission of Morphology Tuned CH₃NH₃PbI₃ Nanostructures

5.1. Background of the work

With remarkable development of industry based urban civilization during the last few decades, a huge requirement of uninterrupted energy supply has also increased. Traditional usage of fossil fuels for power harnessing cannot be a permanent solution to solve this demand. In this regard, several new technologies and advanced materials were developed to harness consumable power from solar energy. Copper based ternary oxides,[1] low dimensional chalcogenides,[2] and metal halides were identified as new age solar cell candidates. However, their applications are still under investigation compared to established effectiveness of silicon in this sector. Silicon based solar cells are still much popular due to their suitable power conversion ability,[3] nontoxicity and availability. Besides, the most important feature of this material is its multipurpose applications. Newer materials for solar cell and any other advanced technology therefore are required to possess easily tunable optical and electrical properties for multipurpose applications in order to be commercialized. Organometallic halides have been identified as a promising group in this regard.[4] Among this group, Methylammonium lead triiodide ($CH_3NH_3PbI_3$) has already shown remarkable power conversion efficiency crossing the certified value of ~ 20 %.[5-7] The craze for this material is solely attributed to its physical properties. $CH_3NH_3PbI_3$ has a perovskite structure where the $CH_3NH_3^+$ cations lie within the framework of PbI_2^- octahedra. In each of these octahedrons, one Pb_2^+ cation resides at the center and coordinates with 6 apical I^- ions.[8] At room temperature it possesses tetragonal crystal structure.[9] This material is under extensive research focus due to its interesting optoelectronic properties like high absorption coefficient,[10] easily tunable band gap,[11] long carrier diffusion lengths,[12] and high carrier mobility.[13] Moreover low temperature synthesis[14] routes have been found out for this material which enables low production cost and better opportunity of fabrication of $CH_3NH_3PbI_3$ based composites without hampering the intrinsic properties of the counterparts. Owing to those features, $CH_3NH_3PbI_3$ is now being used in several extensions of photo induced applications like LEDs,[15] photo detectors,[16] field effect transistors,[17] etc. in

addition to photovoltaic industry.[18]

However, most of the applications based upon this material have been utilizing its photovoltaic character. Some other aspects, apart from the photovoltaic one, have not been investigated properly yet. From our previous experience, metal halides, copper based binary and ternary oxides etc. often show enhanced luminescence and field emission (FE) properties with wide range tuning by variation of synthesis and structural parameters.[19] This type of electron emission has tremendous applications in the area of field emission displays (FEDs), pressure sensors, field emission microscopy (e.g. FESEM), etc. It is observed that low dimensionalsemiconductor nanostructures are in general promising electron emitters. Some well-known fieldemitting materials e.g. CNT,[20] RGO nanocomposites,[21] ZnO,[22] graphene,[23] LaB_6,[24] MoS_2,[25] MoO_2,[26] etc. are well studied and has already been commercialized. However, almost each of them has limitations related to synthesis routes, stability, toxicity etc. To the best of our knowledge, no attempt has so far been reported regarding the field emission behavior of $CH_3NH_3PbI_3$ nanostructures. Additionally, theoretical and experimental studies on the electronic band related properties of this novel halide are also contradictory to each other and are of wide range.[27-29] Even if the photovoltaic applications are considered to be the sole purpose of this material, work function related studies are utmost important to achieve better control over excitation parameters and explanation of experimental outputs. In addition to the mentioned issues, production cost often emerges as a decisive factor for commercial application of any novel and multifunctional material. This work focuses the tuning of FE properties of $CH_3NH_3PbI_3$ in low dimension by cost effective chemical route and variation of shape/ dimension of this novel material has been achieved by simple variation of synthesis parameters which resulted into some encouraging outcomes.

A prior knowledge of the work function value is essential to figure out the enhancement factor and understand the field emission properties of any material. As a way out to overcome the ambiguity related to work function of this material, we employed a theoretical approach using DFT based first principles analysis. The outcome of this study was further used in calculation of various field emission parameters. The dependence of the field emission parameters upon the shape of $CH_3NH_3PbI_3$ emitters has also been studied through ANSYS MAXWEL simulation. The results obtained by this simulation based study were further correlated with experimental output. In order to check the applicability of $CH_3NH_3PbI_3$ in practical devices, the emission current stability current stability is considered as an important factor and the same was also studied for as long as 2

h. The field emission performance executed by this novel halide $CH_3NH_3PbI_3$ as presented in this work clearly indicates this as a future promising candidate for emission based display devices which further may be included into a photo excitable cold emission device.

5.2. Sample preparation and material characterizations

$CH_3NH_3PbI_3$ nanocrystals and nanorods were prepared by the synthesis procedures as described in section 4.1 and 4.2 respectively.

The as synthesized samples were subjected to several characterizations. The proper phase formation was investigated by X-ray diffractometer (Bruker D8 Advanced). The morphological analysis was carried out by field emission scanning electron microscopic studies (FESEM, Hitachi S-4800) whereas exact dimension of the nanostructures and the lattice images were obtained by high resolution transmission electron microscopy (HRTEM, JEOL JEM 2010). Fourier transformed infrared spectroscopy (FTIR, Simadzu) revealed the bonding information of the samples. Finally, all the samples were investigated by our laboratory made high vacuum fieldemission set up to study the field emission properties and cold emission current density and other relevant FE parameters were obtained for all the samples. ANSYS Maxwell was further used to carry out finite element electrostatic simulations study the effects of dimensional variation of the sample. The outcomes of this simulation based study were correlated with experimental results.

5.3. Results and discussion

5.3.1. Structural analysis: XRD

The phase of the as prepared samples was confirmed from X-ray Diffraction with Cu $K\alpha$ radiation ($\lambda = 1.5406$ Å), operating at 40 kV, 40 mA in normal θ-2θ scanning mode at 0.2 sec/step. Figure 5.1 depicts the XRD profiles of the samples. The figure shows the presence of diffraction peaks corresponding to the planes (110), (112), (211), (202), (004), (220), (213), (114), (310), (312), (224), (411), (314) and (404) indexed at 2θ (degree) = 14.1^0, 19.9^0, 23.6^0, 24.5^0, 28.1^0, 28.4^0, 30.9^0, 31.6^0, 31.8^0, 34.9^0, 40.4^0, 42.6^0, 43.1^0 and 50.2^0 respectively which confirm the formation of highly crystalline Tetragonal $CH_3NH_3PbI_3$ (I4/mcm).[30-32] However, some minor peaks arising at 12.68, 26.51 and 52.52 denote the presence of (001), (002) and (004) planes of hexagonal lead iodide (PDF #00-007- 0235) respectively.[33] This subtle presence of PbI_2 is generally accounted for the inevitable small-scale degradation of $CH_3NH_3PbI_3$.[34] However we propose (in next section) an alternative approach to explain the presence of those additional peaks correlating the same with
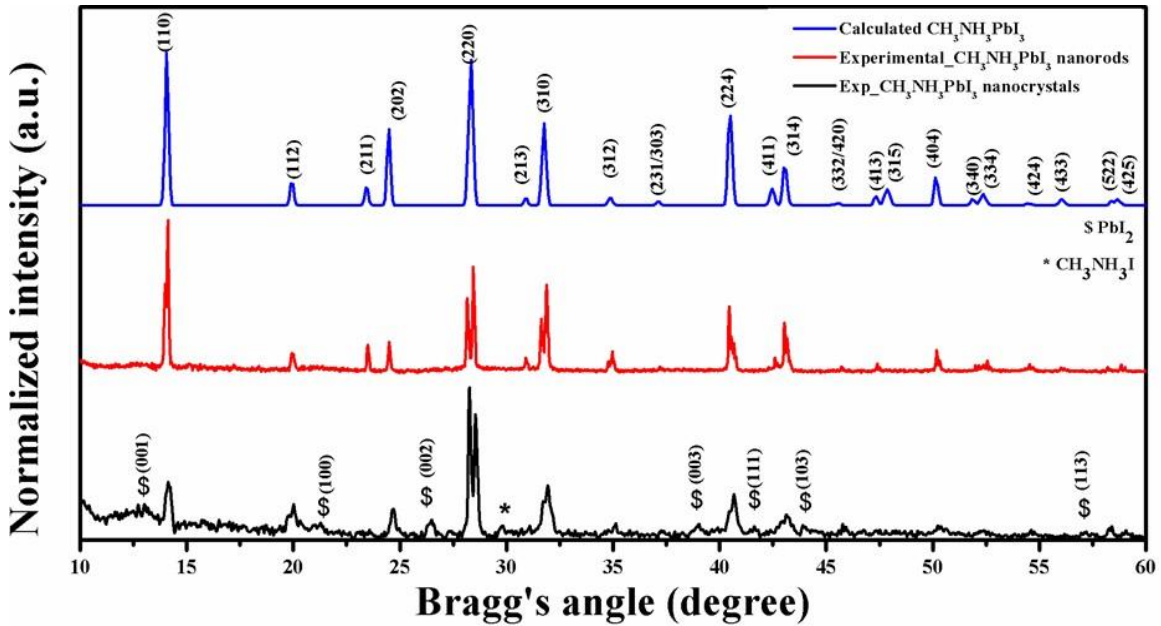
Figure 5.1: XRD patterns of $CH_3NH_3PbI_3$ nanostructures

growth routes. The crystallite sizes of $CH_3NH_3PbI_3$ nanorods and nanocrystals were calculated by using well known Scherrer's Formula: $L = k\lambda/\beta\ cos\theta$

Here L = average crystal size, k = shape factor with typical value 0.94 which actually varies with crystal shape, λ = wavelength of X-ray which is 1.5406 Å, β = full width half maximum (FWHM) of peak which is taken in radians and θ = the diffraction angle of the peak measured in degrees. Lattice parameters of samples were determined from Bragg's relation: $2d\ sin\theta = n\lambda$ where $d = \frac{1}{\sqrt{\left(\frac{h^2}{a^2} + \frac{k^2}{b^2} + \frac{l^2}{c^2}\right)}}$ = the inter-planar spacing of the set of planes (hkl), θ = Bragg angle, n = order of reflection corresponding to (hkl), λ = wavelength of X-ray and a, b, c are the lattice parameters. From our XRD data, we obtained a = b = 8.8757 Å and c = 12.6478 Å which agrees well with other reported values.[35] The obtained values of inter-planar spacing d and grain size L are tabulated in Table 5.1.

It can be seen from the table that the crystallites sizes are smaller for nanocrystals than the nanorods for almost each diffraction planes. An apparent discrepancy related to dimension and crystallites size appeared in view of morphological features of the samples (discussed later) but the same was explained to be occurring due to individual growth process of the crystals and nanorods.

Table 5.1: Derived inter-planar spacing and crystal size for various (hkl) crystal planes of $CH_3NH_3PbI_3$ nanorods and nanocrystals samples

(hkl) indices	d value for nanorods (Å)	d value for nanocrystals (Å)	L for nanorods (nm)	L for nanocrystals (nm)
(110)	6.26	6.26	38.46	31.95
(112)	4.45	4.43	46.57	17.90
(202)	3.63	3.60	73.05	29.96
(004)	3.16	3.15	64.33	51.02
(220)	3.13	3.12	67.56	43.84
(310)	2.80	2.80	54.93	18.98
(224)	2.23	2.22	30.96	21.93
(314)	2.10	2.10	34.19	15.59
(404)	1.82	1.81	96.27	15.39

5.3.2. Compositional study: EDX

Energy dispersive X-ray (EDX) analysis was performed for the two samples to check the stoichiometric balance of the constituent elements and the results are summarized in Table 5.2. The results showed that each sample contains main constituent elements Pb and I in almost accurate stochiometric ratio whereas $CH_3NH_3PbI_3$ nanocrystals were found to contain slightly higher amount of the halide counterpart. This result can be explained by the tricky difference introduced in the synthesis techniques for formation of nanorods and nanocrystals. An appreciable stirring was performed in initial stage of synthesis in case of nanocrystals. This enables higher amount of unreacted Pb precursor to come into contact with unreacted iodine precursor. Hence higher was performed was performed in initial stage of synthesis in case of nanocrystals. This enables higher amount of unreacted Pb precursor to come into contact with unreacted iodine precursor. Hence higher amount of iodine could be included in the compound. On the other side, in case of nanorods, this initial stirring was excluded and the reaction pot was kept still for several hours. After formation of certain amount of the target compound, i.e. $CH_3NH_3PbI_3$ in the reaction medium, unreacted Pb precursor could not come into direct contact with fresh halide ions and hence further iodization is restricted.

Table 5.2: Atomic percentage of Pb and I in $CH_3NH_3PbI_3$ nanocrystals and nanorods

Sample Type	Atom % of Pb	Atom % of I	Pb: I (Atom %)
$CH_3NH_3PbI_3$ nanocrystals	5.18	17.85	1 : 3.45
$CH_3NH_3PbI_3$ nanorods	8.35	25.54	1 : 3.06
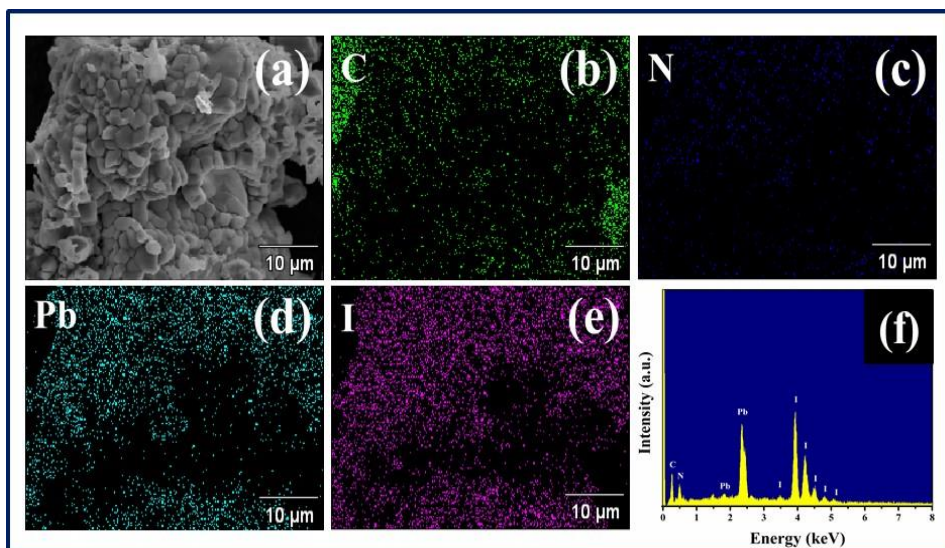
Figure 5.2: (a) FESEM image, (b-e) elemental maps and (f) EDX spectrum of nanocrystals sample
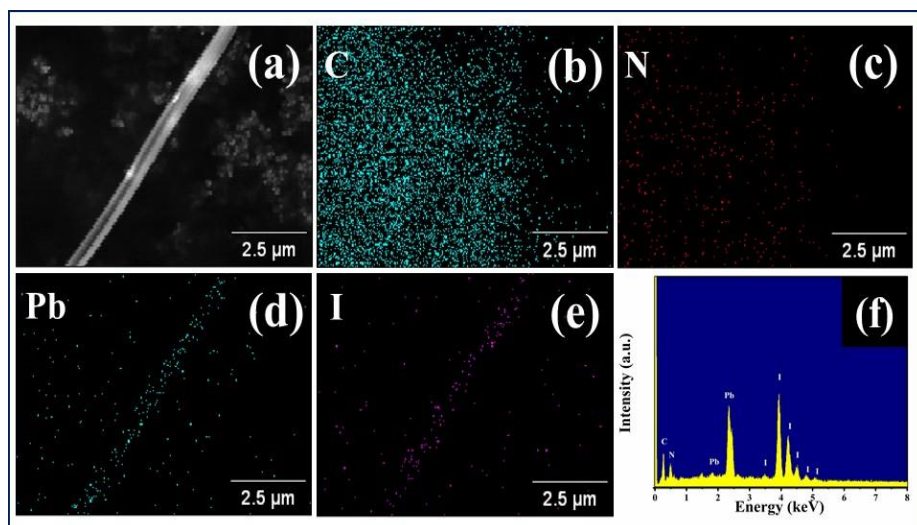
Figure 5.3: (a) FESEM image, (b-e) elemental maps and (f) EDX spectrum of nanorods sample

This can be verified from two aspects of the XRD results also. As mentioned earlier, some peaks corresponding to PbI_2 occurred in both of the samples. The peak intensities of this byproduct were compared to that of the main peaks in case of both samples. It was observed that the relative intensity for PbI_2 is much higher (0.2304) in case of nanocrystal sample than observed in nanorods (0.0785). This observation is in full agreement with the mechanism proposed above. The elemental mapping and the EDX spectra of the nanocrystals and nanorods are respectively presented in Figures 5.2 and 5.3 explicitly.

5.3.3. Microscopic analysis: FESEM & TEM

Field Emission Scanning Electron Microscopy (FESEM) was employed to observe the morphologies of the as synthesized samples. It can be seen from Figures 5.4a and 5.4b that $CH_3NH_3PbI_3$ nanorods have average diameter of ~ 150-200 nm with average length of ~ 5-6 µm while $CH_3NH_3PbI_3$ nanocrystals have an average diameter of ~ 750-800 nm.
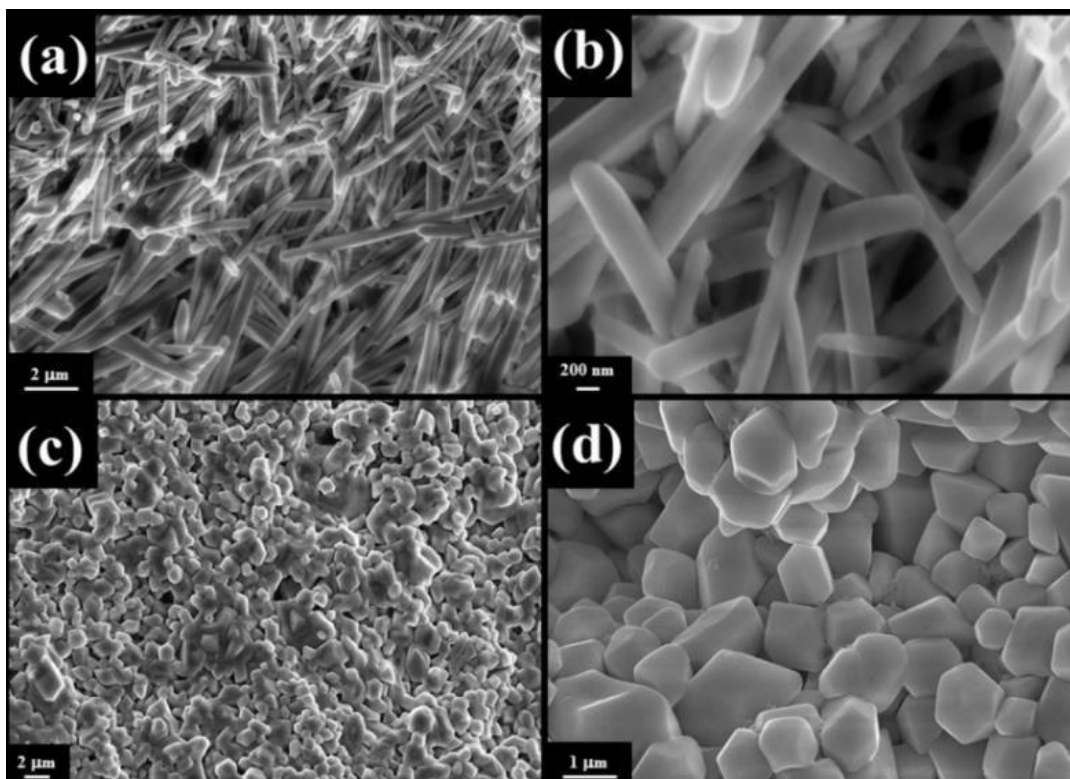
Figure 5.4: Low and high magnification FESEM images of $CH_3NH_3PbI_3$ (a&b) nanorods and (c&d) nanocrystals respectively

As mentioned in the x-ray studies, the nanocrystals samples synthesized in this work show smaller crystallites but higher dimensional particles. But the nanorods are comparatively small in dimension whereas contain larger crystallites. It must be kept in mind that the crystallite size from x-ray diffraction study normally reflects to range of ordering or crystallinity whereas FESEM depicts the actual shape of the sample which may be composed of several grains/crystallites. Considering the synthesis techniques, we know that the nanocrystals were formed in stirring media. Stirring caused frequent exposure of fresh lead ions to iodine and organic ions and hence different combination of lattice planes are formed for a short duration. As a result, different crystallites formed in this case are of small dimension. Those small crystallites are free to coexist adjacent to each other resulting in large microcrystal. As a consequence, huge microcrystals are expected to

occur and they are free to reside in dense distribution as we observed in Figure 5.4d. On the other hand, $CH_3NH_3PbI_3$ nanorods are formed in rest condition; each plane in nanorods was allowed to grow during higher time and might possibly result into higher range ordering with larger crystallite size. However, any crystallite cannot grow infinitely large; several factors like surface energy minimization, chemical potential of precursors, etc. restrict the range of ordering. Thus, the nanorods are expected to contain single or few numbers of lattice planes with high ordering range/crystallites and distinctly separate from each other. The high magnification FESEM image presented in Figure 5.4b shows that the nanorods are distributed in the visible area with comparatively less compact fashion than can be found in case of nanocrystals (Figure 5.4d).
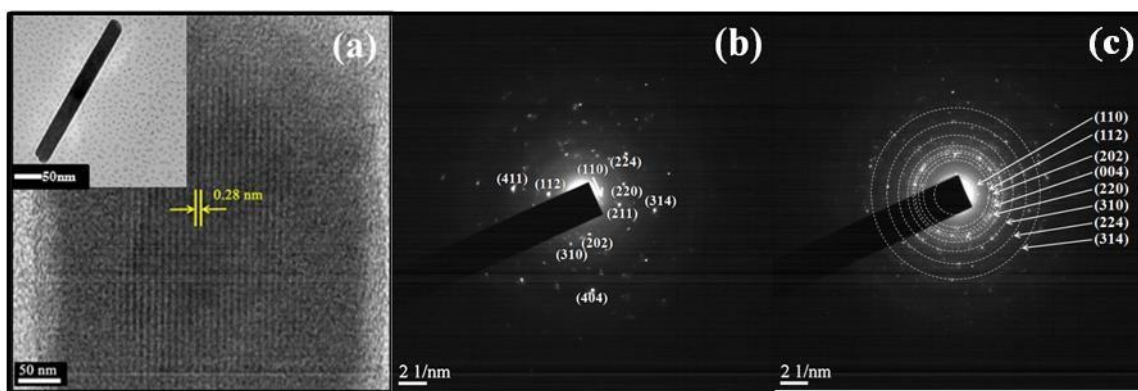
Figure 5.5: (a) HRTEM image of crystalline plane of nanorods (inset showing a single nanorod), (b&c) SAED patterns of $CH_3NH_3PbI_3$ nanorods and nanocrystals respectively

However, if the proposed mechanism has to established properly, lattice images must show the features of long-range ordering in case of nanorods which could only be obtained from TEM analysis. Inset of Figure 5.5a shows a single nanorod with ~1μm length and ~55 nm diameter. Figure 5.5a reveals the d value for $CH_3NH_3PbI_3$ nanorods as ~ 0.28 nm which corresponds to the (310) planes of tetragonal $CH_3NH_3PbI_3$ lattice. A large portion of the rod was found to be containing this plane as the major one which supports our XRD studies inferring long range ordering. The crystalline nature of the nanorods as can be supported by the SAED pattern shown in the next figure 5.5b. The regular arrangement of the bright spots found in the SAED pattern directly indicates to the single crystallinity of the nanorods. On the other hand, FESEM images of Fig. 5.4d shows that $CH_3NH_3PbI_3$ crystals are much higher in dimension as well as thicker and hence it was difficult to obtain lattice images. However, to compare the crystallinity of the two samples (shown in Fig. 5.4b & 5.4d), SAED patterns are compared as shown in Figures 5.5b and 5.5c. It can be seen that the SAED patterns corresponding to the large crystals show a well- defined ring pattern typically found

for polycrystals.

5.3.4. Optical study: UV-Vis and FTIR spectroscopy

UV-Vis spectroscopic measurement was carried out for the as prepared powder samples to figure out their energy band-gaps. $BaSO_4$ was used as a standard reference with respect to which the reflectance data of the samples were recorded. Sharp falls in R (%) was observed indicating the highly crystalline nature of these two samples. The photon energy was calculated using formula:
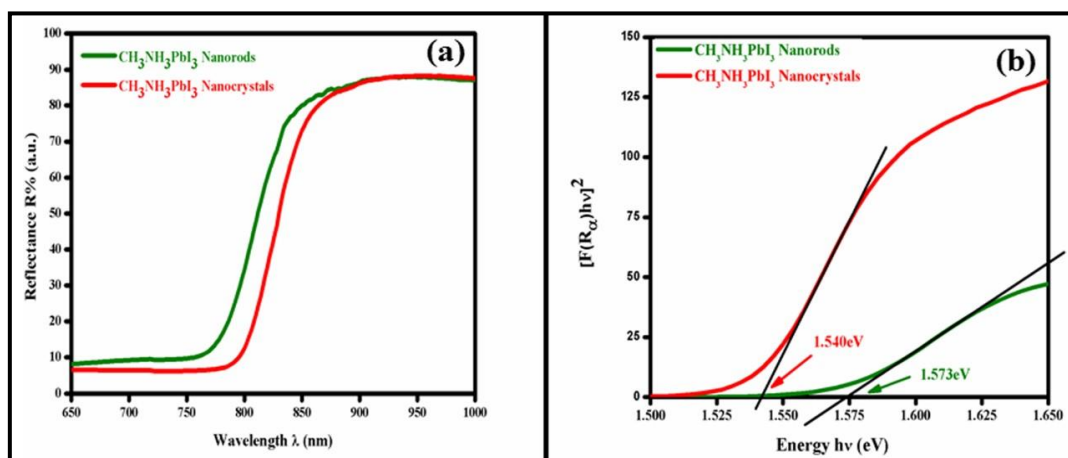
Figure 5.6: (a) Reflectance spectra and (b) Kubelka-Munk plots of $CH_3NH_3PbI_3$ nanocrystals and nanorods

E (eV) $= 1240/\lambda$ (nm) Kubelka – Munk function was plotted with photon energy to calculate the band gap of the samples using the equation: $[F(R_\infty)h\nu]^{1/n} = A(h\nu - E_g)$ Here $F(R_\infty) = (1-R)^2/2R$, A is proportionality constant, $h\nu$ is photon energy in eV unit, E_g is energy band gap and n is an index which characterizes the nature of the energy band transitions depending upon if it is direct or indirect, allowed or forbidden, etc. Now, $CH_3NH_3PbI_3$ being a direct band gap type semiconductor, we have taken n = ½. Extrapolating the linear portion of $[F(R_\infty)h\nu]^2$ vs. $h\nu$ plot, the values of E_g were determined. They optical band gaps turned out to be 1.54 eV and 1.57 eV for $CH_3NH_3PbI_3$ nanocrystals and nanorods respectively which agree well with other reported values.[36,37] The difference in the band gaps of these two samples can be accounted for their different sizes. As obtained from the electron microscopic images, the rods have an average diameter of ~ 150-200 nm while the nanocrystals do the same of ~ 1 µm. This low diameter value of the rods leads to higher band gap value compared to that of the nanocrystals counterpart. The spectra and $[F(R_\infty)h\nu]^2$ vs. $h\nu$ plots are presented in Figure 5.7 below. The bonding information and presence of unaccounted complex organic ions within the samples were studied by FTIR spectroscopy.
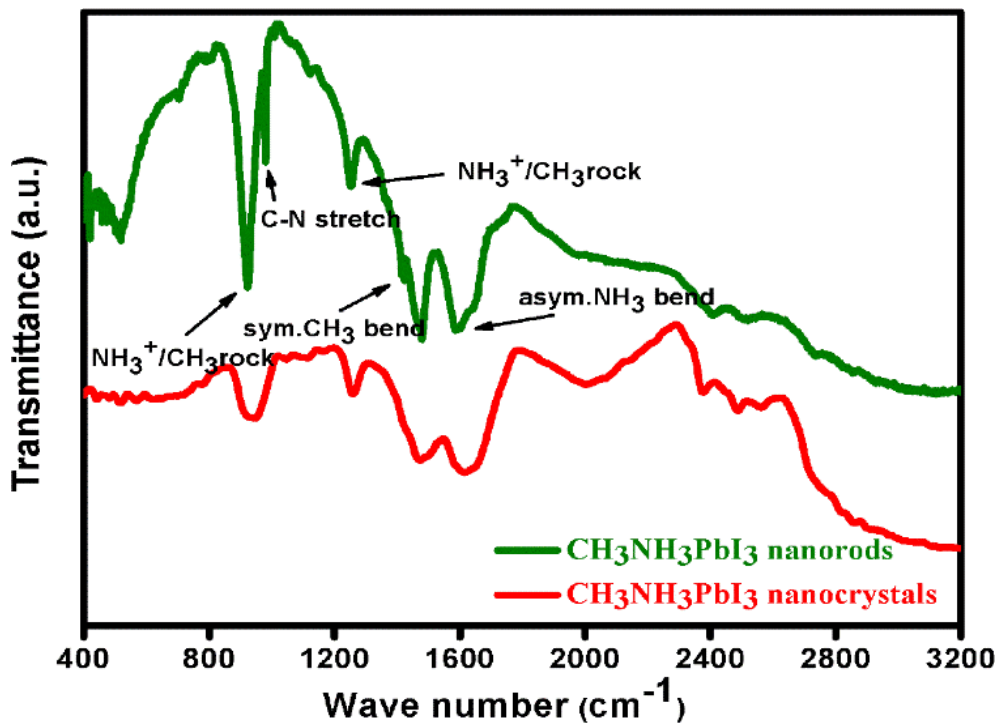
Figure 5.7: FTIR spectra of $CH_3NH_3PbI_3$ nanocrystals and nanorods

The synthesis was carried out in very low temperature and hence auto removal of weakly interacting organic molecule or complex ions like in sol-gel process could not be achieved. They might also not be detected via tools like XRD and EDX. But those loosely bound (if any) attachments are expected to contribute adversely in cold emission process when subjected to external electric field. Absence of any such functionalized groups was confirmed by FTIR studies. The FTIR transmittance spectra showed in this figure showed peaks at 918.7 cm^{-1}, 983.1 cm^{-1}, 1250.6 cm^{-1}, 1415.3 cm^{-1} and 1586.8 cm^{-1} which were assigned to NH_3^+/CH_3 rock, C-N stretch, NH_3^+/CH_3 rock, symmetric CH_3 bend and asymmetric NH_3 bend respectively and agrees well with previous reports for this material. [38,39]

5.3.5. First principle study

A prior knowledge of the work function value is essential to figure out the enhancement factor and understand the field emission properties of any material. As a way out to overcome the ambiguity related to work function of this material, we employed a theoretical approach using DFT based first principles analysis. The outcome of this study was further used in calculation of various field emission parameters. In order to estimate the work function of the (110) surface of tetragonal $CH_3NH_3PbI_3$ through first principles, computations were carried out using Vienna ab-initio simulation package (VASP)[40-43] with projector-augmented-wave (PAW) approach.[44] The

exchange-correlation contributions were taken into account via Perdew-Burke-Ernzerhof (PBE)[45] functional within the generalized gradient approximation (GGA). Plane wave basis set up to an energy cut off 400 eV was utilized throughout the calculation. For geometrical optimizations, the structures were allowed to relax until the total energy converged below 10^{-4} eV/atom. A $2\times2\times2$ k-mesh was used for the geometrical optimization of the tetragonal $CH_3NH_3PbI_3$ structure while a k-mesh of $1\times5\times5$ was used for the calculation of the work function of (110) surface of $CH_3NH_3PbI_3$. A vacuum slab of 30 Å was deployed on the $CH_3NH_3PbI_3$ (110) surface to exclude any false interaction. The work function ϕ was obtained via the following formula: $\Phi = E_{vac} - E_F$ Here E_F is the Fermi energy and E_{vac} is the reference vacuum energy level. E_F and E_{vac} are obtained through a scf calculation in spin restricted condition. Initially, the tetragonal $CH_3NH_3PbI_3$ unit cell was optimized and the lattice parameters were found to be a = 8.79 Å and c = 12.98 Å which agrees well with the previous reports.[46] A (2x2) view from z direction of the optimized $CH_3NH_3PbI_3$ structure is given in Figure 5.8c. Next the (110) surface of $CH_3NH_3PbI_3$ was constructed and relaxed which is shown in Figure 5.8b. In our calculation, the vacuum energy E_{vac} was estimated from the constant value of planar average electrostatic potential at a large distance from the surface
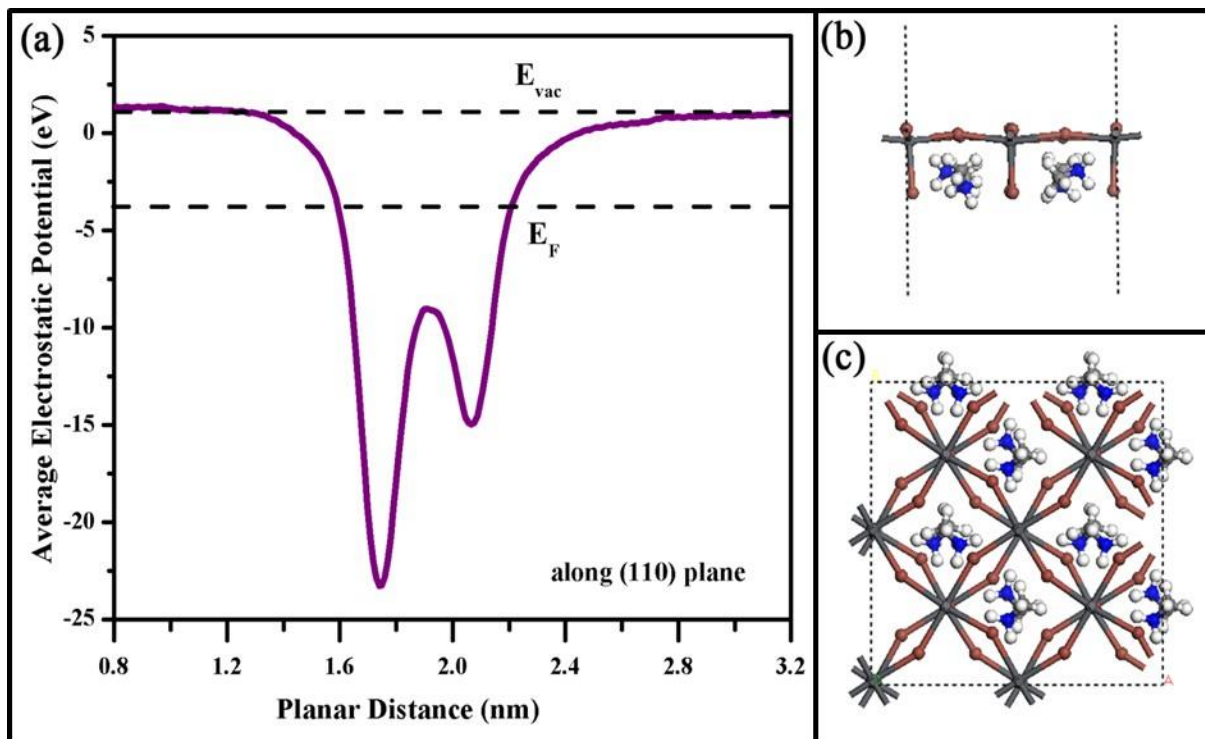
Figure 5.8: (a) Variation of the Average electrostatic potential with distance from the surface, (b) The (110) optimized surface and (c) $CH_3NH_3PbI_3$ (2x2) view from z direction, obtained by DFT analysis

and the Fermi energy E_F was found from the DFT calculation. For the (110) surface of $CH_3NH_3PbI_3$, E_F and E_{vac} were found to be -4.2035 eV and 0.9665 eV respectively, resulting in a work function (ϕ) value of 5.17 eV. The variation of the planar average electrostatic potential with distance from the surface, as found from the first principle calculation, is represented in Figure 5.8a.

5.3.6. Finite element analysis

In order to verify the experimental FE results, finite element method (FEM) using ANSYS Maxwell simulation software was employed and the local electric field distribution of the samples was simulated. For this, firstly the 2-dimensional models for both nanostructures i.e.
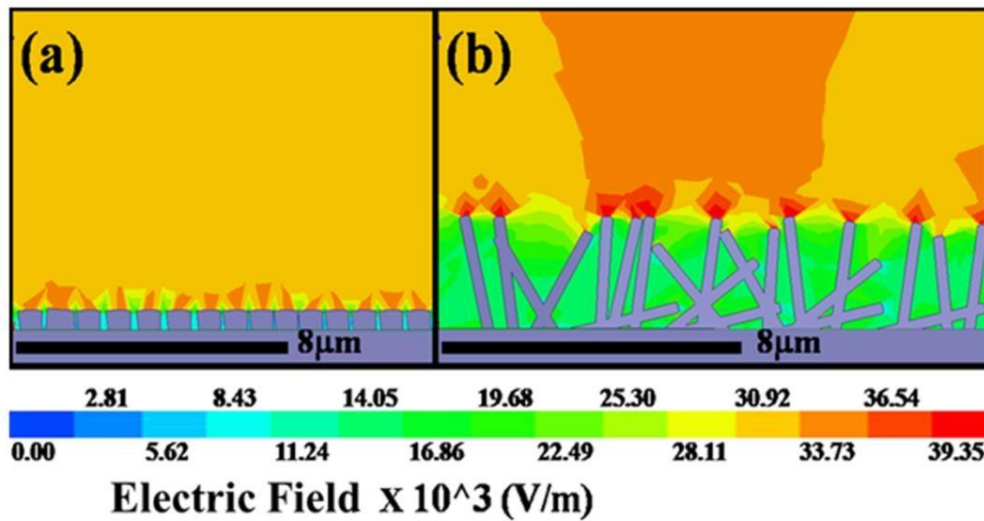
Figure 5.9: Simulated electric field distribution of $CH_3NH_3PbI_3$ (a) nanocrystals and (b) nanorod at 200 μm inter-electrode separation

nanocrystals and nanorods were modeled and the input parameters like electrode separation, dimension of the emitters etc. were selected as per actual basis. Figure 5.9a shows the 2D model of $CH_3NH_3PbI_3$ nanocrystals having dimensions ~ 750 – 800 nm, whereas the nanorods bearing average length ~ 5 - 6 µm and diameter ~ 150 – 200 nm (Figure 5.9b). The anode-emitter distance was maintained to be at 120 µm and the applied electric field was 2 kV for both the models. The horizontal color panel just below Figures 5.9a & 5.9b represents the different output electric field intensity distributions, where the red and blue colors indicating the maximum and minimum field value respectively. From the simulated results it can be clearly observed that the nanorods emit higher electric field than the nanocrystals.

5.3.7. J-E characteristics

Field emission properties of the as synthesized $CH_3NH_3PbI_3$ nanorods and nanocrystals were performed in our homemade high vacuum field emission setup. The set up includes two electrodes

consisting of a stainless-steel platform which acts as the cathode and a stainless-steel conical tip (1.5 mm diameter) which acts as the anode. Mounting the samples on the stainless- steel platform was carefully carried out by placing a double-sided conducting carbon tapes (5mm, Nisshin EM. Co. Ltd.) on this stainless-steel platform at first. Then the as prepared powder samples were pasted onto these double-sided conducting carbon tapes by pressing them adequately to form films. The pasting was performed by using a glass slide to ensure maximum smoothness and uniformity of the emitting surface as well as contact of the emitter nanostructures with the tape. The samples were placed at different inter-electrode distances by a micrometer screw attached to the system. Furthermore, this entire diode system was placed in a transparent chamber which was evacuated up to ~10−6 mbar base pressure using a combination of rotary and oil diffusion pump. The transparency of the chamber enabled us to ensure that no discharge from the surface of the sample took place while applying high electric field. Now emission current I and applied electric field E are theoretically related by:[47,48]

$$I = \frac{Aa\beta^2 E^2}{\emptyset} e^{-b\emptyset^{3/2}/\beta E} \tag{5.1}$$

Here ϕ and β are the local work function and the field enhancement factor respectively, A is the emission area (i.e. area of the anode tip = $(\pi/4) \times 1.5$ mm^2), a, b are called Fowler – Nordheim (F-N) constants having values a =1.54 µA eV/V^2 and b = 6.83×10^3 eV$^{-3/2}$ V/µm. E was calculated by dividing the externally applied input voltage V (in volt) by the inter electrode distance x (in µm). The above relation can be rewritten as:

$$ln\left(\frac{J}{E^2}\right) = ln\left(\frac{a\beta^2}{\emptyset}\right) - \frac{b\emptyset^{3/2}}{\beta E} \tag{5.2}$$

Here J = I/A is emission current density. Hence, a plot of ln (J/E^2) vs. 1/E gives straight line with slope (say m) = - b$\phi^{3/2}$/β and intercept = ln (aβ^2/ϕ). So, from the knowledge of this slope, one can figure out the field enhancement factor β using:

$$\beta = -\left(\frac{b\emptyset^{3/2}}{m}\right) \tag{5.3}$$

Besides, the effective work function ϕ_{eff} i.e. work function reduced locally at the emission sites is obtained from the relation:[48,49]

$$^]\emptyset_{eff} = \left(\frac{\emptyset}{\beta^{2/3}}\right) \tag{5.4}$$
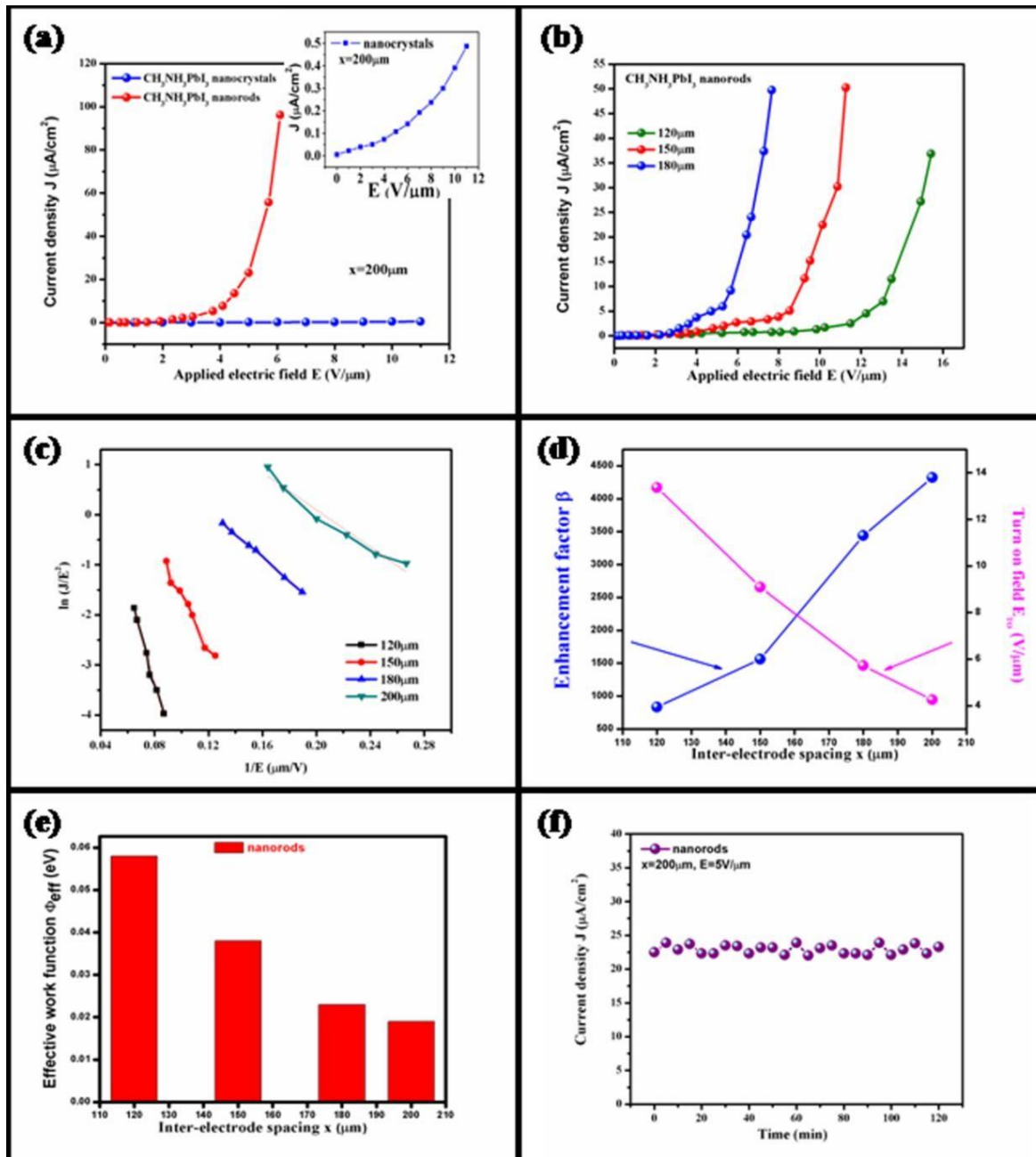
Figure 5.10: (a) J-E characteristics of $CH_3NH_3PbI_3$ nanorods and nanocrystals at x = 200 μm, whereas the inset showing the J-E characteristic of the nanocrystals alone; (b) J-E characteristics of $CH_3NH_3PbI_3$ nanorods at x = 120 μm, 150 μm and 180 μm; (c) F-N plot of $CH_3NH_3PbI_3$ nanorods at x = 120 μm, 150 μm, 180 μm and 200 μm; (d) Plot of field enhancement factor and turn-on field vs. inter-electrode distance; (e) Effective work function vs. inter-electrode distance; (f) Temporal current stability profile at x = 200 μm, E = 5 V/μm for $CH_3NH_3PbI_3$ nanorods

Figure 5.10a shows the J-E curves obtained from the experimentally observed current voltage data for $CH_3NH_3PbI_3$ nanocrystals and nanorods both at x = 200 μm while the inset of this figure gives a

closer view of the J-E characteristics for the nanocrystals. As this figure demonstrates, the nanocrystals yield a current density of the order of 0.5 µA/cm^2 at a large externally applied electric field more than 10 V/µm but the nanorods have attained a current density of 100 µA/cm^2 at 6 V/µm external field. This indicates 200-fold enhancement of current density, indicating the superiority of the 1D nanostructure over its 2D counterpart.

Effect of emitter morphology on FE performance

The better FE performance of $CH_3NH_3PbI_3$ nanorods than nanocrystals can be explained in terms of their morphology and crystallinity. Generally, materials with high curvature points in their geometrical structures possess a tendency to accumulate electric fields at these locations to lower the work function locally and tunnel electrons through the remaining potential barrier. So, the field values at such points are now not just E what was applied externally, but it became enhanced to a value βE (β = local field enhancement factor). From the FESEM images, it is very clear that $CH_3NH_3PbI_3$ nanorods have a higher aspect ratio compared to that of $CH_3NH_3PbI_3$ nanocrystals. So, these nanorods, due to their sharp geometry, make the electric lines of force condensed and pile upnear the edges. Thus effectively, triggering enhanced of the field near these edges. These edges then act like electron emission sites and produce high emission current density. On the contrary, the nanocrystals possess blunt flat surfaces and lacking sharp peripheral edges. So, they cannot converge the field lines and hence not favorable for cold electron emission. Furthermore, the crystallinity of the samples plays a vital role in the electron emission. If we consider that, after applying an electric field, an electron tunnels out of the surface potential barrier of a nanostructure, reaches the anode tip, traverse through the external circuit and finally goes to the ground. Therefore, another electron from the ground must enter back to that nanostructure again to maintain the close channel of electrons which produces the current. This is where the situations differ for nanorods and nanocrystals in our case. The nanorods being quasi single crystalline in nature, as revealed from the TEM images, can easily get electrons supplied from ground. But for the nanocrystals which have polycrystalline nature, the electrons supplied from the ground get obstructed while entering into the nanocrystals. They get scattered whenever they cross an inter-crystalline grain boundary. So only few electrons to survive this energy losses due to scattering and contributes to the emission current.

Effect of electrode separation on FE performance

As the first report of electric field emission of $CH_3NH_3PbI_3$, the investigation was extended to find out the effect of inter-electrode separation on the cold emission behavior. Three more distances of 120 µm, 150 µm and 180 µm were adjusted and the FE experiment was repeated for each case. The obtained J-E characteristics are presented in Figure 5.10b whereas their corresponding F-N plots along with that obtained at 200 µm are depicted in Figure 5.10c. Figure 5.10b indicates that with increasing inter-electrode distance the current densities for $CH_3NH_3PbI_3$ nanorods increased. This is due to the fact that, as we increase the inter-electrode separation, the region of the sample placed right beneath the anode gets more exposed to the anode and due to this, the inter-electrode field acts upon greater number of electrons. From the slopes of all the F– N plots, we have calculated β by putting ϕ = 5.17 eV (calculated from DFT) in eqn. (5.3). Figure 5.10d display the variation of the turn on field (the electric field required to produce the current density of 10 µA/cm^2) and local field enhancement factor β with inter-electrode spacing respectively. This figure demonstrates the same aforesaid phenomenon that increasing the inter- electrode distance leads to increasing number of electrons reaching the anode as a consequence of inclusion of higher number of emitters.[50] However, increasing the electrode separation beyond 200 µm caused inferior FE properties with maximum current
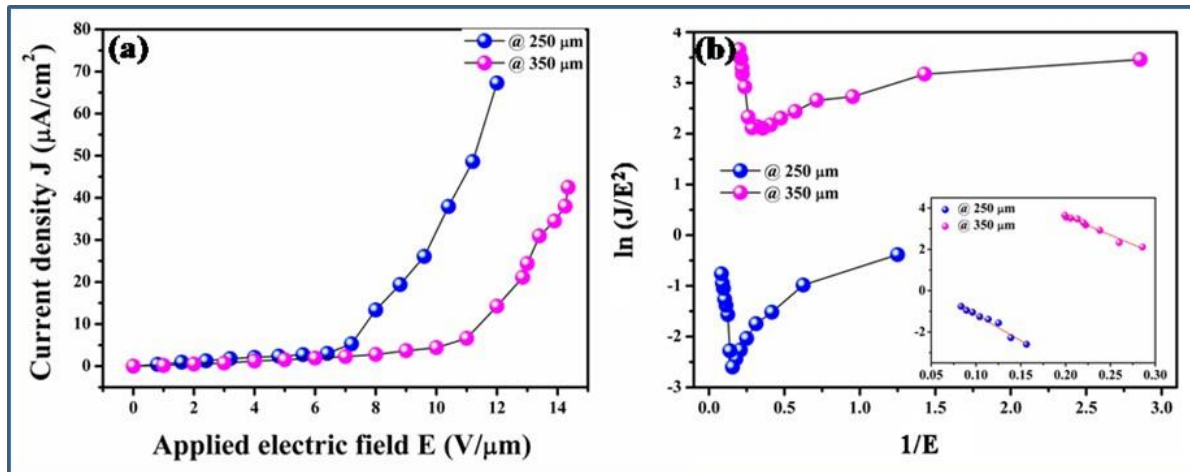
Figure 5.11: (a) J-E characteristic plots and (b) F-N plots for $CH_3NH_3PbI_3$ nanorods at inter-electrode separation of 250 and 350 µm; inset showing the linear segments only

densities 70 and 45 µA/cm^2 for 250 and 350 µm distances respectively (presented in Figures 5.11a & 5.11b). These results may be accounted for the increased potential barrier appearing due to too much increment of inter- electrode distances. As estimated using eqn. (5.4), the values of

effective work function ϕ_{eff} obtained for different inter-electrode separation are presented in Figure 5.10e. The enhancement of FE performance with increasing inter electrode distance can also be considered equivalent to that resulting due to reduced effective work functions.[48,51]

5.4. Temporal stability of emission

To be realized in effective emission based devices, any new proposed emitter material must be tested to check the time stability of cold emission. This is even a more crucial factor for $CH_3NH_3PbI_3$ field emitters. Easy vulnerability of such halide under harsh external reagents might introduce unexpected newer barriers against their real-life applications. The nanorod samples, being the best $CH_3NH_3PbI_3$ nanostructure for FE applications, were subjected to high external field for a long duration and the output current density was studied. This experiment was performed keeping the inter electrode separation 200 µm since this was the best optimized condition. As shown in Figure 5.10f, the output current density maintains an average value of 23.6 µA/cm^2 with appreciable stability when applied with an external bias of 5 V/µm for the period of 2 hrs. This result can also be attributed to the quasi-single crystalline nature of
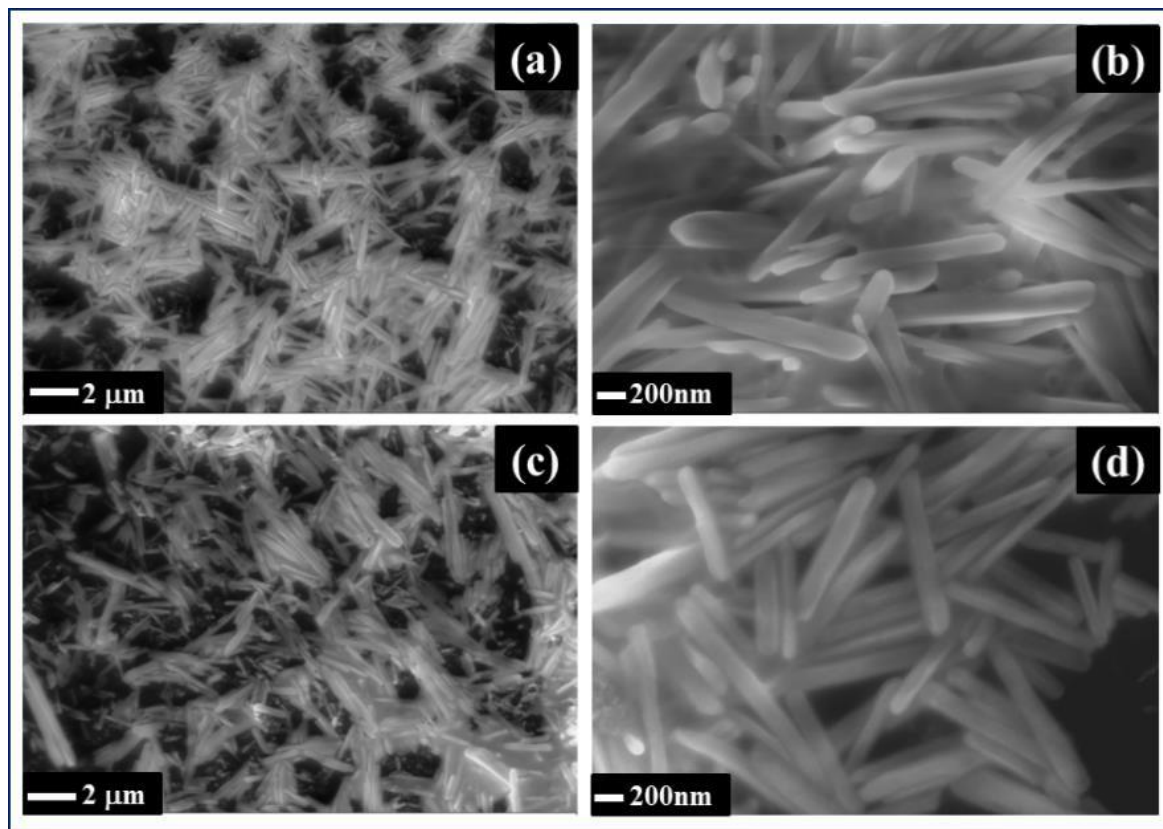
Figure 5.12: Low and high magnification FESEM images of $CH_3NH_3PbI_3$ nanorods (a) before and (b) after FE measurements

CH$_3$NH$_3$PbI$_3$ nanorods. Locally generated heat, even in very small extent can add adverse effects on cold crystallinity, material composition and sharpness of morphology. Those are very strong factors governing the cold electron emission. As field emission properties are often considered as 'local' phenomenon in a very close proximity of the emission site, these factors become even more crucial. As we have already mentioned in the earlier subsection, the long range ordering in CH$_3$NH$_3$PbI$_3$ nanorods enables less scattering of the electrons and hence lower probability of energy dissipation in form of heat. This in turn results into a stable cold emission current density as observed in the mentioned figure. It was also observed that the CH$_3$NH$_3$PbI$_3$ nanorods subjected to high external electric field retained their morphological features entirely (see Figure 5.12).

5.5. Outcomes and achievements

Field emission property of nanocrystals and nanorods of CH$_3$NH$_3$PbI$_3$ has been reported for the first time. The samples were prepared by a very simple wet chemical approach. After proper characterizations by XRD, EDX, FESEM, TEM, UV-Vis. spectroscopy and FTIR spectroscopy, the field emission property of these samples was investigated. The compositional and structural observations were explained as direct consequences of synthesis techniques. Between the two samples, the nanorods showed a considerable field emission behavior with current density reaching ~ 96µA/cm^2 and a turn on field of 4.2 V/µm, owing primarily to their rod like 1D nanostructure. The comparatively lower current density obtained in the case of the nanocrystals has been addressed in terms of their low aspect ratio and poly crystalline nature. The dependence of the FE properties such as field enhancement factor, turn on field etc. upon the inter-electrode separation were also been studied. Temporal stability of the emission current, playing a crucial role from the application point of view, was checked for 2 h. The work function ϕ (5.17 eV) of the material has been calculated from DFT analysis. From both the theoretical and experimental studies, it is clear that CH$_3$NH$_3$PbI$_3$ nanostructures are potential field emitter.

A comparative collection of FE results has been summarized in Table 5.3 for most of the good performing field emitters and it can be seen that the CH$_3$NH$_3$PbI$_3$ have comparable FE characteristics, particularly keeping in mind that this is the first report for the same. This present work leads to a new path way for the potential application of CH$_3$NH$_3$PbI$_3$ to be used in emission based display and other devices. It also provokes to further research on the FE properties of other related halide perovskites with different morphologies.

Table 5.3: Comparison of obtained field emission performance with other materials

Sample/System	Turn on field (V/μm)	Reference
ZnO NW	6 (at J = 0.1 μA/cm^2)	[52]
Patterned ZnO nanorods/Si	4.4 (at J = 10 μA/cm^2)	[53]
ZnO nanowires	2 (at J = 10 μA/cm^2)	[54]
Cl-doped ZnO NW arrays/3D graphene foam	1.6 (at J = 10 μA/cm^2)	[55]
Si NW	5.0 (at J = 10 μA/cm^2)	[56]
Carbon nanoflakes coated Si NW	2.77 (at J = 10 μA/cm^2)	[57]
SWCNT	1.5-4.5 (at J = 10 μA/cm^2)	[58]
CNT films treated using H2 plasma	1.2–0.5 (at J = 0.1 μA/cm^2)	[59]
ZnO incorporated CNT	1.5 (at J = 0.1 μA/cm^2)	[60]
CNT on nanopatterned substrate	0.58 (at J = 10 μA/cm^2)	[61]
CH$_3$NH$_3$PbI$_3$ nanorods	4.2 (at J = 10 μA/cm^2), 2.1 (at J = 1 μA/cm^2),	This work

References

[1]   A. P. Wanninayake, S. Gunashekar, S. Li, B. C. Church and N. Abu-Zahra, *Semicond. Sci. Technol.*, 2015, **30**, 064004.

[2]   J. Tang, Z. Huo, S. Brittman, H. Gao and P. Yang, *Nature Nanotechnology,* 2011, **6**, 568.

[3]   A. Tamang, H. Sai, V. Jovanov, S. I. H. Bali, K. Matsubara and D. Knipp, *Solar Energy Materials & Solar Cells,* 2016, **151**, 81.

[4]   S. Tombe, G. Adam, H. Heilbrunner, D. H. Apaydin, C. Ulbricht, N. S. Sariciftci, C. J. Arendse, E. Iwuohaa and M. C. Scharber, *J. Mater. Chem. C,* 2017, **5**, 1714.

[5]   H. Zhou, Q. Chen, G. Li, S. Luo, T. Song, H. S. Duan, Z. Hong, J. You, Y. Liu and Y. Yang, *Science,* 2014, **345**, 542.

[6]   W.S. Yang, J.H. Noh, N.J. Jeon, Y.C. Kim, S. Ryu, J. Seo and S.I. Seok, *Science,* 2015, **348**, 1234.

[7]   G. E. Eperon et al., *Science,* 2016, **354**, 6314.

[8]   J. S. Manser, J. A. Christians and P. V. Kamat, *Chem. Rev.,* 2016, **116**, 12956.

[9]   Y. Kawamura, H. Mashiyama and K. Hasebe, *Journal of the Physical Society of Japan,* 2002, **71**, 1694.

[10]   J. H. Im, C. R. Lee, J. W. Lee, S. W. Park and N. G. Park, *Nanoscale,* 2011, **3**, 4088.

[11]   D. M. Jang, K. Park, D. H. Kim, J. Park, F. Shojaei, H. S. Kang, J. P. Ahn, J. W. Lee and J. K. Song, *Nano Lett.,* 2015, **15**, 5191.

[12]   G. Xing, N. Mathews, S. Sun, S. S. Lim, Y. M. Lam, M. Grätzel, S. Mhaisalkar and T. C. Sum, *Science,* 2013, **342**, 344.

[13]   H. Oga, A. Saeki, Y. Ogomi, S. Hayase and S. Seki, *J. Am. Chem. Soc.,* 2014, **136**, 13818.

[14]   J. You, Z. Hong, Y. M. Yang, Q. Chen, M.Cai, T. B. Song, C. C. Chen, S. Lu, Y. Liu, H. Zhou and Y. Yang, *ACS Nano,* 2014, **8**, 1674.

[15]   Z. K. Tan, R. S. Moghaddam, M. L. Lai, P. Docampo, R. Higler, F. Deschler, M. Price, A. Sadhanala, L. M. Pazos, D. Credgington, F. Hanusch, T. Bein, H. J. Snaith and R. H. Friend, *Nature Nanotechnology,* 2014, **9**, 687.

[16]   Y. Zhang, J. Du, X. Wu, G. Zhang, Y. Chu, D. Liu, Y. Zhao, Z. Liang and J. Huang, *ACS Appl. Mater. Interfaces,* 2015, **7**, 21634.

[17]   X. Y. Chin, D. Cortecchia, J. Yin, A. Bruno and C. Soci, *Nature Communications,* 2015, **6**, 7383.

[18]   H. S. Kim, J. W. Lee, N. Yantara, P. P. Boix, S. A. Kulkarni, S. Mhaisalkar, M. Grätzel and N. G. Park, *Nano Lett.,* 2013, **13**, 2412.

[19]   S. Saha, R. Roy, S. Das, D. Sen, U. K. Ghorai, N. Mazumder and K. K. Chattopadhyay, *ACS Appl. Mater. Interfaces,* 2016, **8**, 25571.

[20]   W. A. Heer, A. Châtelain and D. Ugarte, *Science,* 1995, **270**, 1179.

[21]   C. S. Rout, P. D. Joshi, R. V. Kashid, D. S. Joag, M. A. More, A. J. Simbeck, M. Washington, S. K. Nayak and D. J. Late, *Sci Rep,* 2013, **3**, 3282.

[22]   C. J. Lee, T. J. Lee, S. C. Lyu and Y. Zhang, *Appl. Phys. Lett.,* 2002, **81**, 9.

[23]   A. Malesevic, R. Kemps, A. Vanhulsel, M. P. Chowdhury and A. Volodin, *J. Appl. Phys.,* 2008, **104**, 084301.

[24]   H. Zhang, J. Tang, Q. Zhang, G. Zhao, G. Yang, J. Zhang, O. Zhou and L. C. Qin, *Adv. Mater.,* 2006, **18**, 87.

[25]   R. V. Kashid, D. J. Late, S. S. Chou, Y. K. Huang, M. De, D. S. Joag, M. A. More and V. P. Dravid, *small,* 2013, **9**, 2730.

[26]   J. Liua, Z. Zhanga, C. Pana, Y. Zhaoa, X. Sua, Y. Zhoua and D. Yu, *Materials Letters,* 2004, **58**, 3812.

[27]   X. Liu, C. Wang, L. Lyu, C. Wang, Z. Xiao, C. Bi, J. Huangc and Y. Gao, *Phys.Chem.Chem.Phys.,* 2015, **17**, 896.

[28]   E. M. Miller, Y. Zhao, C. C. Mercado, S. K. Saha, J. M. Luther, K. Zhu, V. Stevanovic, C. L. Perkins and J. Lagemaat, *Phys.Chem.Chem.Phys.,* 2014, **16**, 22122.

[29]   P. Liu, X. Liu, L. Lyu, H. Xie, H. Zhang, D. Niu, H. Huang, C. Bi, Z. Xiao, J. Huang and Y. Gao, *Appl. Phys. Lett.,* 2015, **106**, 193903.

[30]   L. Dimesso, M. Wussler, T. Mayer, E. Mankel and W. Jaegermann, *AIMS Materials Science,* 2016, **3**, 737.

[31]   T. Oku, M. Zushi, Y. Imanishi, A. Suzuki and K. Suzuki, *Appl. Phys. Express,* 2014, **7**, 121601.

[32]   A. B. Wong, M. Lai, S. W. Eaton, Y. Yu, E. Lin, L. Dou, A. Fu and P. Yang, *Nano Lett.,* 2015, **15**, 5519.

[33]   L. M. Chao, T. Y. Tai, Y. Y. Chen, P. Y. Lin and Y. S. Fu, *Materials,* 2015, **8**, 5467.

[34]   I. Deretzis, A. Alberti, G. Pellegrino, E. Smecca, F. Giannazzo, N. Sakai, T. Miyasaka and A. L. Magna, *Applied Physics Letters,* 2015, **106**, 131904.

[35]   Y. Kawamura, H. Mashiyama and K. Hasebe, *J. Phys. Soc. Jpn.,* 2002, **71**, 1694.

[36]   T. Baikie, Y. Fang, J. M. Kadro, M. Schreyer, F. Wei, S. G. Mhaisalkar, M. Graetzel and T. J. White, *J. Mater. Chem. A,* 2013, **1**, 5628.

[37]   V. D'Innocenzo, G. Grancini, M. J. P. Alcocer, A. R. S. Kandada, S. D. Stranks, M. M. Lee, G. Lanzani, H. J. Snaith and A. Petrozza, *Nat. Commun.,* 2014, **5**, 3586.

[38]   P. Bhatt, K. Pandey, P.Yadav, B.Tripathi, C. K. P., M. K. Pandey and M. Kumar, *Solar Energy Materials & Solar Cells,* 2015, **140**, 320.

[39]   M. A. Perez-Osorio, R. L. Milot, M. R. Filip, J. B. Patel, L. M. Herz, M. B. Johnston and F. Giustino, *J. Phys. Chem. C,* 2015, **119**, 25703.

[40]   G. Kresse and J. Hafner, *Physical Review B.,* 1993, **47**, 558.

[41]   G. Kresse and J. Hafner, *Physical Review B.,* 1994, **49**, 14251.

[42]   G. Kresse and J. Furthmüller, *Computational Materials Science,* 1996, **6**, 15.

[43]   G. Kresse and J. Furthmüller, *Physical Review B.*, 1996, **54**, 11169.

[44]   P. E. Blöchl, *Physical Review B.*, 1994, **50**, 17953.

[45]   J. P. Perdew, K. Burke and M. Ernzerhof, *Physical review letters,* 1996, **77**, 3865.

[46]   F. Zheng, H. Takenaka, F. Wang, N. Z. Koocher and A. M. Rappe, *J. Phys. Chem. Lett.,* 2015, **6**, 31.

[47]   S. Maiti,U. N. Maiti, A. Chowdhury and K. K. Chattopadhyay, *CrystEngComm,* 2014, **16**, 1659.

[48]   A. Jha, D. Banerjee and K.K. Chattopadhyay, *Applied Surface Science,* 2011, **257**, 1946.

[49]   S. Maity, D. Banerjee, N. S. Das and K. K. Chattopadhyay, *Current Applied Physics,* 2016, **16**, 1293.

[50]   D. Banerjee, A. Jha and K.K. Chattopadhyay, *Applied Surface Science,* 2010, **256**, 7516.

[51]   D. Kumar, D. Banerjee, S. Sarkar, N. S. Das and K.K. Chattopadhyay, *Materials Chemistry and Physics,* 2016, **175**, 22.

[52]   C. J. Lee, T. J. Lee, S. C. Lyu, Y. Zhang, H. Ruh, and H. J. Lee, *Appl. Phys. Lett.*, 2002, **81**, 3648.

[53]   N. Liu, G. Fang, W. Zeng, H. Long, L. Yuan and X. Zhao, *Appl. Phys. Lett.*, 2009, **95**, 153505.

[54]   J. B. Chen, C. J. Xu, J. C. She, S. Z. Deng, Jun Chen, and N. S. Xu, *Journal of Applied Physics*, 2010, **107**, 024312.

[55]   D. Shao, J. Gao, G. Xin, Y. Wang, L. Li, J. Shi, J. Lian, N. Koratkar and S. Sawyer, *Small*, 2015, **11**, 4785.

[56]   Q. Shu, J. Wei, K. Wangn, X. Gui, C. Ma, H. Zhu, Y. Jia, X. Li, N. Guo and D. Wu, *Journal of Physics and Chemistry of Solids*, 2010, **71**, 708.

[57]   D. Banerjee, N. S. Das and K. K. Chattopadhyay, *Applied Surface Science*, 2012, **261**, 223.

[58]   J. M. Bonard, J. P. Salvetat, T. Stöckli, W. A. Heer, L. Forró and A. Châtelain, *Appl. Phys. Lett.*, 1998, **73**, 918.

[59]   K. Yu, Z. Zhu, M. Xu, Q. Li, W. Lu and Q. Chen, *Surf. Coat. Technol.*, 2004, **179**, 63.

[60]   J. Kennedy, F. Fang, J. Futter, J. Leveneur, P. P. Murmu, G. N. Panin, T. W. Kang and E. Manikandan, *Diamond & Related Materials*, 2017, **71**, 79.

[61]   S. J. Kim, S. A. Park, Y. C. Kim and B. K. Ju, *J. Vac. Sci. Technol. B*, 2017, **35**, 011802-1.

Enhancing the Emission Behavior Further: Nanostructure Alignment and Light Illumination

6.1. Scope of further improvement

While most of the research activities on Methylammonium lead iodide ($CH_3NH_3PbI_3$) are dedicated towards its photovoltaic and allied applications,[1-5] very few reports are there in the literature on its other application aspects.[6, 7] Electron field emission is one such aspect which is of great technological importance because of its low power consumption with high picture quality when used as a flat panel display unit. In 2017, a detail investigation was carried out by Besra et al. in this direction to explore the field emission properties of $CH_3NH_3PbI_3$ (NRs) for the first time ever.[8] Although the orientation of the NRs was not limited to any particular direction, the results obtained were yet promising. Literatures suggest that materials having vertically aligned nanostructures prove to be superior electron field emitters in comparison with ones having no directionality.[9-11] Therefore the scope of further improvement of the emission behavior was there in that study by aligning the NRs vertically. Numerous documentations on such vertical alignment of $CH_3NH_3PbI_3$ nanostructures can be found in literature.[12-14] However, the use of AAO (Anodic aluminum oxide) templates has its own advantages amongst them, mostly because of its large scale uniformity and independence of the filler material.[15,16] Whatever material is poured and filled into the pores of the template, the scaffold finally shapes the nanostructures of all the materials exactly with identical geometry. Moreover, performance of electron field emission tuned by incident photons has its own importance not only from its application point of view but also for the fundamental understanding of the emitter material under investigation. Metal halide perovskite, $CH_3NH_3PbI_3$ is already renowned for its remarkable optoelectronic features e.g. high absorption coefficient, large carrier diffusion length, etc.[17,18] It possesses excellent detection capability under near infrared (NIR) radiation corresponding to its energy band gap.[19,20] Hence, it would be very much interesting to study the impact of near infrared photons on the electron field emission behavior from vertically aligned $CH_3NH_3PbI_3$

NRs. So here, vertically aligned $CH_3NH_3PbI_3$ NRs were first grown with the help of AAO (Anodic aluminum oxide) template and characterized by X-ray diffraction (XRD), Field emission scanning electron microscopy (FESEM) and UV-Vis spectroscopy to ensure the crystalline phase, morphological features and optical characteristics respectively. Electron field emission properties from these NRs were then investigated. The impact of different illumination conditions on the emission performance was finally probed by shining appropriate photons with varying intensities. The experimental observations were also corroborated with simulation of the local electric field distribution near the NRs under plane polarized light of different field strengths.

6.2. Nanorods alignment and their characterizations

6.2.1. Alignment of nanorods

Vertically aligned $CH_3NH_3PbI_3$ nanorods were grown in AAO (Anodic aluminum oxide) template using the methodology prescribed in section 4.3.

6.2.2. Characterizations

The phase of the sample was confirmed by X-ray diffraction (XRD) patterns recorded on a Bruker D8 diffractometer (Cu K_{α} radiation, wavelength 1.5404 Å). The morphological features were investigated by Field emission scanning electron microscope (FESEM) images taken by a HITACHI S4800 electron microscope. The optical characterization and the band gap were studied by UV-Vis spectrophotometer (JASCO V-750). Finally, the field emission properties of the sample were investigated using a lab made high vacuum field emission set-up.

6.3. Results after alignment

6.3.1. Structural and morphological study

Crystalline phase of pristine $CH_3NH_3PbI_3$ powder was ascertained from its XRD pattern (Figure 6.1). The presence of sharp diffraction signals corresponding to the crystalline planes (110), (112), (211), (202), (004), (220), (213), (114), (310), (312), (224), (411), (314) and (404) in the XRD pattern confirmed the well crystalline formation of the sample in tetragonal phase space group I4/mcm.[21] Figure 6.2 shows top and cross view FESEM images of prepared sample.
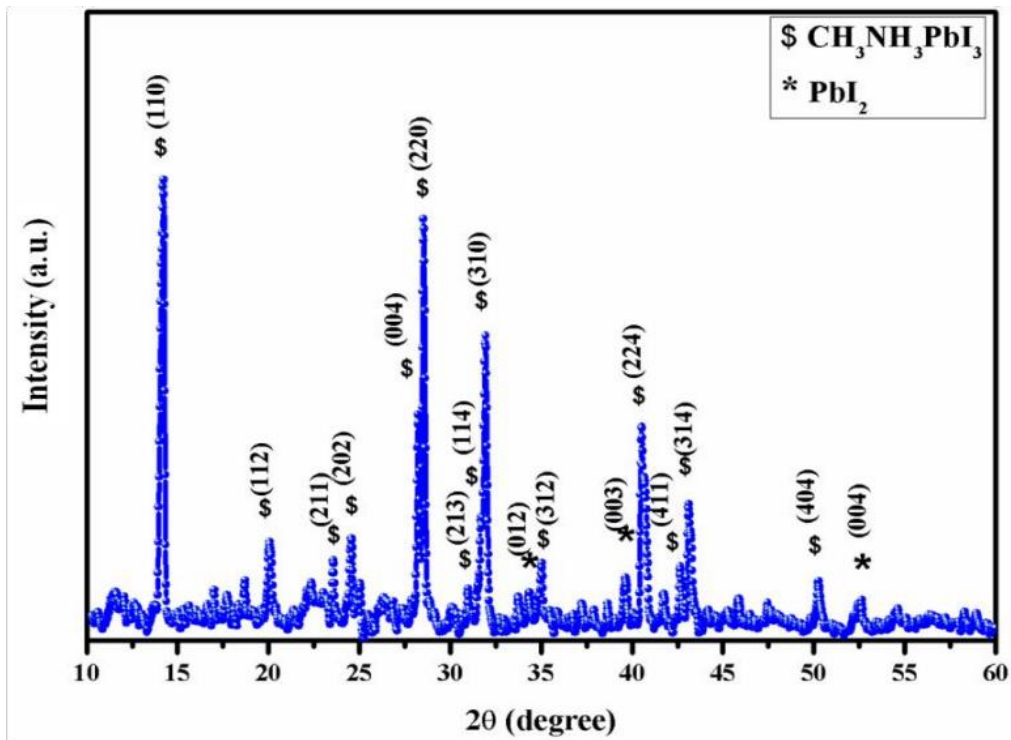
Figure 6.1: X-ray diffraction (XRD) pattern of the as prepared pristine $CH_3NH_3PbI_3$ powder
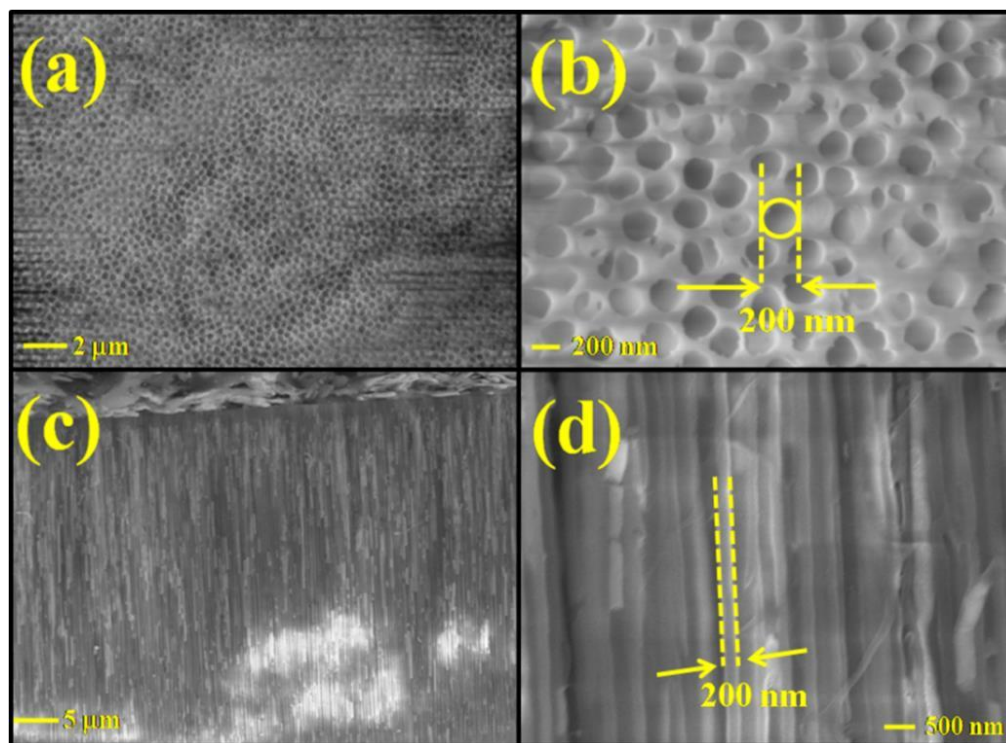
Figure 6.2: (a) Low magnification FESEM image of the upper surface, (b) high magnification FESEM image of the upper surface, (c) low magnification cross FESEM image, (d) high magnification cross image of the sample grown in AAO template respectively

It's clearly evident from these figures that numerous rod- like 1D structures have grown with diameter of ~ 200 nm and length of several tens of micrometers.

6.3.2. Spectroscopic analysis (UV-Vis)

The reflectance spectrum of the as prepared sample was recorded and shown in Figure 6.3. The sharp fall in the reflectance data ensures well crystalline nature of the as prepared sample. The characteristic energy band gap of the material is indicated in the figure by shaded box at the wavelength range ~ 700 - 800 nm. The exact value of the band gap was however pinpointed by taking the X-intercept of the linear part of the reflectance spectrum extrapolated to the wavelength axis (Figure 6.3). The band gap was thus calculated to be 1240/760 (nm) = 1.63 eV using the formula: $E_g = hc/\lambda$. Here E_g is energy band gap, h is Planck's constant (6.67×10^{-34} J-s), c is light speed in vacuum and λ is the wavelength of the incident photons. The obtained energy band gap agrees very well with other reported values in literature. [20]
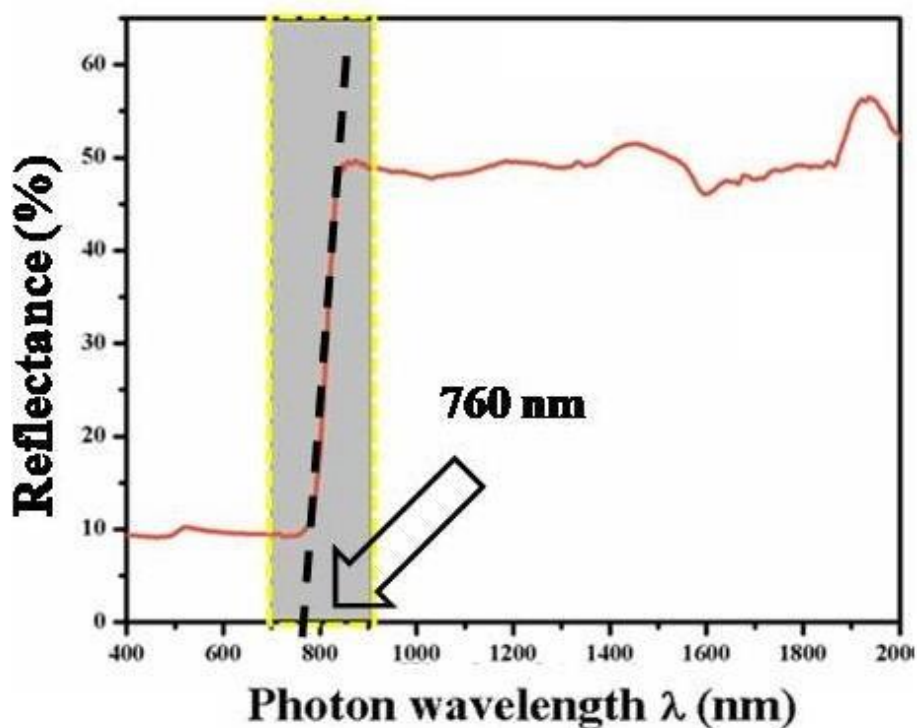
Figure 6.3: UV-Vis. reflectance spectrum of the as synthesized sample

6.3.2. Field emission study

Field emission is nothing but a quantum mechanical process where electrons are forcibly tunneled out through a potential barrier (also called 'work function'), otherwise classically

impossible. High electric field of the order of several tens or hundreds of MV/m is applied and electrons come out of the surface of the sample. The current so built from these collected electrons is defined by Fowler-Nordheim (FN) eqn.[8] as:

$$J = \left(\frac{a\beta^2 E^2}{\emptyset}\right) e^{-b\emptyset^{3/2}/\beta E} \tag{6.1a}$$

Hence, $ln\left(\frac{J}{E^2}\right) = ln\left(\frac{a\beta^2}{\emptyset}\right) - \frac{b\emptyset^{3/2}}{\beta E}$ (6.1b)

Here J = current density, a and b are called FN constants (a = 1.54 x 10^{-6} A. V^{-2}. eV, b = 6.83 x 10^3 V. $eV^{-3/2}$. μm^{-1}), E = externally applied electric field, β = enhancement factor (a measure of the quality of the emission behavior) and Φ = work function of the sample respectively. In our experiment, the sample was mounted on a stainless-steel platform (serving as the cathode) with another stainless-steel conical tip (serving as the anode) of diameter 1.5 mm facing the surface of the sample. This entire arrangement was enclosed within a glass chamber which was evacuated at as low as 10^{-6} mbar pressure. Using a screw gauge shifter attached to that very conical tip, the sample to anode i.e. the inter-electrode distance was adjusted and kept at 200 μm (say, x). A schematic of the setup is given in Figure 6.4a. External high voltage (V) was applied across it andthe emission current (I) which was built from the electrons collected at the anode and flowing through an external circuit was measured. The electric field E and the current density J as mentioned in equations 6.1a & 6.1b were calculated using the formulae: $E = {}^V/_x$ and $J = {}^I/_\alpha$. Here, α is the cross section area of the anode i.e. the conical tip. It is clear from Figure 6.4b that very good emission was obtained from the sample with a turn on electric field (field corresponding to current density 10 $\mu A/cm^2$) of 3.4 V/μm and reaching a current density up to 230 $\mu A/cm^2$. The linear behavior of ln (J/E^2) vs. 1/E plot (also known as FN plot, Figure 6.4c) guarantees the electron emission to be FN type in nature. If known the work function Φ, the slope of this FN plot gives the enhancement factor β by the relation:

$$\beta = \left(\frac{b\emptyset^{3/2}}{m}\right) \tag{6.2}$$

Using b = 6.83x10^3 V. $eV^{-3/2}$. μm^{-1}, ϕ = 5.17 eV (taken from one of our previous works),[8] and slope (m) = -14.6 V/μm (obtained from the FN plot), the enhancement factor came to be 5500.

6.4. Effect of light illumination

Near infrared (NIR) radiation with λ = 750 nm corresponding to the energy band gap of
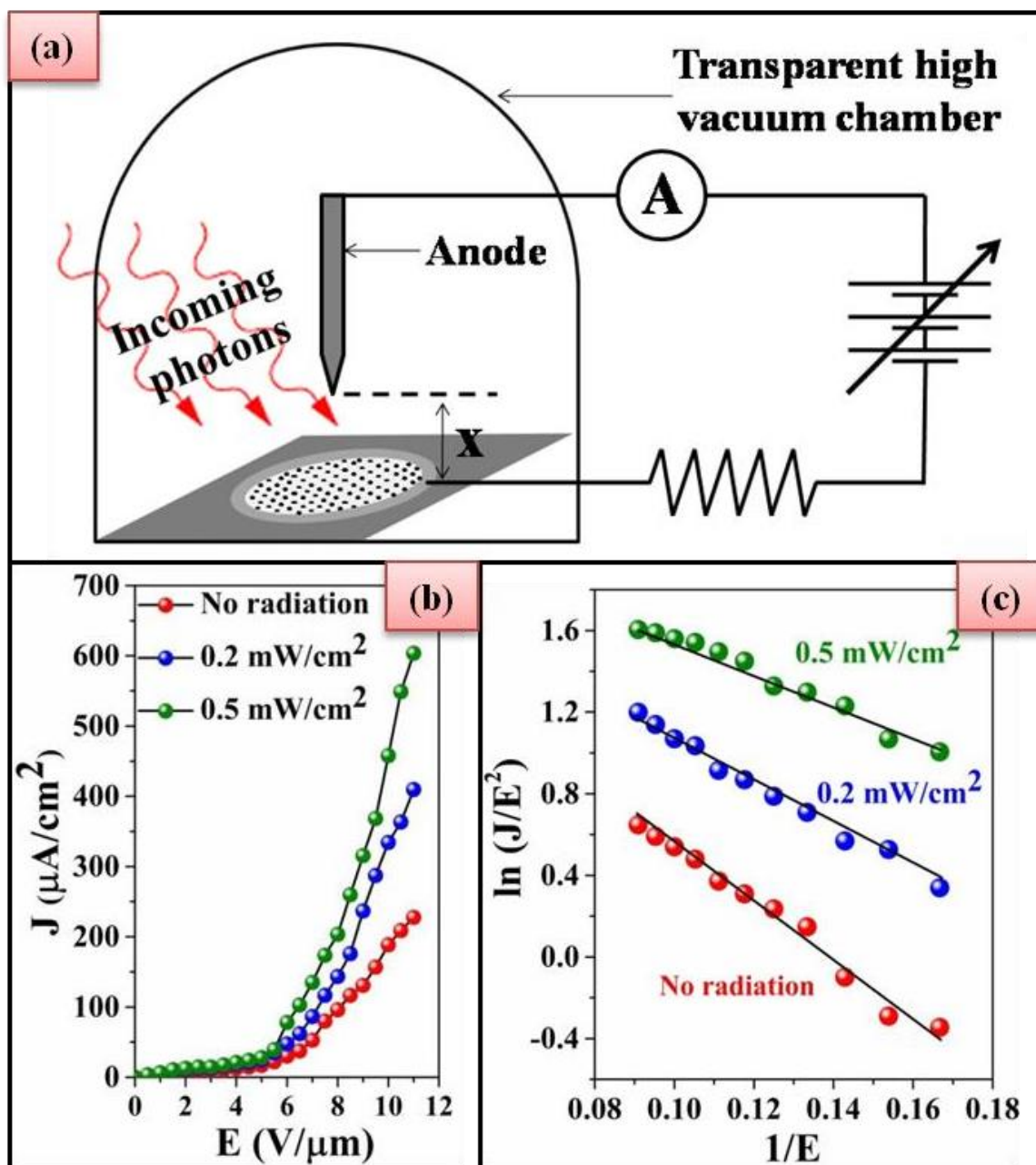
Figure 6.4: (a) Schematic of the FE set up, (b & c) J-E characteristic curves and the corresponding FN plots at different illumination conditions

CH₃NH₃PbI₃ (see Figure 6.3) was incident on the sample. It is to be mentioned that the incoming photon wavelength i.e. 750 nm excludes any possibility of contribution from template in electron emission upon photon impinge. AAO template because of its high energy band gap value [22] effectively behaves to these incident photons as fully transparent. The effect of light exposure with various intensities upon the emission behavior can be readily seen from Figures 6.4b & 6.4c.
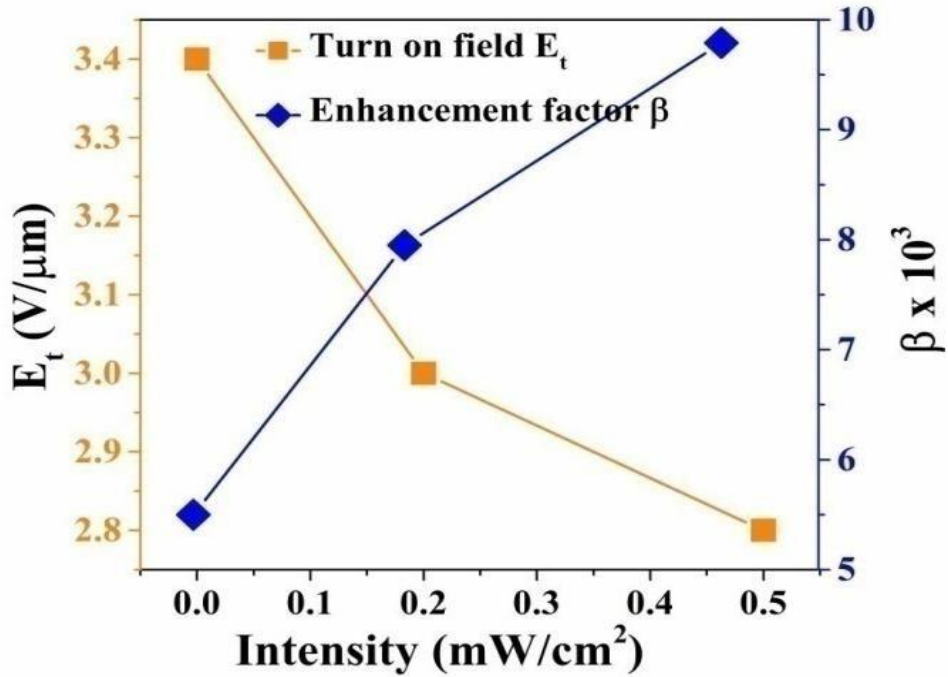
Figure 6.5: Plots of turn on field and enhancement factor at various light intensities

In comparison to the dark condition, the current density showed prominent increase with the increase in light intensity. Looking at a particular electric field of 10 V/μm, the current density increases from 187 μA/cm^2 to 330 μA/cm^2 and then finally to 455 μA/cm^2 with the increase in intensity of illumination. Correspondingly the change in the current density was calculated to be 76.5% and 143.3% at intensities of 0.2 mW/cm^2 and 0.5 mW/cm^2 respectively. As Figure 6.4c depicts, the slope of the FN plots keeps on decreasing with increasing light intensity, thus indicating gradual improvement in the enhancement factor β. Figure 6.5 shows the variation of turn on field (E$_t$) and enhancement factor β with different illumination intensities, the 3.4 to 3 V/μm as light of intensity 0.2 mW/cm^2 is shed upon the sample. The turn on field drops further to 2.8 V/μm, when more intense light of 0.5 mW/cm^2 is exposed on it. At the same time, the enhancement factor keeps on strengthening. Starting from a value of 5500, it becomes 7950 and finally reaches to 9793. To assess the obtained performances, a comparison has been finally made with other similar findings reported by few research groups in Table 6.2. results being tabulated in Table 6.1. As evident from these data, the turn on field decreases from 3.4 to 2.8 V/μm.

Table 6.1: Effect of light upon field emission performance

Light intensity (mW/cm^2)	Turn on field E_t (V/μm)	Enhancement factor β	J (μA/cm^2) at E = 10 V/μm	Change in J ΔJ/J$_0$ (%)
Zero	3.4	5500	187	---
0.2	3	7950	330	76.5
0.5	2.8	9793	455	143.3

Table 6.2: Comparison of field emission performances of different perovskite systems

Different halide perovskites	Turn on field E_t (V/μm)	Enhancement factor β	Ref.
Wet chemically synthesized CH$_3$NH$_3$PbI$_3$ nanorods	4.2	~ 4500	[8]
CsPbCl$_3$ nanobelts	2.62	3553	[26]
CsPbX$_3$ nanorods	4.5-10.1	602-1501	[27]
Template assisted vertically aligned CH$_3$NH$_3$PbI$_3$ nanorods	2.8-3.4	5734-9793	This work

The obtained photosensitivity of the electron emission current density can be attributed to the generation of excess charge carriers i.e. electrons excited from the valence band to conduction band of CH$_3$NH$_3$PbI$_3$.[23-25] With increased illumination intensity, the number of photo-excited electrons increases further and in turn they tunnel out of their semiconductor surface to vacuum producing larger emission current.

The mechanism can be easily understood from the schematic given in Figures 6.6(a- d). Under an electric field E, the potential barrier V(x) seen by an electron while tunneling from a semiconductor surface varies with inter-electrode spacing x as:

$$V(x) = -\frac{e^2}{4x} - eEx \tag{6.3}$$

However, in addition to such tunneling through this triangular potential, photo- excited electrons from conduction band of the semiconductor also penetrate into the anode surface and add up to the resultant current density. The strength of the emission current so generated from these photo-excited electrons naturally increases with the increase in number of photo-generated carriers due to photons having more intensity.
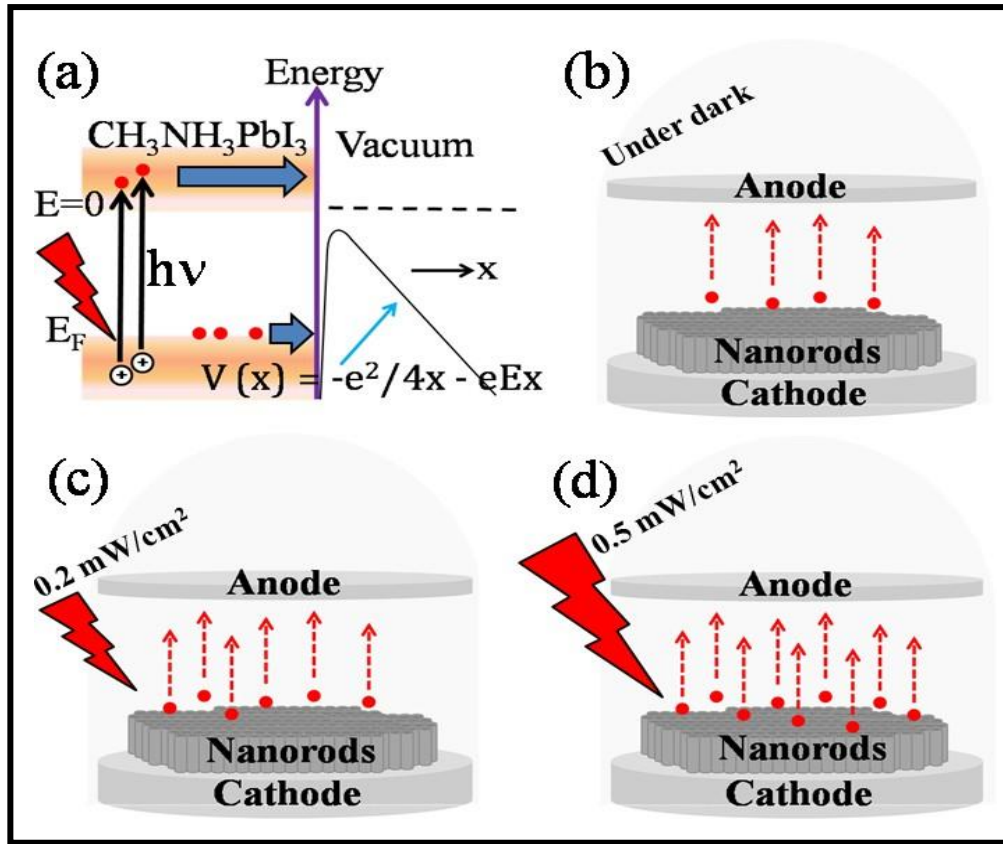
Figure 6.6: Schematic of (a) photo induced field emission, emission mechanism under (b) dark, (c) 0.2 mW/cm^2 and (d) 0.5 mW/cm^2 light intensities

6.5. Simulation of local electric field distribution

Electric field distribution near the $CH_3NH_3PbI_3$ nanostructures was simulated using COMSOL Multiphysics software. Electrostatics in stationary mode under AC/DC module and Electromagnetic waves in frequency domain mode under wave optics module were added in Physics. In the 2D model geometry, uniformly spaced (200 nm inter-spacing) rectangular $CH_3NH_3PbI_3$ structures array with width 200 nm each were built inside another rectangular air block. External electric field was applied by defining electric potential at the top and bottom boundaries of the air medium. Light with varying intensities was applied by defining a Gaussian plane polarized wave with different X-components of its electric field. The frequency of the incident light was set at 400 THz corresponding to illumination of 750 nm. Scattering boundary condition was applied across all the peripheral boundaries of the surrounding air medium ensuring total radiation absorption. Local electric field distribution near the vicinity of the NRs under dark condition was simulated in COMSOL Multiphysics, as shown in Figures 6.7(a&b).
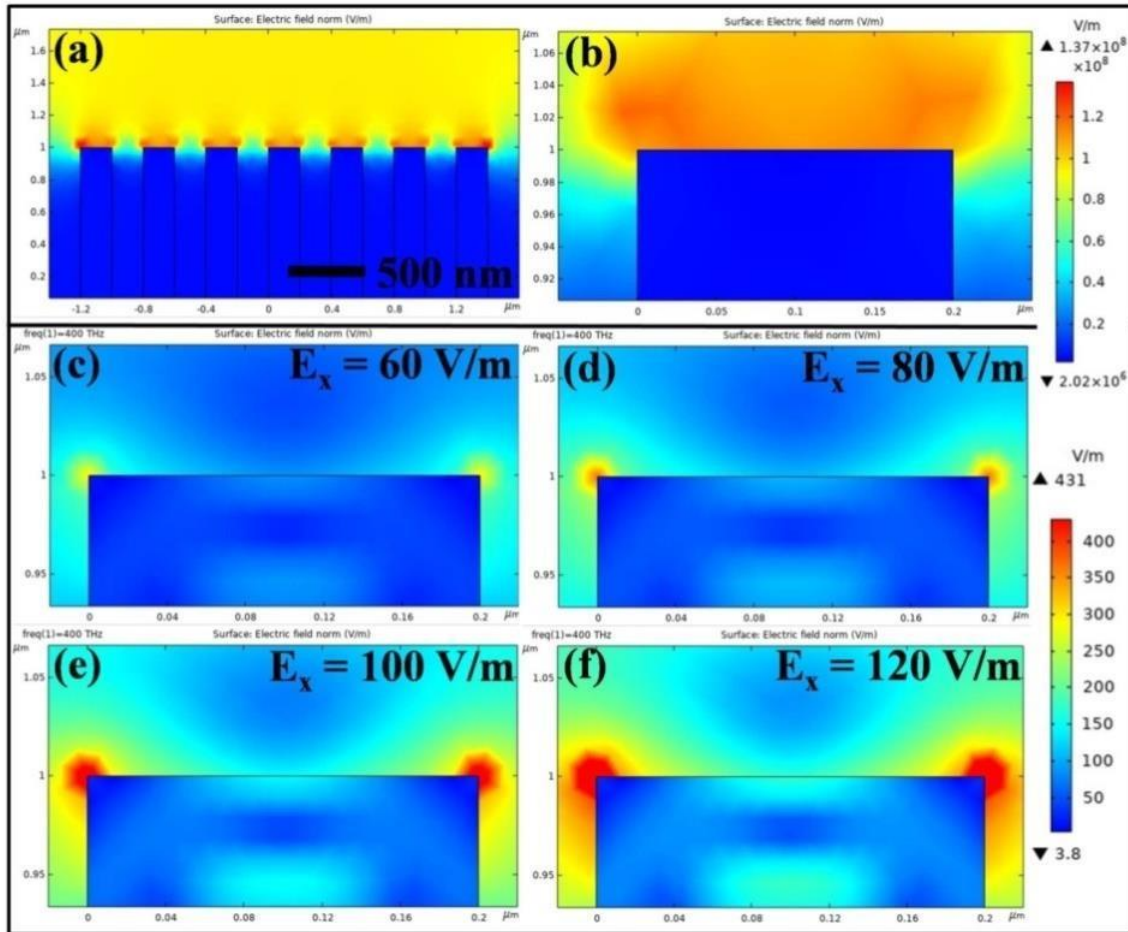
Figure 6.7: 2D electric field simulation for (a) array and (b) single NR under dark; Simulation for single NR under plane polarized light with electric field components (c-f) 60, 80, 100 and 120 V/m respectively under no bias

Under an externally applied test field of 5×10^6 V/m, prominent electron emission from these uniformly oriented vertical nanostructures is obvious from the 2D simulations of the field distribution near NRs (Figure 6.7a) array and a single NR (Figure 6.7b). More field lines accumulated near the sharp corners of the structures is clearly understood to originate from their least radius of curvature. Impact of light upon the emission behavior was experimented by simulating the local electric field near an individual NR, illuminated by an X-polarized Gaussian light wave falling vertically upon it without any bias applied across the rods. By varying the electric field X-components of the incident plane polarized wave, relative increase in the simulated field distribution was observed from Figures 6.7(c-f) for Ex equal to 60, 80, 100 and 120 V/m, thereby supporting the experimentally found emission improvement upon light illumination (Figure 6.4b). As these figures imply, field near the proximity of the structures

builds up to several hundred millions of volts per meter. The gradual strengthening of the electric field near the sharp corners of the NRs (Figures 6.7c-6.7f) unequivocally expresses increasing emission behavior from the NRs when illuminated by light with greater intensities.

6.6. Conclusion

To conclude, $CH_3NH_3PbI_3$ vertical NRs were synthesized using AAO template and finally field emission or cold cathode emission property of these nanostructures was investigated. Considerable electron emission was achieved with 3.4 V/μm turn on field and maximum current density reaching up to 230 μA/cm^2. The turn-on field came to be lower as compared to what obtained in one of our previous works with randomly oriented $CH_3NH_3PbI_3$ NRs. Alignment of the nanostructures towards only a particular direction was assigned to be the key factor for producing this improved emission. Further investigation under different light intensities revealed sensitive optoelectronic behavior of $CH_3NH_3PbI_3$, which was finally supported with theoretical simulation of the local electric field distribution near the NRs emitters. Increased photo-excited carriers led to gradual lowering of turn on field up to 2.8 V/μm under light intensity of 0.5 mW/cm^2. Looking at the current trend of application of $CH_3NH_3PbI_3$, this work plays with an offbeat application aspect apart from solar cells and motivates for further research in this topic.

References

[1] Montoya De Los Santos, Hugo J. Cortina-Marrero, M. A. Ruíz-Sánchez, L. Hechavarría-Difur, F. J. Sánchez-Rodríguez, Maykel Courel, Hailin Hu, Optimization of $CH_3NH_3PbI_3$ perovskite solar cells: A theoretical and experimental study, Sol. Energy 199 (2020) 198-205.

[2] Farzaneh S. Ghoreishi, Vahid Ahmadi, Reza Poursalehi, Mahmoud Samad Pour, Malin B. Johansson, Gerrit Boschloo, Erik M. J. Johansson, Enhanced performance of $CH_3NH_3PbI_3$ perovskite solar cells via interface modification using phenyl ammonium iodide derivatives, J. Power Sources 473 (2020) 228492.

[3] Qi Dong, Lei Lei, Juliana Mendes, Franky So, Operational stability of perovskite light emitting diodes, J. Phys. Mater. 3 (2020) 012002.

[4] Haiyun Dong, Chunhuan Zhang, Xiaolong Liu, Jiannian Yao, Yong Sheng Zhao, Materials chemistry and engineering in metal halide perovskite lasers, Chem. Soc. Rev. 49 (2020) 951-982.

[5] Yifan Li, Yating Zhang, Tengteng Li, Mengyao Li, Zhiliang Chen, Qingyan Li, Hongliang Zhao, Quan Sheng, Wei Shi, Jianquan Yao, Ultrabroadband, Ultraviolet to Terahertz, and High Sensitivity $CH_3NH_3PbI_3$ Perovskite Photodetectors, Nano Lett. 20 (2020) 5646–5654.

[6] Fei Xia, Ying Xu, Bixin Li, Wei Hui, Shiyang Zhang, Lin Zhu, Yingdong Xia, Yonghua Chen, Wei Huang, Improved Performance of $CH_3NH_3PbI_{3-x}Cl_x$ Resistive Switching Memory by Assembling 2D/3D Perovskite Heterostructures, ACS Appl. Mater. Interfaces 12 (2020) 15439–15445.

[7] Kuankuan Ren, Le Huang, Shizhong Yue, Shudi Lu, Kong Liu, Muhammad Azam, Zhijie Wang, Zhongming Wei, Shengchun Qu, Zhanguo Wang, Turning a disadvantage into an advantage: synthesizing high-quality organometallic halide perovskite nanosheet arrays for humidity sensors, J. Mater. Chem. C. 5 (2017) 2504-2508.

[8] Nripen Besra, Shreyasi Pal, Bikram Kumar Das, Kalyan Kumar Chattopadhyay, Perovskites beyond photovoltaics: field emission from morphology-tailored nanostructured methylammonium lead triiodide, Phys. Chem. Chem. Phys. 19 (2017) 26708-26717.

[9] Jingguo Liu, Zhengjun Zhang, Chunyu Pan, Ye Zhao, Xin Su, Ya Zhou, Dapeng Yu, Enhanced field emission properties of MoO_2 nanorods with controllable shape and orientation, Mater. Lett. 58 (2004) 3812-3815.

[10] Y. H. Huang, H. C. Lin, S. L. Cheng, Fabrication of vertically well-aligned $NiSi_2$ nanoneedle arrays with enhanced field emission properties, J. Phys. Chem. Solids 150 (2021) 109892.

[11] Shoushan Fan, Michael G. Chapline, Nathan R. Franklin, Thomas W. Tombler, Alan M. Cassell, Hongjie Dai, Self-Oriented Regular Arrays of Carbon Nanotubes and Their Field Emission Properties, Science 283 (1999) 512-514.

[12] Endre Horváth, Massimo Spina, Zsolt Szekrényes, Katalin Kamarás, Richard Gaal, David Gachet, László Forró, Nanowires of Methylammonium Lead Iodide ($CH_3NH_3PbI_3$) Prepared by Low Temperature Solution-Mediated Crystallization, Nano Lett. 14 (2014) 6761–6766.

[13] Andrew Barnabas Wong et al., Growth and Anion Exchange Conversion of $CH_3NH_3PbX_3$ Nanorod Arrays for Light-Emitting Diodes, Nano Lett. 15 (2015) 5519–5524.

[14] Roberto Gonzalez-Rodriguez, Neta Arad-Vosk, Naama Rozenfeld, Amir Sa'ar, Jeffery L. Coffer, Control of $CH_3NH_3PbI_3$ Perovskite Nanostructure Formation through the Use of Silicon Nanotube Templates, Small 12 (2016) 4477–4480.

[15] Woo Lee, Sang-Joon Park, Porous Anodic Aluminum Oxide: Anodization and Templated

Synthesis of Functional Nanostructures, Chem. Rev. 114 (2014) 7487–7556.

[16]   Liaoyong Wen, Rui Xu, Yan Mi, Yong Lei, Multiple nanostructures based on anodized aluminium oxide templates, Nat. Nanotechnol. 12 (2017) 244-250.

[17]   Sandip R. Kumavat, Yogesh Sonvane, Deobrat Singh and Sanjeev K. Gupta, Two-Dimensional $CH_3NH_3PbI_3$ with High Efficiency and Superior Carrier Mobility: A Theoretical Study, J. Phys. Chem. C 123 (2019) 5231–5239.

[18]   Guichuan Xing, Nripan Mathews, Shuangyong Sun, Swee Sien Lim, Yeng Ming Lam, Michael Grätzel, Subodh Mhaisalkar, Tze Chien Sum, Long-Range Balanced Electron- and Hole-Transport Lengths in Organic-Inorganic $CH_3NH_3PbI_3$, Science 342 (2013) 344-347.

[19]   J. A. Guerra, A. Tejada, L. Korte, L. Kegelmann, J. A. Töfflinger, S. Albrecht, B. Rech, R. Weingärtner, Determination of the complex refractive index and optical bandgap of $CH_3NH_3PbI_3$ thin films, J. Appl. Phys. 121 (2017) 173104.

[20]   Mark E. Ziffer, Joseph C. Mohammed, David S. Ginger, Electroabsorption Spectroscopy Measurements of the Exciton Binding Energy, Electron–Hole Reduced Effective Mass, and Band Gap in the Perovskite $CH_3NH_3PbI_3$, ACS Photonics 3 (2016) 1060–1068.

[21]   Takeo Oku, Masahito Zushi, Yuma Imanishi, Atsushi Suzuki, Kohei Suzuki, Microstuctures and photovoltaic properties of perovskite-type $CH_3NH_3PbI_3$ compounds, Appl. Phys. Express. 7 (2014) 121601.

[22]   S. Canulescu, K. Rechendorff, C. N. Borca, N. C. Jones, K. Bordo, J. Schou, L. Pleth Nielsen, S. V. Hoffmann, R. Ambat, Band gap structure modification of amorphous anodic Al oxide film by Ti-alloying, Appl. Phys. Lett. 104 (2014) 121910.

[23]   Yin Zhang, Juan Du, Xiaohan Wu, Guoqian Zhang, Yingli Chu, Dapeng Liu, Yixin Zhao, Ziqi Liang, Jia Huang, Ultrasensitive Photodetectors Based on Island-Structured $CH_3NH_3PbI_3$ Thin Films, ACS Appl. Mater. Interfaces 7 (2015) 21634–21638.

[24]   Yang Liu, Fushan Li, Chandrasekar Perumal Veeramalai, Wei Chen, Tailiang Guo, Chaoxing Wu, Tae Whan Kim, Inkjet-Printed Photodetector Arrays Based on Hybrid Perovskite $CH_3NH_3PbI_3$ Microwires, ACS Appl. Mater. Interfaces 9 (2017) 11662–11668.

[25]   Nripen Besra, Kausik Sardar, Soumen Maiti, Pranab Kumar Sarkar, Tufan Paul, Subhasish Thakur, Gautam Majumdar, Kalyan Kumar Chattopadhyay, Incorporation of V_2O_5 nanorods into perovskite photodetectors as an alternative approach to enhance device performance: a step towards stability against ambient water species, Dalton Trans. 49 (2020) 15788-15799.

[26]   Zhentao Du, Fulin Jiang, Jinju Zheng, Shanliang Chen, Fenngmei Gao, Jie Teng, Dingfa Fu, Hui Zhang, Weiyou Yang, Field Emission Behaviors of CsPbI3 Nanobelts, J. Mater. Chem. C 8 (2020) 5156-5162.

[27]   Tufan Paul, Soumen Maiti, Nripen Besra, Biplab Kumar Chatterjee, Bikram Kumar Das, Subhasish Thakur, Saikat Sarkar, Nirmalya Sankar Das, Kalyan Kumar Chattopadhyay, Tailored CsPbX3 Nanorods for Electron-Emission Nanodevices, ACS Appl. Nano Mater. 2 (2019) 5942-5951.

Photodetection and Its Improvement

7.1. Background of the work

Within the last one or two decades, metal halide perovskites, especially $CH_3NH_3PbI_3$ (**M**ethyl **a**mmonium **l**ead **i**odide; henceforth MALI), has given us so many remarkable achievements in the field of photovoltaics and other allied technological sectors, that it wouldn't be exaggeration to say that we are at the threshold of what can be called a 'Perovskite age'. Large carrier diffusion length,[1] high mobility,[1] low excitonic binding energy,[2] tunability of the energy band gap over a wide range,[3] etc. are the reasons for its excellent optoelectronic properties. Besides these intriguing features, facile and budgetary preparation methods[4] add up an additional advantage to their widespread usage.

Apart from well documented perovskite solar cells, researchers have also devised photodetectors based on it. However, device performance, in many cases, is restricted to certain limits as they suffer from issues like slow photo response, low efficiency, lack of durability. Such limitations are attributed to the issues associated to perovskite material e.g. narrow spectral absorption, presence of defects in considerable amount, susceptibility to water, temperature and other external conditions, etc. So, for the upgradation of the device performance, scientists have a very clear motto to broaden the spectral absorption range, reduce carrier recombination losses and hence charge transfer resistance and stabilize the device for long run applications, obviously in economical approach. To achieve these qualities, several protocols have been adopted in literature e.g. upgrading crystalline qualities,[5] realization of morphology tailored nanoforms,[6] inducing electric field within the material,[7] optimizing electrode depositions,[5] hybridizing or making heterostructures with different nanomaterials,[8,9] controlling materials interfaces,[10,11] etc. Where the fundamental idea is to minimize the carrier losses and facilitate the charge transfer. Among these aforesaid pathways, realization of heterostructures via rational coupling of different materials with perovskites is immensely pertinent from both research and technological

aspects as it opens up the possibility of functionality enhancement along with noble interface phenomenon generation.

Vanadium pentoxide (V_2O_5), when used in various nanoforms, have huge applications in different technological segments e.g. supercapacitors,[12,13] field emission,[14] photocatalysis,[15] and photodetectors,[16] as well. V_2O_5 possesses a band gap of ~2.5 eV in visible region which motivates researchers to explore their optoelectronic usages such as optical wave guides, photodetectors and photoelectric switches. With the introduction of very tiny nanoparticles of V_2O_x into $CH_3NH_3PbI_{3-x}Cl_x$ matrix, Liu et al. have successfully enhanced the photovoltaic performance of the device.[17] However, a systematic in-depth investigation is still required to explore the eminence of nanoparticles for improvement of the air stability of organometal halide perovskites as well as the electrical performance of the devices.

Motivated by an intuition that a 1D nanoform would carry electrons/ holes far better than particulate one, we took an attempt to upgrade the qualities of perovskite-based photodetector by incorporating V_2O_5 in the form of 1D nanostructure into $CH_3NH_3PbI_3$. Optimized hybrid sample exhibited 3-fold improved performance than the pristine MALI sample. The improved photodetection performance of the modified sample was scrutinized thoroughly by current-voltage characteristics under dark and illumination conditions. Additionally, Mott-Schottky analysis suggested the lowering of the interfacial energy barrier in the optimum sample, which in turn strengthened the dissociation of excitons compared to the pristine perovskite. Equivalent circuit diagram based on the Nyquist plots revealed the low resistive character of the modified sample. The obtained low value of the charge transfer resistance was ascribed to the cross linked V_2O_5 nanorods spread over the entire surface of perovskite matrix. To check the real time applicability of the devices, their detectivity was monitored under ambient condition at some intervals with no encapsulation. The stability of the devices was further probed by bringing them in direct contact with water droplets and constantly recording the contact angles. In this context, generation of Cassie-Baxter (CB) state on the surface of the sample due to increased roughness is proposed which is based on the experimentally observed contact angle measurements and the simulated surface roughness data. From the beginning, perovskite has a universal drawback of degradation due to water species.[18] Our present work provides a possibility to deal with such degradation issues.

7.2. Device preparation and material characterizations

Devices i.e. FTO/CH$_3$NH$_3$PbI$_3$/FTO, FTO/V$_2$O$_5$/FTO and FTO/CH$_3$NH$_3$PbI$_3$:V$_2$O$_5$/FTO with various sample loading were prepared using the procedures as described in sections 4.5, 4.6 and 4.7 respectively. The active materials required for making these devices i.e. CH$_3$NH$_3$PbI$_3$ and V$_2$O$_5$ (nanorods) were prepared by following the synthesis protocols mentioned in sections 4.1 and 4.4 respectively.

The proper phase formation of the as prepared samples was ascertained by X-ray diffraction technique (Bruker D8 diffractometer) with Cu K$_\alpha$ radiation of wavelength 1.5404 Å. The microscopic analysis was performed by field emission scanning electron microscopy (FESEM, HITACHI S-4800). High resolution transmission electron microscopy (HRTEM, JEOL JEM 2010) was used to analyze the crystalline features of the samples. The elemental idea of the samples was derived from X-ray photoelectron spectroscopy (XPS, SPECS, HSA-3500) using Al K$_\alpha$ radiation of energy 1486.6 eV. The interface effects in terms of Mott Schottky study were performed using 302N AUTOLAB. Frequency dependent dielectric data was obtained by Agilent 4294A precision impedance analyzer. The stability of the samples against water was analyzed by contact angle measurements (OCA 15 EC DATA PHYSICS). The surface roughness of the samples was simulated and investigated by using "Image J" software. The current-voltage characteristics under dark and light were studied with Keithley nanovoltmeter 2182A, source meter 2400, and 6221 current source meters interfaced with Lab VIEW program.

7.3. Results and discussion

7.3.1. Structural and morphological analysis

The XRD patterns of all the composites i.e. S1, S2 and S3 along with the pristine perovskite and V$_2$O$_5$ are deployed in Figure 7.1a. The peaks at their respective 2θ positions approve the existence of tetragonal CH$_3$NH$_3$PbI$_3$[19] and orthorhombic V$_2$O$_5$ [JCPDS PDF number 761803]. Not only that, the well crystallinity of the samples is evident from their sharp diffraction signals. Furthermore, a visual evidence of the morphological features of MALI, V$_2$O$_5$ and S2 can be obtained from the typical FESEM images shown in Figure 7.1(b-d) respectively, the insets showing their corresponding high-resolution images. The FESEM images of S1 and S3 are
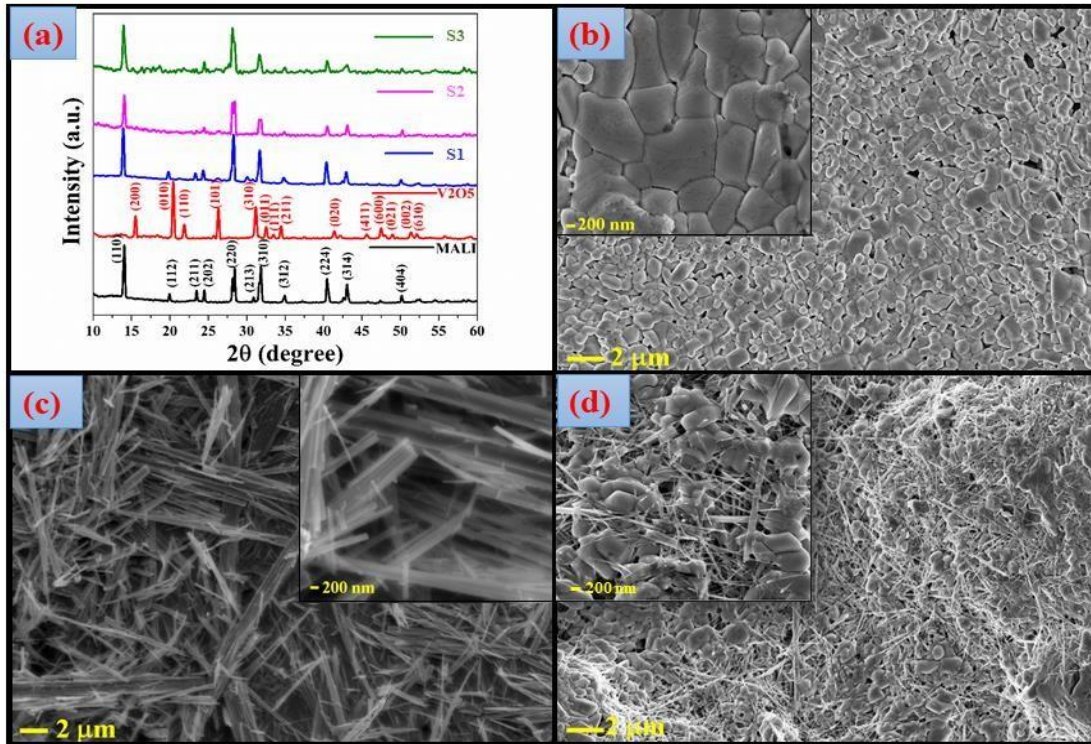
Figure 7.1: (a) XRD patterns of MALI, V_2O_5, S1, S2 and S3; FESEM images of (b) MALI, (c) V_2O_5 and (d) S2; Insets showing their high magnification images respectively
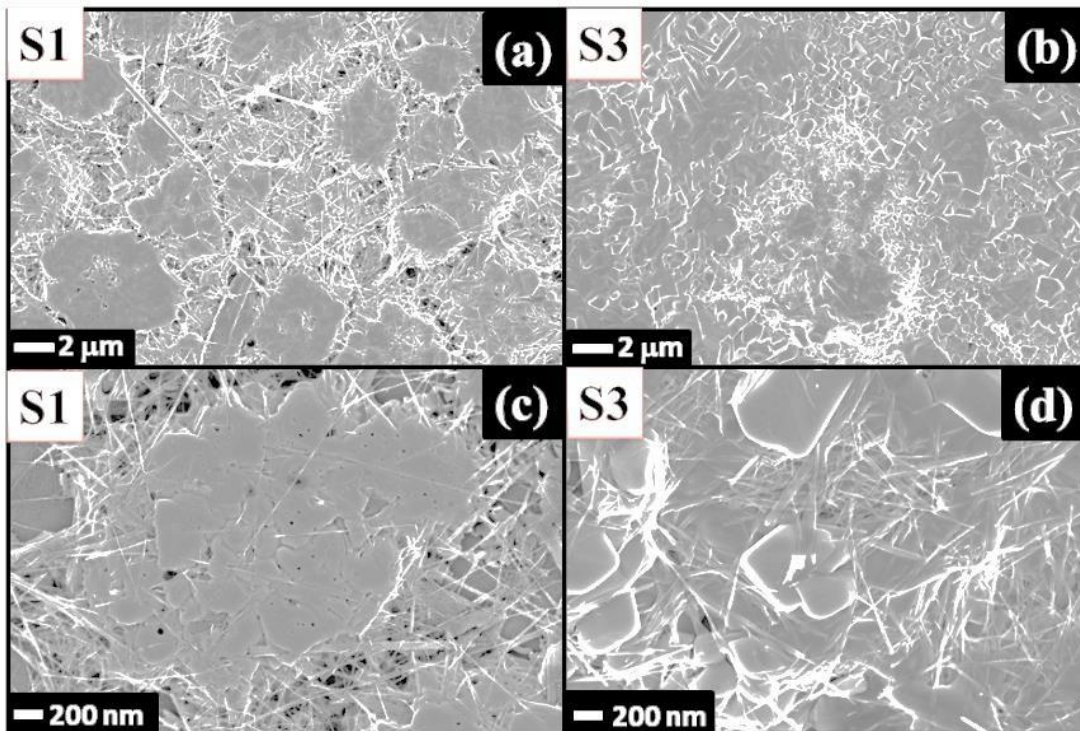
Figure 7.2: (a&b) Low magnification FESEM images of S1 and S3; (c&d) their respective high magnification images

presented in Figures 7.2(a-d). Figure 7.1b depicts the uniform granular formation of perovskite host material with the corresponding inset image showing the crystalline grains very vividly. Besides, Figure 7.1c shows lots of well crystalline nanorods of V_2O_5 guest material which are 10 - 15 μm long with diameters ranging in 50 - 150 nm. Finally Figure 7.1d displays that those nanorods are well embedded into $CH_3NH_3PbI_3$ matrix, which can be better understood from the inset image of that figure. Therefore, the system is nothing but a V_2O_5 network inter- penetrating through the MALI clusters. The images also show that no aggregation of V_2O_5 nanorods took place as a result of optimal spin coating technique. The FESEM images of samples S1 and S3 are also depicted in Figure 7.2a & 7.2b respectively. These figures indicate that S3 comprises V_2O_5 nanorods interpenetrating through large perovskite boulders distributed uniformly throughout the sample. Besides, S1 consists of discrete and localized perovskiteislands
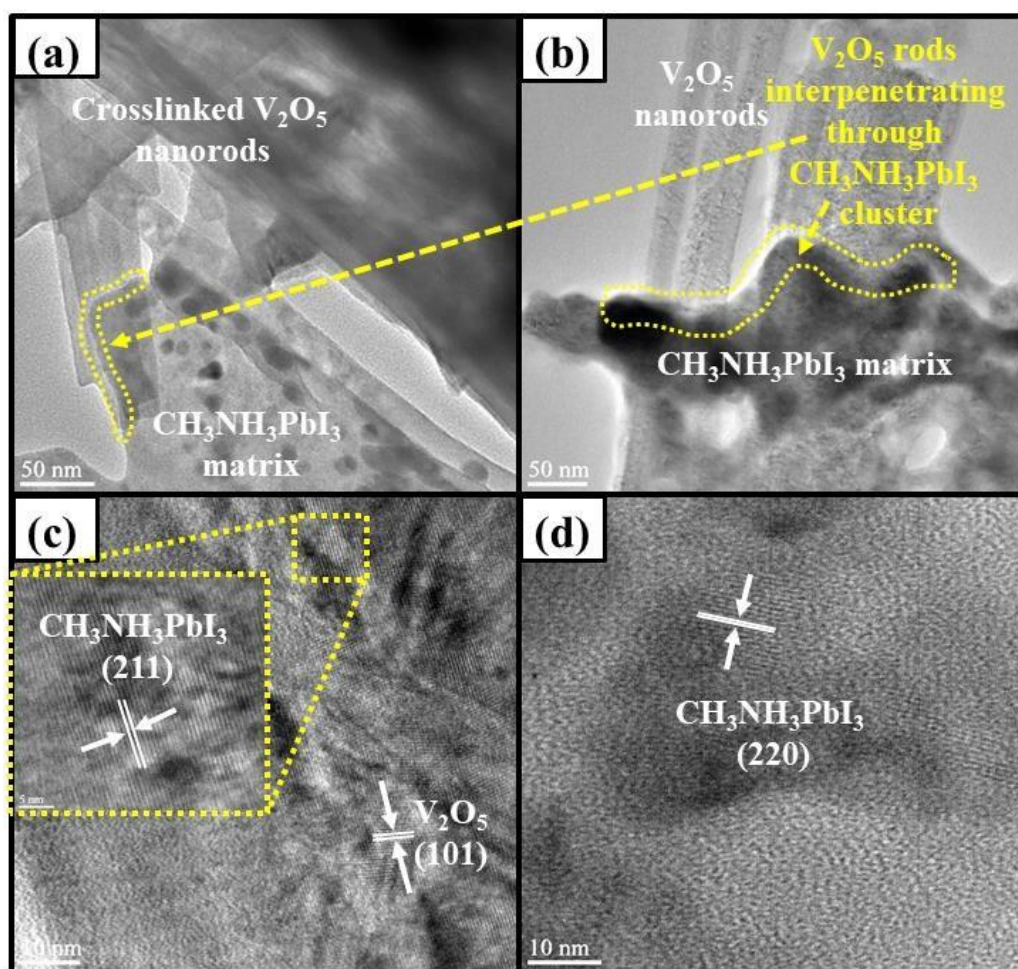
Figure 7.3: (a&b) High resolution TEM images of S2; (c&d) Crystal planes captured in HRTEM images

137

connected by V_2O_5 nanorods.

The transmission electron microscopic (TEM) images (Figure 7.3) provide additional approval in favor of the simultaneous presence of $CH_3NH_3PbI_3$ and V_2O_5 in the form of nanorods. Figure 7.3a & 7.3b clearly indicate the presence of V_2O_5 nanorods interpenetrating through perovskite matrix. The crystalline fringes in Figure 7.3c show the (211) and (101) planar orientations of $CH_3NH_3PbI_3$ and V_2O_5 respectively. An additional crystal plane of $CH_3NH_3PbI_3$ (220) is also deployed in Figure 7.3d. These TEM images signify the high crystalline nature of the synthesized samples and corroborate with the XRD results.

7.3.2. Spectroscopic analysis: XPS

The elemental composition of the as-prepared samples can be obtained from the surface probing by X-ray photoelectron spectroscopy (XPS). Figure 7.4 shows the individual high-resolution spectra of the constituent elements, whereas the full survey scan of all the possible constituent elements of S2 indexed against their appropriate binding energies are provided in Figure 7.5. Considering the adventitious carbon (binding energy = 284.6 eV) as a reference, all the binding energies are charge corrected.
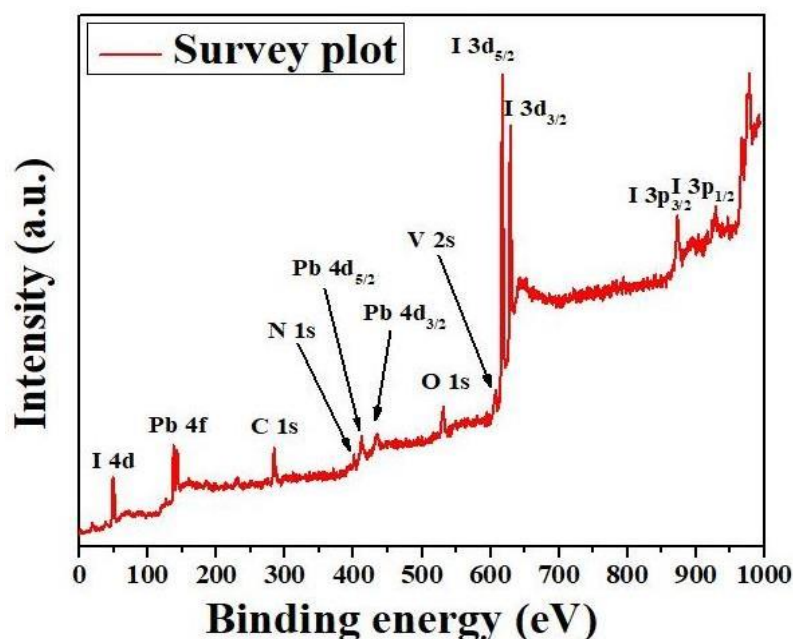
Figure 7.4: Full XPS survey scan of S2 (charge corrected)

The HR signal at 400.7 eV is assigned to N 1s state of $CH_3NH_3PbI_3$. Besides, the signals found at 136.9 eV and 141.6 eV, with the energy splitting of 4.7 eV, are accredited to the spin-orbit doublet of Pb $4f_{7/2}$ and $4f_{5/2}$ respectively. XPS peaks arising at 617.1 eV and 628.8 eV owe to the spin-orbit doublets of I $3d_{5/2}$ and I $3d_{3/2}$ respectively, resulting into an energy gap of 11.7 eV. On

the other hand, the presence of V (Vanadium) in $2p_{3/2}$ and $2p_{1/2}$ states is ascertained from the binding energies at 517.2 eV and 524.5 eV respectively, accompanied by the spin-orbit splitting energy 7.3 eV. Additionally, the peak observed at 530.0 eV infers the presence of O in 1s state. Hence the obtained XPS results approve the coexistence of $CH_3NH_3PbI_3$ and V_2O_5.[20-25]
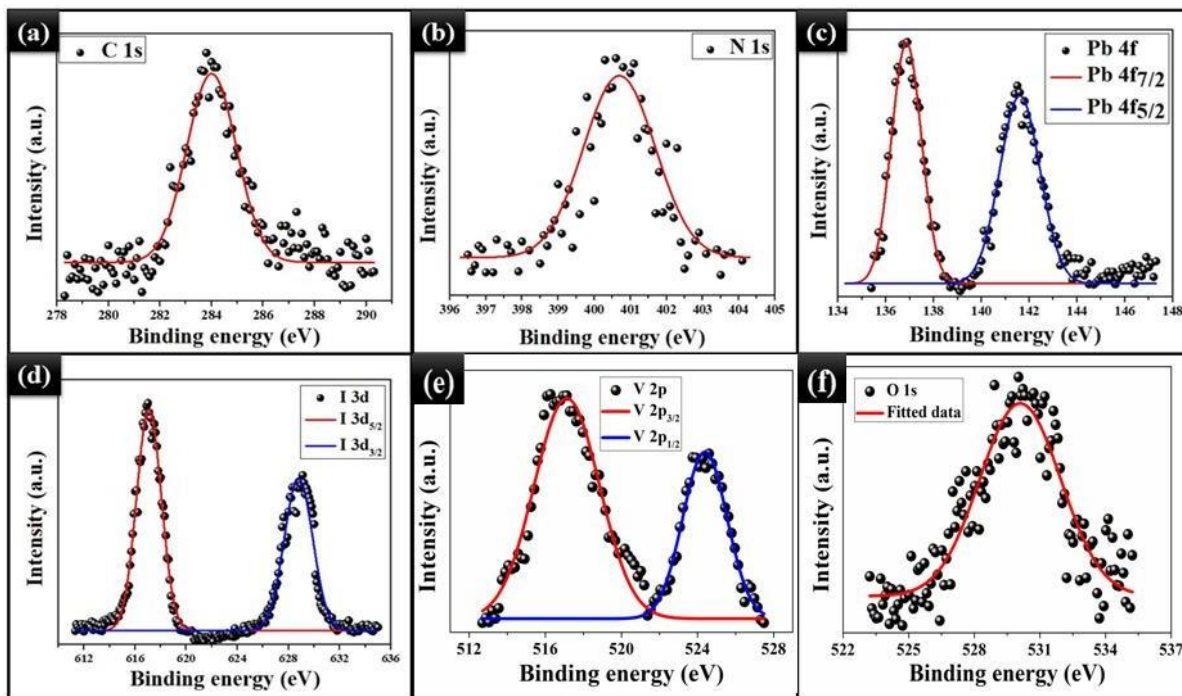
Figure 7.5: High resolution XPS spectra of (a) C 1s, (b) N 1s, (c) Pb 4f, (d) I 3d, (e) V 2p and (f) O 1s respectively

7.4. Effect of V_2O_5 nanorods incorporation

7.4.1. Current-Voltage characteristics under dark and light

Prior to the measurement, all the samples were kept for several hours in complete darkness to attain equilibrium conditions. Current-voltage (I-V) characteristics of MALI, S1, S2 and S3 under dark and light exposure have been studied and plotted in semi logarithmic mode provided in Figures 7.6a, 7.6b, 7.6c and 7.6d respectively. The effect of light illumination upon the samples is very much prominent from their distinct dark and photo I-V curves contained in these above-mentioned figures. The registered values of these dark and photo currents are tabulated in Table 7.1. The entries in this table directly indicate the significant impact of introducing V_2O_5 nanorods into perovskite (MALI) sample. However, the relative change in the photoconductivity ($\Delta\sigma/\sigma$) for S2 achieved the highest magnitude among all other samples.
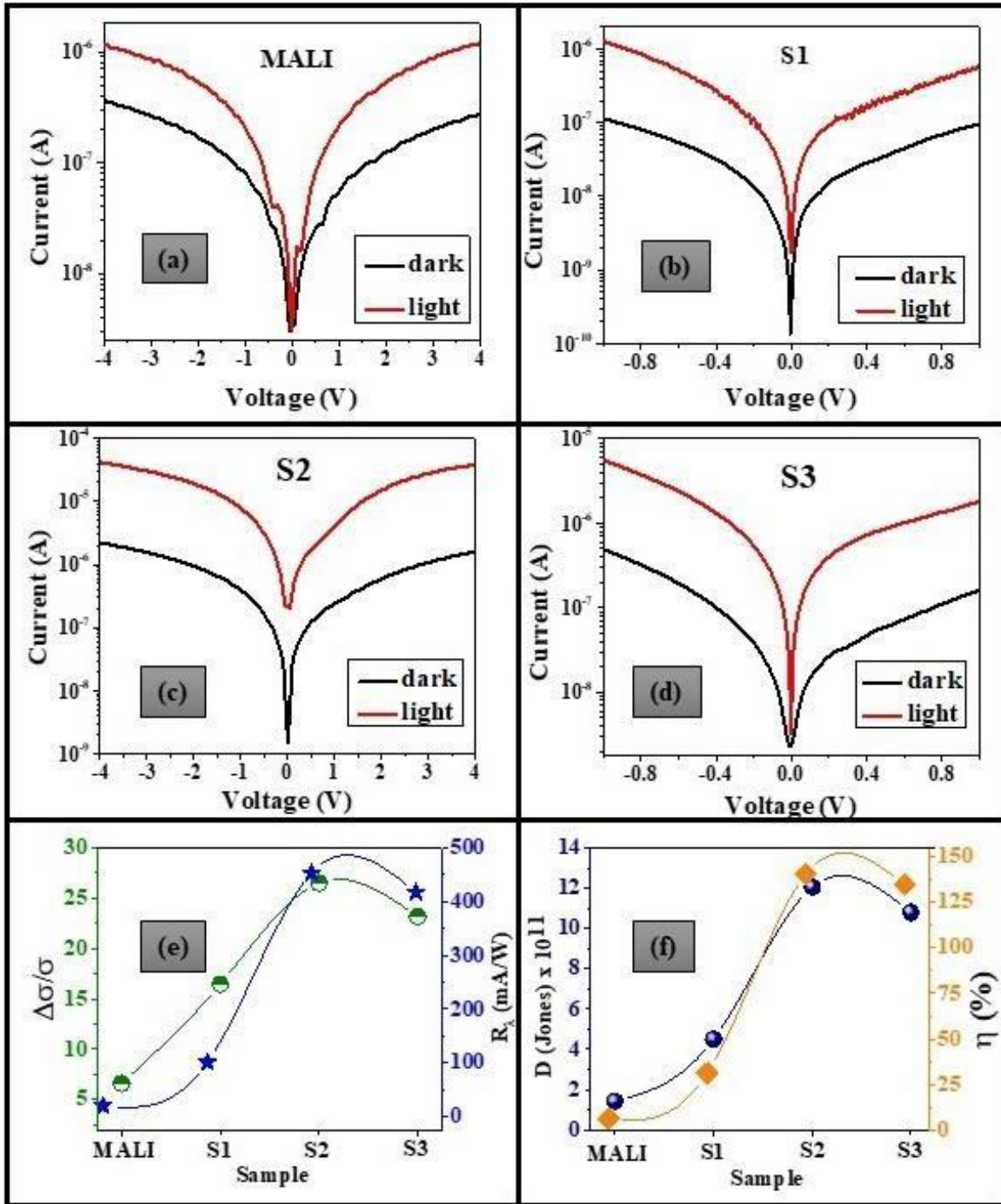
Figure 7.6: Current voltage characteristics of (a-d) MALI, S1, S2 and S3 under dark and light; (e&f) variation of relative photoconductivity change and responsivity with samples

Table 7.1: Dark current, photocurrent and relative photoconductivity change

Sample	Dark current (nA)	Photocurrent (µA)	Δσ/σ
MALI	62.6	0.55	6.6
S1	160	2.62	16.5
S2	460	11.9	25.6
S3	500	11.38	22.4

Furthermore, other important photodetection parameters such as responsivity R_λ (mA/W), detectivity D (cm√Hz/W) and external quantum efficiency (EQE) η (%) were also estimated for them using following equations.

$$R_\lambda = \frac{I_{ph}}{P_{in}}$$ (7.1a)

$$D_\lambda = \frac{R_\lambda}{\sqrt{(2eJ_d)}}$$ (7.1b)

$$\eta = \frac{I_{ph}/e}{P_{in}/h\nu}$$ (7.1c)

Here I_{ph} and J_d denote the photogenerated current and dark current density respectively. Besides, P_{in} and 'e' are power of incident photons and electronic charge respectively. Here h is Planck's constant and ν is frequency of the incident photons. The subscript λ carried by R_λ
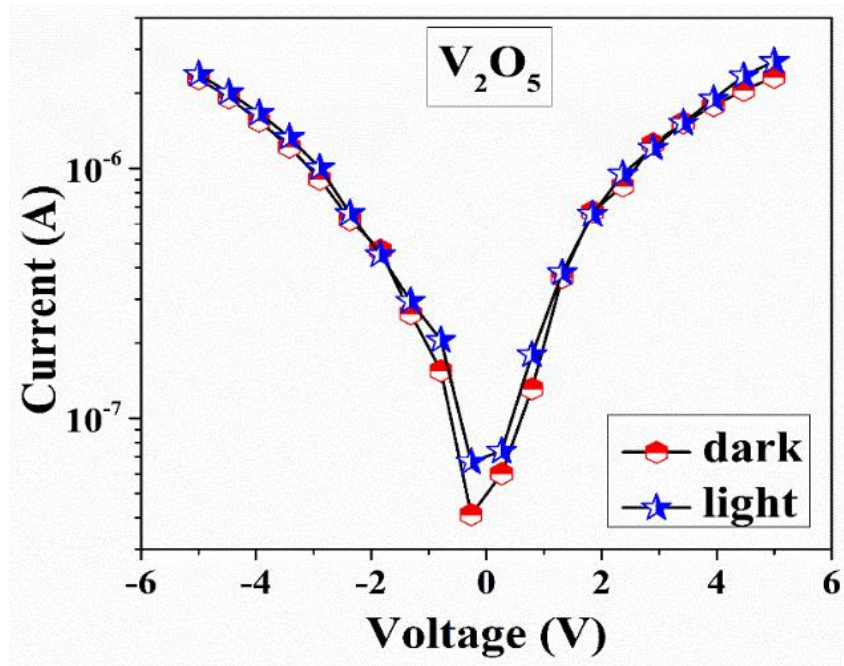
Figure 7.7: Current voltage characteristics of V_2O_5 under dark and light

signifies the fact that photo- responsivity depends on wavelength of the incident photons, supported by the Figure 7.8 which shows the variation of R_λ varies with λ with a characteristic edge near 700 – 750 nm. However, for detail investigation, we chose only 700 nm wavelength (near infra-red radiation) as the incident light, since it fulfills the energy band gap criterion for $CH_3NH_3PbI_3$ which lies somewhere ~ 1.6 - 1.7 eV.
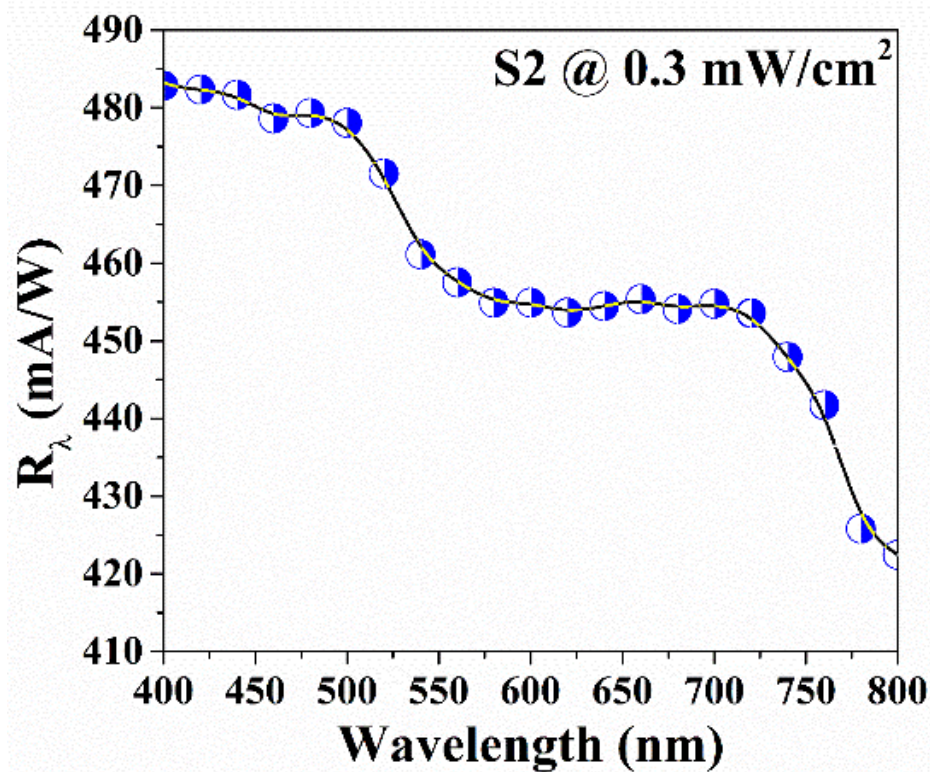
Figure 7.8: Spectral responsivity for S2 at light intensity 0.3 mW/cm^2

This particular choice of wavelength also eliminates the possibility of direct participation of the V_2O_5 NRs, in the sense that they can't provide electron-hole pairs in the system. Therefore, a pair of current-voltage characteristics for the pristine V_2O_5 NR based device were also studied under dark and illuminated condition, which is presented in Figure 7.7. As suggested by this figure, it doesn't show any prominent increase in its photocurrent compared to its dark counterpart. Consequently, we studied the photodetection performances of S1, S2 and S3 thoroughly and compared the obtained parameters with those of pristine MALI sample.

These parameters are tabulated in Table 7.2 and plotted in Figures 7.6e and 7.6f. As evident from Table 7.1 & 7.2, and also from Figures 7.6e & 7.6f, sample S2 revealed the best performance among all the other samples. Hence considering S2 as the most suitable and optimum candidate in our case, time resolved photo-response study was carried out in a comparative fashion with the

pristine perovskite (MALI) in the ambient air by switching the lamp "ON" and "OFF" at a fixed bias of 1V. The spectra thus obtained for MALI and S2 are shown in Figures 7.9a & 7.9b over 6 on/off cycles, along with their high-resolution images (Figure 7.9c & 7.9d) respectively.
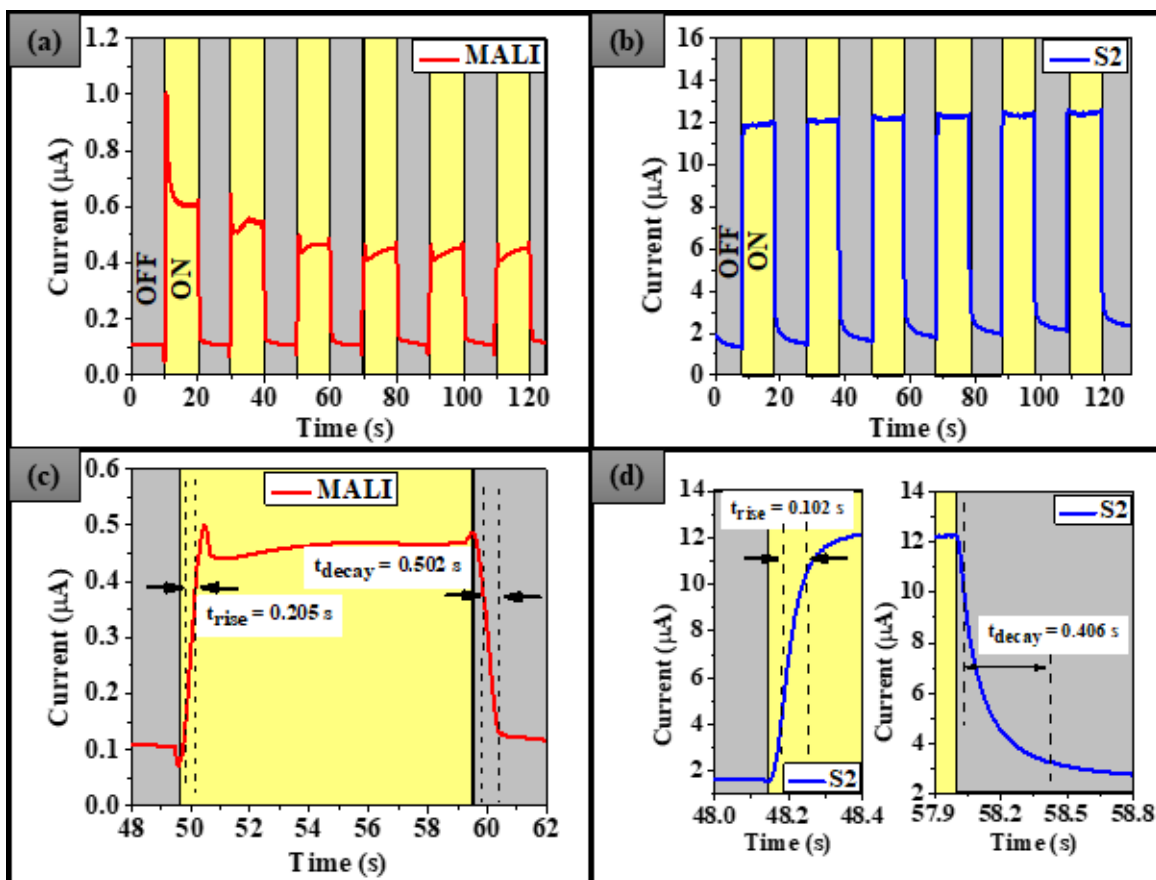
Figure 7.9: Temporal photoresponse curve of (a&b) MALI and S2; High resolution photocurrent rise and decay curves of (c&d) MALI and S2 respectively

Table 7.2: Various photodetection performance parameters for different samples

Sample	On/Off ratio	Responsivity (mA/W)	Detectivity D (cm√Hz/W)	EQE η (%)
MALI	8.66	19.8	1.44×10^{11}	6.1
S1	16.45	100.8	3.6×10^{11}	31.3
S2	25.9	453.6	1.26×10^{12}	140.8
S3	22.75	417.6	1.08×10^{12}	134.6

As suggested by these figures, both the samples showed excellent synchronization with the incident light pulse with a window of light exposure for 10 s. As soon as the light is turned on, current for both the devices sharply rises to 0.55 μA and 11.9 μA for MALI and S2 respectively. Once the light is switched off, the current immediately falls off and settles down at 62.6 nA and 460 nA, thereby achieving their corresponding on/off ratio of 8.66 and 25.9. Now sharp response of a photodetector is be defined in terms of rise time (t_{rise}) and decay time (t_{decay}) i.e. the time a photodetector takes to rise from 10% to 90% of its maximum current and time taken by the same to fall from 90% to 10% of the maximum current.[26] For MALI, the rise time and decay time came to be 0.205 s and 0.502 s respectively. Besides, for S2, they came to be 0.102 s and 0.406 s respectively. The fruitfulness of modifying the perovskite matrix by V_2O_5 nanorods are thus well approved from these data. Whether it is larger photo current, improved responsivity, higher on/off ratio, better detectivity, greater efficiency or faster response, the modified sample S2 proves its superiority over MALI in every aspect. Another very important feature which can readily be inferred from Figure 7.9b is that, as time passes on, the photocurrent for S2 maintains a steady value. But the photocurrent for MALI keeps decaying asymptotically (Figure 7.9a). Such decay in the photocurrent may be led by the ion migration and carrier recombination.[27,28] Therefore, these effects are comparatively reduced in S2, thereby stabilizing the photocurrent. The superior photodetection performance of S2 compared to MALI can be understood in terms of two factors i.e. a) increased built-in potential and b) easy passage for carriers.

7.4.2. Mott-Schottky analysis and reduced carrier recombination

The improved photodetection capability of S2 can be well understood from the charge separation of the photogenerated carriers assisted by the built-in potential developed across the sample/FTO interface because of the equalization of the Fermi levels of the two opposite sides across the junction. Stronger this potential, better is the charge separation.[29] Quantitatively, the strength of this potential can be estimated from Mott Schottky analysis i.e. the variation of the junction capacitance as a function of a bias voltage externally applied across the junction.[30] The junction capacitance C across the interface and the applied bias V can be related as given below.

$$\frac{1}{C^2} = \frac{1}{q\varepsilon_0\varepsilon_r NA^2}\left(V - V_{bi} - \frac{kT}{q}\right) \qquad (7.2)$$

Here, where q is the electronic charge, ε_r is dielectric constant and ε_0 denotes permittivity of free space respectively. N and A represent carrier concentration and sample area. V_{bi} is the built-
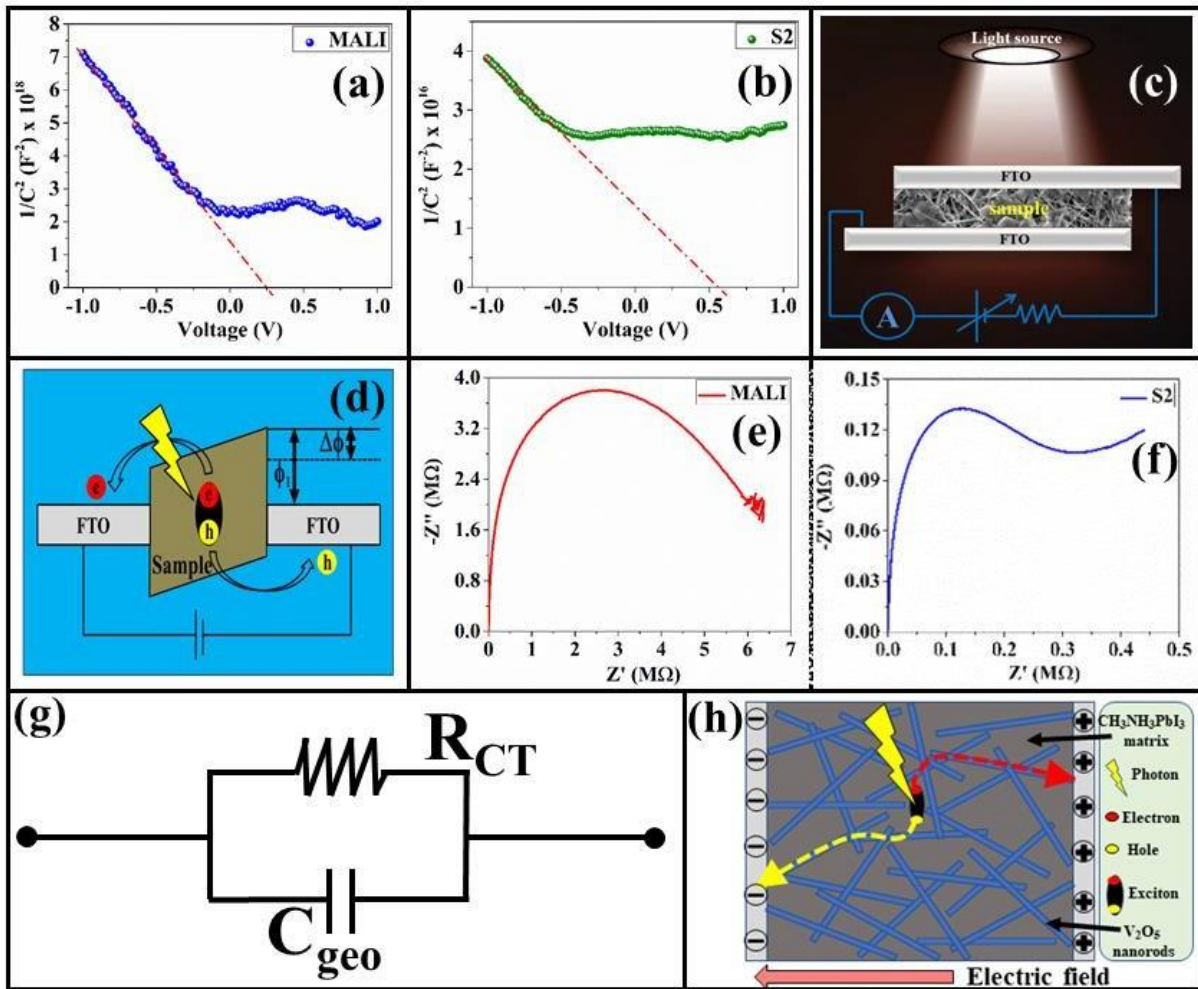
Figure 7.10: Mott-Schottky plots of (a) MALI and (b) S2; Schematic pictures of the (c) device under illumination and (d) separation process of photogenerated charge carriers mediated by energy barrier adjustment; Nyquist plots of (e) MALI and (f) S2; (g) Equivalent circuit diagram; and (h) Schematic of charge flow through low resistive V_2O_5 nanorods

in potential, k = Boltzmann constant and T = absolute temperature. At room temperature, kT/q = 0.026 eV. Therefore, by plotting $1/C^2$ vs. V one can find N and V_{bi} from the slope and x-intercept of the graph. The linear parts in the Mott Schottky plots (Figure 7.10a & 7.10b) approve the junction formation in the system.[31] It is also obvious from these two figures that the slope of the curve (-ve) decreases after the incorporation of V_2O_5 in the perovskite matrix. Such result suggests p-type nature increment which in turn indicates that the movement of hole is more facilitated than that of electron. Furthermore, from the same figure, it is also very clear that the built-in potential formed across the FTO/sample interface increases by 0.32 V when S2 is used instead of MALI. The collective behavior of S2 as a one single unit system can also be

understood by looking at Figures 7.10(c&d). Under light illumination, carriers in S2 experience a reduced energy barrier $(\Phi_1 - \Delta\Phi)$ where Φ_1 stands for the energy barrier across the pristine perovskite/FTO interface and $\Delta\Phi$ stands for the reduction of this interfacial energy barrier when the pristine perovskite is modified by V_2O_5. This barrier energy lowering leads to an additional pull on photo-generated carriers away from the junction and restricts them to recombine. Thus charge separation, which is a key factor in This barrier energy lowering leads to an additional pull on photo-generated carriers away from the junction and restricts them to recombine. Thus charge separation, which is a key factor in photodetectors, becomes much easier.

7.4.3. Easy passage for carriers

A comparative picture of the resistive behavior of the samples was drawn from the Nyquist plots of MALI and S2 as shown in Figures 7.10(e&f) respectively. An equivalent circuit (Figure 7.10g) was also modeled for the two samples based on these two plots where R_{CT} and C_{geo} being the charge transfer resistance and geometric capacitance of the samples respectively. It is observed that the fitted value of the charge transfer resistance (R_{CT}) is 7.9 MΩ and 0.3 MΩ for MALI and S2 respectively, with zero series resistance (R_s) value for both the samples. Thus, R_{CT} gets lowered by 29 times for S2 with respect to the pristine MALI sample. Such a reduction in the charge transfer resistance leads to faster transport of photogenerated carriers to the electrodes through V_2O_5 nanorods which act like low resistance chanels for the carriers. Basically prior to V_2O_5 nanorods addition in perovskite, photo generated carriers i.e. electron and hole reach the electrodes after crossing several grain boundaries throughout the perovskite. As a consequence of this, major fraction of them gets lost and recombined. On the contrary, in V_2O_5 nanorods-perovskite system, 1D geometry of the V_2O_5 nanoform facilitates the transfer of photo generated carriers. Thus, in hybrid system, movements of carriers are more channelized and effortless. This scenario is presented with the help of a schematic diagram (Figure 7.10h) where the typical formation of a photo-generated EHP and the path followed by carriers (red dotted line for electron trajectory & yellow dotted line for hole trajectory) through the bulk to the electrodes are shown.

Effect of aspect ratio on FE performance

Impacts of the length and width of the V_2O_5 nanorods on the photodetector performance were also checked by investigating the responsivity of two more devices based on V2O5 nanorods

with different aspect ratio. Precisely, devices were fabricated using nanorods with different length ~ 8 - 12 µm and ~ 10 - 12 µm and corresponding width ~ 160 - 450 nm and ~ 120 - 350 nm respectively. Device performance in terms of responsivity was plotted against length and diameter of the nanorods (Figure 7.11). Responsivity increased monotonically with the increase in length and decrease in diameter value. The observed trend in responsivity can be attributed to the increased aspect ratio of the nanorods due to less resistance suffered by the carriers in their course of channelized movement inside the materials.
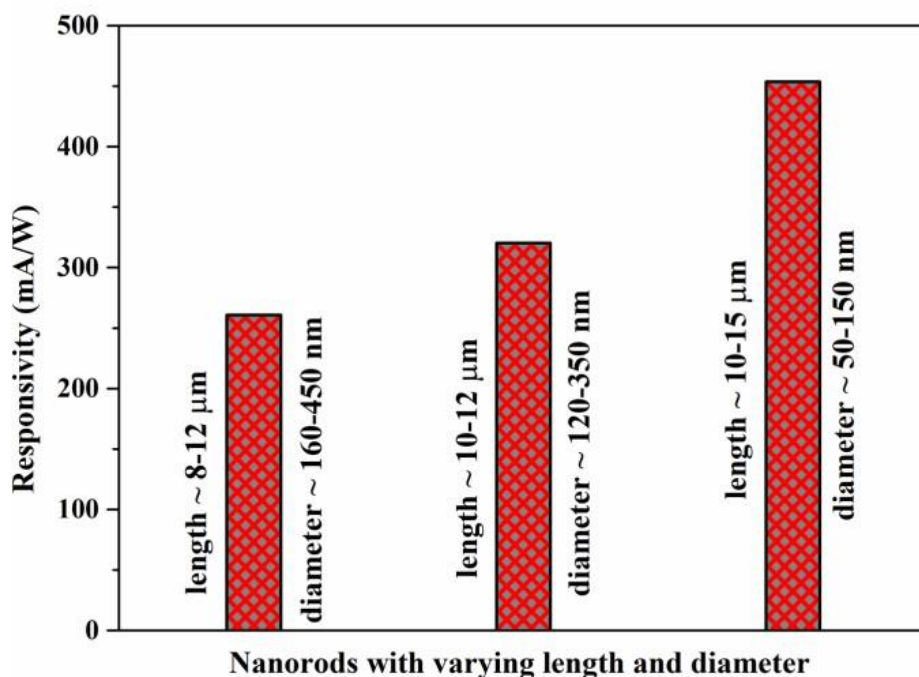
Figure 7.11: Responsivity of devices made of nanorods with various lengths and diameters

7.5. Environmental stability of the devices

Since the scope of application of any device relies on its real time use in regular ambient condition, we tested the performances of the detectors MALI and S2 uncapsulated under open air As Figure 7.12 suggests, the detectivity of the pristine MALI drops from its initial value of 1.44 x 10^{11} Jones to 0.9 x 10^{11} Jones after 1 month from its initial measurement, which amounts to somewhere near 64 % retention in its performance. Beside the detectivity of S2 drops at 1.24 x 10^{12} Jones from its initial reading of 1.26 x 10^{12} Jones, which means sample S2 holds 98 % of its detectivity even after one month. To probe the robustness of S2 under environmental water species, we recorded the contact angles made by a water droplet placed on MALI/FTO and
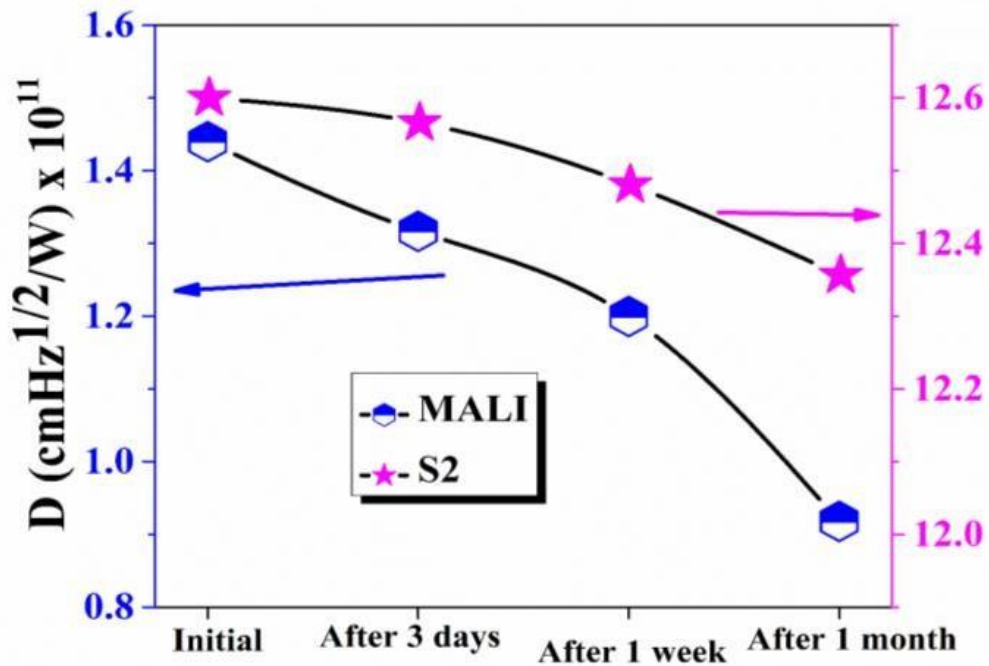
Figure 7.12: Detectivity of the devices based on MALI and S2 at various time intervals
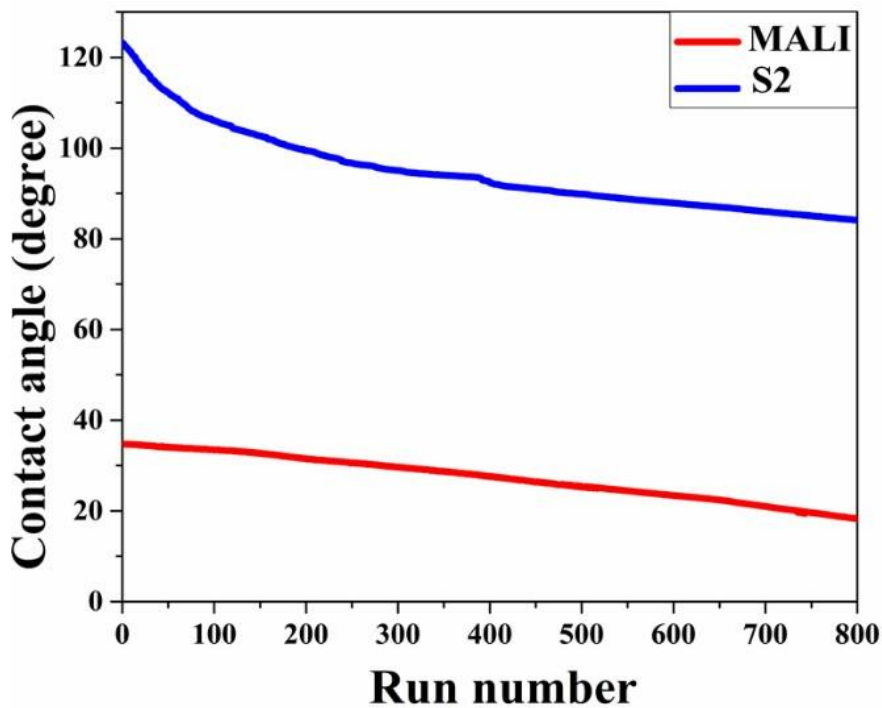
Figure 7.13: Evolution of contact angle (water) for MALI and S2

S2/FTO film at different times. This temporal evolution is pictorially depicted in Figures 7.14a and 7.14b respectively. Additionally, a graphical representation of the same is also given in Figure 7.13 over 800 cycles which corresponds to a time duration as long as 600 s. As evident

from Figures 7.14a and 7.14b, the initial values of the contact angles made by MALI and S2 with the water are 34.50 ($<90^0$) and 118.00 ($>90^0$) respectively. Thus, it reveals the hydrophobic character of S2, in contrast to the hydrophilic nature of the pristine perovskite. Such hydrophobicity can be accounted to the increased surface roughness of hybrid sample compared to that of the pristine one.[32,33] Figures 7.15(a&b) show surface roughness of MALI and S2 simulated from 'Image J' software using their high resolution FESEM images.
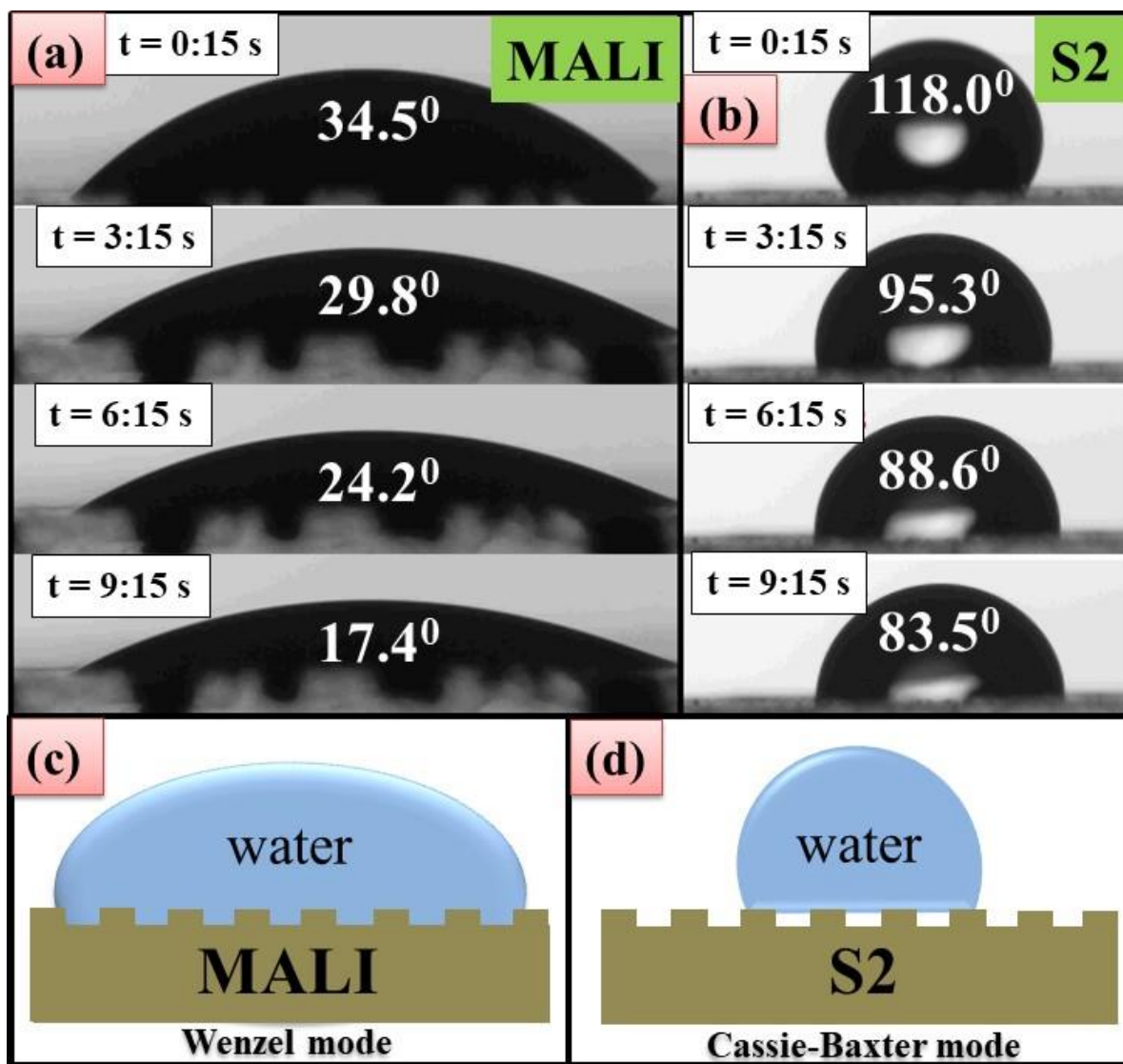
Figure 7.14: Contact angles for (a) MALI and (b) S2 at different time intervals; Schematic of the formation of (c) Wenzel mode for MALI and (d) Cassie-Baxter mode for S2

The vertical color scales in these two figures represent z value i.e. height of the samples at different places on the surface (i.e. XY plane). Insets in these figures show their corresponding smoothened surface profiles. This increase in the surface roughness resulted in transition from

Wenzel mode (Figure 7.14c) to Cassie-Baxter mode (Figure 7.14d), having a direct resemblance with the respective contact angle images of MALI and S2 as shown in Figures 7.14a and 7.14b respectively.[34,35]
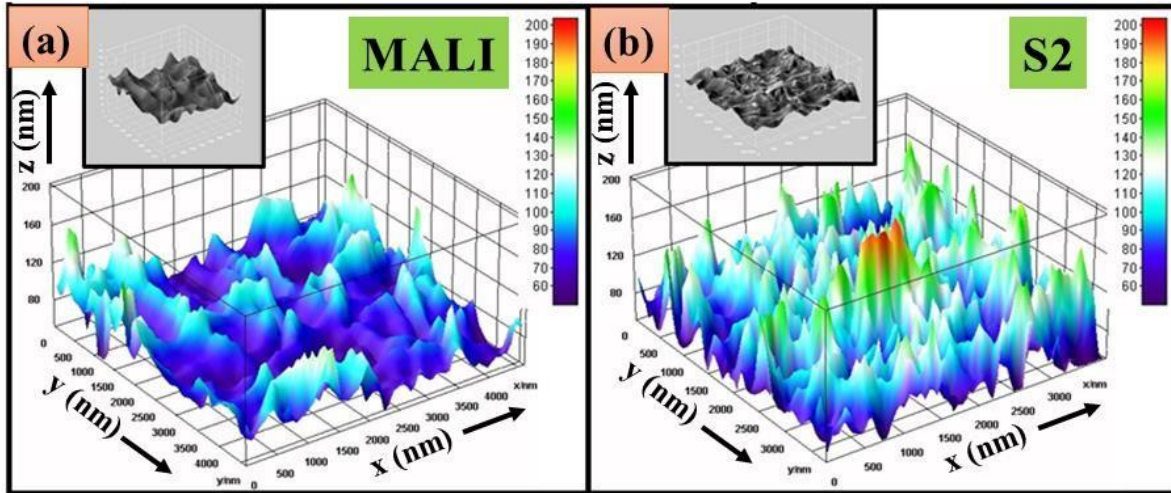
Figure 7.15: Simulated surface roughness profiles of (a) MALI and (b) S2

Table 7.3: Performance comparison of S2 with MALI

Parameters	Pristine MALI	S2	Achievement/Improvement
On/Off ratio	8.7	25.9	~ 3-fold
Responsivity (mA/W)	19.8	453.6	~ 23-fold
Detectivity (cm√Hz/W)	1.44×10^{11}	1.26×10^{12}	~ 9-fold
EQE (%)	6.1	140.8	23-fold
Rise time & decay time	0.2 s & 0.5 s	0.1 s & 0.4 s	Faster response
Retention of detectivity after 1 month	64 %	98 %	More stable under ambient condition
Wettability	Hydrophilic	Hydrophobic	Water stable

Basically, the incorporation of V_2O_5 nanorods into perovskite matrix introduces numerous low dimensional undulations on the sample surface. These small- scale undulations hold the water droplet just like a lotus leaf holding a water drop in perfect rounded shape because of the nanofibrils existing on its surface.[36-38] It is to be noted that the performances of the individual devices were already comparable to other semiconductor photodetectors reported in literatures.[39-45] But here we emphasize more on what improvements we have achieved by

modifying the perovskite with V_2O_5 additives. To get a quick recap of this, the device performance of pristine MALI in comparison with only the best sample i.e. S2 is provided separately in Table 7.3.

7.6. Conclusion

V_2O_5 nanorods have been introduced successfully into $CH_3NH_3PbI_3$ matrix to improve the photodetection ability of the material. Devices were fabricated based on these samples in a cost-effective symmetric electrode fashion. The dark and photo current-voltage characteristics, along with the photoresponse features, were studied which proved the superiority of the modified sample. The modified sample showed manifold improvement in the device performance in terms of on/off ratio, responsivity, detectivity, external quantum efficiency and response times. Equipped with Impedance spectroscopy and Mott Schottky analysis, the carrier dynamics were probed and the improved photoresponse was ascribed to higher interfacial built-in potential, better charge separation and the low resistive channels formation by V_2O_5 nanorods in the $CH_3NH_3PbI_3$ matrix. Not only that, incorporation of V_2O_5 nanorods stabilized the system as far as the sample degradation due to ambient moisture is concerned. The hydrophobic nature in the modified perovskite, as suggested by the contact angle measurement, has been accounted for the increased level of surface roughness triggering a transition from Wenzel to CB mode.

References

[1]   Q. Dong, Y. Fang, Y. Shao, P. Mulligan, J. Qiu, L. Cao, and J. Huang, *Science*. 2015, **347**, 967–970.

[2]   Y. Yang, M. Yang, Z. Li, R. Crisp, K. Zhu, and M. C. Beard, *The Journal of Physical Chemistry Letters.* 2015, **6**, 4688–4692.

[3]   V. D' Innocenzo, A. R. S. Kandada, M. D. Bastiani, M. Gandini, and A. Petrozza, *Journal of the American Chemical Society*. 2014, **136**, 17730–17733.

[4]   X. Jia, Z. Hu, Y. Zhu, T. Weng, J. Wang, J. Zhang, and Y. Zhu, *Journal of Alloys and Compounds*. 2017, **725**, 270–274.

[5]   F. Zhao, K. Xu, X. Luo, W. Lv, Y. Peng, Y. Wang, … S. Xu, *Organic Electronics*. 2017, **46**, 35–43.

[6]   D. H. Chun, Y. J. Choi, Y. In, J. K. Nam, Y. J. Choi, S. Yun, … J. H. Park, *ACS Nano.*

2018, **12**, 8564-8571.

[7]   R. Saraf, and V. Maheshwari, *ACS Applied Materials & Interfaces*. 2018, **10**, 21066–21072.

[8]   F. Cao, W. Tian, B. Gu, Y. Ma, H. Lu, and L. Li, *Nano Research*. 2017, **10**, 2244–2256.

[9]   J. Yu, X. Chen, Y. Wang, H. Zhou, M. Xue, Y. Xu, … H. Wang, *Journal of Materials Chemistry C*. 2016, **4**, 7302–7308.

[10] Y. H. Cao, Z. Y. Deng, M. Z. Wang, J. T. Bai, S. H. Wei, and H. J. Feng, *The Journal of Physical Chemistry C*. 2018, **122**, 17228–17237.

[11] J. Yang, K. Liu, Z. Cheng, P. Jing, Q. Ai, X. Chen, … D. Z. Shen, *ACS Applied Materials & Interfaces*. 2018, **10**, 34744-34750.

[12] E. Uchaker, N. Zhou, Y. Li, and G. Cao, *The Journal of Physical Chemistry C*. 2013, **117**, 1621–1626.

[13] H. Wang, D. Ma, Y. Huang, and X. Zhang, *Chemistry - A European Journal*. 2012, **18**, 8987–8993.

[14] T. Zhai, H. Liu, H. Li, X. Fang, M. Liao, L. Li, … D. Golberg, *Advanced Materials*. 2010, **22**, 2547–2552.

[15] C. W. Zou, Y. F. Rao, A. Alyamani, W. Chu, M. J. Chen, D. A. Patterson, E. A. C. Emanuelsson, and W. Gao, *Langmuir*. 2010, **26**, 11615–11620.

[16] H. S. Kim, K. R. Chauhan, J. Kim, and E. H. Choi, *Applied Physics Letters*. 2017, **110**, 101907.

[17] T. He, Z. Liu, K. Liu, J. Wang, Y. Zhou, J. Yang, H. Liu, Y. Jiang, H. Ma, and M.Yuan, *Journal of Materials Chemistry A*. 2017, **5**, 24282–24291.

[18] J. Yang, B. D. Siempelkamp, D. Liu, and T. L. Kelly, *ACS Nano*. 2015, **9**, 1955-1963.

[19] J. Ding, S. Du, Y. Zhao, X. Zhang, Z. Zuo, H. Cui, X. Zhan, Y. Gu, and H. Sun, *Journal of Materials Science*. 2016, **52**, 276–284.

[20] Z. Ahmad, M. A. Najeeb, R. A. Shakoor, A. Alashraf, S. A. Al-Muhtaseb, A. Soliman, and M. K. Nazeeruddin, *Scientific Reports*. 2017, **7**, 15406.

[21] Y. Li, X. Xu, C. Wang, B. Ecker, J. Yang, J. Huang, and Y. Gao, *The Journal of Physical Chemistry C*. 2017, **121**, 3904–3910.

[22] A. V. Naumkin, A. Kraut-Vass, S. W. Gaarenstroom, and C. J. Powell, *NIST Standard Reference Database 20, NIST, Gaithersburg, Md, USA*. 2012, *Version 4.1*.

[23] J. Mendialdua, R. Casanova, and Y. Barbaux, *Journal of Electron Spectroscopy and*

Related Phenomena. 1995, **71**, 249–261.

[24] G. Silversmit, D. Depla, H. Poelman, G. B. Marin, and R. De Gryse, *Journal of Electron Spectroscopy and Related Phenomena*. 2004, **135**, 167–175.

[25] E. Hryha, E. Rutqvist, and L. Nyborg, *Surface and Interface Analysis*. 2011, **44**, 1022–1025.

[26] S. J. Young, and Y. H. Liu, *Microelectronic Engineering*. 2015, **148**, 14-16.

[27] T. Leijtens, G. E. Eperon, A. J. Barker, G. Grancini, W. Zhang, J. M. Ball, A. R. S. Kandada, H. J. Snaith, and A. Petrozza, *Energy & Environmental Science*. 2016, **9**, 3472–3481.

[28] R. Saraf, and V. Maheshwari, *ACS Applied Materials & Interfaces*. 2018, **10**, 21066–21072.

[29] Y. Zhu, T. Song, F. Zhang, S. T. Lee, and B. Sun, *Appl. Phys. Lett.* 2013, **102**, 113504.

[30] K. Gelderman, L. Lee, and S. W. Donne, *J. Chem. Educ.* 2007, **84**, 685.

[31] W. J. Albery, G. J. O'Shea, and A. L. Smith, *J. Chem. Soc., Faraday Trans.* 1996, **92**, 4083-4085.

[32] Z. Yoshimitsu, A. Nakajima, T. Watanabe, and K. Hashimoto, *Langmuir*. 2002, **18**, 5818–5822.

[33] H. M. Shang, Y. Wang, K. Takahashi, G. Z. Cao, D. Li, and Y. N. Xia, *Journal of Materials Science*. 2005, **40**, 3587–3591.

[34] C. Ran, G. Ding, W. Liu, Y. Deng, and W. Hou, *Langmuir*. 2008, **24**, 9952–9955.

[35] C. Dorrer, and J. Rühe, *Soft Matter*. 2009, **5**, 51-61.

[36] H. C. V. Baeyer, *The Sciences*. 2000, **40**, 12–15.

[37] H. J. Ensikat, P. Ditsche-Kuru, C. Neinhuis, and W. Barthlott, *Beilstein J. Nanotechnol*. 2011, **2**, 152–161.

[38] H. J. Lee, and S. Michielsen, *Journal of the Textile Institute*. 2006, **97**, 455–462.

[39] E. Horvath, M. Spina, Z. Szekrenyes, K. Kamaras, R. Gaal, D. Gachet, and L. Forro, *Nano Lett.* 2014, **14**, 6761−6766.

[40] E. Zheng, B. Yuh, G. A. Tosado, Q. Yu, *J. Mater. Chem. C.* 2017, **5**, 3796−3806.

[41] F. Bai, J. Qi, F. Li, Y. Fang, W. Han, H. Wu, and Y. Zhang, *Adv. Mater. Interfaces*. 2018, **5**, 1701275.

[42] H. C. Liu, M. Gao, J. McCaffrey, Z. R. Wasilewski, and S. Fafard, *Appl. Phys. Lett.* 2001, **1**, 79-81.

[43] Z. Bai, and Y. Zhang, *Journal of Alloys and Compounds.* 2016, **675**, 325-330.

[44] G. Konstantatos, J. Clifford, L. Levina, and E. H. Sargent, *Nature Photonics.* 2007, **1**, 531-534.

[45] Y. Xue, Y. Zhang, Y. Liu, H. Liu, J. Song, J. Sophia, J. Liu, Z. Xu, Q. Xu, Z. Wang, J. Zheng, Y. Liu, S. Li, and Q. Bao, *ACS Nano.* 2016, **10**, 573-580.

Dielectric Study of CH₃NH₃PbI₃ in RF Regime

8.1. Background of the work

Methyl ammonium lead iodide ($CH_3NH_3PbI_3$) perovskite has already set its impression in the scientific communities owing to its high absorption coefficients,[1] large carrier diffusion lengths,[2] high band gap tunability,[3] cost-effective synthesis,[4-6] etc. Starting from the efficiency of 3.8%, the solar cell based upon this new class of perovskites has rapidly crossed efficiency > 20%.[7] Not limiting to only solar cells, the material has also established its potential in other application aspects *e.g.*, LEDs,[8] lasers,[9] photodetectors,[10-12] memory devices,[13,14] sensors,[15] field effect transistors,[16] supercapacitors,[17] field emission devices,[18] etc. But in spite of the impressive outcomes of the researches on perovskite-based solar cells and the related optoelectronics, their commercial manifestation is way too far from a practical reality. The devices suffer from serious degradations due to humidity and several other environmental factors, which collectively hinder its real time applications.[19,20]

Impedance spectroscopy, in this context, is an important tool to quantitatively scrutinize these detrimental effects. In fact, due to the long-term debates on the ferroelectric character and the associated polar phases of $CH_3NH_3PbI_3$,[21,22] dielectric spectroscopy can be considered as the most legitimate electrical characterization technique for exploring the field-dependent polarization bottleneck of the material. We know that photovoltaics work on the principle of separation of photo generated charge carriers. So, it's all about how to make this charge separation more efficient and consistent for longer period. But it is influenced by various relaxation processes taking place inside the system. Study of the dielectric parameters *e.g.* frequency-dependent capacitance, dielectric susceptance and loss helps us reveal these internal relaxation mechanisms in adequate detail. As an example, a study on the dielectric properties of $CH_3NH_3PbI_3$ in the frequency range 42 Hz to 4.8 MHz was carried out by M.S. Sheikh et al., where they demonstrated distributed relaxations and suggested the presence of localized

relaxation process.[23] Often, a hysteresis loop appears in the current-voltage characteristics, which mimics the inferior device performance.[24-26] Study reveals that such hysteresis originates from the capacitive effects generated by electrode polarization and ionic accumulation near the interface.[27-29] From bias-dependent impedance spectroscopy, the low frequency response of perovskite solar cells is also shown to depend upon such ionic movements.[30] Interfacial decomposition induced MA^+ (MA: Methylammonium i.e. CH_3NH_3) vacancies act as trap centers leading to carrier recombination and finally poor device performance.[31] Sometimes, it is seen that negative capacitance (NC) has a direct correlation with device performance of perovskite based solar cells. Francisco et al. demonstrated how presence of NC in halide perovskites produces deleterious impacts on the device performances.[32]

Yet to be supported by any full proof theory, the phenomenon NC has a controversial character in the research community. Although in ferroelectric and non-ferroelectric materials the appearance of NC corresponds to completely different origins,[33-36] pseudo inductance which generally arises in the high frequency regimes can also make the capacitance value negative sometimes.[37] Internal defects, vacancies, delocalized charge-carriers, etc. can also have their additional contributions.[38] However, most of the impedance studies on these aspects in literature are focused mainly in the low and moderate frequency regimes up to the order of a few tens of MHz. It would be interesting to explore the underlying carrier dynamics and other aspects of $CH_3NH_3PbI_3$ halide perovskite by pushing this frequency limit further particularly in the radio-frequency (RF) regime. Therefore, motivated by this ideology, here in this work, we have performed bias-dependent impedance analysis of $CH_3NH_3PbI_3$ near the radio-frequency (RF) region, keeping also in mind the influence of external electric field on carrier movement and ultimately on the device performance. The switching of capacitance from positive to negative values was observed and the spectra across that neighborhood of the transient frequency were modeled with an equivalent LCR circuit. The frequency-dispersion of capacitance with negative values, when fitted as particular functions of frequency, revealed two interplaying relaxation mechanisms. The asymmetry in the line-shape was further modeled by the well-known Breit-Wigner-Fano (BWF) profile and the obtained results were corroborated with density functional theory (DFT)-based calculations.

8.2. Device preparation and material characterizations

$CH_3NH_3PbI_3$ was prepared by following the synthesis protocol mentioned in section 4.1 whereas $FTO/CH_3NH_3PbI_3/FTO$ was prepared using the procedure as described in section 4.5.

8.3. Results and discussion

8.3.1. Crystallographic and microscopic study
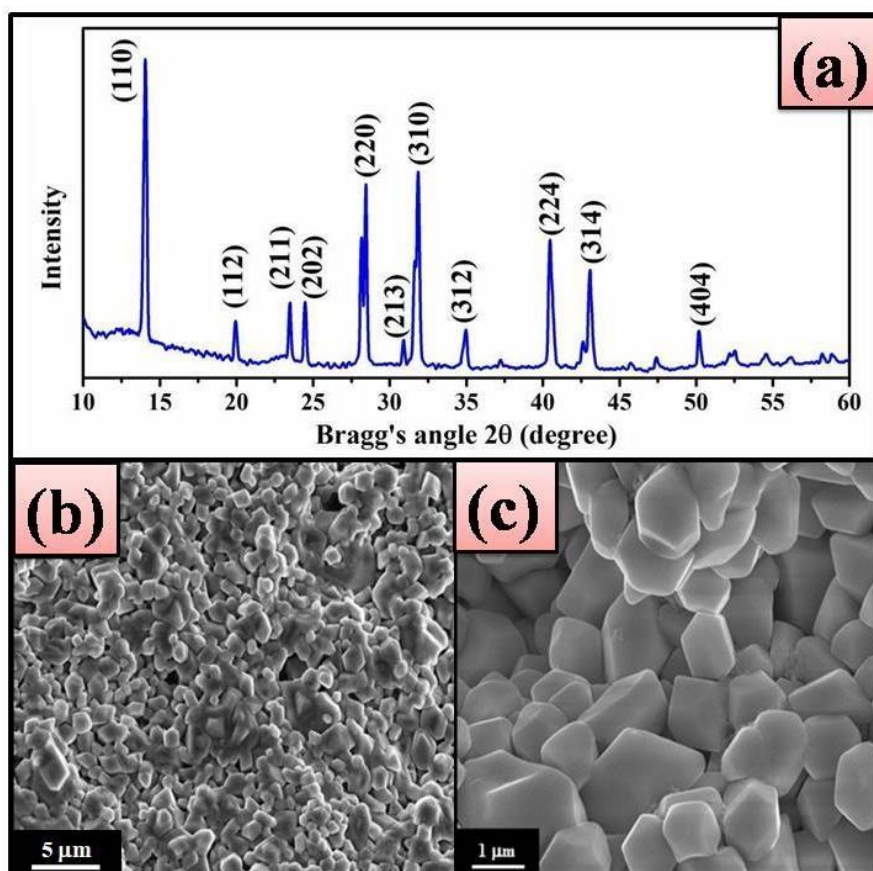
Figure 8.1: (a) XRD profile and (b&c) Low and high magnification FESEM images of $CH_3NH_3PbI_3$

The exhibition of the diffraction peaks, indexed in Figure 8.1a, confirms the formation of $CH_3NH_3PbI_3$ in its room temperature tetragonal phase. Good crystalline quality of the as synthesized $CH_3NH_3PbI_3$ is evident from the distinct diffraction signals [45] along with the polycrystalline nature of the sample. The quality of the crystals can also be checked from its morphological studies. Upon observing under an FESEM microscope, numerous perovskite crystals of the size of ~1 µm are observed (Figures 8.1(b&c)).

8.3.2. Elemental study: XPS
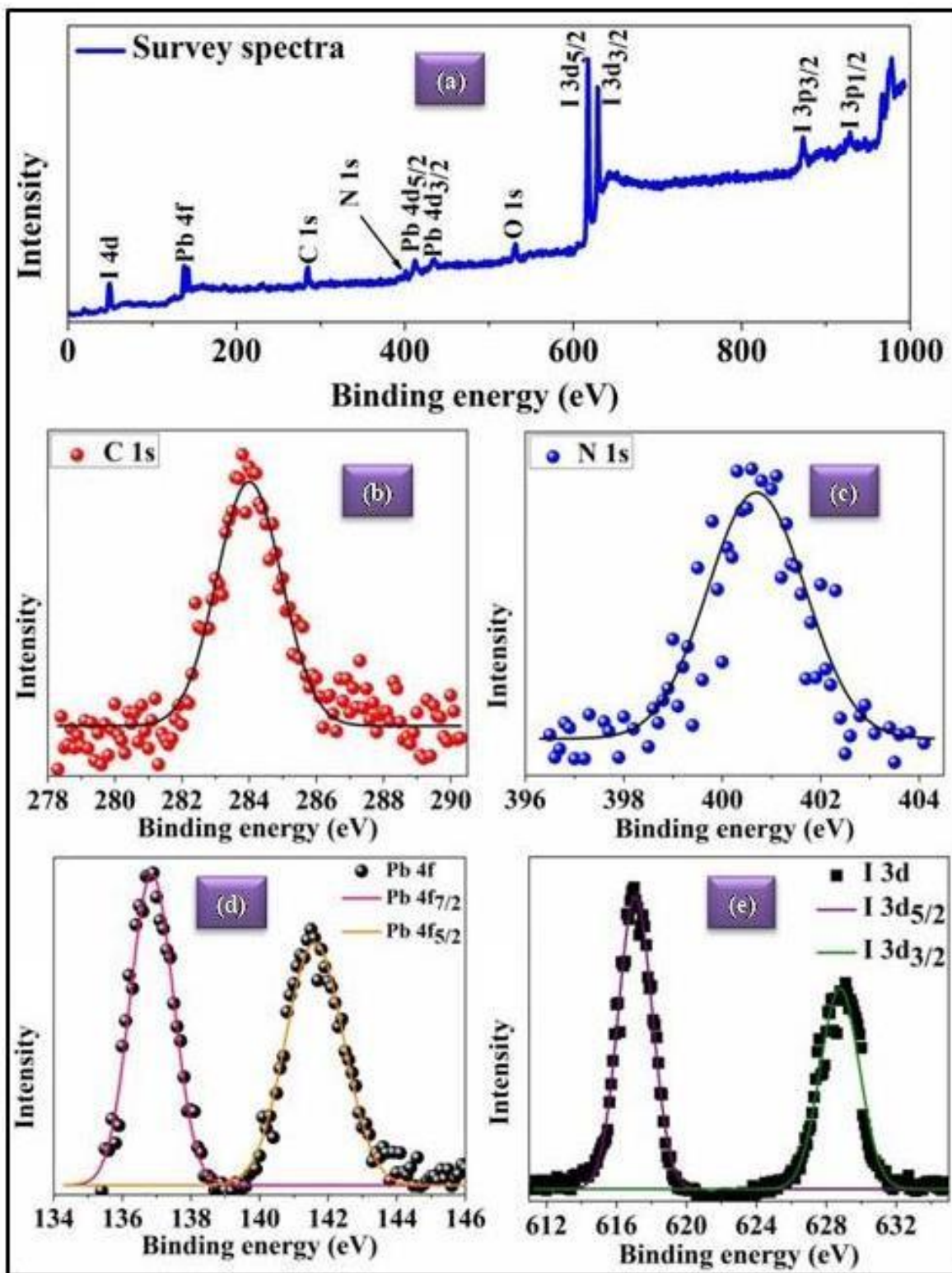
Figure 8.2: (a) Full XPS survey scan of $CH_3NH_3PbI_3$; (b-e) HR XPS spectra of C 1s, N 1s, Pb 4f and I 3d respectively

To investigate the constituent elements of the perovskites, surface probing by X-ray photoelectron spectroscopy (XPS) was carried out. The charge corrected survey scan containing all the elements indexed thereon is displayed in Figure 8.2a. The high resolution (HR) spectra of the individual elements are also provided in Figures 8.2(b-e). The peak situated at 400.7 eV is assigned to N 1s state of $CH_3NH_3PbI_3$. Besides, the peaks observed at 136.9 eV and 141.6 eV, with an energy splitting of 4.7 eV, are attributed to the spin-orbit doublet of Pb $4f_{7/2}$ and $4f_{5/2}$ respectively. XPS peaks arising at 617.1 eV and 628.8 eV are associated with the spin-orbit doublets of I $3d_{5/2}$ and $3d_{3/2}$ respectively, with an observed energy gap of 11.7 eV. The results therefore indicate the typical valence states of the constituents present in $CH_3NH_3PbI_3$, in fair accordance with the reports found in literature.[46-48]

8.3.3. Impedance spectroscopy

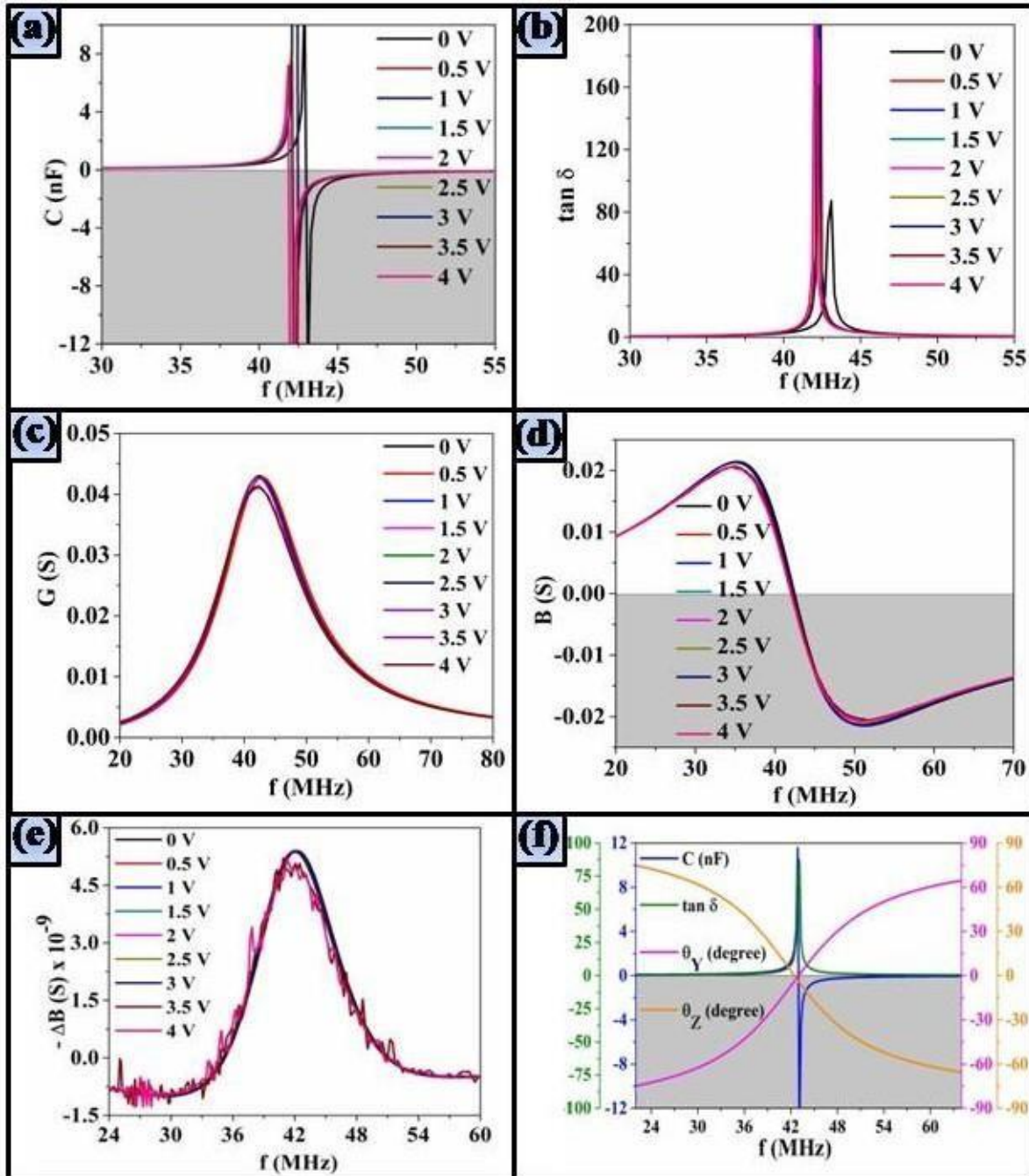The frequency dependent capacitance, loss-tangent, conductance, susceptance, negative differential susceptance and associated phase angles were recorded by the impedance analyzer at different bias voltages. As shown in Figure 8.3a, the capacitance first increases with frequency until a critical or switching frequency (say, f_c) arrives, where it abruptly switches its value from positive to negative. In the negative regime (indicated by the shaded area in Figure 8.3a), capacitance increases asymptotically to its saturation value C (∞). Although the capacitance here seems to be apparently negative, it can't be identified as NC (Negative capacitance). Capacitive impedance, if we recall, is defined in the following way:

$$X_C(\omega) = \frac{1}{j\omega C} , \ \omega = 2\pi f, \ j = \sqrt{(-1)} \tag{8.1}$$

Here, f, ω and C are frequency, angular frequency and capacitance respectively. Putting a negative value for C = -C* (say) in equation (8.1) amounts to inductive interpretation of the system as: $1/j\omega C = 1/j\omega(-C^*) = -1/j\omega C^* = j.j/j\omega C^* = j/\omega C^* = j(1/\omega C^*)$. Therefore, for a particular frequency, the system effectively behaves like an inductor when its familiar ωL part exceeds $1/\omega C^*$. Similarly, the phenomenon which is taking place here is actually inductive in the disguise of NC. However, NC generally originates in the low frequency regimes.[49] But on contrary, the figures here suggest the switching phenomena to be occurring at MHz range. Now capacitive behavior arises in the system due to the Maxwell-Wagner polarization happening across the sample/electrode interface and/or the dielectric peripherals inside the sample. Besides, the inductive effect is the manifestation of the hopping of charge carriers between the localized sites driven by an externally applied electric field.

Figure 8.3: (a-e) Frequency dependent capacitance, tangent loss, conductance, susceptance and negative differential susceptance plots at various DC bias voltages; (f) 4y plot of capacitance, tangent loss, admittance and impedance phase vs. frequency at 0 DC bias voltage

It is the interplay between these two mechanisms which decides the ultimate character (if capacitive or inductive) of the system, depending on the operating signal frequency and the applied bias voltage. Basically, the localized charge carriers which were trapped at the defect sites get energized and detrapped by the externally applied field at high frequency and start

hopping from one site to another through a nonlinear path. As its consequence, what we see macroscopically is that the inductive part dominates and the capacitance switches its sign at a particular frequency (switching frequency). This switching is always accompanied by a sharp peak in the tangent loss spectra which indicates the purely resistive character of the system right at the switching frequency as the capacitive and inductive counterparts precisely balance each other out. At that moment, the entire power delivered by the source is dissipated across the system and undergoes a sudden Dirac delta-type loss peak (Figure 8.3b). The conductance of the system attains a maximum as shown in Figure 8.3c. Figure 8.3d shows the frequency dependent susceptance at different bias voltages. The switching behavior is also prominent from the sharp transitions in susceptance plots. These transition points lead to maxima in the negative differential susceptance plots (Figure 8.3e), which also enables to pinpoint the critical/switching frequencies more precisely. The unbiased frequency dependent capacitance (C), tangent loss (tan δ) and the two phase-angles of admittance and impedance i.e. θ_Y and θ_Z respectively, when presented together in a single plot, gives a beautiful representation of the observed phenomena at a glance (Figure 8.3f). As depicted in the figure, the loss spectrum blows up right at the frequency where the capacitance flips its sign from positive to negative and at the same time, the two phase-angles, which are always out of phase, cross each other.

8.4. Probing the underlying relaxation mechanism

8.4.1. Double relaxation

To probe the underlying mechanism of the observed phenomenon, the negative portion of the capacitance spectra was analyzed separately. In our findings, capacitance in their negative regimes, when fitted, resulted into two characteristic frequencies (f_1, f_2) given by

$$C(f) = C(\infty) + A_1 e^{-f/f_1} + A_2 e^{-f/f_2} \tag{8.2}$$

Here, f is frequency, C(f) is frequency dependent capacitance in negative regime, C(∞) is the limiting value of C(f) as f → ∞ (henceforth, saturation capacitance), A_1 and A_2 are the strengths of these two relaxation modes f_1 and f_2 respectively. As can be seen from Figure 8.4a, the experimental data fitted well with the double relaxation model described by equation (8.2). Similar to the case with no bias voltage, other data also fitted very well under the application of bias voltages up to 4 V (Figure 8.5a). The fitted results for different bias voltages are tabulated in
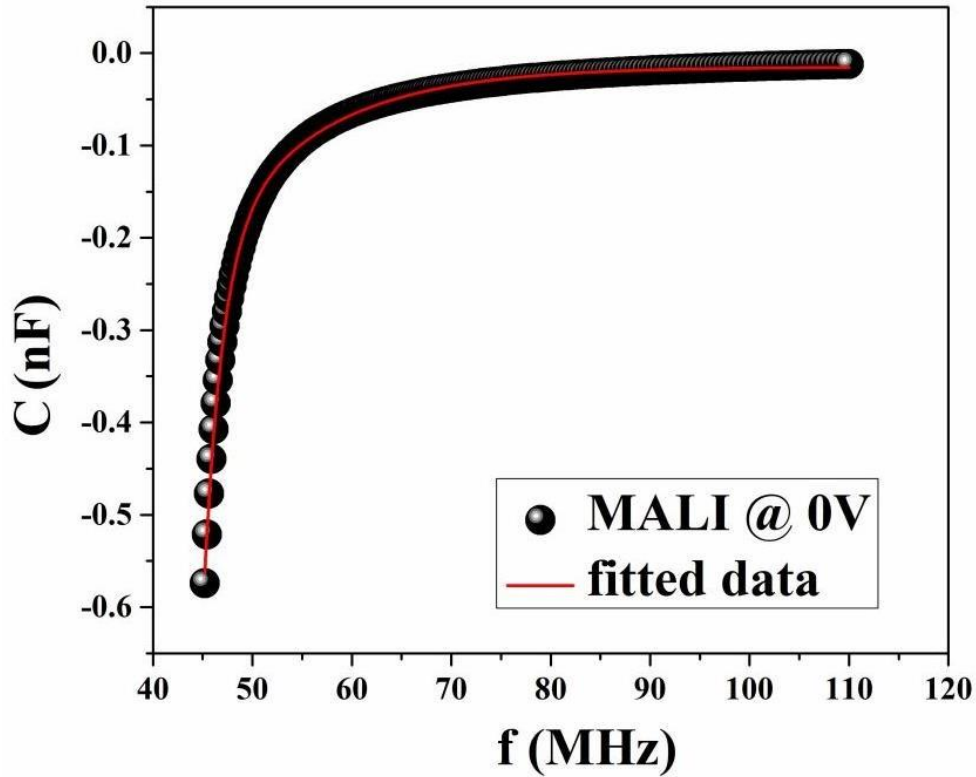
161

Figure 8.4: Fitting of frequency dependent capacitance in negative regime at 0 DC bias voltage
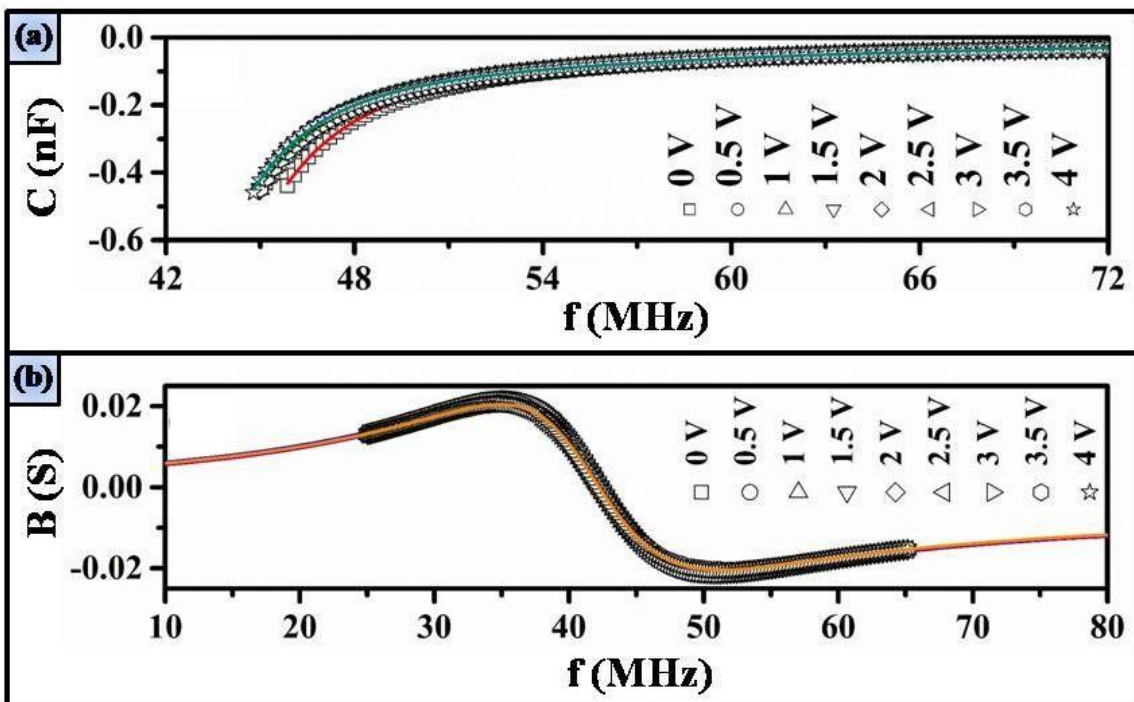

Figure 8.5: Fitted ac (a) capacitance in the negative regime and (b) susceptance at different bias voltages

Table 8.1. The existence of more than one relaxation is not a new phenomenon to us. According to the familiar Debye relaxation model, capacitance varies with frequency as: $C(\omega) = C(\infty) + \frac{\Delta C}{1+\omega^2 c^2}$ where $\Delta C = C(\infty) - C(0)$, τ stands for the relaxation time and $C(0)$ represents the dc limiting value of $C(\omega)$ as $\omega \to 0$ i.e. static capacitance. But this model is based on the assumption of the presence of identical dipoles. Such idealistic scenario is rarely encountered in practice. Hence the actual capacitance of materials deviates from this relationship and several oscillating channels come into the picture instead of one single kind. Sometimes, these oscillators possess distributive nature. The usual Cole-Cole model very elegantly reveals such distributive character of the localized carrier relaxation processes. [23]

Table 8.1: Double relaxation fitting parameters at different bias voltages

Bias voltage (V)	A_1	f_1 (MHz)	A_2 x 10^{-9}	f_2 (MHz)	$C(\infty)$ (pF)	$f_2 : f_1$
0	-2.10	1.98	-8.51	11.62	-13.7	5.87
0.5	-2.10	1.98	-8.51	11.62	-13.7	5.87
1	-4.26	1.95	-9.88	11.45	-14.3	5.87
1.5	-4.95	1.90	-9.71	11.30	-14.1	5.95
2	-5.42	1.89	-9.84	11.28	-14.1	5.96
2.5	-5.52	1.89	-9.87	11.26	-14.1	5.96
3	-5.60	1.89	-9.89	11.26	-14.1	5.96
3.5	-5.25	1.89	-9.80	11.27	-14.1	5.97
4	-13.45	1.82	-10.86	11.03	-14.4	6.10

We have also come across two relaxation processes in the kHz frequency regime due to fast rotation of methylamine groups inside the PbI_6 cage, where the two relaxations are ascribed to longitudinal and transverse types.[50] Distribution in relaxation times of the order of microseconds is also seen to arise because of the recombination of electrons and holes trapped in localized sites through tunneling.[51] Considering all these previous works, we suggest, in our case, these two frequencies (f_1, f_2) to be arising from the two aforesaid relaxation processes i.e. Maxwell-Wagner interfacial polarization leading to the capacitive effect and the detrapped carrier induced polarization leading to the inductive effect, respectively.[52] Attributing the capacitive and inductive effects to f_1 and f_2 respectively and not the other way round as f_2 and f_1, can be understood by the inertia of the respective oscillators. The dipoles involved in the capacitive process mainly consist of bound charge systems which are obviously heavier to respond quickly to the external perturbation signal, while the polarization in the inductive process is developed from the detrapped carriers which are free in the sense that they can tunnel

out of their individual potential wells. Naturally the oscillators involved in the latter case are much lighter and hence oscillate with comparatively higher frequency. Taking the reciprocals of these frequencies, the relaxation times (τ_1, τ_2) of the oscillations for all the bias voltages came to be in the order of microseconds for f_1 and sub-microseconds for f_2. For example, at no bias condition, $(\tau_1, \tau_2) = (f_1, f_2)^{-1} = (1.98 \text{ MHz}, 11.62 \text{ MHz})^{-1} = (0.505\ \mu s, 0.086\ \mu s)$ (values taken from Table 8.1). Both these time scales indicate slow dynamics of the carriers which is very crucial for perovskite materials particularly in connection with its photovoltaic applications.

Hindered charge separation and slow recombination rates result into inferior device qualities e.g. extremely slow response in photoconductivity[53] and small open circuit voltage in solar cells.[54] In this context, various aspects e.g. slow adjustment of the inorganic PbI_6 cage around the field aligned MA^+ ions,[53,55] electron-phonon scattering,[56] coupled ionic-electronic model,[57] interfacial charge recombination and dielectric relaxation,[58] carrier accumulation due to ionic movement near the interfaces[59] are reported by researchers. The saturation capacitance, on the other hand, came to be -13.7 pF when there is no bias applied.

8.4.2. Breit-Wigner-Fano (BWF) anti-resonance

The bias-dependent ac susceptance (Figure 8.3d), which reshapes due to the mutually competing mechanisms associated with the capacitive and inductive behavior, was further analyzed using BWF (Breit-Wigner-Fano) anti-resonance model as defined below.

$$B_f = B_0 + \frac{H\left(1+\frac{f-f_c}{qw}\right)^2}{1+\left(\frac{f-f_c}{w}\right)^2} \tag{8.3}$$

Here, f, B, B_0, H, f_c, w and q represent frequency, susceptance, base, height, centre/switching frequency, line-width and asymmetry parameter of the line shape respectively. As $q \to \infty$, the line shape takes the symmetric BW or Lorentzian structure, whereas $q \to 1$ results in the asymmetric Fano resonance type character. BWF anti-resonance is therefore a combined effect of two distinctive resonance schemes, i.e. Breit-Wigner and Fano resonance structures in the same energy or frequency window whatever, with negative q value. Now Fano resonance typically takes place whenever a rapidly varying resonant process (excitation of a discrete state) interferes with a slowly varying direct or background process (continuum of states). The asymmetry parameter q basically measures how strongly these two processes are coupled to each other. Far from the resonant energy, the process is dominated by the direct scattering process.

In this work, we also have two such processes, i.e. capacitive and inductive. The capacitive behavior arising due to the Maxwell-Wagner polarization can be treated as a continuum, whereas the inductive effect due to the hopping of charge carriers plays the role of discrete state in the system. As evident from Figure 8.5b, the susceptance spectra under different bias voltages showed excellent fitting with the BWF profileiscrete state) interferes with a slowly varying direct or background process (continuum of states).
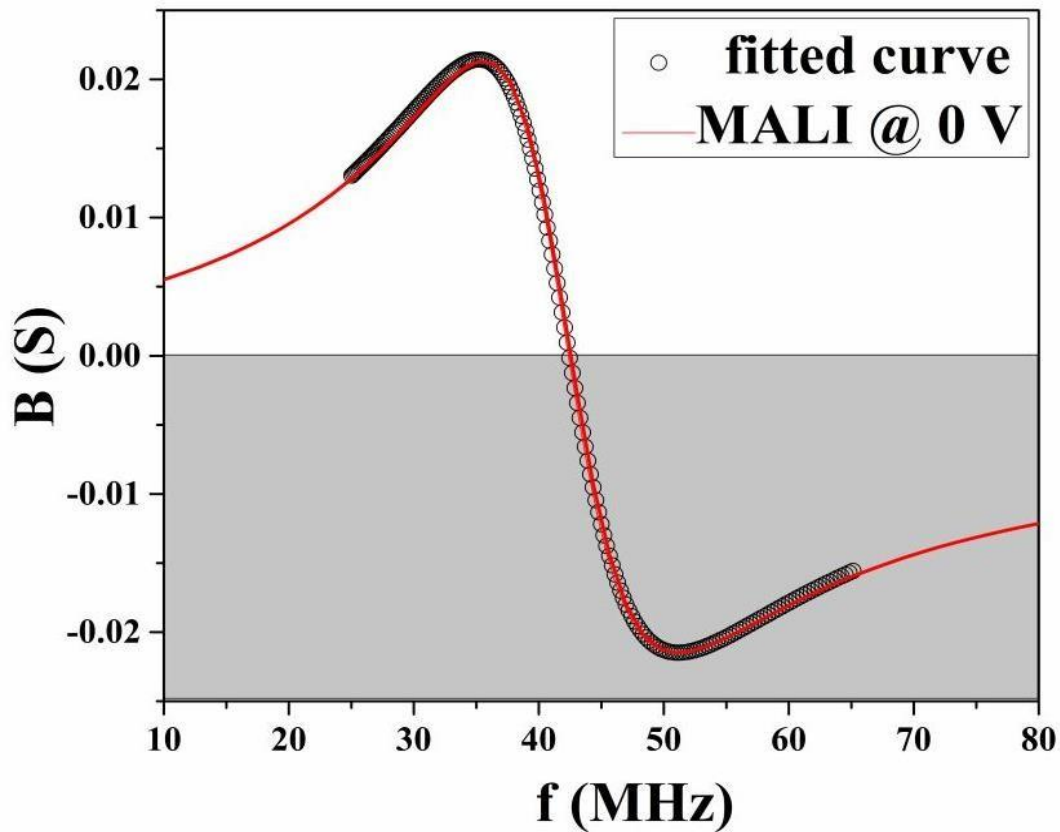
Figure 8.6: Fitting of frequency dependent susceptance at 0 DC bias

From the fitted data of BWF profile (Table 8.2), it is observed that all the spectra have identical q value equal to -1.23. Now q being a measure of the strength of the discrete resonant state over the continuum one, its value greater than 1 in magnitude indicates that the inductive effect dominates over the capacitive one. The identical q value for all the different bias voltages further reveals that the asymmetry of the line shapes and the way the two resonance structures interfere doesn't change.

Table 8.2: BWF fitting parameters at different bias voltages

Bias (V)	B_0 (mS)	f_c (MHz)	H (mS)	w (MHz)	q
0	-21.482	42.493	21.444	7.796	-1.23
0.5	-21.359	42.294	21.352	7.845	-1.23
1	-21.355	42.288	21.350	7.966	-1.23
1.5	-21.351	42.281	21.345	7.968	-1.23
2	-21.350	42.274	21.343	7.970	-1.23
2.5	-21.293	42.254	21.310	7.972	-1.23
3	-21.290	42.252	21.307	7.972	-1.23
3.5	-20.793	42.082	20.692	8.013	-1.23
4	-20.613	42.075	20.565	8.292	-1.23

8.5. Bias dependency: Existence of upper threshold

A graphical analysis of (f_1, f_2) as a function of the externally applied bias (Figure 8.7a) deploys similar decreasing trends for both these frequencies with increase in the bias voltage. By increasing voltage from 0 to 4V, the frequency of the 1st relaxation drops from 1.98 to 1.82 MHz, whereas that of the 2nd one decreases from 11.62 to 11.03 MHz, indicating a larger shift in f_2 of 0.59 MHz in comparison with that in f_1 of 0.16 MHz. Therefore, we see that the 2nd oscillator is more sensitive to the external bias compared to the 1st one. This is not peculiar since the 1st oscillator, as we have already identified it with Maxwell-Wagner polarization, deals with the grain cores, their boundaries and the interfacial regions. The material being polycrystalline in nature, the collective capacitive behavior of these grains undergoes hardly any net change with the application of an external bias. In contrast, the 2nd oscillator which represents the inductive behavior of the material shows prominent response to the external bias because of the field dependency of the detrapped carriers. The trap centers or point-defect sites are essentially potential wells, within which the carriers are confined. If sufficiently energized by applying some external electric field, these carriers tunnel out of those wells and hop throughout. The polarization effect generated by this hopping is proportional to the number of field-activated carriers, which are in turn proportional to the strength of the externally applied dc bias. The externally applied bias also modifies the interfacial built-in potential developed due to ion accumulation.[60] Therefore as the external bias strengthens, the trapped carriers take less energy to come out of their trap centers or potential wells. The fall in this energy demand reflects in the lowering of f_2 with increasing bias voltage. Similar decreasing trend in the switching frequency f_c is also seen with the increase in bias voltage (Figure 8.7b).
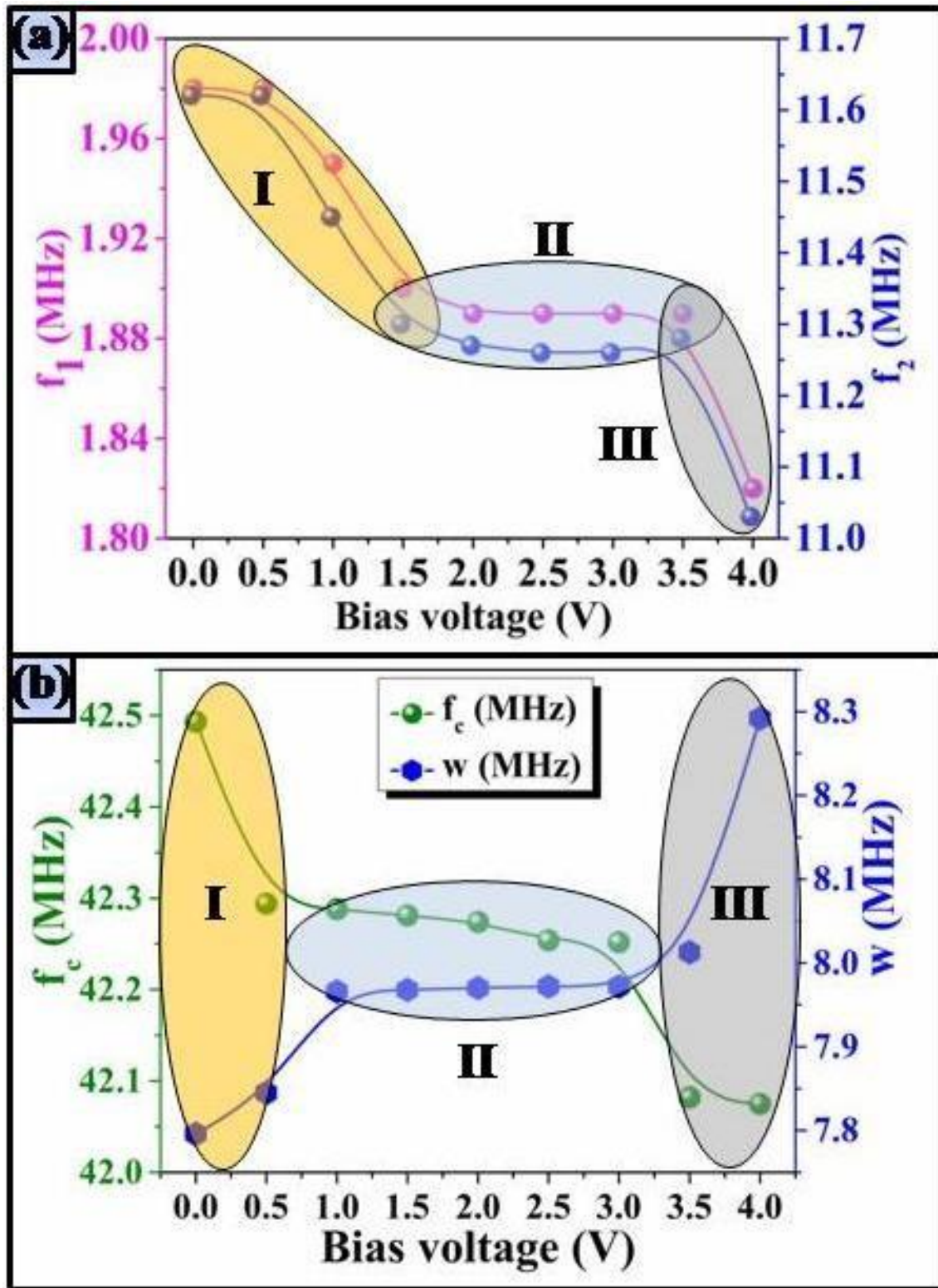
Figure 8.7: Plots of fitting parameters i.e. (a) f_1 and f_2 and (b) f_c and w at various DC bias

The reason behind this red shift of fc is again the same. With increasing strength of the external bias, greater number of carriers gets detrapped from their trap centers, whereas the Maxwell-Wagner polarization which leads to capacitive effect remains almost unaltered with the application/increase in external bias. So, with increased bias, the inductive effect overweighs the capacitive one more easily and thereby scales down the switching frequency to lower values. The variation of BWF line width w against the applied bias voltages is also depicted in Figure 8.7b. It suggests that w, which basically defines the region of interplay of the BWF antiresonance between the two relaxations, increases with the increase in bias voltage. Hence applying an external dc bias in the system effectively makes the two types of oscillators interact over broader frequency range. The behavior of f_1, f_2, f_c and w with external bias were further examined by breaking them into three distinct areas i.e. I-active region, II-equilibrium region and III-breakdown region, as marked out in Figures 8.7(a&b). In the active region (I), the oscillators respond to the external bias and their frequencies keep on changing accordingly. However, such response is not always immediate. A closer look on the region I of Figure 8.7a shows that the kinetics of both the oscillators remains undisturbed until a certain threshold voltage (1 V in our case) is applied in the system. The system needs a minimum energy to trigger the processes on- just like a car standing still on road requires an initial power to drive its engine on. Overcoming this threshold, gradual lowering of the frequencies is observed and then at a certain voltage (1 to 1.5 V in our case) we enter the equilibrium region (II) where the polarizations reach to equilibrium and go on oscillating with a particular frequency. Increase in voltage has no effect on the oscillatory motions in this region. However, further strengthening of the bias voltage leads to the breakdownregion (III) and an upper limit (4V in our case) of the bias voltage appears. The presence of such upper limits of the bias voltage in electrical measurements is quite natural to occur. Above a particular bias, the delocalized/detrapped carriers become high enough to rupture the sample by impact ionization, and finally the sample loses its true semiconducting or insulating nature and becomes an irreversible conductor!

8.6. The equivalent circuit

A device with metal-insulator-metal (MIM) configuration can be modeled as an equivalent LCR circuit.[37] The same goes for our device as well. The simulated spectra of C and tan δ (Figures 8.8a and 8.8b) fitted well with the observed experimental data. However, a little discrepancy arises in the low frequency regimes of the spectra. This is quite natural since the simulation is
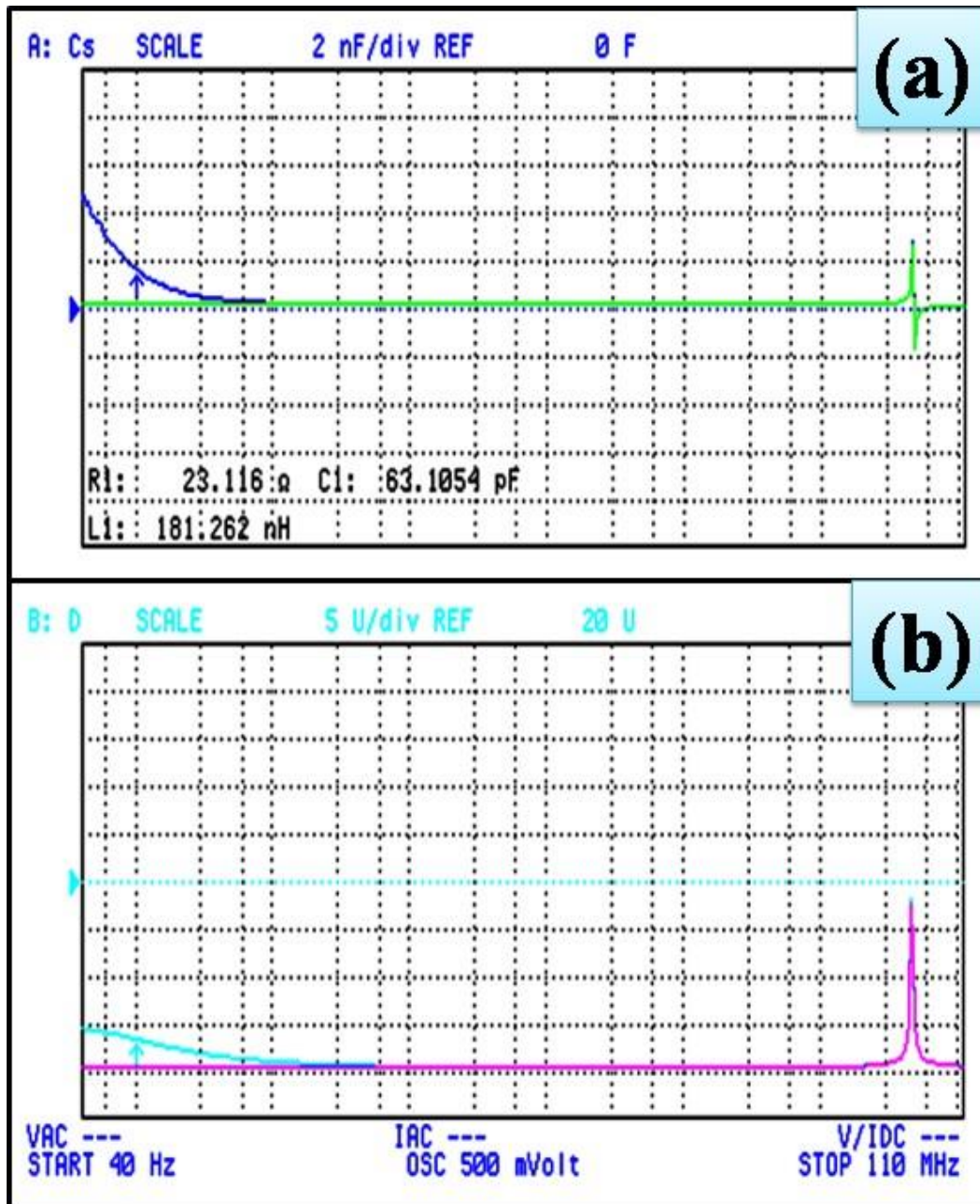
Figure 8.8: Simulated spectra of (a) ac capacitance and (b) tangent loss at 0 DC bias

generally based on the assumption that the sample is a pure crystal. But in practice, there are defects and impurities inside the sample. The simulated spectra can be associated with equivalent circuit with a certain set of LCR parameters. Therefore, the device can effectively be defined in terms of an (L, C, R) triplet i.e. (181 nH, 63 pF, 23 Ω), as obtained in no bias case. Such low inductance value allows the device to be applied as a decoupling capacitor for RF signals. Similar application possibility from oxide perovskite fabricated as MIM (metal- insulator-metal)

structure on Si substrate was also indicated by Emmanuel and his group.[61] Also called a bypass capacitor, this kind of devices is generally used to decouple a particular segment of an electrical circuit from AC signals or sudden voltage surge on a power source. All the unwanted signals are readily shunt right to the ground without affecting the sub-circuit to be protected, whereas the DC part being blocked by the capacitor continues to flow on to the decoupled part of the circuit. Having met the criterion of small inductance and series resistance for a decoupling capacitor, the $CH_3NH_3PbI_3$ based MIM device developed in our study directs to the application possibility of this material as a RF decoupler.

8.7. First principle studies

First principles calculations Vienna ab-initio simulation package (VASP) [39, 40] were carried out to gain further insight into the phenomena observed experimentally. The band structure of MALI calculated within generalized gradient approximation (GGA) and projected augmented wave (PAW) approach[41] is shown in Figure 8.9a, with the exchange- correlation part of the energy Hamiltonian approximated by Perdew–Burke–Ernzerhof (PBE) functional.[42] The correction due to dispersive forces was also taken into account during structural relaxation using the PBE+D2 (Grimme's) method[43] as implemented in the VASP. It is prominent from the band structure that MALI is a direct band gap semiconductor (E_g = 1.54 eV) with both VBM and CBM at the Γ point. Figure 8.9b represents the plot of electron localization function (ELF) where the blue color indicates the isosurface value 0 (min) and red indicates 0.9. The maximum of the isosurface value was set at 0.9. Higher ELF value corresponds to more localized electrons. The localized bond pairs in the C-N bond are visible from this plot. The spherical distribution of the ELF isosurface around 'Pb' readily reveals that all the Pb-I bonds are equivalent. It is also depicted from this plot that electrons are more localized near 'Pb' atom compared to the 'I' atoms, although halide ions have higher electron affinity. This manifests that the iodine atoms are not fixed in the crystal and can migrate through-out the system. As a result, the delocalization of the detrapped carriers and corresponding hopping mechanism become inevitable. Mulliken charge analysis, performed using the Cambridge serial total energy package (CASTEP) code,[44] represented in Figure 8.9c for a (2×2×1) supercell, is in agreement with the as-elaborated perception too.
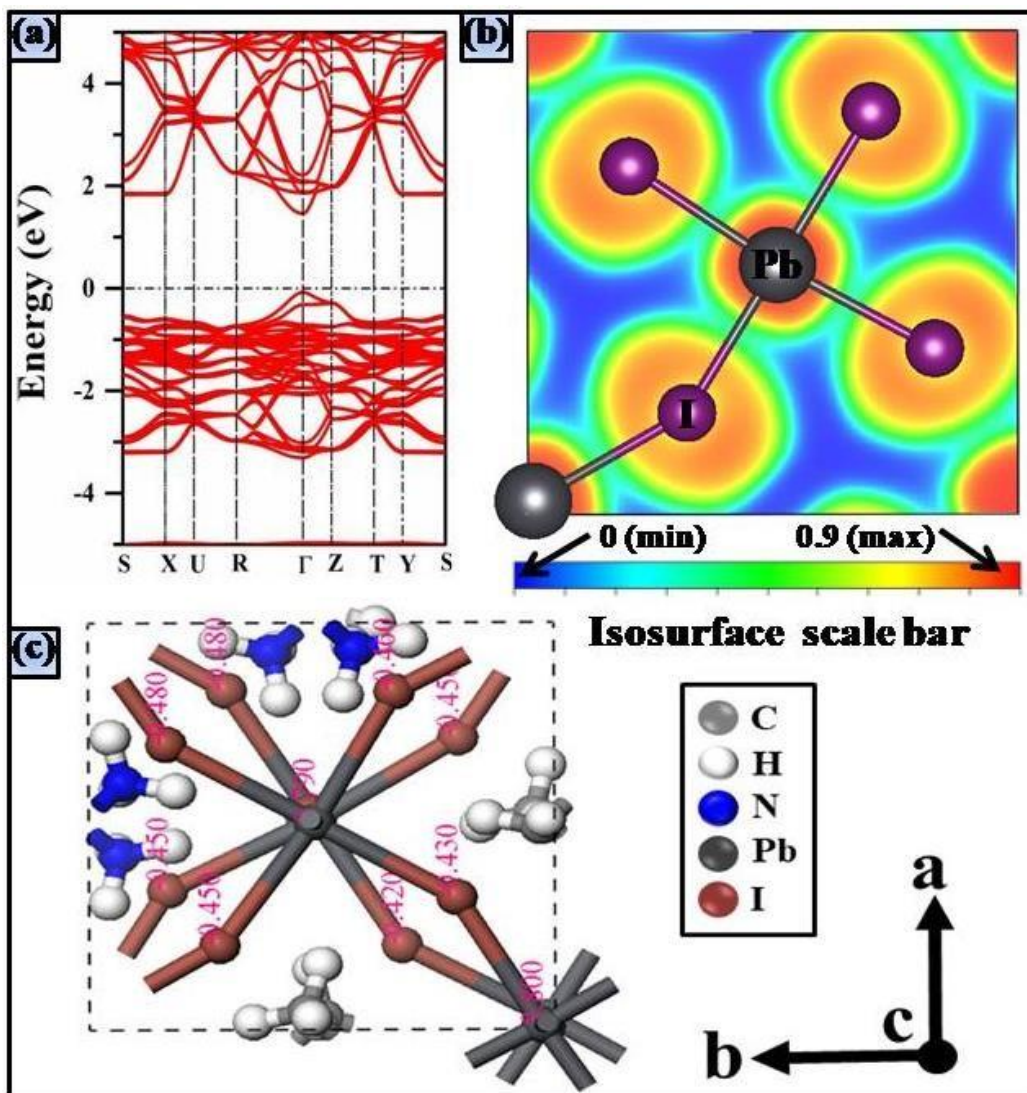
Figure 8.9: (a) Calculated energy band diagram; (b) ELF isosurface plot and (c) Mulliken charge distribution of $CH_3NH_3PbI_3$

8.8. Conclusion

Bias-dependent high frequency impedance analysis of Methyl ammonium lead iodide ($CH_3NH_3PbI_3$) was performed. Apparent NC was identified as switching of capacitance to inductive mode, which was further probed with two coexisting relaxations. The asymmetric susceptance plot followed BWF anti-resonance line shape. The device under investigation, being MIM type, was effectively described by an equivalent LCR circuit. The underlying mechanisms governing Maxwell-Wagner interfacial polarization and delocalized carrier hopping-based polarization are found to be competing mutually through-out the frequency-dispersions, which

are concluded by fitting the obtained data manifesting a number of models. The experimentally obtained results are finally corroborated with theoretical study using energy band diagram, electron localization function and Mulliken charge distribution. In brief, the work mainly highlights the dielectric behavior of $CH_3NH_3PbI_3$ in RF regime and identifies two mutually interfering mechanisms as the cause of capacitive switching which led to pseudo inductive effect. The study also depicts the impact of external bias upon the behavior of these oscillating channels. Looking beyond the trivial photovoltaic applications of halide perovskites, the work indicates that the device could be used as a decoupling capacitor too.

References

[1]   Phillips L J, Rashed A M, Treharne R E, Kay J, Yates P, Mitrovic I Z, Weerakkody A, Hall S and Durose K 2016 Maximizing the optical performance of planar $CH_3NH_3PbI_3$ hybrid perovskite heterojunction stacks *Sol. Energy Mater Sol. Cells* **147** 327-333

[2]   Dong Q, Fang Y, Shao Y, Mulligan P, Qiu J, Cao L and Huang J 2015 Electron-hole diffusion lengths > 175 μm in solution-grown $CH_3NH_3PbI_3$ single crystals *Sci.* **347** 967–970

[3]   D'Innocenzo V, Kandada A R S, Bastiani M D, Gandini M and Petrozza A 2014 Tuning the Light Emission Properties by Band Gap Engineering in Hybrid Lead Halide Perovskite *J. Am. Chem. Soc.* **136** 17730–17733

[4]   Jia X, Hu Z, Zhu Y, Weng T, Wang J, Zhang J and Zhu Y 2017 Facile synthesis of organic–inorganic hybrid perovskite $CH_3NH_3PbI_3$ microcrystals *J. Alloys Compd.* **725** 270–274

[5]   Zhang Y, Kim S G, Lee D K and Park N G 2018 $CH_3NH_3PbI_3$ and $HC(NH_2)_2PbI_3$ Powders Synthesized from Low-Grade PbI_2: Single Precursor for High-Efficiency Perovskite Solar Cells *ChemSusChem* **11** 1813 –1823

[6]   Li X, Li L, Ma Z, Huang J and Ren F 2017 Low-cost synthesis, fluorescent properties, growth mechanism and structure of $CH_3NH_3PbI_3$ with millimeter grains *Optik* **142** 293-300

[7]   Park N G 2015 Perovskite solar cells: an emerging photovoltaic technology *Mater. Today* **18** 65-72

[8]   Wang M, Shi Y, Bian J, Dong Q, Sun H, Liu H, Luo Y and Y Zhang 2016 Electroluminescence from perovskite LEDs with the structure of Ag/Spiro-OMeTAD/CH$_3$NH$_3$PbI$_3$/TiO$_2$/FTO *Chem. Phys. Lett.* **662** 176-181

[9]   Li P, Chen Y, Yang T, Wang Z, Lin H, Xu Y, Li L, Mu H, Shivananju B N, Zhang Y, Zhang Q, Pan A, Li S, Tang D, Jia B, Zhang H and Bao Q 2017 Two-Dimensional CH$_3$NH$_3$PbI$_3$ Perovskite Nanosheets for Ultrafast Pulsed Fiber Lasers *ACS Appl. Mater. Interfaces* **9** 12759–12765

[10]   Gao L, Zeng K, Guo J, Ge C, Du J, Zhao Y, Chen C, Deng H, He Y, Song H, Niu G and Tang J 2016 Passivated Single-Crystalline CH$_3$NH$_3$PbI$_3$ Nanowire Photodetector with High Detectivity and Polarization Sensitivity *Nano Lett.* **16** 7446–7454

[11]   Zhang Y, Du J, Wu X, Zhang G, Chu Y, Liu D, Zhao Y, Liang Z and Huang J 2015 Ultrasensitive Photodetectors Based on Island-Structured CH$_3$NH$_3$PbI$_3$ Thin Films *ACS Appl. Mater. Interfaces* **7** 21634–21638

[12]   Liu Y, Li F, Veeramalai C P, Chen W, Guo T, Wu C and Kim T W 2017 Inkjet-Printed Photodetector Arrays Based on Hybrid Perovskite CH$_3$NH$_3$PbI$_3$ Microwires *ACS Appl. Mater. Interfaces* **9** 11662−11668

[13]   Sun Y, Tai M, Song C, Wang Z, Yin J, Li F, Wu H, Zeng F, Lin H and Pan F 2018 Competition between Metallic and Vacancy Defect Conductive Filaments in a CH$_3$NH$_3$PbI$_3$-Based Memory Device *J. Phys. Chem. C* **122** 6431−6436

[14]   Yoo E J, Lyu M, Yun J H, Kang C J, Choi Y J and Wang L 2015 Memory Devices: Resistive Switching Behavior in Organic–Inorganic Hybrid CH$_3$NH$_3$PbI$_{3−x}$Cl$_x$ Perovskite for Resistive Random Access Memory Devices *Adv. Mater.* **27** 6303

[15]   Kakavelakis G, Gagaoudakis E, Petridis K, Petromichelaki V, Binas V, Kiriakidis G and Kymakis E 2018 Solution Processed CH$_3$NH$_3$PbI$_{3−x}$Cl$_x$ Perovskite Based Self-Powered Ozone Sensing Element Operated at Room Temperature *ACS Sens.* **3** 135−142

[16]   K. Agrawal, V. Gupta and S. S. Rajput, Metal-CH$_3$NH$_3$PbI$_3$-Metal Tunnel FET, *IEEE Trans. on Electron Devices*, 2018, **65,** 1902 – 1909.

[17]   Slonopas A, Ryan H and Norris P 2019 Ultrahigh energy density CH$_3$NH$_3$PbI$_3$ perovskite based supercapacitor with fast discharge *Electrochim. Acta* **307** 334-340

[18]   Besra N, Pal S, Das B K and Chattopadhyay K K 2017 Perovskites beyond photovoltaics: field emission from morphology-tailored nanostructured methylammonium lead triiodide *Phys. Chem. Chem. Phys.* **19** 26708-26717

[19]   Yang J, Siempelkamp B D, Liu D and Kelly T L 2015 Investigation of CH$_3$NH$_3$PbI$_3$ Degradation Rates and Mechanisms in Controlled Humidity Environments Using in Situ Techniques *ACS Nano* **9** 1955–1963

[20]   Shirayama M, Kato M, Miyadera T, Sugita T, Fujiseki T, Hara S, Kadowaki H, Murata D, Chikamatsu M and Fujiwara H 2016 Degradation mechanism of CH$_3$NH$_3$PbI$_3$ perovskite materials upon exposure to humid air *J. Appl. Phys.* **119** 115501

[21]   Sharada G, Mahale P, Kore B P, Mukherjee S, Pavan M S, De C, Ghara S, Sundaresan A, Pandey A, Row T N G and Sarma D D 2016 Is CH$_3$NH$_3$PbI$_3$ Polar? *J. Phys. Chem. Lett.* **7** 2412–2419

[22]   Fan Z, Xiao J, Sun K, Chen L, Hu Y, Ouyang J, Ong K P, Zeng K and Wang J 2015 Ferroelectricity of CH$_3$NH$_3$PbI$_3$ Perovskite *J. Phys. Chem. Lett.* **6** 1155–1161

[23]   Sheikh M S, Sakhya A P, Dutta A and Sinha T P 2017 Dielectric relaxation of CH$_3$NH$_3$PbI$_3$ thin film *Thin Solid Films* **638** 277–281

[24]   Heo J H, You M S, Chang M H, Yin W, Ahn T K, Lee S J, Sung S J, Kim D H and Im S H 2015 Hysteresis-less mesoscopic CH$_3$NH$_3$PbI$_3$ perovskite hybrid solar cells by introduction of Li-treated TiO$_2$ electrode *Nano Energy* **15** 530-539

[25]   Shen H, Jacobs D A, Wu Y, Duong T, Peng J, Wen X, Fu X, Karuturi S K, White T P, Weber K and Catchpole K R 2017 Inverted Hysteresis in CH$_3$NH$_3$PbI$_3$ Solar Cells: Role of Stoichiometry and Band Alignment *J. Phys. Chem. Lett.* **8** 2672–2680

[26]   Wu B, Fu K, Yantara N, Xing G, Sun S, Sum T C and Mathews N 2015 Charge Accumulation and Hysteresis in Perovskite-Based Solar Cells: An Electro-Optical Analysis *Adv. Energy Mater.* **5** 1500829

[27]   Chen B, Yang M, Zheng X, Wu C, Li W, Yan Y, Bisquert J, Belmonte G G, Zhu K and Priya S 2015 Impact of Capacitive Effect and Ion Migration on the Hysteretic Behavior of Perovskite Solar Cells *J. Phys. Chem. Lett.* **6** 4693−4700

[28]   Contreras L, Idígoras J, Todinova A, Salado M, Kazim S, Ahmad S and Anta J A 2016 Specific Cation Interactions as the Cause of Slow Dynamics and Hysteresis in Dye and Perovskite Solar Cells: a Small-Perturbation Study *Phys. Chem. Chem. Phys.* **18** 31033-31042

[29]   Edmands J B, Eperon G E, Johnson R D, Snaith H J and Radaelli P G 2015 Non-ferroelectric nature of the conductance hysteresis in CH$_3$NH$_3$PbI$_3$ perovskite-based photovoltaic devices *Appl. Phys. Lett.* **106** 173502

[30] Yadav P, Prochowicz D, Saliba M, Boix P P, Zakeeruddin S M and Grätzel M 2017 Interfacial Kinetics of Efficient Perovskite Solar Cells *Crystals* **7** 252

[31] Pant N, Kulkarni A, Yanagida M, Shirai Y, Miyasaka T and Miyano K 2019 Investigating the Growth of $CH_3NH_3PbI_3$ Thin Films on RF-Sputtered NiO_x for Inverted Planar Perovskite Solar Cells: Effect of $CH_3NH_3^+$ Halide Additives versus $CH_3NH_3^+$ Halide Vapor Annealing *Adv. Mater. Interfaces* 1901748

[32] Santiago F F, Kulbak M , Zohar A , Pelarda M V, Hodes G, Cahen D and Seró I M 2017 Deleterious Effect of Negative Capacitance on the Performance of Halide Perovskite Solar Cells *ACS Energy Lett.* **2** 2007–2013

[33] Khan A, Chatterjee K and Wang B 2015 Negative capacitance in a ferroelectric capacitor *Nat. Mater.* **14** 182–186

[34] Zubko P, Wojdeł J, Hadjimichael M, Pena S F, Sené A , Luk'yanchuk I , Triscone J M and Íñiguez J 2016 Negative capacitance in multidomain ferroelectric superlattices *Nature* **534** 7608

[35] Bhattacharjee S, Banerjee A, Mazumder N, Chanda K, Sarkar S and Chattopadhyay K K 2020 Negative capacitance switching in size-modulated Fe_3O_4 nanoparticles with spontaneous non-stoichiometry: confronting its generalized origin in non-ferroelectric materials *Nanoscale* **12** 1528-1540

[36] Mazumder N, Mandal P, Roy R, Ghorai U K, Saha S and Chattopadhyay K K 2017 Negative capacitance in $ZnO_{1-x}Ch_x$ (Ch= S, Se, Te): Role of localized charge recombination *J. Appl. Phys.* **121** 135702

[37] Emmanuel D, Floria B, Christophe B, Charles F, Baptiste D J, Laurent L and Ludivine G 2004 Integrated MIM Perovskite Capacitors for RF Applications *Integr. Ferroelectr.* **66** 231–242

[38] Mitra D, Bhattacharjee S, Mazumder N, Das B K, Chattopadhyay P and Chattopadhyay K K 2020 Strain-induced partial phase transition in TiO_2 nanoparticles manifesting frequency dispersive pseudo-inductive switching of capacitance *Ceram. Int.* **46** 20437-20447

[39] Kresse G and Hafner J 1993 Ab initio molecular dynamics for liquid metals *Phys. Rev. B* **47** 558-561

[40] Kresse G and Hafner J 1994 Ab initio molecular-dynamics simulation of the liquid-metal–amorphous-semiconductor transition in germanium *Phys. Rev. B* **49** 14251-14269

[41]   Blöchl P E 1994 Projector augmented-wave method *Phys. Rev. B* **50** 17953-17979

[42]   Perdew J P, Burke K and Ernzerhof M 1996 Generalized Gradient Approximation Made Simple *Phys. Rev. Lett.* **77** 3865-3868

[43]   Grimme S 2006 Semiempirical GGA-type density functional constructed with a long-range dispersion correction *J. Comput. Chem.* **27** 1787-1799

[44]   Segall M, Lindan P J, Probert M J, Pickard C, Hasnip P, Clark S and Payne M 2002 First-principles simulation: ideas, illustrations and the CASTEP code *J. Phys. Condens. Matter* **14** 2717-2744

[45]   Sewvandi G A, Hu D, Chen C, Ma H, Kusunose T, Tanaka Y, Nakanishi S and Feng Q 2016 Antiferroelectric-to-Ferroelectric Switching in $CH_3NH_3PbI_3$ Perovskite and Its Potential Role in Effective Charge Separation in Perovskite Solar Cells *Phys. Rev. Appl.* **6** 024007

[46]   Ahmad Z, Najeeb M A, Shakoor R A, Alashraf A, Al-Muhtaseb S A, Soliman A and Nazeeruddin M K 2017 Instability in $CH_3NH_3PbI_3$ perovskite solar cells due to elemental migration and chemical composition changes *Sci. Rep.* **7** 15406

[47]   Li Y, Xu X, Wang C, Ecker B, Yang J, Huang J and Gao Y 2017 Light-Induced Degradation of $CH_3NH_3PbI_3$ Hybrid Perovskite Thin Film *J. Phys. Chem. C* **121** 3904–3910

[48]   Naumkin A V, Kraut-Vass A, Gaarenstroom S W and Powell C J 2012 *NIST Standard Reference Database 20, NIST, Gaithersburg, Md, USA* **Version 4.1**

[49]   Ershov M, Liu H, Li L, Buchanan M, Wasilewski Z and Jonscher A K 1998 Negative capacitance effect in semiconductor devices *IEEE Trans. Electron Devices* **45** 2196–2206

[50]   Roiland C, Allard G T, Jemli K, Alonso B, Ameline J C, Gautier R, Bataille T, Pollès L L, Deleporte E, Even J and Katan C 2016 Multinuclear NMR as a Tool for Studying Local Order and Dynamics in $CH_3NH_3PbX_3$ (X = Cl, Br, I) Hybrid Perovskites *Phys. Chem. Chem. Phys.* **18** 27133-27142

[51]   Saxena R, Kumar A, Jain N, Kumawat N K, Narasimhan K L and Kabra D 2018 Photophysical Model for Non-Exponential Relaxation Dynamics in Hybrid Perovskite Semiconductors *J. Phys. Chem. C* **122** 1119-1124

[52]   Wang C C, Liu G Z, He M and Lu H B 2008 Low-frequency negative capacitance in $La_{0.8}Sr_{0.2}MnO_3$/Nb-doped $SrTiO_3$ heterojunction *Appl. Phys. Lett.* **92** 052905

[53] Gottesman R, Haltzi E, Gouda L, Tirosh S, Bouhadana Y, Zaban A, Mosconi E and Angelis F D 2014 Extremely Slow Photoconductivity Response of $CH_3NH_3PbI_3$ Perovskites Suggesting Structural Changes under Working Conditions *J. Phys. Chem. Lett.* **5** 2662-2669

[54] Mohammadian N, Moshaii A, Alizadeh A, Gharibzadeh S and Mohammadpour R 2016 Influence of Perovskite Morphology on Slow and Fast Charge Transport and Hysteresis in the Perovskite Solar Cells *J. Phys. Chem. Lett.* **7** 4614-4621

[55] Sanchez R S, Pedro V G, Lee J W, Park N G, Kang Y S, Sero I M and Bisquert J 2014 Slow Dynamic Processes in Lead Halide Perovskite Solar Cells, Characteristic Times and Hysteresis *J. Phys. Chem. Lett.* **5** 2357-2363

[56] Zheng F, Tan L Z, Liu S and Rappe A M 2015 Rashba Spin–Orbit Coupling Enhanced Carrier Lifetime in $CH_3NH_3PbI_3$ *Nano Lett.* **15** 7794-7800

[57] Pockett A, Eperon G E, Sakai N, Snaith H J, Peter L M and Cameron P J 2017 Microseconds, milliseconds and seconds: deconvoluting the dynamic behavior of planar perovskite solar cells *Phys. Chem. Chem. Phys.* **19** 5959-5970

[58] Pascoe A R, Duffy N W, Scully A D, Huang F and Cheng Y B 2015 Insights into Planar $CH_3NH_3PbI_3$ Perovskite Solar Cells Using Impedance Spectroscopy *J. Phys. Chem. C* **119** 4444−4453

[59] Contreras L, Idígoras J, Todinova A, Salado M, Kazim S, Ahmad S and Anta J A 2016 Specific cation interactions as the cause of slow dynamics and hysteresis in dye and perovskite solar cells: a small-perturbation study *Phys. Chem. Chem. Phys.* **18** 31033-31042

[60] Tress W, Marinova N, Moehl T, Zakeeruddin S M, Nazeeruddin M K and Gratzel M 2015 Understanding the rate-dependent J–V hysteresis, slow time component, and aging in $CH_3NH_3PbI_3$ perovskite solar cells: the role of a compensated electric field *Energy Environ. Sci.* **8** 995-1004

[61] Emmanuel D, Floria B, Christophe B, Charles F, Jean-Baptiste D, Laurent L and Ludivine G 2004 Integrated MIM Perovskite Capacitors for RF Applications *Integr. Ferroelectr.* **66** 231-242

Summary and Future Outlook

9.1. Summary of the work

To summarize, this thesis work describes facile wet chemical synthesis approaches to prepare organic-inorganic hybrid metal halide perovskites such as Methylammonium lead halide and to fabricate some devices thereof. Moreover, some application aspects have also been explored and discussed here. Chapter 1 starts with a basic and preliminary introduction of the perovskite structures, their classifications, etc. It also sketches a brief profile of the emergence and applicational importance of Methylammonium lead halide amongst perovskite family. Along with the benefits of easy synthesis protocols and large band gap tuning, the chapter also covers some of its intriguing properties and current challenges. The chapter finally concludes with the thesis objective and its organization structure. Chapter 2 mainly deals with the literature survey on few topics such as the adopted material synthesis procedures, application of the material under interest in electron field emission and photodetection, with a brief idea of these two application segments. The chapter also gives short account of the impedance studies and charge relaxation mechanisms as reported by various research groups working in this field. The chapter ends by describing the effect of cation and halide mixing and the strategies taken to stabilize the material against environmental factors. Chapter 3 basically presents the materials synthesis and devices fabrication procedures followed in this work, with schematic pictures given where ever felt necessary. All the used characterization methods and the associated instrumental facilities are discussed in chapter 4 briefly. The lack and necessity of exploring electron field emission from such perovskite materials was realized and hence, detail investigation in this direction was carried out which is contained in chapter 5. Corroborated with simulation findings, it shows prominent and stable field emission properties of room temperature solution processed methylammonium lead iodide nanostructures, with turn on of 4.2 V/μm. Chapter 6 gives a thorough description on how this emission performance could be further enhanced by tuning the emitter morphology in a certain way. As described in this chapter, $CH_3NH_3PbI_3$ vertical NRs

were synthesized using AAO template from which considerable electron emission was achieved with 3.4 V/μm turn on field and maximum current density reaching up to 230μA/cm^2. The turn-on field came to be lower as compared to the earlier investigation which involved randomly oriented $CH_3NH_3PbI_3$ NRs. Alignment of the nanostructures towards only a particular direction was assigned to be the key factor for producing this improved emission. Further investigation under different light intensities revealed sensitive optoelectronic behavior of $CH_3NH_3PbI_3$, which was finally supported with theoretical simulation of the local electric field distribution near the NRs emitters. Increased photo-excited carriers led to gradual lowering of turn on field up to 2.8 V/μm under light intensity of 0.5mW/cm^2. Chapter 7 addresses degradation of perovskite photodetectors under ambient moisture or water species and demonstrates improvement of photodetection performance with robust moisture resistance by low dimensional V_2O_5 incorporation into $CH_3NH_3PbI_3$. The improvement was ascribed to higher interfacial built-in potential, better charge separation and low resistive channels formation by V_2O_5 nanorods. Enhanced system stabilization against environmental water species was probed by contact angle measurement which revealed hydrophic nature of the V_2O_5 modified perovskite owing to higher surface roughness. Chapter 8 furnishes the bias dependent impedance spectroscopy which was attempted to unlock the associated relaxation mechanisms particularly in radio frequency regime. As it describes, two relaxation entities were identified from the frequency dependency of capacitance which manifested into capacitive/inductive switching in form of pseudo-negative capacitance due to their mutual interference in anti-resonance shape.

9.2. Future outlook of the work

The electron field emission performance obtained from $CH_3NH_3PbI_3$ nanostructures seeks more research attention. Employing AAO template for synthesizing uniform and scalable emitters can be a good technique to extend this exploration area further to other perovskites as well. Tuning the emission behavior by controlling light illumination upon such materials is another interesting field which must be taken up further. More attempts should be taken to stabilize and improve the photodetection performance of hybrid metal halide perovskites. A holistic approach, which can address all the degradation factors and also can improve the device performance at the same time, is what we are looking at in coming future. The application possibility of methylammonium lead iodide to be used as a decoupling capacitor in an electrical circuit paves the way for similar expeditions with other perovskite materials.